EXPERIMENTAL INVESTIGATIONS OF MOLECULE-MOLECULE AND ELECTRON-MOLECULE SCATTERING

Thesis by

Michael John Coggiola

In Partial Fulfillment of the Requirements

for the Degree of

Doctor of Philosophy

California Institute of Technology

Pasadena, California

1975

(Submitted September 19, 1974)

To My Parents

ACKNOWLEDGMENTS

While this thesis bears only the name of a single author, it is nonetheless the product of the combined efforts of many. Foremost among these is Aron Kuppermann who, as advisor, colleague, and friend has provided me with the essential ingredients needed in the course of this work. These include guidance, support, enlightenment, encouragement, and especially, faith in my ability.

I wish to express my thanks to Professors Dan Winicur and Bob Gordon for their help in many aspects of the work described in Part I. Similar thanks must be accorded to Oren Mosher and Wayne Flicker without whose assistance, the work of Part II would not have been possible. More important to me than their cooperation as scientists, though, has been their understanding as friends. Both Jon Burke and Don Mintz must likewise be counted among the latter. I can truthfully say that my association with this research group has been a source of enjoyment to me, and that each member, both past and present, is due acknowledgment.

Among all those I have come to know here at Caltech, it is Joel Bowman to whom I owe the greatest debt of gratitude. His knowledge and scientific acumen have been a constant source of help, and his friendship and humor a constant source of pleasure. He and

his wife Karen are deserving of more than this simple acknowledgment.

As are all the experimentalists of this group, I am indebted to the many support personnel throughout this Institute. It is with much pleasure and respect that I thank Mr. William W. T. Schuelke, and the members of his instrument shop, especially Anton Stark and Villy Jorgensen. Their many talents have meant the difference between failure and success.

I wish to thank the Department of Chemistry, the Shell Oil Company, and the Atomic Energy Commission for their financial support throughout the course of this work.

Finally, I wish to thank my family and friends for their unending support which has meant so much to me, especially Elaine, Tom, and Jon.

ABSTRACT

Part I. Crossed molecular beam methods have been used to measure the differential elastic scattering of molecular hydrogen and deuterium with a number of diatomic and polyatomic secondary molecules. In particular, $H_2 + O_2$, SF_6, NH_3, H_2O, CO, and CH_4 and $D_2 + O_2$, SF_6, NH_3, and H_2O were all studied using thermal energy beams. The $H_2 + NH_3$ and $H_2 + SF_6$ systems were further studied using an H_2 beam cooled to liquid nitrogen temperature. In addition, the $H_2 + SF_6$ system was remeasured using a beam of cooled para-hydrogen in place of the normal-hydrogen. These studies cover a wide range of anisotropy, size and initial relative collision energy of the scattering partners, as well as the corresponding de Broglie wavelengths. Each system studied yielded rapid quantum oscillations in the differential cross section which were used to determine central-field intermolecular potentials. These potentials were found to be independent of the energy and the hydrogen isotope used as well as their assumed mathematical form. As a result, the effects of anisotropy on the differential elastic scattering of these H_2 and D_2 systems do not seem important.

Part II. Variable angle electron impact spectroscopy has been applied to the systematic study of the electronic structure of the fluoroethylenes. Excitation spectra were obtained at 40 eV and 20 eV

or 25 eV impact energies, and scattering angles from 0° to 80°. Each of the molecules shows an absorption maximum between 4.2 eV and 4.7 eV, corresponding to the singlet→triplet, $\pi \rightarrow \pi^*$ transition similar to the N→T transition seen in ethylene. A weak absorption at 6.45 eV observed only in monofluoroethylene is assigned to the second singlet→triplet transition. Also observed in each spectrum is the strong singlet→singlet N→V transition, as well as a number of Rydberg features. Beyond the first ionization potential, a number of broad absorption features are observed in each molecule, corresponding to superexcited state transitions. Using a method based on term values, a number of these transitions have been assigned to Rydberg series converging to higher ionization potentials. The implications of these results for the photochemistry of the fluoroethylenes is also discussed.

Chlorotrifluoroethylene has also been studied by the electron impact method, and the results are similar to those found for trifluoroethylene.

TABLE OF CONTENTS

PART I

The Determination of Intermolecular Potentials from Crossed Molecular Beam Elastic Scattering

PART II

Electronic Escitation Spectroscopy of the Fluorine-Substituted Ethylenes by Electron Impact

PART I

THE DETERMINATION OF INTERMOLECULAR POTENTIALS BY CROSSED MOLECULAR BEAM ELASTIC SCATTERING

1. INTRODUCTION

1.1 The Study of Intermolecular Forces

It has long been recognized that an understanding of the nature of the forces acting between atoms and molecules is essential to the understanding of a wide variety of phenomena. In fact, most dynamical, non-equilibrium and steady-state equilibrium properties and characteristics of gaseous, liquid and solid systems depend upon the interactions between individual particles as described by a potential energy function. Despite this fundamental role which the intermolecular (or interatomic) potential has in the description of many physical and chemical properties, very little accurate quantitative information on these potentials is available. This deficiency exists both with respect to theoretical and experimental information. While the concept of an interaction potential between two particles is relatively simple, no straightforward methods exist for its determination.

It is important to realize that while many types of phenomena are directly governed by the interaction potential, no direct measurement of that potential is possible. However, it is possible to make an experimental observation of some property which can be related theoretically to the intermolecular potential function. Once such a theoretical connection has been established, and the experimental observations made, it becomes necessary to extract the desired information from the data with a high degree of accuracy. In general, it is not possible to reconstruct uniquely a potential function from the observed properties of a system. As Mason and Monchick [1] have

pointed out, the situation may be regarded as a mapping procedure, where the interaction potential becomes mapped into some observable property. As will be discussed below, this mapping procedure often takes the form of multiple integrals involving the intermolecular potential. These integrations (for that matter, even a single integration) destroy the one-to-one correspondence of the mapping, and hence a direct inversion of the experimental data may not yield a unique potential function. Even in those few cases where a direct inversion is possible (see Section 3.4), no guarantee of uniqueness exists.

In the face of these restrictions, the generally adopted procedure is to assume a fixed mathematical form for the potential function, and then to apply the appropriate theoretical treatment to generate results which may be directly compared with the experimental observations. Using some convenient method, the variable parameters of the model function are adjusted until satisfactory agreement is obtained between theory and experiment. The success of this procedure requires that several conditions be met. First, the model potential function used must be of a realistic nature (see Chapter 2) if the results are to have any physical significance. Also, the theory which is used to connect this model function to the experimental data must be sufficiently rigorous to account for the observed processes. Finally, the measured properties of the system must be sensitive to the quantitative nature of the intermolecular potential which is to be determined. The degree of sensitivity often determines the accuracy with which information about the interaction potential may be learned.

From the theoretical point of view, the accurate calculation of an intermolecular potential is possible, at least in principle, by solving the exact quantum mechanical Schrödinger equation. In practice, of course, only the most simple systems (such as two ground state hydrogen atoms) are exactly soluble. These calculations first require a determination of the nature of the types of interactions (dipole-dipole, spin-orbit, electronic-nuclear, etc.) which contribute to the overall potential. Once these effects are identified as being important, a means must be found to determine the magnitude of the contribution of each. For this purpose, ab initio, semiempirical and model type calculations are used, depending on the degree of difficulty involved. Often, the intermolecular potential is not entirely determined by one method, but rather long- and short-range segments are calculated by different means and then joined together. The accuracy and reliability of these theoretical determinations of intermolecular potentials vary greatly with the system and the method employed. A closer look at several of these theoretical results will be taken in the next chapter on intermolecular potentials.

With respect to the experimental determination of intermolecular potentials, a number of commonly used methods are summarized below, including the technique of molecular beams, which is the focus of this work.

1.2 Methods of Determining Intermolecular Potentials

During the past fifty years, many varied techniques have been developed and refined for the study of intermolecular potentials.

Several of these methods are based on the observations of macroscopic bulk properties of systems, while other methods are more closely related to the direct interaction of particles on a microscopic level. Depending on the method, the system, and the experimental conditions, different segments of the potential function may be probed. As a result, some techniques are better suited for studying short-range (attractive and repulsive) interactions while other methods yield information mainly about the long-range (attractive) interactions. In addition, some methods will only be sensitive to the overall shape of the potential, while others will be sensitive to the quantitative features of the potential. Clearly, the best methods will be those which can yield accurate information over the longest range of interaction.

1.2.1 Molecular Beam Scattering

The first use of beams of neutral particles for the study of their gas phase behavior was made in 1911 by Dunoyer [2, 3]. While the method was quite crude, the beam of sodium atoms served to demonstrate the straight line trajectories taken by neutral gas particles. Several years later, Stern began his extensive studies involving molecular beams [4]. He began by studying the distribution of thermal velocities in a beam [5], and progressed to the study of magnetic moments [6, 7], in collaboration with Gerlach. The field began to expand rapidly with the major efforts being made by Stern, Rabi, and Estermann. Many reviews of this early work are now found in the literature [4, 8-14]. It was pointed out by Stern in one of his earliest reports on molecular beam research [15] that this method could

provide valuable information concerning the intermolecular forces which govern the scattering. Despite this early recognition of the usefulness of molecular beam scattering for potential determinations, it is only within the last ten to fifteen years that extensive use of the method has been realized [16]. A partial explanation for this delay was the need for more advanced experimental techniques, such as vacuum systems and sensitive detection methods, to be developed. Also of great significance during this period was the development of the quantum theory of scattering by Massey and co-workers [17, 18].

Before discussing the various types of scattering measurements and their connections with the intermolecular potential, several important points must be made. If the information to be obtained from a scattering experiment is to be of significance for potential determination, then the following prerequisites must also be satisfied: (1) the scattering must be elastic only, that is to say, no energy transfer processes may be allowed to occur. Since at low (thermal) energies, no electronic or vibrational excitation will be energetically possible, and the probability for rotational excitation is much smaller than the elastic process, this condition is easily satisfied. At intermediate and higher energies (0.1 eV and above), some care must be taken to measure only the elastic scattering. In some cases, the possibility of chemical reactions must also be considered [19]. (2) Only a single electronic energy surface must be involved in the scattering. If two or more surfaces are involved, as would be the case with the ionic and covalent curves of an alkali and

a halogen, the scattering is much more complicated, and the desired potential information may not be simply obtained. Recently, however, work involving such systems has begun to produce useable information on the several potential functions involved [20]. (3) An important assumption which is at the heart of the usefulness of the beam method, is that of single encounters. If the observed scattering is the result of multiple collisions, then ability to describe the process by the usual scattering theories is lost, and so is the worth of the method. (4) Finally, to avoid undue complication, the scattering is assumed to be governed by a spherically symmetric, central potential. This is tantamount to assuming that no orientational dependence exists in the scattering. While this assumption may not always be strictly valid, especially for molecule-molecule scattering, the effects due to non-spherical scattering are often very small. It is actually to test this final assumption that the present studies of elastic scattering were undertaken, and hence a more thorough analysis of this aspect of the potential determination will be given later.

If the scattering partners and the experimental conditions are properly chosen, then these four requirements can be fulfilled, and a wide variety of scattering measurements made. While the ideal type of scattering experiment would involve measuring all of the final parameters associated with the scattered particle (velocity, internal states, asymptotic trajectory, etc.), the actual experiments are much more limited in scope.

The most simple type of scattering experiment involves passing a thermal energy beam of particles through a small chamber

filled with gas at a known pressure. By measuring the attenuation of the beam as a result of scattering occurring within the chamber, a measure of the total elastic scattering cross section is obtained. If one assumes that the majority of the scattering results from purely attractive interactions of the type $V(r) \approx -C/r^s$, then according to Massey and Mohr [17], the total cross section is proportional to $(C/\hbar v)^{2/(s-1)}$. In order to apply this analysis, however, it is necessary to measure this total cross section in absolute magnitude. This is a very difficult experimental problem since it requires a knowledge of the gas densities, detection efficiency, velocity distributions and the angular resolution of the apparatus. Application of these latter two corrections to the measured cross section (as a function of velocity, v) involves integrating over Δv and $\Delta\theta$, the velocity and angular spreads, respectively. The relationship between the total cross section and a realistic potential involves two integrals, one over all impact parameters ($b = 0, \infty$), the other over all scattering angles ($\chi = 0, \pi$), [21]. Hence, four "layers" of integration separate the measured results from the desired intermolecular potential. Some improvement in this situation may be obtained by replacing the scattering chamber by a second beam, and by velocity selecting (greatly narrowing the spread, Δv) the incident beam. Very careful collimation of the beams can also reduce the influence of the angular resolution, and thereby eliminate two of the four integrals.

The actual techniques involved in these types of experiments are discussed in a great many reviews [16], while representative

scattering results and derived potentials are also numerous [22].

As early as 1933, Knauer [13] recognized that measurements of the angular distributions of particles scattered in a crossed beam experiment could yield much more information than the total cross section measurements. These so-called differential cross sections (DCS) could now be related to the potential through only a single integral. This greatly simplified result has allowed certain DCS measurements to be used in an inversion technique (see Section 3.4) which yields the intermolecular potential directly without recourse to a fixed mathematical form. Even when such a procedure is not feasible, certain features of the angular distribution of scattered particles are such that absolute measurements (as in the total cross section case) are not needed to determine accurate potential parameters. These features (rainbow scattering, rapid oscillations, etc.) do, however, require more sensitive and sophisticated measuring techniques. It is only recently, therefore, that many of these features of the DCS have been fully explored and utilized, as in this work, to determine accurate potential functions.

The additional effort required to measure the differential cross section rather than the total cross section is rewarded in the type of information available from the former. In total cross section studies, the velocity dependence of the total integrated scattering is measured. From this data, it is usually only possible to determine a quantity which is proportional to the area of the potential well [23]. The result, then, is a measure of the product of the well depth, ϵ and the

range parameter σ (see Chapter 2). In contrast to this situation, the results of DCS measurements permit the independent determination of these two important parameters. While some product value $\epsilon\sigma$ may adequately describe total scattering results (for a given model potential function), little knowledge is gained concerning the quantitative details about the intermolecular potential. Often, independent (and possibly unreliable) estimates must be made of one of the parameters to yield a true potential function. This of course is not necessary in the analysis of DCS results, and hence these experiments provide more information than total cross section results. The latter experiments are, however, complementary, since the independent values of ϵ and σ determined from the DCS studies should give a product value which adequately describes the total cross section results. The results of the present studies demonstrate quite well that this is indeed the case (see Chapter 5 and Appendix A).

Most of the experimental work mentioned thus far covers the energy range from 0.01 eV to 0.1 eV (essentially thermal). In this energy range, the scattering is most affected by the long-range (4-10 A) attractive forces (see Chapter 2), and hence this part of the potential is most closely examined by these experiments. Fortunately, however, the wave-like nature of the particles allows information to be obtained even about regions of the potential which are not probed, such as the potential well and the repulsive wall. By using high energy beams ($>$ 10 eV) Amdur and co-workers have produced a great deal of data related to the highly repulsive upper regions of the intermolecular

potential [24-27]. In some cases, it has been possible to combine the high and low energy measurements to yield potentials which span a very large range of intermolecular separations [28].

As might be expected, some of the most extensive investigations of interaction potentials by the molecular beam method have involved the rare gases, [29-34]. Many of the rare gas-rare gas potentials are now quite accurately known from such work, and are found to agree with those potentials determined in other ways (see below).

1.2.2 Bulk Properties

Another of the more commonly used methods of determining intermolecular potentials has been the use of virial coefficient and transport properties measured in macroscopic, bulk systems. Unlike the molecular beam method, measurements made of bulk properties are necessarily obscured by the natural averaging processes which connect micro- and macroscopic quantities. Despite this averaging, many bulk properties are still capable of yielding accurate intermolecular potential information. As with the beam experiments, several requirements are essential to ensure the usefulness of any macroscopic measurements. First, some connection must exist between the potential function V(r) and the measured quantities. When dealing with microscopic properties averaged over macroscopic systems, statistical mechanics will generally provide the necessary relationships. This gives rise to a second point, which is that these theoretical connections must not be so complex as to obscure the

sensitivity of the measured properties to the exact nature of the potential. This situation is analogous to the scattering case mentioned above where increasing "layers" of integration reduced the sensitivity of the cross sections to the intermolecular potential.

According to the classical statistical mechanical picture, the second virial coefficient B(T) is related to the intermolecular potential by the equation

$$B(T) = 2\pi N_0 \int_0^\infty [1 - e^{-V(r)/kT}] r^2 \, dr \quad . \tag{1}$$

This expression only accounts for two-body interactions, which in dense gases or the condensed phase may be in serious error. By measuring the temperature dependence of B(T), and using equation (1) along with a fixed form for V(r), many potential functions have been evaluated. As early as 1950, Yntema and Schneider [35] applied this method to the He-He interaction assuming an exponential (6, 8) potential form (see Chapter 2). A great deal of work has been done toward relating second virial coefficient data to a variety of potential forms [36-42]. Extensive listings of second virial coefficients and potentials evaluated from them are found in Hirschfelder, Curtiss, and Bird [43]. Despite the great difficulty involved, Jonah and Rowlinson [44] attempted a direct inversion of the high temperature second virial coefficient of helium. Although their result was not a unique determination of the complete potential function, some regions of the repulsive wall were reasonably well established.

Attempts to include corrections based upon the third virial coefficient have proven to be of little value [45-47]. Presumably, this failure is a result of three-body interactions which cannot be accounted for by assuming pairwise additivity of the forces [48, 51].

As determined by Klein [39], the various transport properties provide a better means of evaluating intermolecular potentials. Accordingly, numerous such determinations have been made using viscosity and diffusion coefficients, principally [36, 52-55]. The connections between these properties and the interaction potential are somewhat more complex than for the second virial coefficient. For example, the coefficient of viscosity is given by,

$$\eta = \frac{5}{16} (mkT/\pi)^{\frac{1}{2}} [f/\sigma^2 \Omega^{(2,2)*}] \quad , \tag{2}$$

where m is the particle mass, f is a slowly varying function of T (see for example, [43]), σ is the potential range parameter, and the so-called reduced collision integrals $\Omega^{(\ell, s)*}$ are related to the potential function. These functions are actually found from the same expression which describes the differential elastic scattering, $I(\chi)$ (see Chapter 3).

$$\Omega^{(\ell, s)*} \alpha \int_0^\infty S^{(\ell)} e^{-\gamma^2} \gamma^{2S+3} \, dr \tag{3}$$

where

$$\gamma^2 = \tfrac{1}{2} \mu v^2/kT \tag{4}$$

and

$$S^{(\ell)} = 2\pi \int_0^{\pi} (1 - \cos^{\ell}\chi) I(\chi) \sin\chi \, d\chi \quad . \tag{5}$$

While equations (2)-(5) appear to obscure greatly the relationship between V(r) (which enters through χ and $I(\chi)$) and η, the fact that viscosity is mostly a manifestation of scattering for which $\chi \approx \pi$, results in a reasonably strong sensitivity of η to V(r). Several schemes have been developed to determine accurately potential parameters for a given form of V(r) using not only viscosity and diffusion data, but also adiabatic Joule-Thompson coefficients [39, 56]. One very important consideration must be made when dealing with both transport properties and second virial coefficients, and that is the temperature range over which each property is determined. It has been shown that in general the lower temperature viscosity data are most reliable in giving information about the long range potential, while certain other temperature regions are appropriate for the virial coefficient results [39, 57, 58].

1.2.3 Other Methods

As a result of the importance of the interaction potential in describing many physical processes, a wide variety of other properties have been used to gain information on these potentials. Some of the more reliable and often used methods will be briefly mentioned here.

The well-known method developed by Rydberg, Klein and Rees [59-61] utilizes experimental information obtained from spectroscopic

measurements to reconstruct a potential function. Based on quantization of the vibrational phase integral, the classical turning points for a given vibrational level can be found. These turning points form the boundaries of the electronic potential energy function appropriate to the interaction of the two vibrating masses of the molecule. Quite accurate results have been obtained using this RKR method for such systems as, I-I [62-64], H-H [62], N-N, O-O, and N-O [65].

While this method yields reasonable results, it requires a large amount of very accurate spectroscopic data. In a few limited cases, this spectroscopic data reveals a curve crossing between potential energy functions. This occurrence gives rise to a breaking off of rotational structure in the emission spectrum due to predissociation [66]. By analyzing these spectra, some information about the shape of the intermolecular potential may be determined, as in the case of N_2 [67]. This technique is often referred to as the limiting curve of dissociation method [68].

An additional use of spectroscopic methods is the study of the pressure broadening of absorption lines in the microwave region [69-71]. The broadening is presumed to arise as a result of bimolecular collisions which perturb the absorbing molecules. Since the theoretical foundations of this effect are not fully developed, only limited studies have been made [72-76].

Recently, Mikolaj and Pings [77] have developed a very different method of obtaining interaction potentials using X-ray diffraction studies of liquids. By relating the radial distribution function of the

particles to the potential, it is possible to use an iterative method to determine V(r). This method must be applied carefully to ensure that three-body effects do not contribute extensively. At very low gas densities of argon, such effects have been predicted to be small [78, 79], and the results of Mikolaj and Pings seems to confirm this.

One final method which has received some attention in the study of interaction potentials is the analysis of crystalline properties. At very low temperatures (extrapolated to 0°K) the specific heat, thermal expansion, bulk modulus and other equilibrium properties of solids are all related to local pairwise interactions. In some cases, three-body forces can become important; however, reliable results have been obtained for argon [80-82], and sodium and potassium chloride [83].

1.3 Conclusions

As noted before, the study of intermolecular potentials is still in a developmental state, despite the availability of these many possible experimental methods. The great difficulties encountered in systematic studies of interaction potentials can clearly be traced to the lack of a direct one-to-one relationship between the potential and the experimental observable. This lack of a direct path of determination results in the use of many forms of model potential functions which may only be fair approximations to the actual intermolecular potential. Perhaps the most promising technique to circumvent this problem is the direct inversion of molecular beam scattering results (see Section 3.4). Unfortunately, these methods require data of a quality not yet

readily achievable except for a few select systems. In this regard, differential elastic scattering is much better suited to the task than total elastic scattering. This remains true even when inversion is not feasible, since total cross sections require an absolute calibration to be useful, whereas differential measurements contain a built-in calibration in the form of quantum interference effects.

In the course of this work, measurements of these quantum effects in a variety of molecular systems have been made using the crossed molecular beam technique. By using several distinctly different forms for the intermolecular potential, some conclusions have been reached concerning the degree to which a central field assumption is valid for describing molecule-molecule scattering.

References

1. E. A. Mason and L. Monchick, in "Advances in Chemical Physics," Vol. XII, J. O. Hirschfelder, Ed., Interscience, New York, 1969, p. 329.
2. L. Dunoyer, Le Radium 8, 142 (1911); ibid. 10, 400 (1913).
3. L. Dunoyer, Compt. Rend. 152, 594 (1911).
4. For a summary of this work, see, I. Estermann, "Recent Research in Molecular Beams," Academic Press, New York, 1959.
5. O. Stern, Z. Physik 2, 49 (1920); ibid., 3, 417 (1920).
6. O. Stern, Z. Physik 7, 249 (1921).
7. W. Gerlach and O. Stern, Z. Physik 8, 110 (1921); ibid. 9, 349 (1922); ibid. 9, 353 (1922).
8. R. Fraser, "Molecular Rays," Cambridge University Press, Cambridge, 1931.
9. R. Fraser, "Molecular Beams," Methuen and Co., Ltd., London, 1937.
10. K. F. Smith, "Molecular Beams," Methuen and Co., Ltd., New York, 1955.
11. N. F. Ramsey, "Molecular Beams," Oxford University Press, Oxford, 1956.
12. I. Estermann, Rev. Mod. Phys. 18, 300 (1946).
13. F. Knauer, Z. Physik 80, 80 (1933).
14. J. W. Trischka, in "Methods of Experimental Physics," Vol. 3, D. Williams, Ed., Academic Press, New York, 1962, p. 589.

15. O. Stern, Z. Physik 39, 751 (1926).

16. See, for example, (a) H. Pauly, Fortschr. Physik 9, 613 (1961); (b) W. Fite and S. Datz, Ann. Rev. Phys. Chem. 14, 61 (1973); (c) R. B. Bernstein, Science 144, 141 (1964); (d) V. B. Leonas, Soviet Physics Vsp. 7, 121 (1964); (e) H. Pauly and J. P. Toennies, in "Advances in Atomic and Molecular Physics," Vol. I, D. R. Bates and I. Estermann, Eds., Academic Press, New York, 1965; (f) H. Pauly and J. P. Toennies, in "Methods of Experimental Physics," Vol. 7A, B. Bederson and W. Fite, Eds., Academic Press, New York, 1968; (g) Chapters 2-4, Vol. X, "Advances in Chemical Physics," J. Ross, Ed., Interscience, New York, 1966; (h) R. B. Bernstein and J. T. Muckerman, in "Advances in Chemical Physics," Vol. XII, J. O. Hirschfelder, Ed., Interscience, New York, 1969, p. 389.

17. H. S. W. Massey and C. B. O. Mohr, Proc. Roy. Soc. (London) A144, 188 (1934).

18. H. S. W. Massey and R. A. Buckingham, Nature 138, 77 (1936).

19. E. F. Greene, A. L. Moursund, and J. Ross, in "Advances in Chemical Physics," Vol. X, J. Ross, Ed., Interscience, New York, 1966, p. 135.

20. (a) K. J. Kaufmann, J. R. Lawten, and J. L. Kinsey, J. Chem. Phys. 60, 4016 (1974); (b) B. S. Duchart, M. A. D. Fluendy, and K. P. Lawley, Chem. Phys. Lett. 14, 129 (1972).

21. See, for example, T. Wu and T. Ohmura, "Quantum Theory of Scattering," Prentice-Hall, New Jersey, 1962, p. 14.

22. (a) For an excellent review, see Table II, reference 16h, pp. 425-459; also, (b) M. Cavallini, L. Mengeghetti, G. Scoles, and M. Yealland, Phys. Rev. Lett. 24, 1469 (1970); (c) E. W. Rothe and R. K. Helbing, J. Chem. Phys. 53, 2501 (1970); (d) K. G. Anlauf, R. Bickes, Jr., and R. B. Bernstein, J. Chem. Phys. 54, 3647 (1971); (e) M. Cavallini, M. G. Dondi, G. Scoles, and U. Valbusa, Chem. Phys. Lett. 10, 22 (1971); (f) R. Gengenbach, J. Strunck, and J. P. Toennies, J. Chem. Phys. 54, 1830 (1971); (g) F. G. Collins and F. C. Hurlbut, J. Chem. Phys. 56, 2609 (1971); (h) T. R. Powers and R. J. Cross, Jr., J. Chem. Phys. 56, 3181 (1971); (i) V. Buck, M. Kick, and H. Pauly, J. Chem. Phys. 56, 3391 (1971); (j) F. P. Tully and Y. T. Lee, J. Chem. Phys. 57, 866 (1972); (k) J. M. Farrar and Y. T. Lee, J. Chem. Phys. 57, 5492 (1972); (l) J. M. Parson, T. P. Schafer, F. P. Tully, P. E. Siska, Y. C. Wong, and Y. T. Lee, J. Chem. Phys. 58, 4044 (1973); (m) R. B. Bernstein and R. A. LaBudde, J. Chem. Phys. 58, 1109 (1973).

23. E. F. Greene and E. A. Mason, J. Chem. Phys. 57, 2065 (1972).

24. I. Amdur and J. E. Jordon, in "Advances in Chemical Physics," Vol. X, J. Ross, Ed., Interscience, New York, 1966, Chapter 2.

25. J. E. Jordon and I. Amdur, J. Chem. Phys. 46, 165 (1967).

26. E. A. Mason and I. Amdur, J. Chem. Phys. 41, 2695 (1964).

27. I. Amdur, in "Progress in International Research on Thermodynamics and Transport Properties," American Society of Mechanical Engineers, New York, 1962, p. 369.

28. See, for example, Section V., reference 24.

29. J. M. Parson, T. P. Schafer, F. P. Tully, P. E. Siska, Y. C. Wong, and Y. T. Lee, J. Chem. Phys. 53, 2123 (1970).

30. P. E. Siska, J. M. Parson, T. P. Schafer, F. P. Tully, Y. C. Wong, and Y. T. Lee, Phys. Rev. Lett. 25, 271 (1970).

31. P. E. Siska, J. M. Parson, T. P. Schafer, and Y. T. Lee, J. Chem. Phys. 55, 5762 (1971).

32. P. Cantini, M. G. Dondi, G. Scoles, and F. Torello, J. Chem. Phys. 56, 1946 (1972).

33. J. M. Farrar and Y. T. Lee, J. Chem. Phys. 56, 5801 (1972).

34. J. M. Parson, P. E. Siska, and Y. T. Lee, J. Chem. Phys. 56, 1511 (1972).

35. J. L. Yntema and W. G. Schneider, J. Chem. Phys. 18, 646 (1950).

36. J. S. Rowlinson, Disc, Faraday Soc. 40, 19 (1965).

37. R. J. Munn, J. Chem. Phys. 40, 1439 (1964).

38. R. J. Munn and F. J. Smith, J. Chem. Phys. 43, 3998 (1965).

39. M. Klein, J. Res. Natl. Bur. Stds. 70A, 259 (1966).

40. M. L. Klein and R. J. Munn, J. Chem. Phys. 47, 1035 (1967).

41. M. Klein and H. J. M. Hanley, Trans. Faraday Soc. 64, 2927 (1968).

42. G. C. Maitland, Mol. Phys. 26, 513 (1973).

43. J. O. Hirschfelder, C. F. Curtiss, and R. B. Bird, "Molecular Theory of Gases and Liquids," Wiley, New York, 1964.

44. D. A. Jonah and J. S. Rowlinson, Trans. Faraday Soc. 62, 1067 (1966).

45. T. Kihara, in "Advances in Chemical Physics," Vol. I, I. Prigogine, Ed., Interscience, New York, 1958, p. 267.

46. H. W. Graben, R. D. Present, and R. D. McCulloch, Phys. Rev. 144, 140 (1966).

47. A. E. Sherwood and J. M. Prausnitz, J. Chem. Phys. 41, 413 (1964).

48. B. M. Axilrod, J. Chem. Phys. 19, 724 (1951).

49. L. Jansen and E. Lombarbi, Disc. Faraday Soc. 40, 78 (1965).

50. J. Corner, Trans. Faraday Soc. 35, 711 (1939).

51. E. A. Mason and W. E. Rice, J. Chem. Phys. 22, 843 (1954).

52. I. Amdur and T. F. Schatzki, J. Chem. Phys. 27, 1049 (1957); ibid. 29, 1425 (1959).

53. B. N. Srivastava and K. P. Srivastava, J. Chem. Phys. 30, 984 (1959).

54. R. J. Munn, J. Chem. Phys. 42, 3032 (1965).

55. E. A. Mason, R. J. Munn, and F. J. Smith, Disc. Faraday Soc. 40, 27 (1965).

56. J. Corner, Trans. Faraday Soc. 44, 914 (1948).

57. L. S. Tee, S. Gotoh, and W. E. Stewart, Ind. Eng. Chem. Fundamentals 42, 2801 (1965).

58. L. S. Tee, S. Gotoh, and W. E. Stewart, Physics of Fluids 9, 1222 (1966).

59. R. Rydberg, Z. Physik 73, 376 (1931); ibid. 80, 514 (1933).

60. O. Klein, Z. Physik 76, 226 (1932).

61. A. L. G. Rees, Proc. Roy. Soc. (London) 59, 998 (1947).

62. S. Weissman, J. T. Vanderslice, and R. Battino, J. Chem. Phys. 39, 2226 (1963).

63. W. G. Richards and R. F. Barrow, Proc. Roy. Soc. (London) 83, 1045 (1964).

64. R. N. Zare, J. Chem. Phys. 40, 1934 (1964).

65. F. R. Gilmore, J. Quant. Spectry. Radiative Transfer 5, 369 (1965).

66. G. Herzberg, "Molecular Spectra and Molecular Structure," Vol. 1, D. van Nostrand, London, 1967, p. 412.

67. P. K. Carroll, J. Chem. Phys. 37, 805 (1962).

68. R. B. Bernstein, Phys. Rev. Lett. 16, 385 (1966).

69. U. Fano, Phys. Rev. 131, 259 (1963).

70. G. P. Reck, H. Takebe, and C. A. Mead, Phys. Rev. 137, A683 (1965).

71. G. Birnbaum, in "Advances in Chemical Physics," Vol. XII, J. O. Hirschfelder, Ed., Interscience, New York, 1967, p. 487.

72. H. Mangenau and H. C. Jacobson, J. Chem. Phys. 38, 1259 (1963).

73. H. Mangenau and H. C. Jacobson, J. Quant. Spectry. Radiative Transfer 3, 35 (1963).

74. A. Watanabe and H. L. Welsh, Phys. Rev. Lett. 13, 810 (1964).

75. A. Watanabe and H. L. Welsh, Can. J. Phys. 43, 818 (1965).

76. A. Kudian, H. L. Welsh, and A. Watanabe, J. Chem. Phys. 43, 3397 (1965).

77. P. G. Mikolaj and C. J. Pings, Phys. Rev. Lett. 16, 4 (1965).

78. B. J. Alden and R. H. Paulson, J. Chem. Phys. 43, 4172 (1965).

79. N. R. Kester and O. Sinanoglu, J. Chem. Phys. 38, 1730 (1963).

80. P. G. Mikolaj and C. J. Pings, J. Chem. Phys. 46, 1401 (1967).

81. J. A. Barker and A. Pompe, Aust. J. Chem. 21, 1683 (1968).

82. M. V. Bobetic and J. A. Barker, Phys. Rev. B 42, 4169 (1970).

83. E. A. Guggenheim and M. L. McGlashan, Disc. Faraday Soc. 40, 76 (1965).

2. INTERMOLECULAR POTENTIALS

2.1 Introduction

As early as 1743, Clairault [1] recognized the existence of some form of molecular interaction which was responsible for a number of physically observed phenomena, such as capillary action. In the years that followed, many theories were developed by Laplace, Gauss, Maxwell, Bernoulli, Clausius, Meyer, and others. Much of this work was involved with the construction of mathematical model potential functions. Subsequently, the application of rigorous quantum theory provided the most important and accurate contributions to the theoretical understanding of the forces between atoms and molecules.

During the past forty years, a number of theoretical methods have been established to facilitate the calculation of accurate intermolecular potentials. These methods include both ab initio and semi-empirical techniques as well as a wide variety of more approximate methods. For the purposes of describing and analyzing the types of experimental results presented in this work, these methods are of less interest than are the theories associated with the model functions. Consequently, only a few points concerning the former will be discussed below, with the remainder of the chapter devoted to enumerating several of the more useful model potentials.

Normally, any discussion of the calculation of the forces acting between two atoms or molecules is divided into a discussion of the "short-range" interactions and the "long-range" interactions. The

reasons behind this are obvious since in general, interactions over tens of Ångstroms are weakly attractive (van der Waals), while interactions over a few Ångstroms are strongly repulsive. As a result, the methods associated with calculating each type of interaction are quite different. Many excellent reviews now exist which discuss both long- and short-range calculational methods and results [2].

2.2 Theoretical Methods

Often the treatment of long-range interactions has been based on perturbation theory, since the magnitude of the forces involved are usually quite small. One of the more straightforward results of applying perturbation methods was derived by London [3, 4] and Margenau [5]. If the potential is written as,

$$V(r) = -C/r^6 \quad , \tag{1}$$

then C is given by,

$$C = \frac{3}{2} \frac{E_1 E_2}{E_1 + E_2} \alpha_1 \alpha_2 \quad , \tag{2}$$

where α_1 and α_2 are the polarizabilities of the two interacting particles, and E_1 and E_2 are their ionization potentials. Quantum mechanically, the potential is seen to arise from the mutual perturbation of the electrons in each particle as they approach. These forces are referred to as dispersion forces, and assume the existence of no permanent dipole moments. If such moments are present, additional terms must be added to (2) above, such as,

$$C_{ind} = \alpha_1\mu_2^2 + \alpha_2\mu_1^2 + \frac{2\mu_1^2\mu_2^2}{3kT} \quad , \tag{3}$$

where the μ's are the dipole moments [6].

Slater and Kirkwood [7] used a variational method with the additional assumption of closed shell atoms to obtain,

$$C = -\frac{3}{2}\frac{e\hbar}{m^{\frac{1}{2}}}\frac{\alpha_1\alpha_2}{(\alpha_1/N_1)^{\frac{1}{2}} + (\alpha_2/N_2)^{\frac{1}{2}}} \quad , \tag{4}$$

where m is the electron mass and N_1 and N_2 can either be interpreted as the number of outershell electrons [7], or the total number of electrons in each atom [8]. An additional formula for the dispersion forces was found by Kirkwood [9] and also Mueller [10],

$$C = -\frac{6mc^2}{N_0}\frac{\alpha_1\alpha_2}{\alpha_1/\chi_1 + \alpha_2/\chi_2} \quad , \tag{5}$$

where χ is the diamagnetic susceptability per mole.

A number of calculations of these dispersion constants have been made [8, 11-14] and when compared with values determined by molecular beam methods, have been found to be too small by 10-50% [15]. To account for this, Fontana [16] has added higher order terms to equation (1), that is,

$$V(r) = -\frac{C}{r^6} - \frac{C'}{r^8} - \frac{C''}{r^{10}} \quad . \tag{6}$$

He found, however, that these higher order quadrupole and octapole terms did not contribute significantly to the long-range attractive interaction.

For atom-molecule and molecule-molecule interactions, the simple form for the dipole-dipole potential given by equations (1) and (2) must be modified because of the anisotropy associated with the molecular polarizability. A standard treatment [17, 18] of this added complication is the inclusion of an angularly dependent term in the potential function, such as,

$$V(r,\gamma) = -\frac{C}{r^6}\left[1 + qP_2(\cos\gamma)\right] , \tag{7}$$

where C is given by equation (2) but the polarizabilities are now taken as,

$$\alpha = \tfrac{1}{3}\left(\alpha^{\parallel} + 2\alpha^{\perp}\right) , \tag{8}$$

and

$$q = \frac{\alpha^{\parallel} - \alpha^{\perp}}{\alpha^{\parallel} + 2\alpha^{\perp}} . \tag{9}$$

Here, the parallel and perpendicular components of the molecular polarizability are used to account for the anisotropy in the potential. Again, many higher order terms can be added to the atom-molecule and molecule-molecule long-range potential function [2c, 5, 19].

Many of the simplifying assumptions that were made above in the perturbation formulations and calculations cannot be used when dealing with the short-range repulsive forces. Unlike the long-range interactions, short-range forces can become very large, and hence the perturbation method is not applicable. Furthermore, with substantial overlap of the charge distributions occurring, some account

must be taken of the exclusion principle. In general, two types of approaches are used to formulate the short-range interaction potential. The first is a valence-bond method due to Heitler and London [20] where the total system wavefunction is constructed from properly anti-symmetrized molecular wavefunctions. The second method is essentially the molecular orbital technique which treats all electrons and nuclei as a united system [21].

Much of the theoretical work on the repulsive parts of the potential function has been performed on the simple H–H and H–He type systems [19, 22-26]. More recently, calculations of increasing quality and complexity have been made using Hartree-Fock wave-functions [27]. Comparatively little work has been performed in the area of non-spherical repulsive potentials. Roberts [28] has fitted calculations on the He–H_2 system to a potential of the form,

$$V(r, \gamma) = Ae^{-kr} [1 + \delta P_2(\cos \gamma)] \quad . \tag{10}$$

Even though only 1s atomic wavefunctions were used, a reasonable fit was found with $\delta = 0.375$. Potentials such as given by (10) can be used for the calculation of inelastic scattering at high impact energies [29, 30].

For the most part, the theoretical calculation of both long- and short-range interatomic and intermolecular potentials is as yet not fully developed. While limited ranges of the interaction potential can be found with some accuracy, the complete potential function, valid over the range from strong repulsion to weak attraction is still difficult to establish. One exception to this is the recent method due to Gordon

and Kim [31] for closed-shell atoms and molecules. The method makes use of additive electron densities calculated from a Thomas-Fermi-Dirac statistical model. For rare gas-rare gas interactions, the entire potential functions from less than 0.1 A to 5 A were found to be in excellent agreement with those determined experimentally. Such methods may someday be extended to cover more complex systems, and thus greatly improve the usefulness of the theoretical approach.

2.3 Model Potential Functions

Due to the many difficulties inherent in the ab initio calculation of interaction potentials, the use of models functions is often necessary and sometimes desirable. Many model intermolecular potentials permit the direct analytical solution of some of the transport and scattering equations. These models have been formulated with various degrees of complexity, starting from a simple one parameter rigid sphere model and proceeding up to many parameter mixtures of functions. Naturally, the more adjustable parameters a model has, the more flexible will be the function, and hence the more useful. On the other hand, the use of multiparameter functions requires considerably more effort to yield significant values for those parameters. As a result, the most often used potentials are those which require only a few parameters, yet give an adequate description of the forces between the two interacting particles.

The simplest function which can be used to describe hard sphere collisions is,

$$V(r) = \begin{cases} \infty & r < \sigma \\ 0 & r > \sigma \end{cases} \quad . \tag{11}$$

Here, only account of the repulsive forces is made by using a rigid wall. The only parameter is σ, the distance of closest approach. Another strictly repulsive model, involving two variables, is the line of centers model,

$$V(r) = \alpha r^{-\delta} \quad . \tag{12}$$

In addition to the exponent of r, the constant α has been added to adjust the magnitude of the potential. Since most realistic interactions involve both repulsive and attractive forces, the square well potential is often used for simple model calculations. This function has three adjustable variables,

$$V(r) = \begin{cases} \infty & r < \sigma \\ -\epsilon & \sigma < r < \alpha\sigma \\ 0 & r > \alpha\sigma \end{cases} \quad . \tag{13}$$

The variables: the range, σ, the depth of the well, ϵ, and the width of the well, α. Even though this function is the simplest to include both types of interactions, it is quite crude. Nonetheless, both second and third virial coefficients and various transport properties have been calculated using the square well [19].

A second example of a model which incorporates both attraction and repulsion is the Sutherland potential [32],

$$V(r) = \begin{cases} \infty & r < \sigma \\ -\alpha r^{-\gamma} & r > \sigma \end{cases} \quad . \tag{14}$$

This potential essentially represents rigid spheres of diameter σ which attract each other according to an inverse power law. Despite its ease of use, the Sutherland potential still lacks the ability to mimic closely the actual behavior of two interacting particles. One of the most widely used models which can represent the full range of interactions is the Lennard-Jones function. As originally formulated [33], the potential had the form,

$$V(r) = \frac{\alpha}{r^{\delta}} - \frac{\beta}{r^{\gamma}} \quad . \tag{15}$$

The first term accounts for the repulsive forces, while the second represents the attractive forces. The more commonly used form is,

$$V(r) = 4\epsilon \left[\left(\frac{\sigma}{r}\right)^{12} - \left(\frac{\sigma}{r}\right)^{6} \right] \quad . \tag{16}$$

Again ϵ is the well depth, and σ is a range parameter. An example of this potential function is shown in Figure 2-1. One additional distance can be identified in the figure, that is, r_m, the location of the potential minimum. This is not an independent parameter, but rather it is related to σ, as

$$r_m = (2^{1/6})\,\sigma \quad . \tag{17}$$

The use of an inverse sixth power to represent the long-range attraction is based on the known dependence of the dipole-dipole forces

Figure 2.1: Lennard-Jones potential with a repulsive exponent of 12. The two parameters are ϵ, the well depth, and r_m the location of the minimum. Note that $\sigma = r_m(2^{-1/6})$.

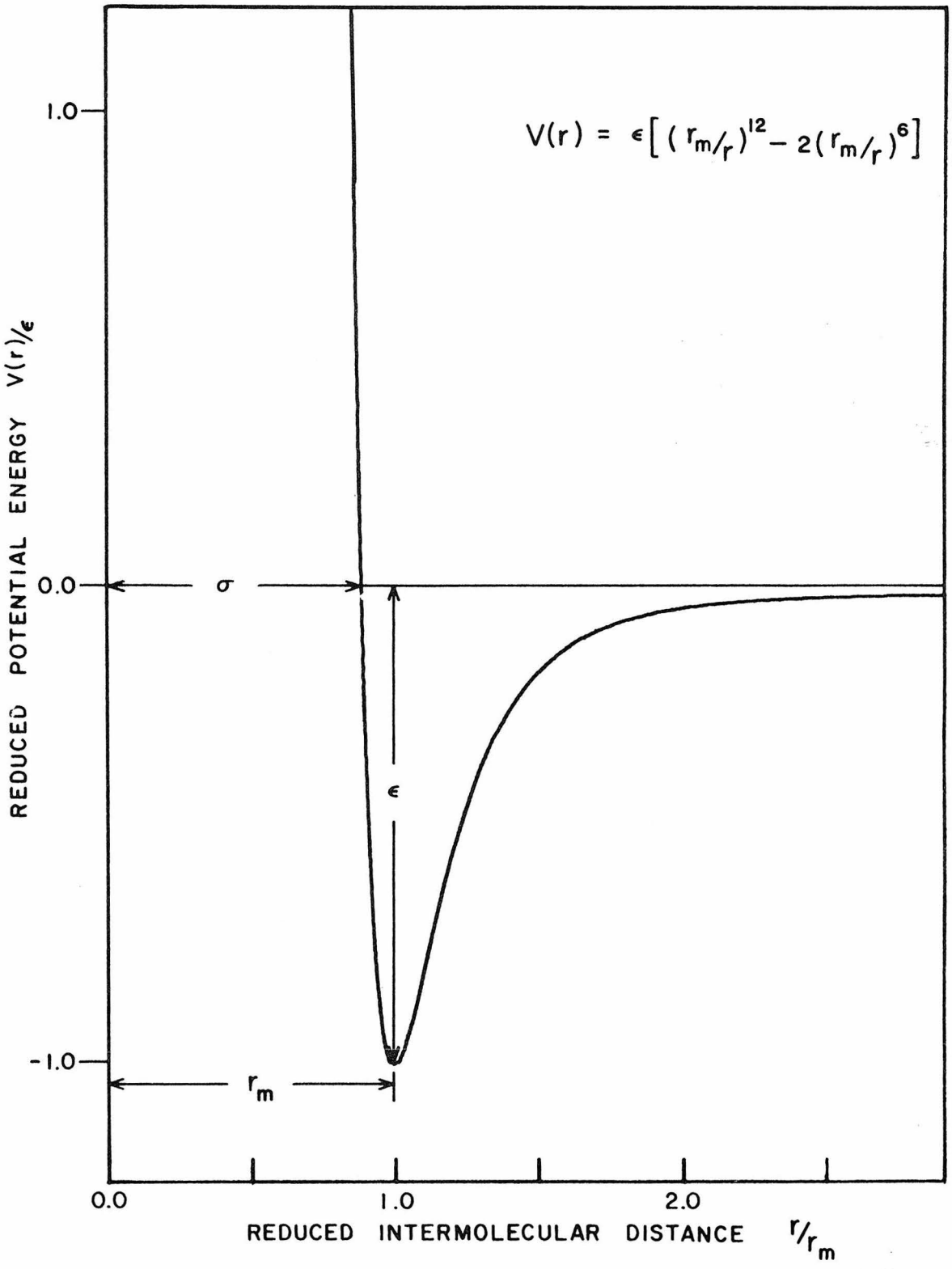
$V(r) = \epsilon\left[(r_m/r)^{12} - 2(r_m/r)^6 \right]$
1.0
0.0
-1.0
σ
ε
r_m
REDUCED POTENTIAL ENERGY $V(r)/\epsilon$
0.0
1.0
2.0
REDUCED INTERMOLECULAR DISTANCE r/r_m

2.1

(see equation 1). The choice of 12 for the repulsive index is arbitrary, and is in fact chosen for mathematical and computational convenience. This value may be taken as a variable parameter, and optimized along with ϵ and σ. Extensive tabulations of bulk properties calculated using equation (16) have been made [19], and its use in describing scattering results is nearly universal. One of the most serious drawbacks of this potential function is the lack of flexibility in adjusting the curvature of the potential well, or the location of its minimum with respect to σ. To overcome this, some use has been made of the so-called double Lennard-Jones potential [34],

$$V(r) = \begin{cases} \dfrac{\kappa_1 \epsilon}{m^2 - \kappa_1} \left[\left(\dfrac{r_m}{r} \right)^m - \dfrac{m^2}{\kappa_1} \left(\dfrac{r_m}{r} \right)^{\frac{\kappa_1}{m}} \right] & r \leq r_m \\ \dfrac{36\epsilon}{\kappa_2 - 36} \left[\left(\dfrac{r_m}{r} \right)^{\frac{\kappa_2}{6}} - \dfrac{\kappa_2}{36} \left(\dfrac{r_m}{r} \right)^6 \right] & r \geq r_m \quad . \end{cases} \tag{18}$$

By adjusting m and the curvature parameters κ_1 and κ_2, the location of the well and its shape may both be varied independently.

A more realistic four parameter function has also received considerable attention recently for the fitting of scattering data. It is the Morse-cubic spline-van der Waals (MSV) potential [35], defined as,

$$V(r) = \begin{cases} \epsilon \{ \exp[-2\beta(r - r_m)] - 2 \exp[-\beta(r - r_m)] \} & r < r_1 \\ \text{cubic spline} & r_1 \leq r \leq r_2 \\ -C_6 r^{-6} & r > r_2 \quad . \end{cases} \tag{19}$$

Normally, r_1 and r_2 are fixed (see Appendix A) and the parameters to

be determined are ϵ, r_m, β, and C_6. The high degree of flexibility of this potential arises from the ability of the cubic spline function to join smoothly the two segments of the potential. Even more flexibility may be introduced into the MSV potential by using a second spline function to join a repulsive exponential segment to the Morse function [35]. In general, for low energy interactions the MSV form is adequate as given by (19).

Several other potential functions which have received some attention recently are the following:

the Buckingham potential,

$$V(r) = \beta \exp(-\alpha r) - Cr^{-6} - C' r^{-8} \quad ; \tag{20}$$

the Buckingham-Corner potential,

$$V(r) = \begin{cases} \beta \exp[-\alpha(r/r_m)] - (Cr^{-6} + C'r^{-8}) \exp[-4(r_m/r - 1)^3] & r \leq r_m \\ \beta \exp[-\alpha(r/r_m)] - (Cr^{-6} - C'r^{-8}) & r \geq r_m; \end{cases} \tag{21}$$

the Modified Buckingham (6-exp) potential,

$$V(r) = \begin{cases} \dfrac{\epsilon}{1 - 6/\alpha} \left[\dfrac{6}{\alpha} \exp\left(\alpha \left[1 - \dfrac{r}{r_m} \right] \right) - \left(\dfrac{r_m}{r} \right)^6 \right] & r \geq r' \\ \infty & r \leq r' \end{cases} \tag{22}$$

where r' is defined as,

$$\left(\frac{r'}{r_m}\right)^7 \exp\left(\alpha\left[1 - \frac{r'}{r_m}\right]\right) = 1 \quad ; \tag{23}$$

and the Kihara potential [36],

$$V(r) = \begin{cases} \epsilon\left[\left(\frac{1-\alpha}{r/r_m - \alpha}\right)^{12} - 2\left(\frac{1-\alpha}{r/r_m - \alpha}\right)^{6}\right] & r/r_m \geq \alpha \\ \infty & 0 \leq r/r_m < \alpha \quad . \end{cases} \tag{24}$$

A number of these forms, as well as several other model potential functions have been compared and discussed in various articles [37-43].

A few attempts have been made to represent non-spherical intermolecular potentials. One particularly simple form is the Stockmayer potential [19], which is actually a modified Lennard-Jones potential, given by,

$$V(r, \theta, \theta_2, \phi_1-\phi_2) = 4\epsilon\left[\left(\frac{\sigma}{r}\right)^{12} - \left(\frac{\sigma}{r}\right)^{6}\right] + \frac{\mu_1\mu_2}{r^6}\, g(\theta_1, \theta_2, \phi_1-\phi_2) \tag{25}$$

where

$$g(\theta_1, \theta_2, \phi_1-\phi_2) = \cos\theta_1\cos\theta_2 - \sin\theta_1\sin\theta_2\cos(\phi_1-\phi_2) \quad . \tag{26}$$

Often the effects of anisotropy in the potential function are represented by using Legendere polynomials [44],

$$V(r,\gamma) = \epsilon\left\{\left(\frac{r_m}{r}\right)^{12}\left[1 + a_1\cos\gamma + a_2P_2(\cos\gamma)\right]\right.$$

$$\left. - 2\left(\frac{r_m}{r}\right)^{6}\left[1 + b_2P_2(\cos\gamma)\right]\right\} \quad . \qquad (27)$$

Naturally, none of these functions listed above can be expected to represent the actual intermolecular potential function between two real atoms or molecules. However, in view of the difficulties encountered in calculating the exact potentials quantum mechanically, these model functions are necessary for describing the results of scattering experiments such as those performed in this study. Some caution must be exercised in the final interpretation of the results obtained using model potentials. However, it is often possible to learn a great deal about the nature of the actual intermolecular potential from these models. The aim of the present study is, in fact, to determine the extent of the affect of potential anisotropy on the observed elastic scattering of small molecules, where only model potential functions are used.

References

1. A. C. Clairault, "Théorie de la figure de la terre," 2nd ed., Courcier, Paris, 1743.
2. See, for example, (a) H. Margenau and N. R. Kestner, "Theory of Intermolecular Forces," Pergamon Press, New York, 1969; (b) J. O. Hirschfelder, Ed., "Advances in Chemical Physics," Vol. XII, Interscience, New York, 1967, Part I; (c) H. Pauly and and J. P. Toennies in "Advances in Atomic and Molecular Physics," Vol. I, Academic Press, New York, 1965, p. 195; (d) "Intermolecular Forces," Disc. Faraday Soc. 40, (1965); (e) I. M. Torrens, "Interatomic Potentials," Academic Press, New York. 1972.
3. F. London, Trans. Faraday Soc. 33, 8 (1937).
4. F. London, Z. Physik 63, 245 (1930).
5. H. Margenau, Rev. Mod. Phys. 11, (1939).
6. W. H. Keesom, Physik Z. 22, 129 (1921).
7. J. C. Slater and J. G. Kirkwood, Phys. Rev. 37, 682 (1931).
8. C. Mavroyannis and M. J. Stephens, Mol. Phys. 5, 629 (1962).
9. J. G. Kirkwood, Physik Z. 33, 57 (1932).
10. A. Mueller, Proc. Roy. Soc. (London) A154, 624 (1933).
11. L. Salem, Proc. Roy. Soc. (London) A264, 379 (1961).
12. A. E. Kingston, Phys. Rev. A135, 1018 (1964).
13. J. A. Barker and P. J. Leonard, Phys. Lett. 13, 127 (1964).
14. R. J. Bell, Proc. Phys. Soc. (London) 86, 17 (1965).
15. A. Dalgarno and A. E. Kingston, Proc. Phys. Soc. (London) 73, 455 (1959).

16. P. R. Fontana, Phys. Rev. 123, 1865 (1961).

17. F. London, J. Phys. Chem. 46, 305 (1942).

18. K. S. Pitzer, in "Advances in Chemical Physics," Vol. II, I. Prigogine, Ed., Interscience, New York, 1959, p. 59.

19. J. O. Hirschfelder, C. F. Curtiss, and R. B. Bird, "Molecular Theory of Gases and Liquids," Wiley, New York, 1954.

20. W. Heitler and F. London, Z. Physik 44, 455 (1927).

21. See, for example, (a) C. Ballhausen and H. B. Gray, "Molecular Orbital Theory," Benjamin, New York, 1965; (b) J. C. Slater, "Quantum Theory of Molecules and Solids," Vol. I. McGraw-Hill, New York, 1963.

22. A. A. Abrahamson, Phys. Rev. 130, 693 (1963).

23. R. A. Buckingham, Planetary Space Sci. 3, 205 (1961).

24. T. L. Cottrell, Disc. Faraday Soc. 22, 10 (1956).

25. W. Kolos and C. C. J. Roothaan, Rev. Mod. Phys. 32, 219 (1960).

26. W. Kolos and L. Wolniewicz, Rev. Mod. Phys. 35, 473 (1973); ibid. J. Chem. Phys. 41, 3663, 3674 (1964).

27. See reference 2a for an extensive bibliography of calculations.

28. C. S. Roberts, Phys. Rev. 131, 203 (1963).

29. K. Takayanagi, Progr. Theoret. Phys. (Kyoto) 25, 1 (1963).

30. J. D. Craggs and H. S. W. Massey, in "Handbuch der Physik," Vol. 37, S. Flügge, Ed., Springer, Berlin, 1959.

31. R. G. Gordon and Y. S. Kim, J. Chem. Phys. 56, 3122 (1972).

32. W. Sutherland, Phil. Mag. 36, 507 (1893).

33. J. E. Lennard-Jones, Trans. Faraday Soc. 28, 334 (1932).

34. V. Buck and H. Pauly, Z. Physik 208, 390 (1968).

35. P. E. Siska, J. M. Parson, T. P. Schafer, and Y. T. Lee, J. Chem. Phys. 55, 5762 (1971).

36. T. Kihara, Progr. Theoret. Phys. 40, 177 (1967).

37. D. Steele, E. R. Lippincott, and J. T. Vanderslice, Rev. Mod. Phys. 34, 239 (1962).

38. J. H. Dymond, M. Rigby, and E. B. Smith, Physics of Fluids 9, 1222 (1966).

39. I. N. Levine, J. Chem. Phys. 45, 827 (1966).

40. R. F. Borkman and R. G. Parr, J. Chem. Phys. 48, 1116 (1968).

41. D. A. Copeland and N. R. Kestner, J. Chem. Phys. 49, 5214 (1968).

42. J. P. Toennies, Chem. Phys. Lett. 20, 238 (1973).

43. A. J. Thakkar and V. H. Smith, Jr., Chem. Phys. Lett. 24, 157 (1974).

44. R. J. Cross, Jr., J. Chem. Phys. 52, 5703 (1970).

3. THEORY OF ELASTIC SCATTERING

In order to gain any information concerning the nature of neutral-neutral interactions from elastic scattering experiments, it is necessary to establish some relationship between the two. Specifically, the goal of this theoretical treatment of the scattering of two particles is to relate the observable differential elastic scattering to the potential function which governs their interaction. Unfortunately, no simple relationship exists between the interatomic or intermolecular potential and the measurable scattering. Despite this, it is still possible to derive considerable information from the results of elastic scattering experiments. In the following, no attempt will be made to provide either a comprehensive or a completely rigorous treatment of the scattering of two particles. Many such complete theoretical descriptions of scattering can be found based on classical [1], semi-classical [2], and quantum mechanical [3] foundations. Only the principle features of each of these approaches will be given here, with special emphasis placed upon those methods and techniques actually used in explaining and analyzing the experimental results of these studies.

The common basis for each of these approaches will be two particles (masses m_1 and m_2), separated by a distance r, and interacting via a spherically symmetric central potential, V(r). Somewhat later, a non-central potential, which may give rise to non-elastic scattering, will also be considered.

3.1 Classical Mechanics

The classical mechanical description of two particle elastic scattering is straightforward, and involves only an analysis of the classical equations of motion. The most common development of these equations begins by first removing the motion of the center-of-mass, and then reducing the two-particle system to the equivalent one-particle plus potential system. The result of the first step is the following expression for the total energy of the system,

$$E_T = \tfrac{1}{2}\left(\frac{m_1 m_2}{m_1+m_2}\right)\left[\left(\frac{dr}{dt}\right)^2 + r^2\left(\frac{d\theta}{dt}\right)^2\right] + V(r) \quad . \tag{1}$$

The variables r and θ are the polar coordinates locating one mass point with respect to the other. In this scheme, the total angular momentum about the center-of-mass is written as,

$$\vec{L}_T = \left(\frac{m_1 m_2}{m_1+m_2}\right) \vec{r} \times \frac{d\vec{r}}{dt} \tag{2}$$

while the scalar force acting on each particle along the line of centers is,

$$F = -\nabla V(r) = -\frac{\partial V(r)}{\partial r} \quad . \tag{3}$$

Equations (1)-(3) serve to describe completely the motion of two particles with interaction potential V(r). However, they also determine the motion of a single particle of reduced mass $\mu = (m_1 m_2/m_1+m_2)$ located at (r, θ) from the potential V(r). As a direct consequence of the spherical symmetry of V(r), the motion of the mass point μ is constrained to always lie in the plane perpendicular to $\vec{L}$. As a result

then, the description of the scattering process involving one particle acting in a potential field due to V(r) can be formulated using only two mathematical dimensions.

To obtain the two equations of motion, (1) and (2) are rearranged to yield,

$$dr = \pm \left[\frac{2}{\mu} \left(E - V - \frac{L^2}{2\mu r^2} \right) \right]^{\frac{1}{2}} dt \qquad (4)$$

and,

$$d\theta = \frac{L}{\mu r^2} \, dt \quad . \qquad (5)$$

These two equations can now be integrated to obtain the particle trajectory as a function of E, L and the initial conditions, once some suitable V(r) is specified. As a realistic model for V(r) (see Chapter 2), a potential with long range attraction and short range repulsion will be assumed. Under these conditions, a typical trajectory would be as shown in Figure 3.1. Initially, the particle moves toward the potential with a relative velocity v, at an impact parameter b. The particle is first attracted toward the center of interaction until the forces acting on the particle are just balanced. At this point, the particle begins to move away and approaches an asymptotic final direction. The angle between the initial and final directions is just the scattering angle, χ. The classical turning point, or distance of closest radial approach, is designated (r_c, θ_c), and the trajectory is symmetric about this point. As a result of this symmetry, we can

Figure 3.1: Typical classical trajectory for a two particle system reduced to one particle of mass $\mu = (m_1 m_2/(m_1+m_2))$ scattering from a potential located at the origin. The incoming particle has velocity v and impact parameter $b = (\ell/\mu v)$. The polar coordinates r and θ describe the motion (equation 8), with r_c and θ_c corresponding to the classical turning point. The center-of-mass scattering angle χ is measured with respect to the asymptotic velocity vectors. Note that the trajectory is symmetric about the turning point.

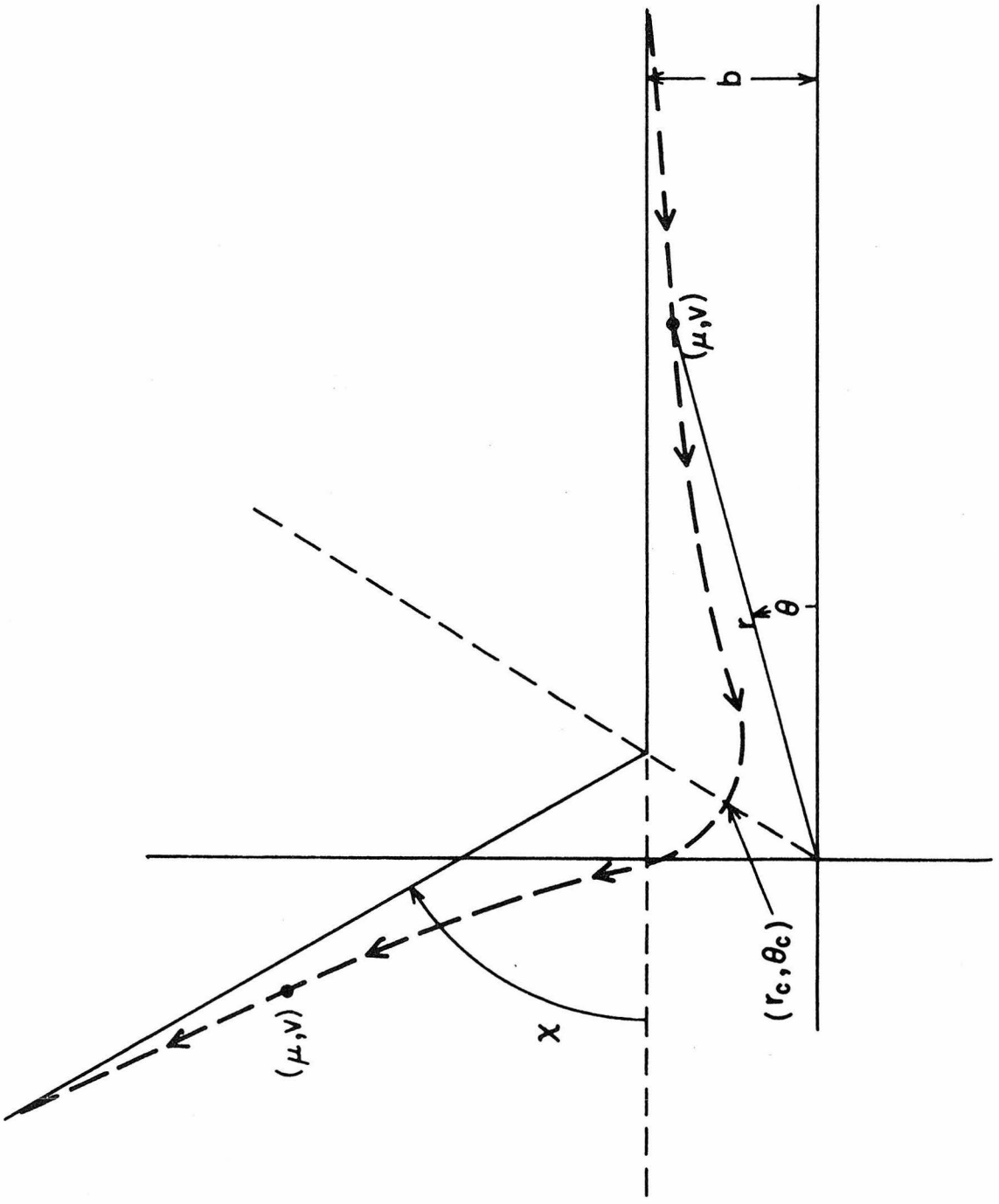

3.1

relate the measured deflection angle χ (in the center of mass) to the variable θ,

$$\chi = \pi - 2\theta_c \quad . \tag{6}$$

Now, by eliminating dt from equations (4) and (5), and using the fact that $L = \mu v b$, we have,

$$\theta(r) = b \int_r^\infty \left(1 - \frac{b^2}{r^2} - \frac{V}{E}\right)^{-\frac{1}{2}} \frac{dr}{r^2} \quad . \tag{7}$$

Using (7) to find $\theta_c \equiv \theta(r_c)$ and (6), it is possible to determine the scattering angle χ,

$$\chi(v, b) = \pi - 2b \int_{r_c}^\infty \left(1 - \frac{b^2}{r^2} - \frac{V}{E}\right)^{-\frac{1}{2}} \frac{dr}{r^2} \quad . \tag{8}$$

The lower limit of integration is just the closest radial approach, and is found by equating the kinetic and potential energies,

$$E = \tfrac{1}{2}\mu v^2 = \frac{L^2}{2\mu r_c^2} + V(r_c) \tag{9}$$

to give,

$$r_c^2 = b^2\left[1 - \frac{V}{E}\right]^{-1} \quad . \tag{10}$$

At this point, we need only specify v, b (or E, L) for a given V(r) and μ to determine completely the motion of the particle, and hence its scattered direction χ. Since a scattering experiment simultaneously

samples a very wide range of impact parameters, a correspondingly large distribution of final scattering angles will result. The distribution of particles over this angular range is the differential cross section, $I(\chi)$. If I_0 represents the incident flux density, that is, the number of particles per unit area (normal to v) per unit time, then define

$$I(\chi)d\omega = \begin{pmatrix}\text{number of particles scattered into unit solid} \\ \text{angle } d\omega \text{ per unit time}\end{pmatrix}/I_0 \tag{11}$$

By this definition, $I(\omega)d\omega$ has the units of an area. The solid angle element $d\omega$ is easily related to the scattering angle as

$$d\omega = 2\pi \sin \chi \, d\chi \tag{12}$$

which follows directly from the cylindrical symmetry of the scattering about the incident direction. The RHS of equation (11) is just the fraction of incident particles scattered between χ and $\chi + d\chi$, which for a given velocity is just $2\pi bdb$, hence,

$$I(\chi)\, d\omega = 2\pi\, bdb \tag{13}$$

which when combined with (12) gives an expression for scattered flux distribution,

$$I(\chi) = \frac{b}{\sin \chi} \left|\frac{db}{d\chi}\right| \quad . \tag{14}$$

Thus, the fraction of scattered incident flux with a final asymptotic direction χ degrees from the incoming direction can be ascertained by using equations (8) and (14). As will be seen below, (14) must often be modified since several impact parameters b_i (i = 1-3) can contribute to the flux at one angle.

In general, $\chi(v, b)$ can only be determined by performing a numerical integration of equation (8), although some approximations may be used when χ is small (b large). Kennard [4] has shown that for a potential of the form $V(r) = -Cr^{-s}$,

$$I(\chi) \cong [(s-1)f(s)]^{2/s} s^{-1} [\frac{C}{E}]^{2/s} / \theta^{1+2/s} \sin \theta \qquad (15)$$

where,

$$f(s) = \tfrac{1}{2}\pi^{\frac{1}{2}} \Gamma(\tfrac{1}{2}s - \tfrac{1}{2})/\Gamma(\tfrac{1}{2}s) \quad .$$

Since the long range attractive potential is known to vary as r^{-6} (see Chapter 2), equation (15) reduces to the limiting form,

$$I(\chi) \approx (\frac{C}{E})^{1/3} \theta^{-7/3} \quad . \qquad (16)$$

Hence, for small angle scattering (where $\sin\theta \approx \theta$), the differential cross section should decrease rapidly as $\theta^{-7/3}$.

In addition to the differential cross section, a total cross section is commonly defined [1] as

$$\sigma = 2\pi \int_0^{\pi} I(\chi) \sin\chi \, d\chi \quad . \qquad (17)$$

Several interesting features of both the differential and the total cross section can now be seen. First, according to equation (14), $I(0) \rightarrow \infty$. That is, the differential cross section diverges at 0 degrees. This so-called forward glory is also responsible for the divergence of the total cross section according to (17). Two other sources of singularities in

the differential cross section are apparent from the form of the classical deflection function. A typical function for a realistic Lennard-Jones potential is shown in Figure 3.2. Collisions at small impact parameters are essentially repulsive, and give rise to the positive branch of the deflection function. As the scattering angle decreases (increasing b), the attractive and repulsive forces eventually balance, (at b_0) no net deflection is seen ($\chi = 0$, the forward glory). For larger impact parameters, the scattering angle becomes negative, passes through a maximum at b_r (see below) and then approaches zero as $b \rightarrow \infty$. Since experimental measurements are only sensitive to $|\chi|$, then for $\chi < \chi_r$, three impact parameters (b_1, b_2, b_3) will contribute to (8), which must now be written as

$$I(\chi) = \sum_{i=1}^{3} \frac{b_i}{\sin\chi} \left|\frac{db_i}{d\chi}\right| \quad . \tag{18}$$

As $b \rightarrow 0$, $\chi \rightarrow \pi$, that is, the incoming particles just rebound off the target. Since $\sin\pi = 0$, (14) will again diverge as a result of this backward glory. The other divergence in $I(\chi)$ will occur when $\left|\frac{db}{d\chi}\right| \rightarrow \infty$ as $b \rightarrow b_r$. The corresponding angle, χ_r, is called the rainbow angle [5] in the analogy to the optical scattering responsible for rainbows. Note that for $\chi < \chi_r$, three terms contribute to (18), while for $\chi > \chi_r$, only one term (due to b_1) contributes to $I(\chi)$. The former situation is referred to as the bright side of the rainbow, while the latter is known as the dark side. By expanding $\chi(b)$ about χ_r, it is possible to determine the contribution to the cross section near the rainbow angle as,

Figure 3.2: The upper curve is a typical semiclassical deflection function calculated from a potential such as shown in Figure 2.1. Its shape is characteristic of a potential which combines both attractive and repulsive regions. b_0 is the impact parameter corresponding to no net deflection, while b_r is the impact parameter which gives rise to rainbow scattering. b_1, b_2, and b_3 are discussed in the text.

The lower curve is the phase shift function derived from the same potential. The relationship between the two (see equation 32) is such that b_0 in the deflection function corresponds to the maximum in the phase shift curve, and b_r corresponds to the inflection point in large impact parameter region of the phase shift curve.

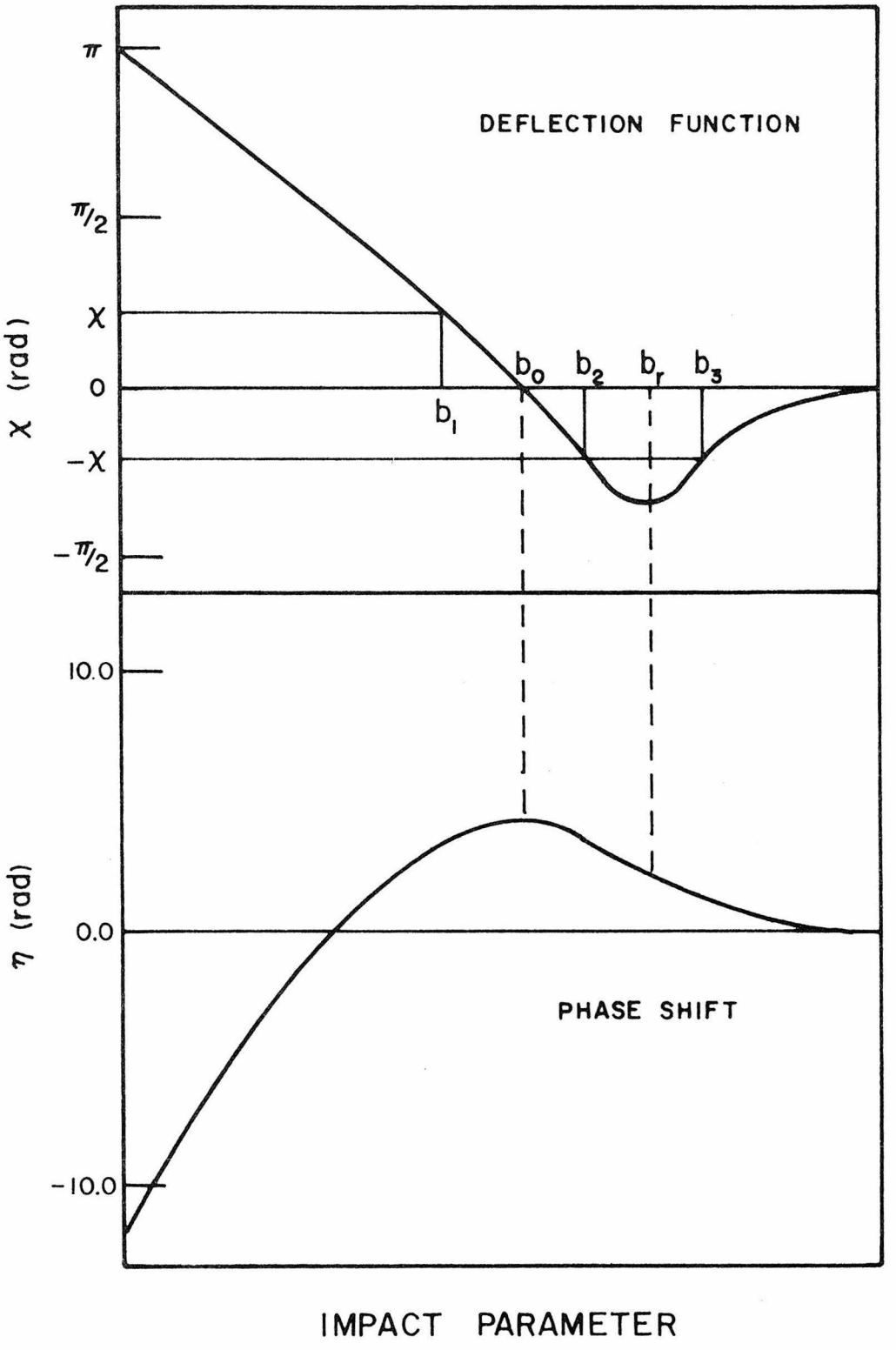
DEFLECTION FUNCTION
π
π/2
χ
0
−χ
−π/2
χ (rad)
b0
b2
br
b3
b1
10.0
0.0
−10.0
η (rad)
PHASE SHIFT
IMPACT PARAMETER

3.2

$$I(\chi) = \frac{b_r}{\sin\chi_r \left| \frac{1}{2}(\chi-\chi_r)\left(\frac{d^2\chi}{db^2}\right)_{\chi=\chi_r} \right|^{\frac{1}{2}}} \quad . \tag{19}$$

Because of the wave-like nature of matter, a classical description of scattering will only be valid under conditions where the particle wavelength is much shorter than the approximate range of the potential. In general, for atomic and molecular scattering at near thermal energies, this is not the case, and the classical description must give way to the exact quantum mechanical treatment. Under these conditions even such a useful concept as the deflection function has no quantum analog, since we cannot simultaneously specify both L (or b) and χ due to the uncertainty principle.

3.2 Quantum Mechanical Treatment [6]

In the quantum approach, the incident particles are represented by a traveling plane wave (taken along the z-axis) of the form,

$$\psi_{inc} = \frac{1}{(2\pi)^{3/2}} e^{ikz} \quad , \tag{20}$$

where k is the wavenumber, $\mu v/\hbar$. The particles scattered after interaction are represented by an outgoing spherical wavefunction,

$$\psi_{scat} \sim \frac{1}{(2\pi)^{3/2}} f(\chi) \frac{e^{ikr}}{r} \quad . \tag{21}$$

The scattering amplitude $f(\chi)$ is dependent on both the wavenumber k,

and the scattering angle χ, but is independent of ϕ (out-of-plane angle) due to the spherical nature of V(r). Based on the definition of the differential cross section given by equation (11), the quantum equivalent is just the ratio of the scattered to incident flux densities, or

$$I(\chi) = \frac{j_{scat}(\chi)}{j_{inc}} \quad . \tag{22}$$

Note that j_{scat} has the dimensions of particle/sec, while j_{inc} has dimensions of particles/sec/area. Using (20) and (21) to determine these fluxes, one finds that [3],

$$I(\chi) = \left| f(\chi) \right|^2 \quad . \tag{23}$$

In order to determine $f(\chi)$, one must solve the Schröedinger equation with $\psi = \psi_{inc} + \psi_{scat}$. The most commonly used method involves expanding ψ in the complete orthonormal set of Legendre polynomials [7]

$$\psi(r, \chi) = \sum_{\ell=0}^{\infty} \frac{R_\ell(r)}{r} P_\ell(\cos\chi) \quad , \tag{24}$$

where $R_\ell(r)$ is a solution to the radial Schröedinger equation,

$$-\frac{\hbar^2}{2\mu}\frac{1}{r^2}\frac{d}{dr}\left(r^2\frac{dR_\ell}{dr}\right) + \left[\frac{\ell(\ell+1)\hbar^2}{2\mu r^2} - E + V(r)\right] R_\ell(r) = 0 \quad . \tag{25}$$

This is the method of partial waves, since the wavefunction ψ is decomposed into a linear combination of spherical waves, each

corresponding to an orbital angular momentum of $[\ell(\ell+1)]^{\frac{1}{2}}\hbar \approx (\ell+\frac{1}{2})\hbar$. Classically, the corresponding impact parameter would be $b = (\ell+\frac{1}{2})/\mu v$.

In the absence of any interaction ($V(r) = 0$), the radial equation (25) reduces to a form of Bessel's equation, and the asymptotic solution for large r may be expanded and written as,

$$\psi \sim \sum_{\ell=0}^{\infty} (2\ell+1) e^{i\frac{\ell\pi}{2}} \frac{\sin(kr - \frac{\ell\pi}{2})}{kr} P_\ell(\cos\chi) \quad . \tag{26}$$

The corresponding solution in the presence of a potential can be written as,

$$\psi \sim \sum_{\ell=0}^{\infty} (2\ell+1) e^{i(\frac{\ell\pi}{2} + \eta_\ell)} \frac{\sin(kr - \frac{\ell\pi}{2} + \eta_\ell)}{kr} P_\ell(\cos\chi) \quad . \tag{27}$$

The net effect of the scattering process then is to introduce a phase factor (or phase shift) η_ℓ into the asymptotic radial wavefunction. Since for large r both solutions oscillate with the same constant frequency, η_ℓ/k will be the separation between corresponding nodes of the two wavefunctions. The sum of the two solutions, (26) and (27), represents the general solution for the scattered wave, and hence it is possible to express $f(\chi)$ in terms of these solutions.

$$f(\chi) = \frac{1}{2ik} \sum_{\ell=0}^{\infty} (2\ell+1)(e^{2i\eta_\ell} - 1) P_\ell(\cos\chi) \quad . \tag{28}$$

Combining this with (23), the differential cross section can now be

represented as a sum of partial waves, each weighted by a phase shift factor,

$$I(\chi) = \frac{1}{4k^2}\left[\left(\sum_{\ell=0}^{\infty}(2\ell+1)\sin 2\eta_\ell\, P_\ell(\cos\chi)\right)^2 + \left(\sum_{\ell=0}^{\infty}(2\ell+1)(\cos 2\eta_\ell - 1)\, P_\ell(\cos\chi)\right)^2\right] \quad . \quad (29)$$

The total cross section according to (17) is

$$\sigma = \frac{4\pi}{k^2}\sum_{\ell=0}^{\infty}(2\ell+1)\sin^2\eta_\ell \quad . \quad (30)$$

Since all of the scattering information is contained in the phase shifts, it is necessary to calculate these η_ℓ in order to predict the differential cross section quantum mechanically.

3.2.1 Phase Shift Calculations

Depending on the nature and strength of the potential, the total energy and the ℓ value, various methods may be used to determine the phase shifts. These methods include an exact numerical solution of the wave equation (25), as well as a number of approximate techniques. Since in general, approximate methods require much less effort than exact methods, it is important to determine under what conditions each may be used.

Pauly and Toennies [6b] have established two criteria for deciding on the best method of phase shift calculation. The criteria

are the magnitudes of the ratios a/λ and a/δ, where a is a measure of the range of the potential ($a \approx r_m$), λ is the incoming particle wavelength ($= 2\pi/k$), and δ is the approximate uncertainty in the position of the particle. Exact, JWKB and high energy phase shift calculations are the most commonly employed, and these will each be briefly outlined and compared below.

If both $a/\lambda \gg 1$ and $a/\delta \gg 1$, then the incoming particle will closely follow a classical trajectory, and the results of Section 3.1 may be used to determine the differential cross section directly. If these ratios have just the opposite magnitudes, that is, $a/\lambda \ll 1$, $a/\delta \ll 1$, then the exact quantum treatment must be followed. Bernstein [8] and others [9-11] have performed a number of complete quantum calculations of the phase shifts, differential and total cross sections (see below). The usual technique for performing an exact phase shift calculation is to numerically integrate the standard form of the radial wave equation starting with $r < r_c$ (the classical turning point), and continuing until $|V(r)| \ll k^2$. A step size of $\Delta r \approx 0.01$ A is common, and the estimated accuracy of the phase shifts is ± 0.002 radians [9]. A number of exact quantal phase shifts determined in this manner are given in Table I (see below).

A very common situation for thermal energy elastic scattering of small atomic and molecular systems is $a/\lambda \gg 1$ and $a/\delta \approx 1$. Under these conditions, the well-known JWKB approximation is valid, and is often used to calculate η_ℓ. A large number of derivations of the JWKB approximation as it applies to the calculation of scattering phase shifts exist [3, 12, 13], including a uniform semi-classical (Langer)

formulation [14]. The condition for validity of this method $a/\lambda \gg 1$, is often stated as $d \ln V(r)/dr \gg \lambda$ [15]; that is, that the de Broglie wavelength λ be small enough so that the fractional change in the potential over a wavelength is very small. Under these conditions, the asymptotic form of the JWKB radial wave function is used to determine the phase shift as,

$$\eta_\ell = k\left[\int_{r_0}^{\infty}\left[1 - \frac{V(r)}{E} - \frac{b^2}{r^2}\right]^{\frac{1}{2}} dr - \int_{b_0}^{\infty}\left(1 - \frac{b^2}{r^2}\right)^{\frac{1}{2}} dr\right] \tag{31}$$

where r_0 and b_0 are the outermost zeros of the respective integrands. It is possible to further reduce (31) to a form requiring the evaluation of a single quadrature, which in turn can be evaluated by summation methods (see below). Comparison of equation (31) for the JWKB phase shifts with equation (7) for the classical deflection function gives a very significant relationship between the two,

$$\frac{d\eta_\ell}{d\ell} = \tfrac{1}{2}\,\chi(\ell) \tag{32}$$

using $(\ell + \frac{1}{2}) = kb$. Equation (32) is known as the semiclassical equivalence relationship [16, 17], and is easily verified by inspection of the $\theta(b)$ and η_b curves in Figure 3.2.

In a situation where the expected deflection of the incoming particle is small, that is for large impact parameters ($\ell \gg 1$), or high energy, a considerable simplification of equation (31) can be made. Under these circumstances, a straight line trajectory is assumed,

given by

$$r = b^2 + z^2 \quad ,$$

and equation (31) is expanded in powers of V/E. The first term is retained in the so-called high energy approximation [18], and the result is,

$$\eta_\ell = \frac{1}{2\hbar v} \int_{-\infty}^{\infty} V(z)\, dz \quad . \tag{33}$$

If V is chosen as a simple Lennard-Jones (6, 12) potential,

$$V(r) = 4\epsilon \left[\left(\frac{\sigma}{r}\right)^{12} - \left(\frac{\sigma}{r}\right)^{6} \right] \tag{34}$$

then the integral in (33) may be performed analytically [19], to give

$$\eta_\ell = \frac{\pi k \sigma \epsilon}{E} \left(c_1 \left(\frac{\sigma}{b}\right)^5 - c_2 \left(\frac{\sigma}{b}\right)^{11} \right) \quad , \tag{35}$$

where c_1 and c_2 are numerical constants. It is clear from equation (35) that $\eta_\ell \rightarrow -\infty$ as $\ell \rightarrow 0$, so that this high energy approximation will only be useful for $\ell \gg 1$, regardless of the energy.

While criteria for the applicability of these various approximate methods have been given, it is nonetheless important to compare the results obtained by each method in the range of parameters of interest. Such a comparison was performed by Marchi and Mueller [20] between the exact and JWKB phase shifts calculated using a Lennard-Jones potential with $a/\lambda \approx 1$. The LJ (6, 12) potential parameters were chosen to correspond to the H_2 - Hg elastic scattering with

$\epsilon = 2.46 \times 10^{-14}$ ergs and $\sigma = 2.9 \times 10^{-8}$ cm. Experimental measurements on this system by Knauer [21], and exact quantum calculations by Bernstein [8] using these parameters allowed for a more complete comparison to be made. Marchi and Mueller found that, in general, the JWKB and quantum phase shifts for this system were comparable to within a few percent for all ℓ values. Since only the differential cross section is measured experimentally, it is important to compare this quantity calculated using both exact and JWKB (or high energy) phase shifts. As a check on several computational methods to be used in Chapter 5 for data analysis, a similar comparison of phase shifts and cross sections was undertaken in this study using the same parameters as given above.

The exact phase shifts $(\eta_0 - \eta_{50})$ were obtained from Table III of reference [8a] for $A = (k\sigma) = 20$ and $B = (2\mu\epsilon\sigma^2/\hbar^2) = 125$, and were, in addition, recalculated using a method due to Gordon [22]. This method is a general technique for integrating the wave equation to determine the wavefunction in a piecewise analytic form. By approximating the potential by a series of straight line segments, the solution of the radial wave equation is found analytically in terms of Airy functions. Any desired degree of accuracy can be obtained in the solution by adjusting the size of the line segments. As with the direct integration method, the solution is determined by propagating from $r < r_c$ to a point where the wavefunction approaches the zero order Bessel function $j_0(r)$. While the method was originally designed to evaluate S matrix elements arising from coupled differential equations,

only slight modifications are necessary, since $S = e^{2i\eta_\ell}$ for elastic scattering [23].

The results of these calculations are listed in Table I along with the exact results obtained by Bernstein from the direct integration of the wave equation. Computation of the former required approximately 13.3 seconds for $\eta_0 \rightarrow \eta_{50}$ using an IBM 370/165 computer.

Values of the JWKB phase shifts were evaluated using a Gauss-Mehler quadrature [17, 24] formula to evaluate equation (31). The general method closely follows that used by Smith and Munn [25], where the integral is replaced by a sum. The phase shift is calculated by successively doubling the number of terms in the sum until the desired degree of convergence is achieved. The resulting phase shifts are listed in Table I.

Finally, for comparison, several of the higher ℓ value high energy phase shifts are listed in the last column of Table I. These were obtained by direct evaluation of equation (35). In general, these high energy phase shifts are used only when $\eta_\ell < 0.01$ radians where agreement with both JWKB and exact results is within 5%.

The results in Table I show that either method of calculating the "exact" phase shifts is valid, and that the JWKB values are in quite good agreement over the full range of orbital angular momentum waves calculated. As expected, the high energy results are somewhat poorer even for the larger ℓ values. A more significant comparison between these various methods for evaluating the phase shifts is by examining the resultant differential cross sections as determined from equation (29). Using the exact and JWKB phase shifts listed in

Table I

Phase Shift Comparisons

V(r) = LJ (12, 6) A = 20.0 K = 3.2

ℓ	η_ℓ			
	Exact		JWKB	High Energy
	Ref. [8]	Present		
0	-16.933	-16.940	-16.909	$-\infty$
1	-15.420	-15.423	-15.393	
2	-13.964	-13.962	-13.932	
3	-12.547	-12.555	-12.525	
4	-11.197	-11.203	-11.173	
5	- 9.898	- 9.902	- 9.876	
6	- 8.662	- 8.667	- 8.636	
7	- 7.471	- 7.485	- 7.452	
8	- 6.351	- 6.357	- 6.325	
9	- 5.278	- 5.290	- 5.256	
10	- 4.266	- 4.281	- 4.246	
11	- 3.32	- 3.332	- 3.296	
12	- 2.431	- 2.444	- 2.408	
13	- 1.61	- 1.621	- 1.582	
14	- 0.846	- 0.861	- 0.821	
15	- 0.156	- 0.167	- 0.126	
16	0.472	0.456	0.499	
17	1.03	1.008	1.054	
18	1.503	1.485	1.533	
19	1.89	1.882	1.934	0.390
20	2.219	2.194	2.252	2.406
21	2.46	2.423	2.482	3.006
22	2.576	2.553	2.619	2.982
23	2.607	2.584	2.655	2.708
24	2.531	2.506	2.584	2.360
25	2.344	2.323	2.405	2.012
26	2.08	2.054	2.128	1.696
27	1.768	1.745	1.798	1.422
28	1.469	1.451	1.480	1.190
29	1.213	1.148	1.214	0.996
30	1.008	0.992	1.003	0.834
31	0.840	0.829	0.836	0.700

Table I (Continued)

ℓ	η_ℓ			
	Exact		JWKB	High Energy
	Ref. [8]	Present		
32	0.707	0.697	0.703	0.590
33	0.600	0.589	0.596	0.498
34	0.57	0.504	0.509	0.422
35	0.432	0.432	0.437	0.360
36	0.37	0.373	0.378	0.308
37	0.32	0.323	0.328	0.264
38	0.28	0.281	0.286	0.226
39	0.25	0.246	0.251	0.196
40	0.219	0.216	0.221	0.168
41	0.20	0.190	0.195	0.146
42	0.17	0.167	0.173	0.128
43	0.15	0.149	0.153	0.112
44	0.14	0.131	0.137	0.098
45	0.12	0.117	0.122	0.086
46	0.11	0.105	0.109	0.076
47	0.10	0.094	0.098	0.066
48	0.08	0.084	0.088	0.058
49	0.08	0.075	0.080	0.052
50	0.070	0.068	0.072	0.046

Table I, and equation (20), two differential cross sections were generated. These are shown in Figure 3.3. It is quite clear that no significant differences are apparent in the two curves over the angular range shown.

It is significant to note that while the results of the classical treatment of scattering (Section 3.1) predicted a smooth decrease in the scattered flux as a function of increasing angle (see equation 16), the results of the quantum treatment (Figure 3.3) show oscillatory structure of substantial magnitude. In fact, as might be expected from the correspondence principle [26], the quantum structure oscillates about the classical cross section. The nature of these quantum effects has been dealt with using a semiclassical approach to the scattering, as described in the following section.

3.3 Semiclassical Scattering

According to Ford and Wheeler [2], the semiclassical approximation is based on four mathematical assumptions. They are:

(1) The phase shift η_ℓ is determined by the JWKB method, which also ensures that the semiclassical equivalence relationship of equation (32) is valid.

(2) The Legendre polynomials in (28) are replaced by either of the following asymptotic expressions,

$$P_\ell(\cos\theta) \cong \left[\tfrac{1}{2}(\ell+\tfrac{1}{2})\pi \sin\theta\right]^{-\frac{1}{2}} \sin\left[(\ell+\tfrac{1}{2})\theta + \pi/4\right] \qquad (36)$$

for $\sin\theta \geq 1/\ell$, or,

Figure 3.3: A comparison of the differential elastic scattering cross section from 0° to 40° calculated using both exact phase shifts (solid curve) and JWKB phase shifts (dashed curve). The Lennard-Jones (6, 12) potential parameters used were ϵ = 15.5 meV (K = 3.2) and σ = 2.91 A (A = 20.0). The cross section has been transformed to the laboratory system.

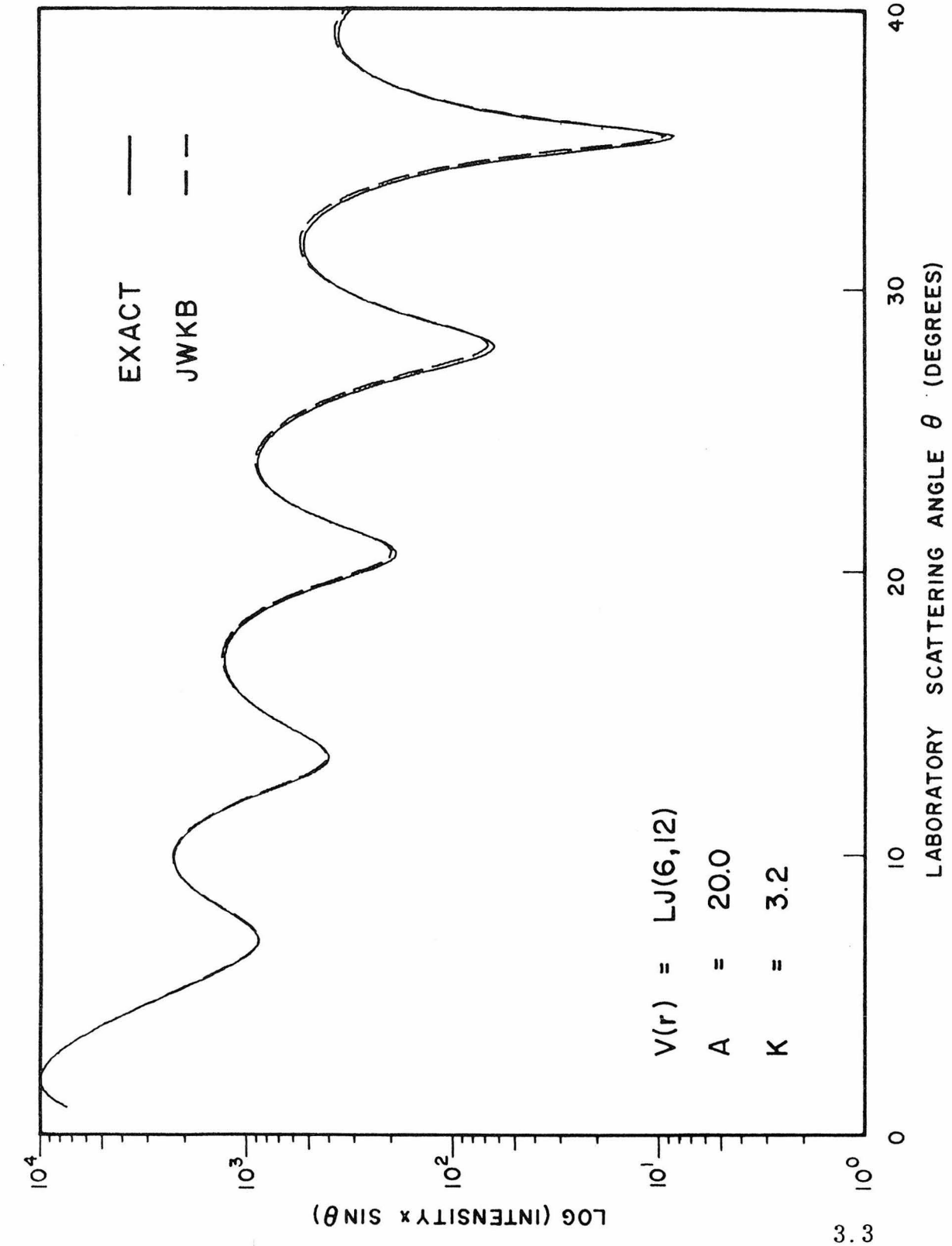
EXACT
JWKB
V(r) = LJ(6,12)
A = 20.0
K = 3.2
LOG (INTENSITY x SIN θ)
LABORATORY SCATTERING ANGLE θ (DEGREES)
10^4
10^3
10^2
10^1
10^0
0
10
20
30
40

3.3

$$P_\ell(\cos\theta) \cong (\cos\theta)^\ell \, j_0[(\ell+\tfrac{1}{2})\theta] \tag{37}$$

for $\sin\theta \leq 1/\ell$.

(3) The summation in equation (28) is replaced by an integral. This approximation could only be made after η_ℓ and $P_\ell(\cos\theta)$ were assumed to be continuous functions of ℓ, and it will be valid in cases where many ℓ waves contribute to the cross section. At this point, the semiclassical scattering amplitude can be expressed as

$$f_{sc}(\chi) \cong \frac{-1}{k(2\pi\sin\chi)^{\frac{1}{2}}} \int_0^\infty \ell^{\frac{1}{2}} \left[e^{i\phi_+} - e^{i\phi_-}\right] d\ell \tag{38}$$

where

$$\phi_\pm = 2\eta_\ell \pm (\ell+\tfrac{1}{2})\chi \pm \pi/4 \quad . \tag{39}$$

(4) The final assumption in the semiclassical approximation is that (38) be evaluated by means of stationary phase. This assumption reduces to finding values of ℓ for which

$$\frac{d\phi_+}{d\ell} = 0 \qquad \text{or} \qquad \frac{d\phi_-}{d\ell} = 0 \quad . \tag{40}$$

In general, the result of applying (40) to (39) is just the semiclassical equivalence relationship,

$$\frac{d\eta}{d\ell} = \eta'_L = \tfrac{1}{2}\chi(L)$$

where L corresponds to a stationary value of $\phi_\pm$. As a result of this stationary phase approximation, as many as three values of L (or b) will correspond to one $\chi(L)$, these b values (b_1, b_2, b_3) are just those

shown in Figure 3.2. It is possible then to write the semiclassical scattering amplitude as a sum of these three contributions,

$$f_{sc}(\chi) = f_1(\chi) + f_2(\chi) + f_3(\chi) \quad . \tag{41}$$

When the differential cross section is determined by equation (23),

$$I(\chi) = \left|f_{sc}(\chi)\right|^2 = \left|f_1(\chi) + f_2(\chi) + f_3(\chi)\right|^2 \tag{42}$$

oscillatory terms will result due to interference effects between the different branches of the deflection function (different $f_i(\chi)$).

Two distinct types of interference effects would be predicted on the basis of this semiclassical analysis. For small angle scattering, two impact parameters (b_1 and b_2) very near to b_0 would contribute most strongly to the cross section. The corresponding b_3 contribution would be much smaller since $b_3 \gg 1$. The resulting small angle cross section would be dominated by interference oscillations whose wavelength is given by [6a],

$$\Delta\chi = 2\pi/(b_1 + b_3) \quad . \tag{43}$$

As $\chi \rightarrow 0$, $b \rightarrow b_0$ which corresponds exactly to σ, the zero of the potential, hence, we can approximate the spacing of these "rapid quantum" type oscillations as

$$\Delta\chi = \pi\hbar/\mu v\sigma = \lambda/2\sigma \quad . \tag{44}$$

For larger angles, all three impact parameters will make significant contributions to $I(\chi)$, and no simple structure can be predicted from

equation (41). As the rainbow angle χ_r is approached, b_2 and b_3 will both approach b_r, and strong oscillations would be expected in the vicinity of the rainbow scattering. Such structure, termed supernumerary rainbow scattering [27, 28] would have a spacing of

$$\Delta\chi = 2\pi(b_r + b_1) \quad . \tag{45}$$

Using a uniform semiclassical approach, Ford and Wheeler have eliminated the singularity in the differential cross section at $\chi = \chi_r$, and have replaced it by a finite maximum. For scattering angles greater than χ_r, only the repulsive branch of the deflection function will contribute to the cross section. Whenever the deflection function becomes single valued, as it does for $\chi > \chi_r$, the cross section reduces to the single classical result. Hence, strong oscillations are predicted for $\chi \leq \chi_r$, but only a smoothly falling scattered flux is predicted for $\chi > \chi_r$. A number of other consequences of the semiclassical scattering analysis can be derived for total cross section and glory scattering, however, those effects are not important in the current studies, and will only be mentioned here.

Following the same semiclassical development as for the differential cross section, the total cross section is predicted to show undulations as a function of velocity [29, 30]. Specifically, an undulation will occur whenever the maximum positive phase shift $\eta(k)_{max}$ is given by,

$$\eta(k)_{max} = (N - \tfrac{3}{8})\pi \tag{46}$$

where N = 1, 2, 3, ... correspond to maxima in the cross section, and

$N = 1.5, 2.5, 3.5, \ldots$ correspond to minima. Since η_{max} is a function of the wavenumber (or velocity) and the potential, it has been shown that the positions of the extrema in the total cross section (for a Lennard-Jones potential) are given as,

$$(N - \frac{3}{8}) \quad \propto \quad \frac{\epsilon \sigma}{v_N} \quad . \tag{47}$$

Here, v_N is the velocity at which an undulation occurs, and ϵ and σ are the two Lennard-Jones parameters (see equation 34). Numerous experimental studies have verified the correctness of (47), and have allowed the determination of the product value $\epsilon\sigma$ [31-34]. While it is possible to relate σ to the amplitudes of the oscillations [30, 35] (at least semiclassically), even small amounts of velocity averaging in the measured cross section will greatly affect these amplitudes, and hence no additional information on σ can be obtained in this way. Basically then, total cross section measurements yield no independent values for ϵ and σ, but rather only their product. This is, of course, in contrast to the differential cross section measurements which are sensitive to both parameters independently. The results of total cross section measurements can, however, be combined with differential cross section results to better characterize the potential.

From the classical, semiclassical, and quantum analysis of scattering outlined above, it is clear that the measured differential scattering cross section is related to the intermolecular potential V(r) only through the integral relationship of either the deflection function,

or equivalently, the phase shifts. If the relationship between impact parameters and scattering angles is one-to-one, then in principle, the deflection function could be constructed from the measured scattering. A direct inversion of the deflection function to give the potential could then be performed (see next section). For the case of a double valued deflection function, the inversion procedure would still yield a unique potential function. However, for the more common situation where three impact parameters contribute to the scattering at one angle, this inversion may no longer be possible. Fortunately, however, the measured scattering is sensitive to the shape and magnitude of the potential. Specifically, for thermal energy scattering where the region of the potential sampled is near σ, then equation (44) provides a means of determining this parameter so long as oscillatory structure is resolved experimentally. In order to gain a quantitative estimate of the sensitivity of $I(\chi)$ on $V(r)$, several cross sections were calculated using a LJ(12, 6) potential function holding either ϵ or σ constant while varying the other parameter. The results of these calculations are shown in Figures 3.4 and 3.5. Clearly, variations in σ affect the spacing of the oscillations as predicted by equation (44), while variations in ϵ result in changes in the amplitudes of the oscillations. Any changes in the overall shape of the potential function will produce similar variations in the calculated differential cross section. In principle then, if such rapid quantum oscillations can be experimentally resolved (see Section 4), it should be possible to vary the size and shape (or mathematical form) of $V(r)$ until the predicted and measured

Figure 3.4: Variations in the calculated differential elastic scattering cross section as a result of varying the σ parameter of a Lennard-Jones (6, 12) potential. With a fixed ϵ (i.e., K), 10% changes in σ (A) shift the locations of the rapid oscillations approximately according to equation (44). The cross sections have not been adjusted vertically, so that the amplitude variations are as shown.

Figure 3.5: (Overleaf). This figure corresponds to Figure 3.4 where the varying parameter is now the well depth ϵ (K). The major effect of this variation on the differential elastic scattering occurs in the amplitudes of the oscillations, rather than their angular spacing. Note that the dashed curve (K = 4.0) here is the same as the dashed curve in Figure 3.4.

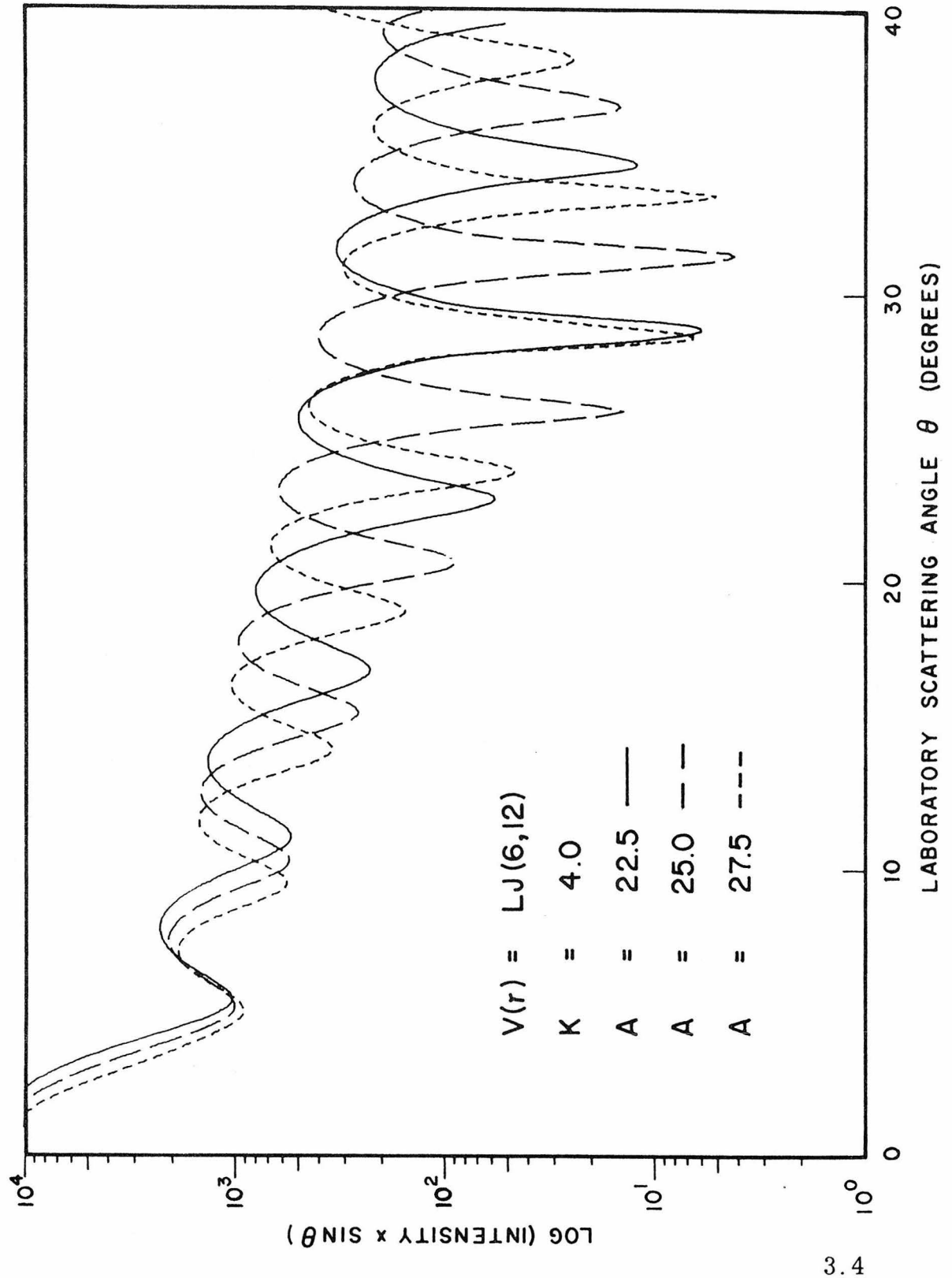
V(r) = LJ(6,12)
K = 4.0
A = 22.5
A = 25.0
A = 27.5
LOG (INTENSITY x SIN θ)
LABORATORY SCATTERING ANGLE θ (DEGREES)
10^4
10^3
10^2
10^1
10^0
0
10
20
30
40

3.4

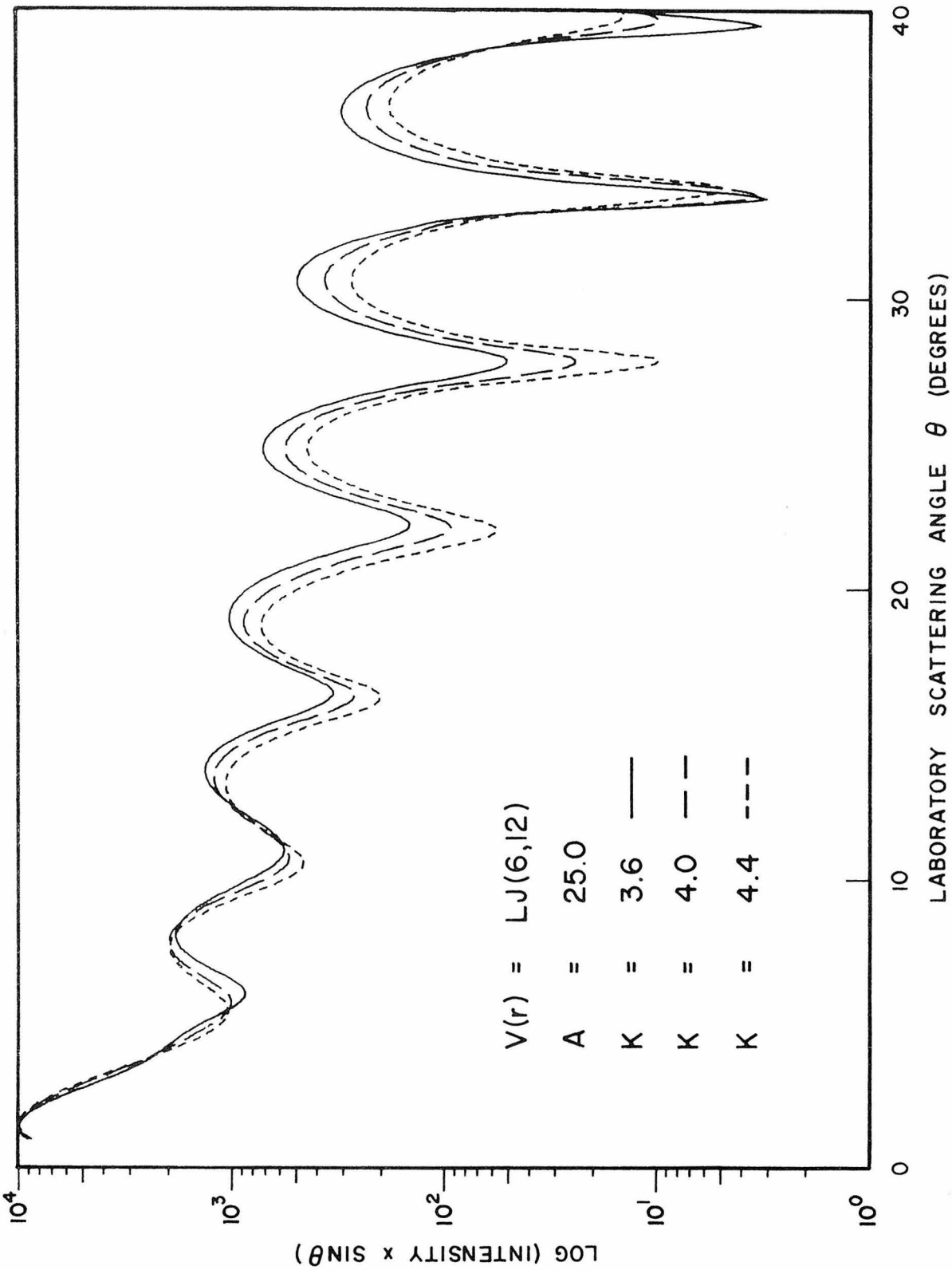
V(r) = LJ(6,12)
A = 25.0
K = 3.6
K = 4.0
K = 4.4
LOG (INTENSITY x SIN θ)
LABORATORY SCATTERING ANGLE θ (DEGREES)
10^4
10^3
10^2
10^1
10^0
0
10
20
30
40

3.5

scattering distributions agree. This is in fact the general method used (in Section 5) for determining intermolecular potential parameters from the measured scattering data.

At this point, it is important to note that while the semiclassical analysis of Ford and Wheeler accurately predicts the existence of the rapid quantum oscillations, the analysis itself is not valid for treating the results of the present studies. This failure of the semiclassical approach to scattering is generally expected when the incident de Broglie wavelength becomes comparable to, or shorter than, the range of the potential. For thermal energy scattering of H_2 (D_2) by heavier diatomic and polyatomic molecules, the de Broglie wavelength is normally about 1 A, while the range of the potential is on the order of several Ångstroms. The breakdown of the semiclassical description of the scattering process can be seen in at least two ways. First, despite predictions to the contrary, many elastic scattering systems exhibit no rainbow scattering either experimentally, or quantum mechanically. For example, the differential cross sections shown in Figures 3.4 and 3.5 were calculated using parameters suitable for describing the scattering of H_2 by O_2 (see Section 5). Semiclassically, the rainbow angle χ_r is approximately 15° in the center of mass system. Not only is no rainbow structure apparent in the calculated (quantum mechanically) cross sections, but the rapid oscillations continue well beyond 15° where the semiclassical results would predict only a smooth classical fall off. In addition to this obvious inconsistency, the rapid interference oscillations predicted by the semiclassical description

are found to occur in the quantum mechanically determined differential scattering using a hard sphere potential [36]. This potential has no attractive well, and hence has only a single valued monotonic deflection function, which could not give rise to interference scattering.

It would seem apparent then, that only a complete quantum description of the scattering will be valid for these studies, and an explanation of the observed oscillatory structure must be found within that framework. Based on the hard sphere scattering studies [36], and others [37], it would appear that these rapid oscillations are due to a diffraction effect of the incident wavepacket upon encountering the sharp repulsive wall of the potential. Such diffraction would produce an interference pattern with a spacing of just that predicted by equation (43) [37]. Furthermore, these diffraction oscillations would not be restricted as to angular range, and so could dominate the differential elastic scattering up to quite large ($\sim 40°$) angles.

3.4 Potential Inversion

It was noted earlier that in principle, differential cross sections which are the result of contributions from at most two impact parameters could be used to determine directly the phase shift curve. It was demonstrated many years ago by Firsov [38] that a knowledge of the complete phase shift function would allow for the determination of the unique potential which generated the scattering (see below). While this type of direct inversion, that is determination of an intermolecular potential directly from the scattering data, may not always be possible

for three valued deflection functions, much recent work has been performed toward this end. The value of such an inversion procedure is that it removes the severe restrictions placed on the potential function by the limited flexibility of the mathematical models used in the normal fitting procedure. While multiparameter model potentials can have a reasonable degree of flexibility, the demonstrated sensitivity of the scattering to the detailed shape of the potential [20] makes a directly determined numerical potential clearly superior.

The formal inversion problem has been treated quantum mechanically [39-41], however, the generalized results are not very practical. These procedures, aimed at inverting high energy nuclear scattering data are difficult to apply to low energy atomic scattering where many more partial waves are involved. Much more practical approaches have been based on classical and semiclassical methods.

These latter techniques usually consist of a determination of the phase shift or deflection function curves from the data, followed by application of a Firsov-type procedure to obtain the potential. Basically, this method involves inverting the integral expression for the deflection function (equation 8). By defining two new functions [42],

$$u(r) = r\left[1 - V(r)/E\right]^{\frac{1}{2}} \tag{48}$$

and

$$T(u) = \frac{1}{\pi} \int_u^\infty (b^2-u^2)^{-\frac{1}{2}} \chi(b)\, db \quad , \tag{49}$$

it is possible to write the potential function as

$$V(r) = E[1 - \exp(-2T(u))] \quad . \tag{50}$$

Due to the form of equations (48) and (49), the method is restricted to energy ranges where no classical orbiting can occur. This is not a serious restriction, and the method is otherwise generally applicable to any form of $\chi(b)$. The main aspect of the inversion procedure is therefore the determination of $\chi(b)$ or η_ℓ from the measured scattering data.

Mueller and co-workers [43, 44] have shown that for many atomic systems, the large negative phase shifts associated with the strong repulsive scattering make little contribution to the smaller angle scattering, and hence only the positive phase shifts need be considered. Rather than deal with the phase shifts directly, a five parameter function was developed to represent the phase shift curve which was used to calculate the differential cross section. A least squares method could then be used to adjust the phase shift function parameters to optimize the agreement with the experimental results. A method developed by Sanders and Mueller [45] was utilized to obtain the intermolecular potential parameters starting with the phase shift curve. In general, this method is not suitable for systems where repulsive potential scattering (such as diffraction) is significant, nor is it applicable to experimental results with considerable velocity averaging.

Several inversion methods have been developed which depend upon the experimental resolution of rainbow scattering for the determination of the full phase shift curve. The method due to Miller [42]

requires a knowledge of the asymptotic form of the potential (usually $\sim 1/r^6$) and also the incomplete total cross sections,

$$Q(\chi) = 2\pi \int_{\chi}^{\pi} \sin\theta \ \sigma(\theta) \, d\theta$$

at each χ measured. From these, a function is constructed in terms of χ and χ_r. Inversion of this function yields the numerical potential. It is quite unlikely that this method could successfully be applied to many systems due to the large amount of input information required.

An inversion method formulated by Buck and Pauly [46] used both rainbow and supernumerary rainbow structure, as well as the velocity dependence of the total cross section to determine the deflection function. For $\chi > \chi_r$, $\chi(b)$ was generated directly from the data, while for smaller angles, an analytical form for the deflection function was fitted using the input data. The two parts of $\chi(b)$ were smoothly joined, and the potential generated by the Firsov method. A similar procedure developed by Buck [47] used the rainbow and quantum oscillations to determine the attractive region of the deflection function, and wide angle scattering to construct the repulsive region. Both methods required high resolution (nearly monoenergetic) scattering data.

To partially overcome the unphysical requirement of monoenergetic scattering results, Luoma and Mueller [48,49] suggested the use of an angular scaling function. This function relates the locations of the maxima of the differential cross section at any velocity

(in a distribution) to the corresponding maxima locations for some fixed velocity (the center of the distribution). Again using a functional form to represent the phase shift curve associated with the central velocity, its parameters were adjusted to provide a least squares fit of the data. In calculating the velocity averaged differential cross section for comparison with the data, use was made of the approximate scaling function described above. The resulting averaged cross section is not the same as would be obtained by averaging together many cross sections, each calculated exactly for various velocities in a given distribution. Despite these approximations, some degree of success was achieved in fitting the velocity averaged data of Knauer [21].

Yet another method has recently been advanced by Klingbeil [50], where the phase shifts themselves are treated as individual parameters. Generally, it was found the smaller η values (large ℓ) could be approximated by a simple analytical function. This reduced the number of parameters that had to be dealt with. Despite this reduction, it is not unusual for several hundred phase shifts to contribute to the cross section, and hence a large number of parameters must be varied. As a result, an equally large number of independent data points is required in order to allow a least squares fitting procedure to be used. Any optimized least squares method, such as that due to Marquardt [51] requires the derivatives of the fitted function (in this case, the differential cross section $I(\chi)$) with respect to each of the parameters (the phase shifts). If the fitted function is really the velocity averaged differential cross section, then these derivatives

must be determined numerically, which would require very large amounts of computational effort. In addition, since the final step of the inversion requires a smooth phase shift function, much of the flexibility of this procedure is lost when the individually determined phase shifts must be least squares fit to ensure this smoothness. Under certain conditions, however, Klingbeil was able to apply successfully this method to both ion-atom [52] and atom-atom [53] scattering.

In view of the nature of the experimental results of the present studies (see Section 5), the methods of Luoma and Mueller and Klingbeil appeared the most applicable. Several attempts were made to directly invert the differential elastic cross sections measured in this work. In general, both methods failed due to the lack of their ability to deal adequately with the problem of velocity averaging. The scaling function method of Luoma and Mueller was found to be a poor approximation for the systems under consideration, and in addition, neither method could be simply adapted to perform the fitting procedure in the laboratory frame.

A number of test calculations were carried out using a hybrid approach. A large number of phase shifts were used as parameters as in Klingbeil's method, however, they were smoothed by fitting the functional form proposed by Luoma and Mueller. At a single velocity, the calculated cross section could be properly transformed into the laboratory frame and the required derivatives determined for the least squares Marquardt method to be used. Using calculated test data, a Lennard-Jones potential function could be accurately reproduced with

only moderate effort. Any attempt to generalize this procedure to process velocity averaged scattering data met with failure, mainly due to the subsequent need to calculate derivatives numerically, and the extreme slowness with which the method converged. As a result, the only potential information obtained from these studies was in the form of parameters associated with several mathematical models.

3.5 Nonspherical Potentials and Inelastic Scattering

The entire treatment of scattering up to this point has been based on two assumptions. First, that only elastic scattering (no translational $\rightarrow$ internal energy transfer) is occurring, and second that the interaction potential is spherically symmetric. For low energy atom-atom collisions, these assumptions are certainly reasonable. For atom-molecule or molecule-molecule scattering, however, both of these assumptions must be more carefully examined. The interaction potentials are certainly no longer spherically symmetric, and some estimate must be made as to the degree of anisotropy and its effect on the measured distribution of scattered flux. In addition to possible vibrational excitation of the molecular species at even modest energies, non-spherical potentials give rise to non-central forces (torques) which may cause rotational excitations. In general, the cross sections for vibrationally and rotationally inelastic scattering are much smaller than the corresponding elastic cross section, so that at thermal energies, their contributions to the observed scattering will be small. Furthermore, for rapidly rotating molecules that scatter at fairly large

impact parameters (small angles), the effective potential governing the interaction may be nearly spherical. In a scattering experiment without product velocity analysis, inelastically scattered particles cannot be distinguished from the bulk of elastically scattered products. The only possible indication of inelasticity would arise when theoretical cross sections computed for purely elastic scattering failed to account for the observed distribution. Since rotationally (or vibrationally) inelastic events would likely require close interaction (small impact parameters), evidence for such scattering might only be expected at larger scattering angles. To some extent, recent experimental observations [54] of rotationally inelastic scattering support this intuitive idea.

Theoretically, the orientational dependence introduced into the scattering by a non-spherical potential greatly complicates the situation. The equations presented previously for the classical and semiclassical trajectories (deflection functions) and the quantum mechanical radial wave equation must all be modified. Starting with the classical equations of motion, Cross and Herschbach [55] have studied the scattering of an atom from a diatomic rigid rotor. Using as the interaction potential a modified Lennard-Jones of the form,

$$V(r, \theta) = 4\epsilon \left[\left(\frac{\sigma}{r}\right)^{12} - \left(\frac{\sigma}{r}\right)^{6}\right] \left[1 + a\, P_2(\cos\theta)\right] \qquad (51)$$

the deflection angle deviates from the spherically symmetric case, roughly in proportion to the magnitude of a. This deviation in χ

results in a significant broadening of the cross section in the rainbow region, and also leads to quenching of the magnitudes of the glory undulations in the total cross section. Such quenching has been observed experimentally for a large number of systems [56-60].

A number of semiclassical approaches to non-spherical scattering have been advanced [61-63]. In the simplified method of Cross [64], the effects of potential anisotropy on the differential cross section were considered. By assuming that the molecule was a rigid rotor whose orientation did not change during a collision (sudden approximation), and further that only small angle scattering was occurring (eikonal approximation [65]), analytical expressions were obtained for the semiclassical scattering amplitude. This treatment indicated that quenching and angular shifting of both rainbow and rapid (quantum) oscillations would occur as a result of the anisotropic potential.

Most fully quantum mechanical treatments of non-spherical scattering are based either on a close coupling or a distorted wave method [66-69]. The basic scattering problem reduces to solving a set of coupled second order differential wave equations. The coupling terms arise because of the mixing of different angular momentum states during inelastic collisions. Using this type of formalism, Miller [70] has shown that anisotropy parameters (such as a in equation 51) may be determined from total cross section measurements. Recently, such information has been obtained from measurements of the total cross section using oriented molecular beams to probe the non-spherical

potential [71-73]. In general, these effects have been found to be quite small. The direct observation of inelastic scattering by rotational [54, 74], vibrational [75, 76], and electronic [77, 78] energy transfer has been achieved experimentally, and further information concerning non-spherical intermolecular potentials is now becoming available.

References

1. J. O. Hirschfelder, C. F. Curtiss, and R. B. Bird, "Molecular Theory of Gases and Liquids," Wiley, New York, 1964.
2. K. W. Ford and J. A. Wheeler, Ann Phys. 7, 259 (1959).
3. See, for example, N. F. Mott and H. S. W. Massey, "Theory of Atomic Collisions," Clarendon Press, Oxford, 1949; T. Y. Wu and T. Ohmura, "Quantum Theory of Scattering," Prentice Hall, Englewood Cliffs, New Jersey, 1962; A. Messiah, "Quantum Mechanics," Wiley, New York, 1962.
4. E. H. Kennard, "Kinetic Theory of Gases," McGraw-Hill, New York, 1938.
5. E. A. Mason, J. Chem. Phys. 26, 667 (1957).
6. For recent reviews, see, (a) R. B. Bernstein, "Advances in Chemical Physics," 10, 75 (1966); (b) H. Pauly and J. P. Toennies, "Advances in Atomic and Molecular Physics," 1, 201 (1965).
7. H. Faxen and J. Holtsmark, Z. Physik. 45, 307 (1927).
8. (a) R. B. Bernstein, J. Chem. Phys. 33, 795 (1960); (b) ibid., 34, 361 (1961).
9. O. Halpern and R. A. Buckingham, Phys. Rev. 98, 1626 (1955).
10. R. A. Buckingham, A. R. Davies, and D. C. Gilles, Proc. Roy. Soc. 71, 457 (1958).
11. C. R. Mueller and J. W. Brackett, J. Chem. Phys. 40, 654 (1964).
12. N. Fröman and P. Fröman, "JWKB Approximation," North-Holland Publishing Co., Amsterdam, 1965.

13. H. S. W. Massey and C. B. O. Mohr, Proc. Roy. Soc. (London), A144, 188 (1934).

14. R. E. Langer, Phys. Rev. 51, 669 (1937).

15. R. J. Munn, E. A. Mason, and F. J. Smith, J. Chem. Phys. 41, 3978 (1964).

16. R. B. Bernstein, J. Chem. Phys. 36, 1403 (1962); ibid., 38, 515 (1963).

17. F. J. Smith, Physica 30, 497 (1964).

18. R. J. Glauber, Lectures Theoret. Phys. 1, 315 (1959).

19. I. S. Gradshteyn and I. M. Ryshik, "Table of Integrals, Series, and Products," Academic Press, New York, 1965.

20. R. P. Marchi and C. R. Mueller, J. Chem. Phys. 38, 740 and 745 (1963).

21. F. Knauer, Z. Physik 80, 80 (1933); ibid., 90, 559 (1934).

22. R. G. Gordon, J. Chem. Phys. 51, 14 (1969).

23. The assistance of Dr. A. F. Wagner in programming these modifications is greatfully acknowledged.

24. Z. Kopal, "Numerical Analysis," Wiley, New York, 1955, pp. 381-384.

25. F. J. Smith and R. J. Munn, J. Chem. Phys. 41, 3560 (1964).

26. E. J. Williams, Rev. Mod. Phys. 17, 217 (1945).

27. E. A. Mason and L. Monchick, J. Chem. Phys. 41, 2221 (1964).

28. E. Hundhausen and H. Pauly, Z. Naturforsch. 19a, 810 (1964).

29. R. B. Bernstein, J. Chem. Phys. 37, 1880 (1962); ibid., 38, 2559 (1963).

30. R. B. Bernstein and T. J. P. O'Brien, Disc. Faraday Soc. 40, 35 (1965).

31. E. W. Rothe, P. K. Rol, S. M. Trujillo, and R. H. Neynaber, Phys. Rev. 128, 659 (1962).

32. E. W. Rothe, P. K. Rol, and R. B. Bernstein, Phys. Rev. 130, 2333 (1963).

33. M. A. Fluendy, R. M. Martin, E. E. Muschlitz, Jr., and D. Herschbach, J. Chem. Phys. 46, 2172 (1967).

34. W. C. Stwalley, A. Niehaus, and D. R. Herschbach, J. Chem. Phys. 51, 2287 (1969).

35. R. Düren and H. Pauly, Z. Physik 175, 227 (1963); ibid., 177, 146 (1964).

36. J. Adams, Ph.D. Thesis, University of Arkansas (1969).

37. R. J. Gordon and M. Griss, to be published.

38. O. B. Frisov, Zh. Eksp. Teor. Fiz. 24, 279 (1953).

39. R. G. Newton, "Scattering Theory of Waves and Particles," McGraw-Hill, New York (1966), pp. 610-632.

40. R. G. Newton, J. Math. Phys. 3, 75 (1962).

41. P. C. Sabatier, J. Math. Phys. 8, 905 (1967).

42. W. H. Miller, J. Chem. Phys. 51, 3631 (1969).

43. J. W. Brackett, C. R. Mueller, and W. A. Sanders, J. Chem. Phys. 39, 3564 (1963).

44. R. E. Olson and C. R. Mueller, J. Chem. Phys. 46, 3810 (1967); ibid., 45, 2519 (1966).

45. W. A. Sanders and C. R. Mueller, J. Chem. Phys. 39, 2572 (1963).

46. U. Buck and H. Pauly, J. Chem. Phys. 51, 1662 (1969); ibid., 54, 1927 (1971).

47. U. Buck, J. Chem. Phys. 54, 1923 (1971).

48. J. Luoma and C. R. Mueller, Disc. Faraday Soc. 40, 45 (1965).

49. J. Luoma and C. R. Mueller, J. Chem. Phys. 46, 680 (1967).

50. R. Klingbeil, J. Chem. Phys. 56, 132 (1972).

51. D. W. Marquardt, J. Soc. Indust. Appl. Math. 11, 431 (1963).

52. R. Klingbeil, J. Chem. Phys. 57, 1066 (1972).

53. R. Klingbeil, J. Chem. Phys. 59, 797 (1973).

54. J. M. Farrar, J. M. Parson, and Y. T. Lee, Proceedings IVth International Symposium on Molecular Beams, Cannes (1973).

55. R. J. Cross and D. R. Herschbach, J. Chem. Phys. 43, 3530 (1965).

56. E. A. Gislason and G. H. Kwei, J. Chem. Phys. 46, 2838 (1967).

57. H. L. Kramer and P. LeBreton, J. Chem. Phys. 47, 3367 (1967).

58. R. K. B. Helbing and E. W. Rothe, J. Chem. Phys. 48, 3945 (1968).

59. E. W. Rothe and R. K. B. Helbing, J. Chem. Phys. 50, 3531 (1969).

60. H. P. Butz, R. Feltgen, H. Pauly, and H. Vehmeyer, Z. Physik 247, 70 (1971).

61. K. P. Lawley and J. Ross, J. Chem. Phys. 43, 2930, 2943 (1965).

62. K. H. Kramer and R. B. Bernstein, J. Chem. Phys. 44, 4473 (1966).

63. R. J. Cross and R. G. Gordon, J. Chem. Phys. 45, 3571 (1966).

64. R. J. Cross, J. Chem. Phys. 52, 5703 (1970).

65. H. Van Dop and A. Tip, Physica 61, 607 (1972).

66. A. M. Arthurs and A. Dalgarno, Proc. Roy. Soc. (London) A256, 540 (1960).

67. A. Dalgarno and R. J. W. Henry, Proc. Phys. Soc. 85, 679 (1965).

68. R. B. Bernstein, A. Dalgarno, H. S. W. Massey, and I. C. Percival, Proc. Roy. Soc. (London) A274, 427 (1963).

69. W. Erlewein, M. von Seggern, and J. P. Toennies, Z. Physik 211, 35 (1968).

70. W. H. Miller, J. Chem. Phys. 50, 3410 (1969).

71. H. Moerkerken, M. Prion, and J. Reuss, Physica 50, 499 (1970).

72. S. Stolte, J. Reuss, and H. L. Schwartz, Physica 57, 254 (1972); ibid., 66, 211 (1973).

73. H. L. Schwartz, S. Stolte, and J. Reuss, Chem. Phys. Lett. 2, 1 (1973).

74. H. E. van den Bergh, M. Faubel, and J. P. Toennies, Disc. Faraday Soc. 55, 203 (1973).

75. H. Udseth, U. F. Giese, and W. R. Gentry, J. Chem. Phys. 54, 3642 (1971).

76. R. David, M. Faubel, P. March, and J. P. Toennies, Abstracts of the VII Int. Conf. Electron. and Atomic Collisions, North-Holland, Amsterdam, 1971, p. 252.

77. R. W. Anderson, V. Aquilanti, and D. R. Herschbach, Chem. Phys. Lett. 4, 5 (1969).

78. E. Gersing, H. Pauly, E. Schädlich, and M. Vonderschen, Disc. Faraday Soc. 55, 211 (1973).

4. CROSSED BEAM APPARATUS

4.1 Ideal System

In order to measure accurately the outcome of any scattering event, whether it be elastic, inelastic, or reactive, a system with several basic experimental characteristics is required. Before considering these characteristics as they exist in the actual experimental apparatus, it is worthwhile first to examine the origin of these requirements as they would arise in an ideal system.

Normally, an "ideal" system is described as one consisting of two perfectly collimated, monoenergetic beams of high intensity. The resultant scattered signal is detected with 100% efficiency and a very high signal-to-noise (S/N) ratio. While this certainly represents an ideal situation, for the purpose of describing the desired features of an actual system, a more realistic ideal must be chosen. Therefore, the model used will consist not of idealized components, but rather of optimized components.

Of a fundamental nature in all scattering experiments is the assumption of single collisions as the origin of the product signal. In order for this assumption to be valid, it is necessary to ensure that any scattered species traverse the distance from the scattering center to the detector without undergoing a second encounter. Therefore, the density of background gas in this region must be maintained as low as possible. Expressed more simply,

$$\lambda \gg \ell \qquad (1)$$

where λ is the mean free path of the scattered molecule, and ℓ is the scattering center to detector distance. For a typical system, $\ell \approx 10$ cm, so that if $\lambda \approx 1000$ cm, essentially no signal would be lost to secondary scattering. Such a mean free path can be achieved with an average background pressure of 5×10^{-6} torr. Our first requirement then is to enclose the scattering apparatus within a vacuum system capable of producing and maintaining a background pressure of this magnitude. Such a system can readily be realized with standard vacuum components.

An additional assumption of our scattering system is that the detected event occurred within a well defined volumn, specifically the volumn defined by the intersection of the two crossed beams. The basis for this assumption in elastic scattering lies in the inability of the detector to distinguish between those molecules which have been scattered by the target gas molecules, and those which have passed through the scattering region and been reflected from wall surfaces within the apparatus. Since the scattered signal represents only a very small fraction of the incident beam flux, (as little as 1 part in 10^6) even minor amounts of such internal wall scattering can give rise to a background noise signal comparable to, or greater than, the true scattered signal. For beams of condensible gases, cryogenic traps may be effectively used to capture the excess beam flux before it can scatter from the walls. In situations where this is not possible, alternate methods must be used. The most common technique employed is to modulate on "chop" one or both of the incident beams. The scattered

signal will then be transformed from a DC signal to the sum of a DC and an AC signal. Now, the DC signal represents a constant (unmodulated) background noise level, while the AC component is due to the scattered signal. By the use of selectively tuned AC detectors, the scattered signal may be recovered and thus distinguished from the unscattered background. Due to the finite flight time of the molecules from the modulator to the detector, a time delay or phase shift is introduced into the AC signal. The in-phase component of this signal results from molecules which have originated at the modulation source, and have been scattered into the detector via a collision within the scattering volumn. Quadrature, or out-of-phase components are due to molecules which have traversed a path of different length, that is, those which have been reflected from internal surfaces. While a small percentage of reflected molecules may achieve a time delay which is an integral multiple of the fundamental time delay of the true scattered signal, and thus be incorrectly detected as real signal, the great majority of the background signal will be properly ignored. The potential degree of S/N enhancement of this "phase sensitive detection" method, as well as a more complete description of its operation will be given in Section 4.2.5.1.

These first two requirements of a scattering apparatus have been aimed at reducing the effects due to background scattering, while the next several features will be aimed at increasing the level of the scattered signal without substantially increasing the background noise. Before proceeding, it is important to recall the salient features of differential elastic scattering which are the goals of these measurements.

First of all, since the scattered signal I is measured as a function of the in-plane angle θ, (it may also be a function of ϕ, the out-of-plane angle although that will not be considered here) it is clear that any angularly dependent features (diffraction oscillations, rainbow scattering, etc.) will only be resolved if the angular resolution of the apparatus is sufficiently high. In fact, the measured signal is related to the scattered signal by,

$$I_{measured}(\theta, \Delta\theta) = \langle I(\theta)\rangle_{\Delta\theta} = \int_{-\frac{\Delta\theta}{2}}^{+\frac{\Delta\theta}{2}} I_{scattered}(\theta')h(\theta')\, d\theta' \qquad (2)$$

where $\Delta\theta$ is the full width at half maximum (FWHM) of the angular resolution function, h. Ideally, we would like $\Delta\theta$ to be as small as possible. Even if it were possible to make $\Delta\theta$ very small, some angular smearing of the differential cross section would result due to the finite width of each beam. In the simple treatment given by Ramsey [1], a beam source of width w_s and a collimator of width w_c are considered in Figure 4.1. In the region of width 2p (the umbra region), the intensity is assumed to be constant, while in the regions between $|d\text{-}p|$, the detected intensity is assumed to fall linearly with distance. The actual values of p and d are,

$$\begin{aligned} p &= \tfrac{1}{2}\left|w_c + (w_c - w_s)a\right| \\ d &= \tfrac{1}{2}(w_c + (w_c + w_s)a) \\ a &= \ell_{cd}/\ell_{sc} \end{aligned} \qquad (3)$$

Figure 4.1: Simple source/collimator slit geometry, after Ramsey [1]. w_s and w_c are the respective slit widths, while L_{sc} is the source-to-collimator distance and L_{cd} is the collimator-to-detector distance. The regions of width 2p and 2d at the detector plane are the umbra and penumbra, respectively. The full width at half maximum (FWHM) of the resulting detected beam is $\Gamma (= p + d)$.

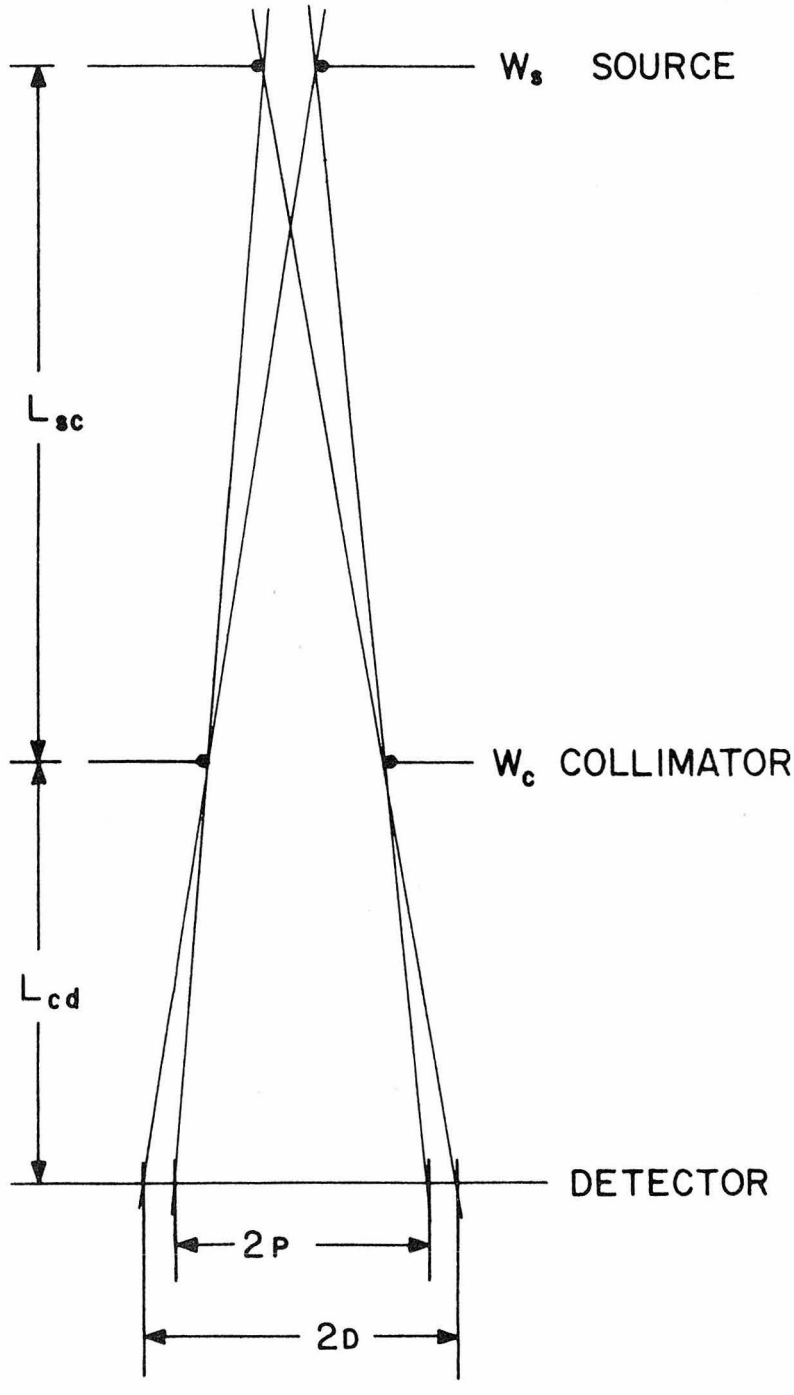

$$\Gamma = P + D$$

4.1

Assuming an infinitely narrow detector, the resultant beam shape would be trapezoidal, with a FWHM of

$$\Gamma = 2p + |d-p| = p+d \quad . \tag{4}$$

While equation (4) applies to the shape of a beam as seen in the forward direction by a detector of width $\Delta\theta \ll \Gamma$, it can be used to derive some guidelines for improving the overall angular resolution of the system. Such a treatment is given in Appendix A of Part I. In general, however, $h(\theta)$ will not be a simple function, nor will $\Delta\theta$ be easily determined even if the beam geometry is well known.

Often, the beam intensity can be increased, and its angular spread kept small by using a differential pumping system. Here, the source is located in a chamber that is isolated from the scattering region by one or more intermediate buffer chambers. Each such chamber has its own pumping system, and communicates with successive chambers only by means of small apertures through which the beam passes. These apertures also serve to collimate further the beam.

For the purposes of computing $I(\theta, \Delta\theta)$ in equation (2), h is often represented by either a rectangular or a triangular function, and $\Delta\theta$ is estimated from the known geometry. In some cases, it is also possible to determine $\Delta\theta$ experimentally. The effect of $h(\theta)$ on a theoretically calculated differential cross section is shown in Figure 4.2 for the triangular function,

$$h(\theta'-\theta) = 1 - \frac{|\theta-\theta'|}{\Delta\theta}, \qquad |\theta-\theta'| < \Delta\theta$$
$$= 0 \qquad\qquad |\theta-\theta'| \geq \Delta\theta \tag{5}$$

From the results given in Figure 4.2, it is clear that good angular resolution is an important feature of any scattering system.

Similarly, good energy, or velocity, resolution is also very important. While the effect of ΔE on the measured cross section is not as straightforward as the effect of $\Delta\theta$, if we assume that I is also a function of the relative velocity, then we can write,

$$I_{measured}(\theta, \Delta\theta, v_R, \Delta v_R) = \langle I(\theta, v_R)\rangle_{\Delta\theta, \Delta v_R}$$

$$= \int\int\int I(\theta', v_R)h(\theta')P_1(v_1)P_2(v_2)v_{12}dv_1dv_2d\theta' \tag{6}$$

where $P_i(v_i)$ is a function describing the velocity distribution of species i. In general, this function will depend on the temperature of the gas, its thermodynamic properties, and the method by which the beam was produced. The most obvious choice for such a distribution function is the Maxwellian distribution [2],

$$f(v) = \frac{4v^2}{\sqrt{\pi}\ \alpha^3}\ e^{-v^2/\alpha^2} \tag{7}$$

with

$$\alpha = \left(\frac{2kT}{m}\right)^{\frac{1}{2}} \quad . \tag{8}$$

As defined by equation (8), α is the most probable velocity for a molecule of mass m at temperature T. Equations (7) and (8) apply to a volume of gas at constant T. However, molecular beams are generally formed by effusion of a gas through an orifice, or by hypersonic expansion through a nozzle system. In either case, the probability of a molecule emerging from the source is proportional to v, and hence (7) must be multiplied by v and then renormalized to give,

$$f(v) = \frac{4v^3}{\alpha^4} e^{-v^2/\alpha^2} \quad . \tag{9}$$

To observe the effect of such a velocity distribution on the differential cross section, equation (6) was evaluated assuming $\Delta\theta = 0$, that is, velocity averaging only. The results using the same parameters as before are shown in Figure 4.3. As was the case for angular averaging, velocity averaging has a significant effect on the measured cross sections. As a result, it is important to reduce the overall Δv_R as much as possible.

Several means are available to produce the desired results. Early efforts by Kantrowitz and co-workers [3, 4] and later by Fenn and Anderson [5, 6] showed that the use of supersonic expansion of a gas through a small nozzle and skimmer system could produce a molecular beam of narrower velocity spread and higher intensity than conventional effusion sources. The isoenthalpic expansion produces a velocity distribution given by,

Figure 4.2: Calculated differential elastic scattering cross sections including the effects of detector angular resolution Γ (according to the form given by equation 5). The Lennard-Jones parameters correspond approximately to those determined from $H_2 + O_2$ scattering measurements (see Chapter 5). The actual experimental resolution is approximately $\Gamma \approx 2°$. No velocity averaging has been included (see Figure 4.3).

Figure 4.3: Calculated differential elastic scattering cross sections showing the effects of velocity averaging due to nominal beam distributions (see equation 9). The potential parameters used are the same as in Figure 4.2. The approximate experimental velocity spread is $\Delta v/v \approx 12\%$. No angular averaging has been included.

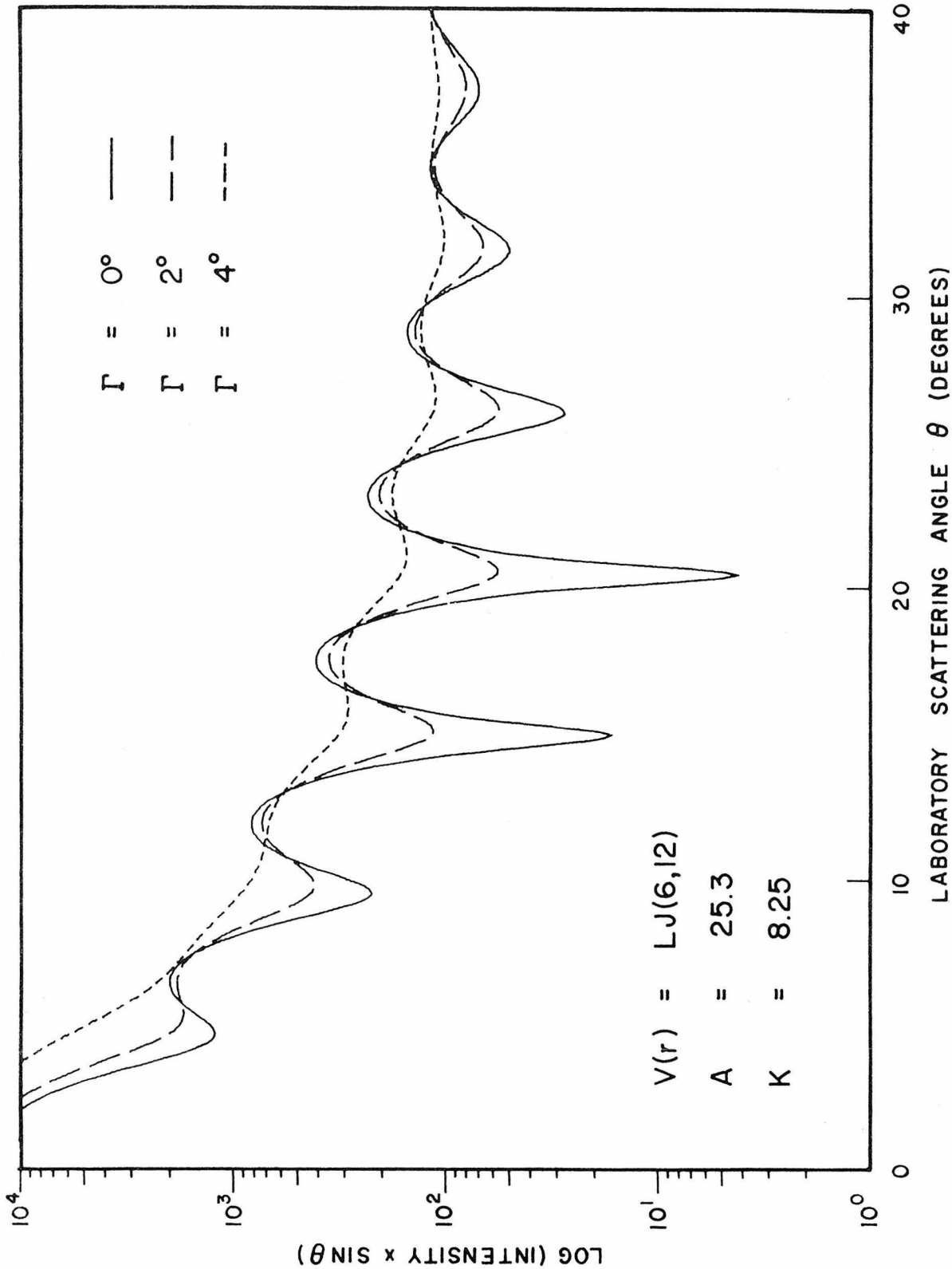
Γ = 0°
Γ = 2°
Γ = 4°
V(r) = LJ(6,12)
A = 25.3
K = 8.25
LOG (INTENSITY x SIN θ)
LABORATORY SCATTERING ANGLE θ (DEGREES)
0
10
20
30
40

4.2

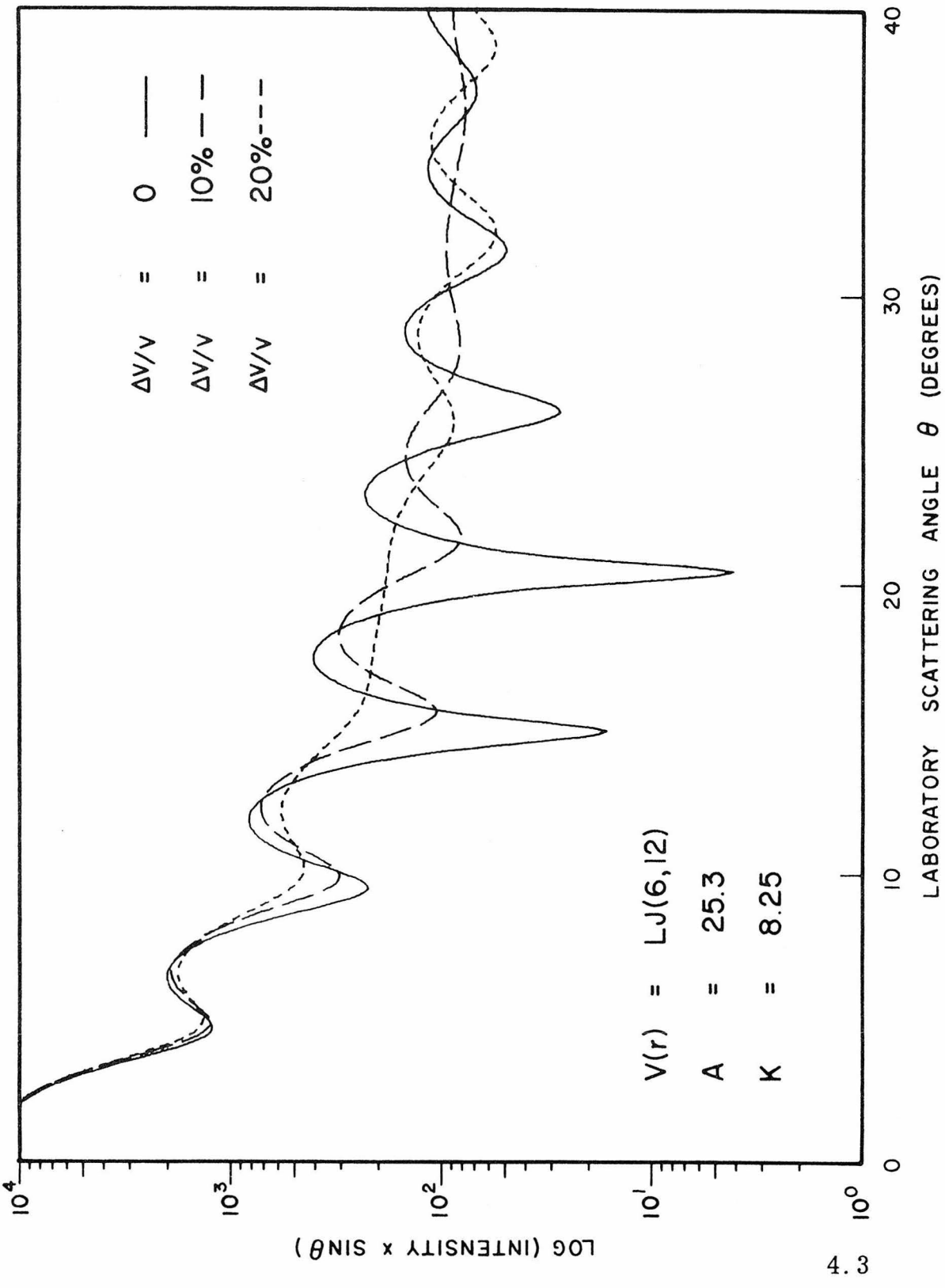
ΔV/v = 0
ΔV/v = 10%
ΔV/v = 20%
V(r) = LJ(6,12)
A = 25.3
K = 8.25
LOG (INTENSITY x SIN θ)
LABORATORY SCATTERING ANGLE θ (DEGREES)
0
10
20
30
40

4.3

$$f(v) = \frac{1}{\sqrt{\pi}} \left(\frac{\gamma M^2}{2}\right)^{3/2} \left(\frac{v}{\alpha_s}\right)^3 e^{-\frac{\gamma M^2}{2\alpha_s^2}(v-\alpha)^2} \tag{10}$$

where,

$$\alpha_s = \left(\frac{2kT}{m}\right)^{\frac{1}{2}} \left(\frac{\gamma M^2}{2}\right)^{\frac{1}{2}} = \alpha \left(\frac{\gamma}{2}\right)^{\frac{1}{2}} M \tag{11}$$

Here, M is the terminal Mach number, related to the local temperature in the beam, $\gamma = C_p/C_v$ the ratio of specific heats. The net effect of the supersonic expansion on the velocity distribution is to shift somewhat the center (most probable) velocity, and more importantly to reduce the FWHM considerably. Figure 4.4 shows several such velocity distributions calculated from equations (10) and (11) for different values of M. Notice that the higher Mach numbers produce beams of narrower velocity spread, while not increasing the most probably velocity beyond a maximum of $[\frac{2}{3}(\frac{\gamma}{\gamma-1})]^{\frac{1}{2}}$. In addition to producing the desired narrowing effect on the velocity distribution, such supersonic sources also increase the centerline beam intensity by a factor of,

$$\left(\frac{\gamma}{3}\right)^{3/2} M^2 e^{3/2} \quad . \tag{12}$$

Although from equation (12) it may appear possible to increase the intensity at will by producing beams of higher Mach numbers, a practical limit is always reached. The higher pressures needed to produce higher M values result in increased gas densities in the skimmer area, and this condition leads eventually to severe interference (scattering out

Figure 4.4: Velocity distributions calculated according to equations (10) and (11), as a function of the final Mach number, M. The vertical scale is arbitrary, while the horizontal scale is in reduced units (α = most probable velocity). The effective heat capacity ratio γ was chosen to correspond to a polyatomic gas.

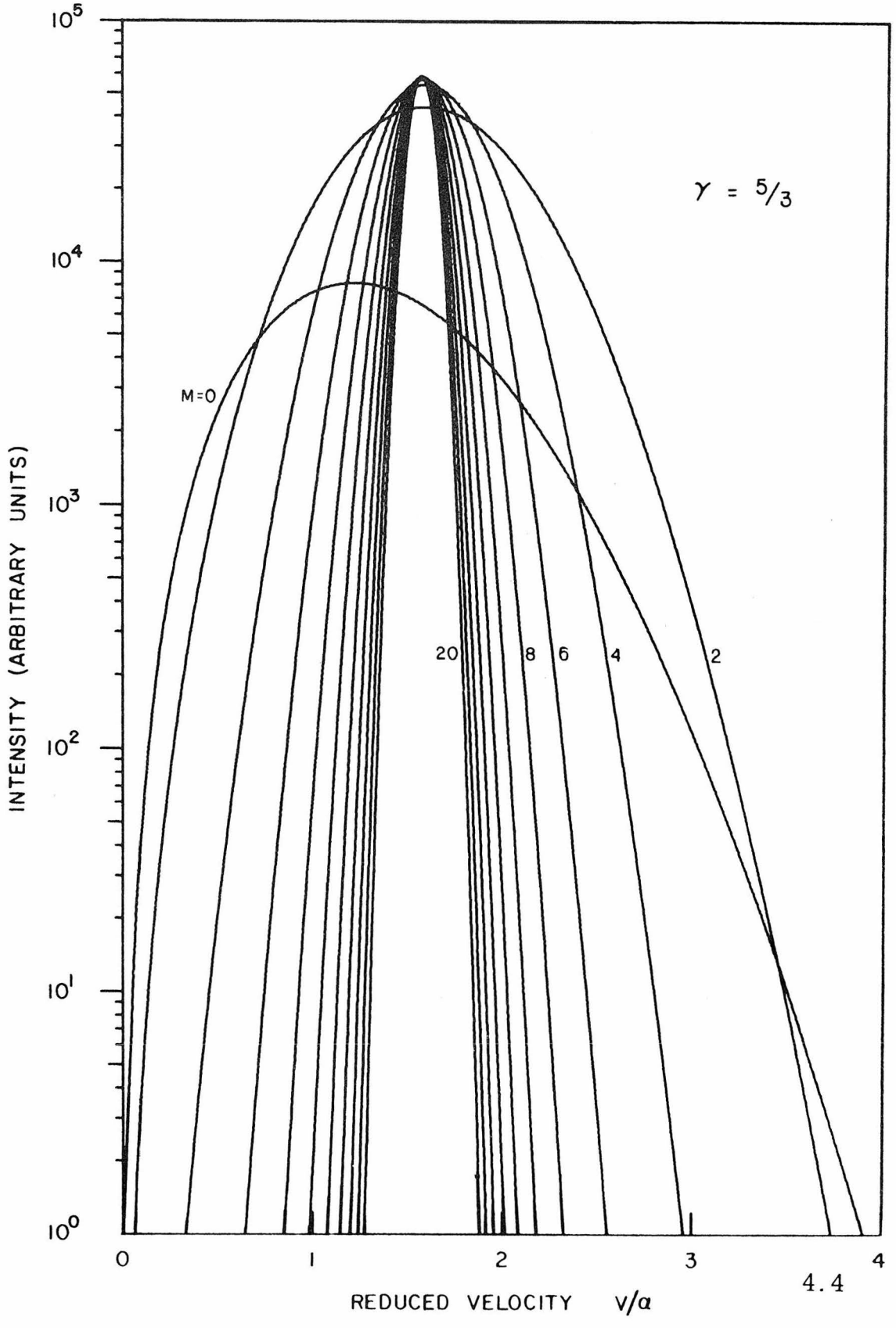
10^5
10^4
10^3
10^2
10^1
10^0
INTENSITY (ARBITRARY UNITS)
$\gamma = 5/3$
M=0
20
8
6
4
2
0
1
2
3
4
REDUCED VELOCITY V/α

4.4

of the beam) and a corresponding loss of intensity. In view of this restriction, the largest practical pump is used, and the nozzle driving pressure adjusted to provide the maximum intensity. The use of small nozzle apertures and downstream skimmer type collimators also tends to produce beams of small angular divergence.

If further reduction in the FWHM of the velocity distribution is desired, or if use of a supersonic source is not possible, a mechanical velocity selector may be employed. Several designs exist [7-9], however, the most common slotted disk type [10] can reduce Δv to 5%. Unfortunately, a concomitant loss of intensity by a factor of 50-100 is typical.

While the use of velocity selected or supersonically narrowed beams is highly desirable in differential elastic scattering studies, it is often not necessary to make use of these techniques for the production of both beams. As seen previously, $\Delta v_{\text{Relative}}$ can have a significant effect upon the measured results. However, with certain mass combinations, one of the beams may have a Δv considerably larger than the other, without adversely affecting Δv_R. Specifically, since

$$E_R = \tfrac{1}{2}\mu v_R^2 = \tfrac{1}{2}\mu(v_1^2 + v_2^2)$$

$$= \tfrac{1}{2} m_1 v_1^2 \left(\frac{m_2}{m_1+m_2}\right) + \tfrac{1}{2} m_2 v_2 \left(\frac{m_1}{m_1+m_2}\right) \qquad (13)$$

the contribution of each beam to the total relative energy (and hence velocity) is weighted by a mass factor which favors the lighter

component. Therefore, if $m_1 \ll m_2$, then $\Delta v_R \approx \Delta v_1$. In this manner, it is possible to produce a beam of particle 1 with a narrow velocity distribution, and to produce a beam of particle 2 without regard to its velocity spread, and yet maintain the desired condition of $\Delta v_R / v_R \ll 1$. The advantage of this situation is twofold. First, it is much easier to produce an effusive type beam than a supersonic beam since the pumping requirements are much less, and second, certain types of effusive beams can be made more intense than typical supersonic sources.

With regard to beam production then, the scattering apparatus can be equipped with one supersonic beam and one effusive beam source, provided that masses of the beam components are suitably chosen. Clearly, these are not the only choices for beam production; however, this arrangement can provide a high flux of scattered particles allowing for good quantitative differential elastic scattering measurements to be made. Examples of other systems which produce satisfactory results are now numerous [11-13].

The final major area of consideration in a scattering apparatus is the detector stage. While a lack of refinements in the beam production stage can be tolerated, and even to some extent accounted for in the data analysis, a less than optimum detector can render the entire apparatus incapable of attaining high quality results. Even though a large number of factors enter into the design of a good detection system for scattering measurements, only the most basic ideas will be considered here. A more thorough description of the experimental system will be reserved for the next section.

To understand the nature of the problems faced in detecting the results of a scattering event, it is only necessary to realize that the intensity of the scattered signal is often comparable to, and in many cases less than the background density. For example, a typical intense beam will have a density of $\sim 10^{10}$ particles/cm^3, which is comparable with the density of the background gas at a pressure of 10^{-6} torr. This beam density refers to the centerline intensity. However, measurements even a few degrees from the beam centerline will require detection of much smaller densities. In fact, since the forward beam contains between 95% and 99% of the total intensity, only a few percent will appear as a scattered signal. At 10° from the forward direction, the scattered elastic signal will generally be on the order of 5×10^5 particles/cm^3, and at 40° only 10^4 particles/cm^3. This latter density corresponds to a partial pressure of 10^{-12} torr. Two things are obvious from this consideration; first, the background gas density must be reduced, and second, the highest possible detection efficiency must be attained.

The first of these requirements can be approached in two ways. Either the background gas must be kept from (or removed from) the detector region, or the detector itself must be sufficiently selective so as to ignore any background gas which does reach it. Of course, methods which apply to both these areas simultaneously will be most effective.

As seen earlier, a pressure on the order of 10^{-6} torr was adequate to preclude significant multiple scattering, however, as just

shown, this pressure is much too high for the purposes of effective signal detection. The solution clearly lies in increased pumping of gases in the detector region to reduce further background densities. As a result of this, the detector system is normally enclosed in a separately evacuated chamber, often separated from the scattering region by one or more stages of intermediate differential pumping. Such a system could allow the pressure in each successive chamber to be lowered from the previous one by a factor of 10-100. The net result then of placing the detector within three nested chambers could be a pressure reduction of from 10^3 to 10^6. Realistically, a reduction of 10^4 can be achieved, resulting in a background pressure in the detector of $\sim 10^{-10}$ torr.

The second approach to the background problem is closely related to the matter of overall detection efficiency. Many early scattering experiments were carried out with beams of alkali metal atoms and molecules. These systems have the unique property (due to their low ionization potentials) of being selectively ionized on contact with certain types of hot metal surfaces. The efficiency of such surface ionization detection approaches 100% in the so-called Langmuir-Taylor configuration [14]. This combination of high efficiency and nearly complete selectivity of detection allows very weak scattering signals (10-100 particles/cm^3) to be measured.

Naturally, the desire to study other, non-alkali systems requires the use of a more suitable detector. Since the range of product species studied can vary widely, the detector must be of a

"universal" type, that is, a mass spectrometer. Such mass spectrometers consist of an ion source, a mass filter and a transmitted ion detector.

The first stage in this detector scheme is the ion source. Unlike the surface ionization technique, electron bombardment exhibits no selectivity except with respect to the ionization cross section. As a result, any steps which increase the efficiency of this ion source will increase both the signal and the background ion intensities. Despite this, most ion sources used are designed to provide optimum ion currents. In general, sources of the Weiss type [15] are used, that is space charge focused electron bombardment ionizers with efficiencies between 0.05% and 0.1%.

Due to the lack of selectivity in the ionizer, some means is needed to separate the background ions from the signal ions. The choice of a mass filter type is based on the range of masses to be measured, and on the size and weight of the unit. Generally, a Paul [16-18] type quadrupole mass filter is used because it requires no heavy magnet as in a sector type spectrometer. Also, a small unit can be tuned to provide very good resolution and a high transmission efficiency. The only conceivable disadvantage of this method is the need for both high voltage DC and RF potentials to be generated and passed through the vacuum system.

The final component in the detector system is the actual ion detector. If the transmitted ion current were of sufficient magnitude, a simple negatively biased Faraday cup collector could be employed.

This system would have a maximum detectable limit of about 10^{-14} amperes. This would not be adequate for the detection of the expected signal levels of 10^{-15} - 10^{-18} amperes arising from elastic scattering. The solution is to replace the simple Faraday cup with either a multistage or continuous dynode electron multiplier. Either unit will provide signal gains from 10^4 to 10^7 when used in the current mode. This mode involves the continuous measurement of the electron flux or current, in contrast to a discrete or counting mode where individual ion pulses are measured. While a discrete dynode multiplier can operate in both modes, it is best suited to the current mode. As a result, when large signals are to be measured, such as at low angles, the current mode is preferred. On the other hand, the continuous dynode type of multiplier is best suited for fast pulse counting methods, and hence is useful for measuring small signals, such as at wide angles in differential elastic scattering. In order to take advantage of both modes of operation, both units could be incorporated into the detector.

In summary then, an optimized molecular beam scattering apparatus should exhibit the following general features: (1) a vacuum system capable of maintaining pressures in the scattering chamber low enough to prevent multiple collisions; (2) beam sources selected to generate intense beams while providing sufficient angular and velocity resolution to allow the desired features of the scattering process to be manifest; (3) a differentially pumped detector of high sensitivity and selectivity to permit suppression of unwanted background noise while maximizing the signal of interest.

In the following sections, such an apparatus is described, and a more quantitative analysis of each component is given along with its overall operating characteristics and specifications.

4.2 Description of the Apparatus

Over the past several years the crossed molecular beam apparatus has evolved from the initial configuration as described by Cross [19] and Crawford [20] to the present configuration as described here. During that period, many modifications and changes have been made, and while these changes will be the main focus of this section, an overall description of all major aspects of the apparatus will be included. Where appropriate, reference will be made to the original, more detailed, description of those components which have remained essentially unchanged.

4.2.1 Vacuum System

The entire molecular beam apparatus is contained within a large, bakeable vacuum chamber. The chamber consists of a fixed base and a removable bell jar. Both components were fabricated from type 304 stainless steel. The base has a 50" inner diameter, while the bell has a maximum height of 31 $^{11}/16$". The total volume of the chamber is approximately 1200 liters.

The base (see Figure 4.5) which supports all major components has eight 6" diameter flanged ports equally spaced around a $32\frac{1}{2}$" circle to allow pumping access to both the main chamber and the

Figure 4.5: Diagram of the vacuum chamber base. (1)-(3) are mercury vapor diffusion pumps; (4)-(8) are oil vapor diffusion pumps; (9) is the outer primary beam differential chamber containing the velocity selector and the beam chopper; (10) is the inner primary source chamber; (11) is the movable mass spectrometer housing; (12) is the 50" diameter flange (with 50 bolt holes for sealing) which mates with the upper chamber bell jar; (13) is the capillary array secondary.

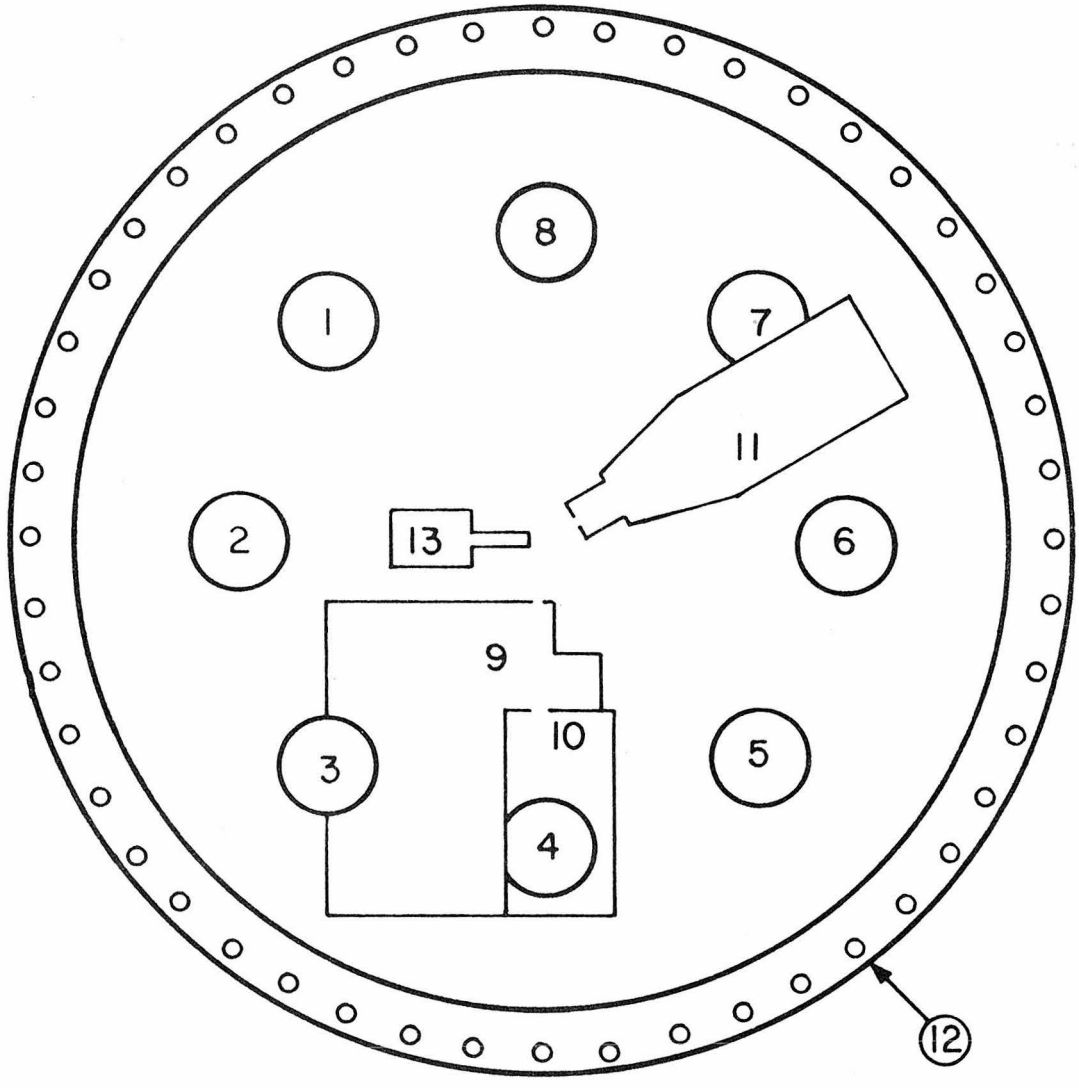

VACUUM CHAMBER BASE

4.5

differential chambers. The base is also provided with 50 $2\frac{3}{4}$" Varian conflat type flanges arranged around a 6" high collar that forms an integral part of the base. It is through these flanges that all of the internal electrical, mechanical, water, air, and cryogenic connections are made. Atop the collar is a 50" diameter flange which mates with a similar flange on the movable bell jar. A vacuum seal between these two flanges is accomplished by means of either a Viton or butyl rubber O-ring. An aluminum washer (50" I.D. × 52 $\frac{7}{8}$" O.D. × 0.20") is used to maintain the position of the O-ring and also to prevent excessive compression during sealing.

The bell jar has four, 4" conflat flanges equally spaced about the circumference of the outside at a height of 10" above the sealing flange. These flanges are coaxial with the beam directions, and two are fitted with Pyrex view ports. In addition, one of these ports contains a Veeco nude ionization gauge which is used to monitor the main chamber pressure. A 20" diameter opening is also provided at the top of the bell jar, and is sealed by a blank flange using an annealed gold wire gasket. The bell jar can be raised and lowered from the base by three motor driven lifting screws. The total vertical travel is approximately 38", and allows the bell jar to clear the highest internal components of the apparatus. The entire lifting mechanism is located on a movable platform which may be translated a total of 75", thus allowing the bell jar unit to be raised and moved horizontally completely clear of the base. The platform travels along fixed tracks suspended from the ceiling, and is also driven by a motorized screw system.

Both the vertical and horizontal drive motors are equipped with electromagnetic clutch units which allow precise alignment of the mating flanges.

Originally, the base and upper bell jar were equipped with integral heaters to allow a complete bake out of the vacuum chamber (see reference 19, Section 4.2.1.1). During the course of this work, it was not found necessary to make use of this provision.

The main components of the vacuum pumping system are eight 6" (nominal) diameter vapor diffusion pumps. The pumps are of two types; numbers 1, 2, and 3 (see Figure 4.5) are Edwards Model 6M3A mercury diffusion pumps, while numbers 4 through 8 are NRC (Varian) VHS6 oil diffusion pumps. The operating fluid for the latter is Convalex 10 (Bendix Corp.) oil, a polymeric ether compound with a vapor pressure of $\sim 10^{-9}$ torr at 200°C, and excellent oxidation retardation properties. The mercury pumps are equipped with freon cooled chevron baffles which are maintained at -25°C. All eight pumps are fitted with liquid nitrogen traps. The mercury pump traps have a 3-4 hour capacity, and are filled automatically using a preset timer system. The oil pump traps are connected in series, and are kept filled by a continuous flow system when in use. Each pump is isolated from the main system by a 6" manual gate valve.

A 4" diameter fore line manifold services the mercury pump via air actuated solenoid valves. The fore line is pumped by a 50 CFM two stage Welch Duo-Seal mechanical pump model 1398m. The mechanical pump, a 6" water cooled baffle and a 6" remotely operated

gate valve are located in an adjacent utility area. Approximately 40' of 6" diameter pipe connects these components to a 6" freon cooled baffle just ahead of the manifold.

Normally, the main chamber is maintained in a standby mode using only two of the mercury pumps, with all other pumps remaining off. To provide protection from a possible over-pressure due to pump failure or loss of liquid nitrogen cooling, the entire vacuum system is interlocked. The heart of the interlock system is a Veeco-type RG-83 ionization gauge controller and a type RG-88 control center. The control center provides a set of relay contacts that are actuated when the pressure as measured on the gauge controller exceeds a pre-set limit. The controller can monitor any of eight ion gauges by means of a switching system, and is usually set to monitor either the main chamber pressure or the pressure at the throat of one of the pumps (each pump is equipped with a Veeco RG-75 ion gauge tube). If the pressure exceeds the set limit (usually 10×10^{-4} torr), the controller will turn off the heater power to all pumps in operation, as well as close the manifold solenoid valves. Simultaneously, the gate valve located above the mechanical pump is closed, and this pump is vented. This prevents any possible contamination of the line by mechanical pump oil.

Under operating conditions, all diffusion pumps are utilized, and for this purpose, the five oil pumps are backed by a 75CFM freon baffled mechanical pump. This pump is the same type as used for the mercury manifold, with the addition of a faster motor to achieve the

higher pumping speed. Pumping is via another 4" diameter manifold connected to the diffusion pumps by 2" manually operated gate valves. Since much of the gas load consists of hydrogen and occasionally noxious gases, the outlets of both mechanical pumps are vented directly to the roof of the building.

In addition to the vapor diffusion pumps, an auxillary titanium sublimation pump [21] is located within the main chamber. This unit consists of a 12" high, 9" diameter coil of $\frac{3}{8}$" O.D. stainless steel tubing surrounding four 6" long pure titanium filaments (Varian-type 916-0024). The coil is cooled by circulation of liquid nitrogen, and sublimation accomplished by passing 40-50A of current at $\sim$8 volts through one of the filaments. Each filament is wired separately to eliminate the need of breaking the vacuum in the event of a failure.

4.2.2 Beam Sources

4.2.2.1 Primary Beam

The primary beam used throughout the course of these experiments was a differentially pumped supersonic nozzle source. While the basic source chamber has not changed significantly, several important changes in the source itself will be examined.

The pumping chamber for the primary beam source is a two-chamber unit containing the nozzle-skimmer system in the innermost section, and a mechanical velocity selector and chopper in the outer section. This all stainless steel chamber is mounted on the base of the main chamber directly above diffusion pump port 4 (see Figure 4.5) which serves to evacuate the source region. Pumping of the outer buffer section is by diffusion pump 3.

Figure 4.6: Cutaway view of the primary beam. (1) is the gas inlet line ($\frac{1}{8}$" I.D. copper tubing), (2) and (4) are the inlet and outlet lines for changing the source temperature using the cooling jacket (3); (5) supports the beam nozzle in the tubular housing (6); a stainless steel cap (7) holds the aperture plate (8) in position aligned with the conical brass skimmer (9); the mounting flange (10) holds the assembly against the chamber bulkhead (11).

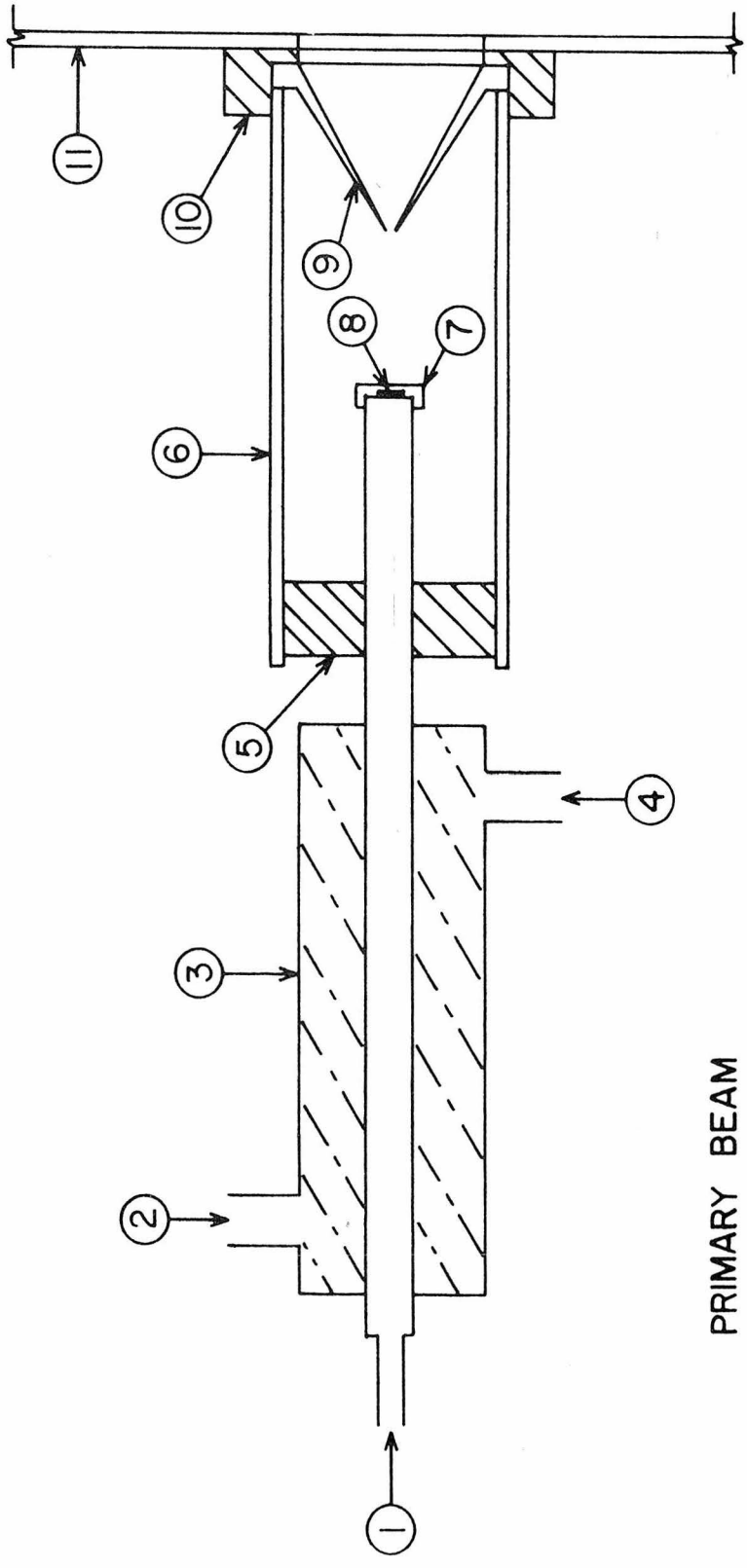

4.6

The source itself is a two piece nozzle and skimmer type shown in Figure 4.6. The nozzle is a 3" × 0.250" O.D. × 0.175" I.D. stainless steel tube with a threaded removable cap on the end used to retain an aperture disk. This disk is 0.100" in diameter with a 0.0028" diameter opening, and was originally designed as an electron microscope lense element [22]. Gas is fed into the source through $\frac{1}{8}$" copper tubing at the opposite end of the nozzle tube. The tube is surrounded by a cooling jacket which allows circulation of a temperature controlled fluid for the purpose of altering the primary beam energy. An iron-constantan thermocouple is attached to the nozzle for temperature indication. This entire unit is mounted on a holder assembly which allows the nozzle to be moved $\frac{1}{2}$" horizontally while maintaining axial alignment to within 0.001". The base of this holder mounts directly onto the chamber bulkhead, and also serves to hold in place an interchangeable conical brass skimmer. The skimmer has an outer half angle of 34° and an inner half angle of 28°; with an overall length of ~1" [23]. The tip was carefully machined to give an opening of 0.025" diameter with a very sharp clean edge to ensure no skimmer turbulence at the throat.

The one piece holder unit ensured constant accurate alignment of the nozzle and skimmer. In addition, the holder unit itself could be moved ~ 0.050" about the theoretical beam centerline position to allow for overall alignment. Early studies of the effect of both nozzle size and skimmer tip size as well as nozzle-skimmer distance were greatly facilitated by this arrangement. An additional feature of this

system was a motor driven translator capable of remotely adjusting the critical nozzle-skimmer separation. By means of such studies, the results of which will be described in Section 4.4, a set of optimum operating parameters was established which allowed the subsequent removal of the motor unit.

The outer buffer chamber of the primary beam source contains an eight rotor slotted disk type velocity selector of the Hostettler and Bernstein design [10]. The critical design parameters and dimensions are given in Section 4.2.3 of reference 19, along with a complete description of the variable frequency power supply used to operate the selector. The entire selector unit is suspended from the removable lid of the chamber by a hinge system that allows it to be moved in and out of the beam path. This motion is accomplished by a metal bellows unit. To ensure that the entire selector is rotating in synchrony with the frequency of the driving circuit, a reference signal is generated by a light and photocell combination. The light is directed onto a small photocell through a 1/16" diameter hole drilled through the motor shaft, thus providing a pulsed signal at twice the rotation frequency. This reference signal is fed into the horizontal input of an oscilloscope, while the oscillator driving signal is fed into the vertical input. When synchronization has been established, a stable 1:2 Lissajous figure is generated. Two small electrical contacts have also been added to the selector unit which provide positive identification of the in/out status of the unit.

As noted previously, modulation of the primary beam greatly enhances the overall detection efficiency by use of AC techniques. Generation of a modulated signal is accomplished simply by using a single rotating notched disk to periodically interrupt the beam path. Such a unit is located in the buffer chamber of the primary beam source. A water cooled 20 Hz synchronous motor rotates an eight slotted chopper wheel thus giving a modulation frequency of 160 Hz. The blade also modulates the light falling on a photocell from a small lamp mounted directly opposite to the beam. This arrangement provides a reference square wave in phase with the beam modulation.

The final exit aperture leading from the buffer chamber into the main chamber is a 0.080" diameter hole drilled through a flat plate mounted on the outer face of the chamber. The plate unit may be moved ~ 0.030" about the beam centerline for alignment purposes. Located immediately in front of this aperture is a pneumatically operated beam flag. Approximately $\frac{1}{2}$" linear movement of the flag is accomplished by evacuating or admitting air into a flexible metal bellows. Control of this bellows is by an electrically switched solenoid valve. A similar arrangement is used to move the velocity selector.

4.2.2.2 Secondary Beam

Originally, the crossed molecular beam machine was equipped with a differentially pumped secondary beam source similar in design to the primary source. Using this arrangement, the maximum attenuation of the primary beam was only $\sim 0.5\%$. In an attempt to

increase this somewhat low figure, a high intensity effusive type source was installed. While many designs exist for these types of sources, including crinkly-foils [24], bundled hypodermic needles [24] and simple slits, a glass capillary array was chosen.

With the advent of commercially available arrays of both glass [25] and metal [26] in a variety of sizes, construction of this type source is particularly simple. As with any effusive source, a compromise must be reached between intensity and angular divergence. Based on tests performed with several array sizes as well as theoretical predictions [27-29], this compromise was realized using a 0.025" thick, 0.100" diameter glass disk having 2μ diameter pores. The disk is secured to the end of the source tube by a threaded cap, as shown in Figure 4.7. The cap has a 0.062" diameter opening which defines the secondary beam diameter. Gas inlet is provided at the opposite end of the tube.

The customary method of measuring the scattered intensity in a beam experiment is by detecting the signal with the secondary beam both unflagged and flagged. The first measurement yields the signal due to scattering by secondary beam particles plus background, while the latter gives just the background signal. The difference, therefore, represents the scattered signal. In order to make these measurements, a means must be provided to flag, or interrupt, the secondary beam. Normally, a simple movable plate such as used with the primary beam is employed; however, this method can seriously alter the background signal by deflection. To overcome this problem, a secondary

Figure 4.7: Diagram of the tilting secondary beam source. A screw-on cap (1) holds the glass array onto the nozzle tube (2), shown in the down position. Removing air via (7) from the bellows (6) will pivot the source about the bearing (4) to approximately 20° (indicated by the line 3). Gas inlet is by a $\frac{1}{8}$" I.D. copper tube (5). Rigid support for the source is provided by the base plate (8). The pivot axle is indicated by (9), while (10) represents the exit aperture ($\sim$0.125" dia.).

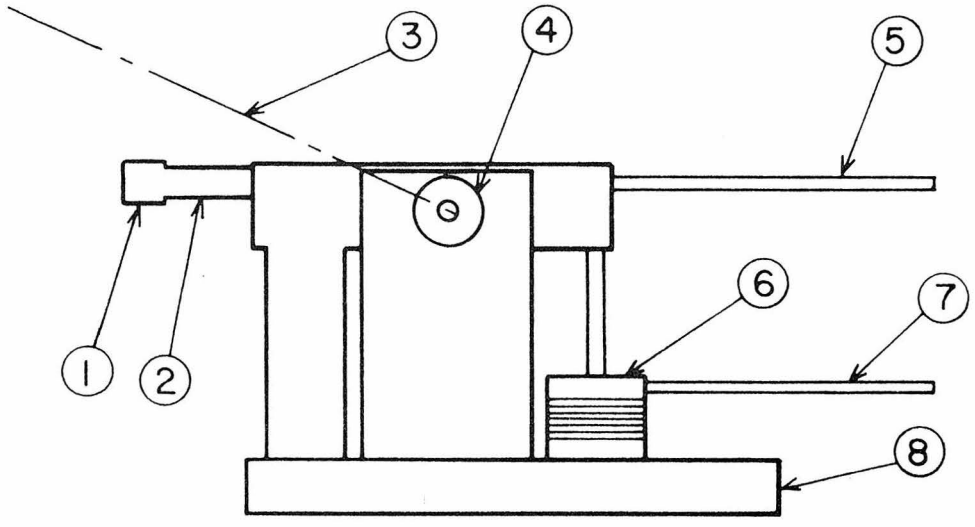

SIDE VIEW

SECONDARY BEAM

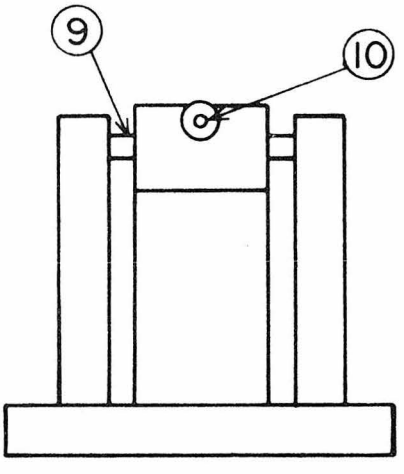

FRONT VIEW

4.7

source was used which can simply be tilted up at an angle from the scattering plane, thus uncrossing the beams. This allows the beam to be flagged effectively without altering the background significantly. The base plate of this beam source rests on an optically flat track to allow its distance from the scattering center to be adjusted without affecting the alignment.

The use of this type of effusive source has increased the attenuation of the primary beam tenfold to $\sim 5\%$.

4.2.3 Gas Inlet System

Stable, well regulated gas flow must be provided for each beam source to ensure a constant flux and thus minimize undue signal fluctuation. An all welded, all stainless steel gas inlet system was designed and constructed for this purpose. A schematic of the system is shown in Figure 4.8. The primary side is provided with two inlet lines, as well as two Wallace and Tiernan absolute pressure gauges in overlapping ranges of 0-200 torr and 0-800 torr. The secondary side has only a single inlet, and a low range 0-20 torr Wallace and Tiernan gauge. In all other aspects, the two sides are the same. A combination of a $\frac{1}{4}$" Nupro needle valve and a Granville-Phillips leak valve on each line provides excellent regulation and flow stability. A pair of three way valves allow a Pace differential pressure transducer to measure the pressure of either beam gas with respect to vacuum reference, or alternatively, the difference of the beam pressures. An electrical output from this transducer allows a long term record of the

Figure 4.8: Schematic diagram of the gas inlet system. Two primary (left side) and one secondary (right side) gas inlet lines (1) are provided with shut off valves (2); $\frac{1}{4}$" needle valves (3) and Granville-Phillips variable leak valves (4) control the gas flow on each side; inlet pressures are indicated by Wallace and Tiernan direct reading gauges (5). Snap action on/off valves (8) control flow to the beam inlets (9) (4 VCR Cajon fittings are used for connection to the source inlets). Inputs to a Pace differential transducer (6) are controlled by two three-way valves (7) allowing either side to be measured against a vacuum reference or against each other in a differential mode. Pumpout of the lines is by the lower two valves through a small mechanical pump (10).

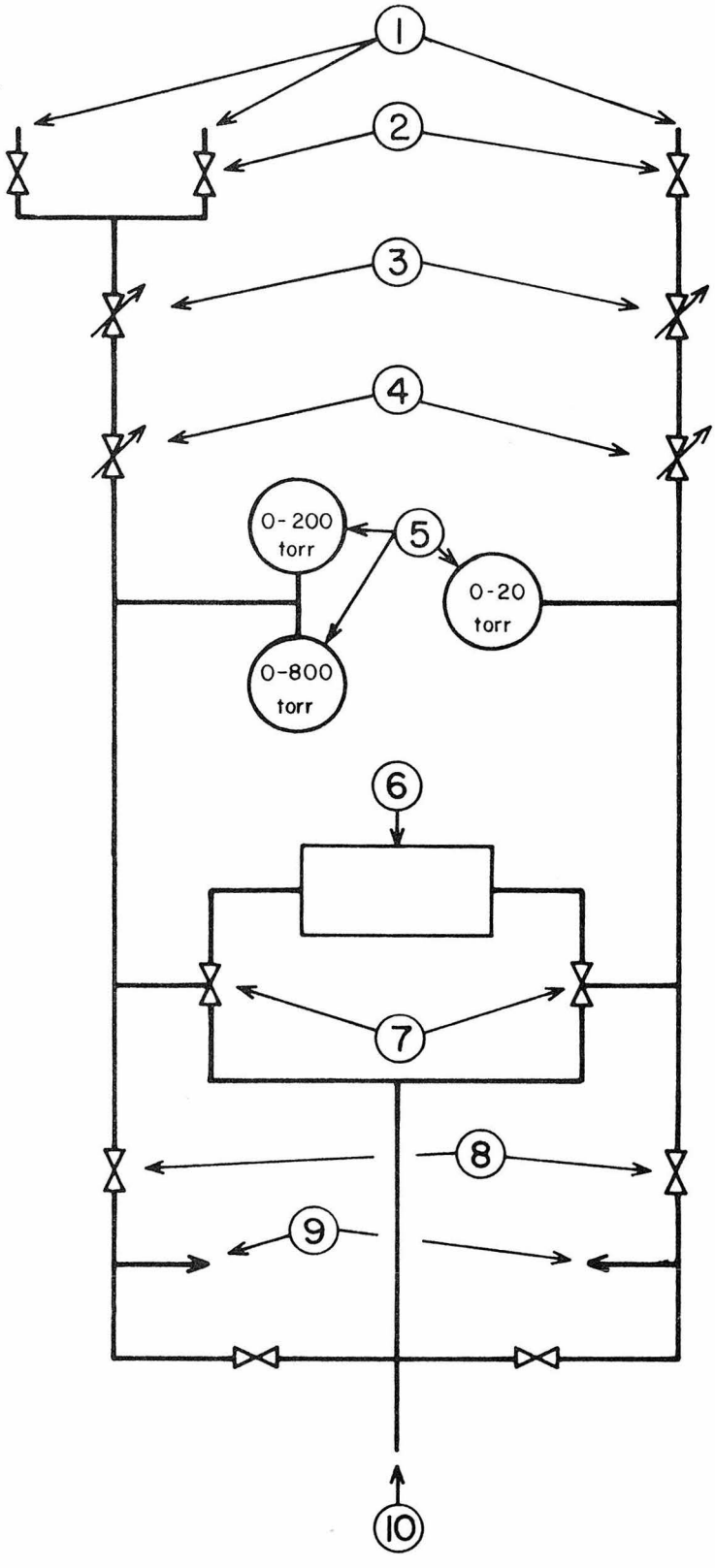

4.8

GAS INLET SYSTEM

beam pressures to be made on a strip chart recorder. A quick action snap valve is provided at the outlet of each side just ahead of the inlet line into the apparatus so that either or both beams can be shut off rapidly in a critical situation. All other valves used are Whitey type 1KM4 with Kel-F stems. All tubing is $\frac{1}{4}$" O.D. stainless steel, as are the TEE and cross pieces. Several feet of $\frac{3}{8}$" O.D. stainless flexible tubing are used for connections to the supply cylinders as well as connections to the apparatus inlet lines. All pieces were Heli-arc welded and leak tested. A single mechanical pump serves to evacuate both sides of the inlet system, its exhaust being vented to the roof for safety.

For experiments utilizing a secondary beam of H_2O, the above secondary inlet line was bypassed in favor of a simple temperature regulated barostat. A pure water sample was contained in a glass bulb immersed in a covered 2 liter dewar filled with 20% ethylene glycol in water. Surrounding the bulb were several turns of a copper cooling coil through which a refrigerated ethylene glycol solution was circulated. Cooling and circulation of the solution was done by a Forma Temp Jr. bath. Regulation of the temperature was better than $\pm 0.1\,^{\circ}C$, giving a measured beam stability of ± 0.03 torr.

4.2.4 Detector

As stated earlier, the measurement of elastic scattering requires a detector of high sensitivity, located in an ultra-high vacuum chamber which can be scanned over a wide range of angles. The

detector system used in these studies satisfies these requirements. It comprises three separate subsystems; (1) the quadrant arm orienting unit, (2) the differentially pumped housing, (3) the quadrupole mass spectrometer. Each system will be described separately in the following sections.

4.2.4.1 Quadrant Arm

Movement of the mass spectrometer detector within the vacuum chamber is accomplished by a rotating, semi-circular, quadrant arm assembly. The spectrometer housing is attached to a carriage unit which rides along the quadrant arm track for out-of-plane (ϕ) motion, while the entire system rotates about the scattering center, thereby varying the in-plane angle (θ). As a result, then, the entire solid region of space defined by the limits of these two motions is accessible to scattering measurements. With the present configuration, those limits are: $-15° < \theta < 105°$; $-15° < \phi < 15°$.

A complete description of the quadrant arm and carriage assembly fabrication and operation is given in reference 19, Section 4.2.5.1. Essentially, the arm is a one-piece casting having a 16.000" inner radius, an 18.000" outer radius, and a width of 1.75". This unit is supported by ball bearings riding on a hardened steel pin fixed to the exact center of the base of the scattering chamber. The actual motion, that is positioning of the quadrant arm, is by means of a steel cable pulley assembly. A Varian, magnetically coupled, rotary motion feed-thru transmits sufficient torque to move the entire assembly. Remote indication of the quadrant arm position is achieved by a Bendix 3-wire

synchro unit geared to the base of the arm. The signal generated by this synchro is decoded and displayed by a Bendix electromechanical readout device. Use of a 4-to-1 gear ratio on the resolver drive gives an angular reproducibility of ± 0.5°. The main source of inaccuracy in the angular reading was due to the readout unit, which has recently been replaced by a DDC digital indicator, giving ± 0.05° accuracy. Excitation power for the synchro was obtained from a 400.0 Hz oscillator and power amplifier system, California Instruments models 101T and 815T, respectively.

The carriage unit is held in constant contact with the quadrant arm by spring loaded rollers. This configuration supports approximately 150 lbs of weight while maintaining its position to within ± 0.002" along the entire length of the quadrant arm. During these experiments the detector was maintained in the plane of the crossed beams, and so the carriage was fixed in this position by a support block bolted to the arm.

As required by any positioning system, this assembly ensured that the entrance aperture of the mass spectrometer was always exactly aligned with the scattering center, regardless of the orientation of the detector in space. Several checks, made over a span of five years, showed no significant changes in alignment caused by fatigue, stress or warpage of any of the components.

4.2.4.2 Spectrometer Housing

A common feature of many molecular beam detector systems is a differentially pumped housing [11-13]. The theory behind such a

design as mentioned before is simply to provide separately pumped buffer regions between the scattering zone and the actual detector thereby reducing the background pressure in stages. A variety of pumps are used with these chambers, but the net effect is generally between 2 and 4 orders of magnitude reduction in the pressure. The present system employs two separate stages of differential pumping, with provisions made for adding a third chamber.

A cutaway view of the housing is shown in Figure 4.9. The entire outer chamber, including the lower arm, was fabricated by welding together sections of type 304 stainless steel pipe. Varian conflat flanges were welded to the chamber where indicated. The overall length of the housing is 19" with a maximum inner diameter of 7.5".

The front face of the chamber is fitted with a $2\frac{3}{4}$" conflat flange to which is attached the removable entrance aperture plate. These studies were performed with a 0.060" diameter aperture. Also mounted on this flange is a bellows operated gate valve assembly shown in Figure 4.10. When air is admitted to the bellows, a plunger rod forces an O-ring to seal against the sloped valve seat. When the bell jar is under vacuum, atmospheric pressure suffices to seal this valve; however, if this valve is to be used when the bell jar is raised (see below), a supply of regulated air (20-25 PSIG) is directed into the bellows. When the valve is open, the O-ring retainer is retracted sufficiently to preclude any interference with the detection process.

The entrance aperture opens directly into the first buffer chamber. This chamber is formed by a bulkhead welded into the housing, and

Figure 4.9: Cutaway view of the differentially pumped mass spectrometer chamber. The front flange (1) ($2\frac{3}{4}$" Varian conflat) holds the entrance aperture plate and gate valve (see Figure 4.10). The first buffer chamber (2) is pumped by the lower arm titanium sublimation pump. A liquid helium cryopump (see Figure 4.13) mounts on an NCR 6" flange (3), while a 5 ℓ/sec ion pump and the bakeout valve (Figure 4.11) mount via a $2\frac{3}{4}$" Varian conflat flange (4). A 4" NRC Orbion pump mounts on a 6" Varian conflat flange (5) and along with the cryopump pumps on the second chamber (6). The mass spectrometer is supported by a 8" rear flange (Varian conflat) (7). The 4" Varian flange (8) holds the titanium sublimator assembly which is cooled by a liquid nitrogen jacket (9). Two ionization gauges also mount on this housing, one on the bakeout valve, the other on the sublimator rear flange (8).

Figure 4.10: Cutaway view of the mass spectrometer front gate valve. A $2\frac{3}{4}$" Varian flange insert (1) is held onto the mass spectrometer front flange (see Figure 4.9) by a standard retainer ring (2). The gate valve sealing surface (3) contains the 0.060" diameter entrance aperture (4). The O-ring retainer (5) is fixed to the driving shaft (6), which in turn is attached to the bellows (8) and guided by the housing assembly (7). Air pressure (valve closed) or vacuum (valve open) is applied via a $\frac{1}{4}$" stainless steel flex line (9).

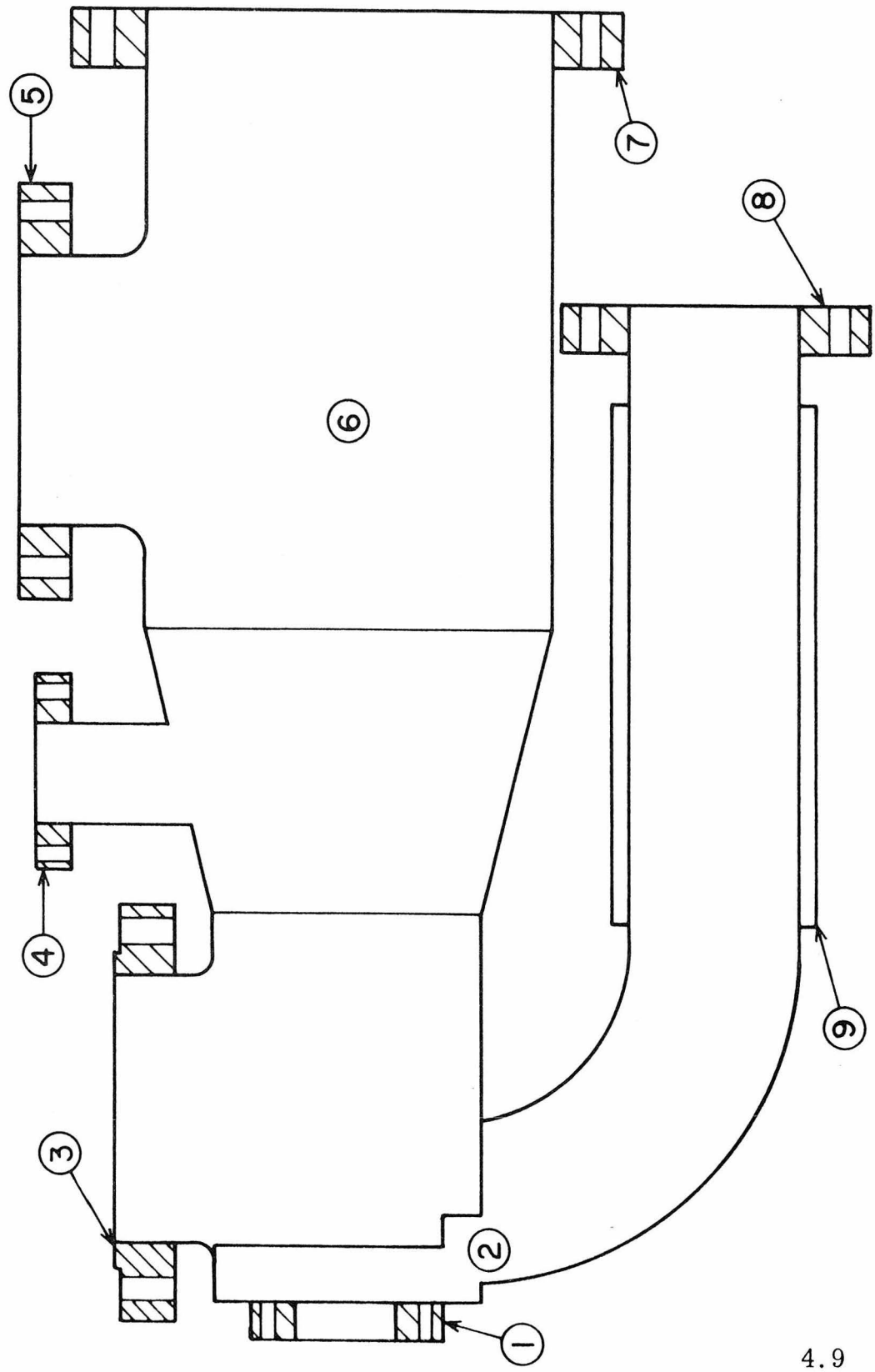

4.9

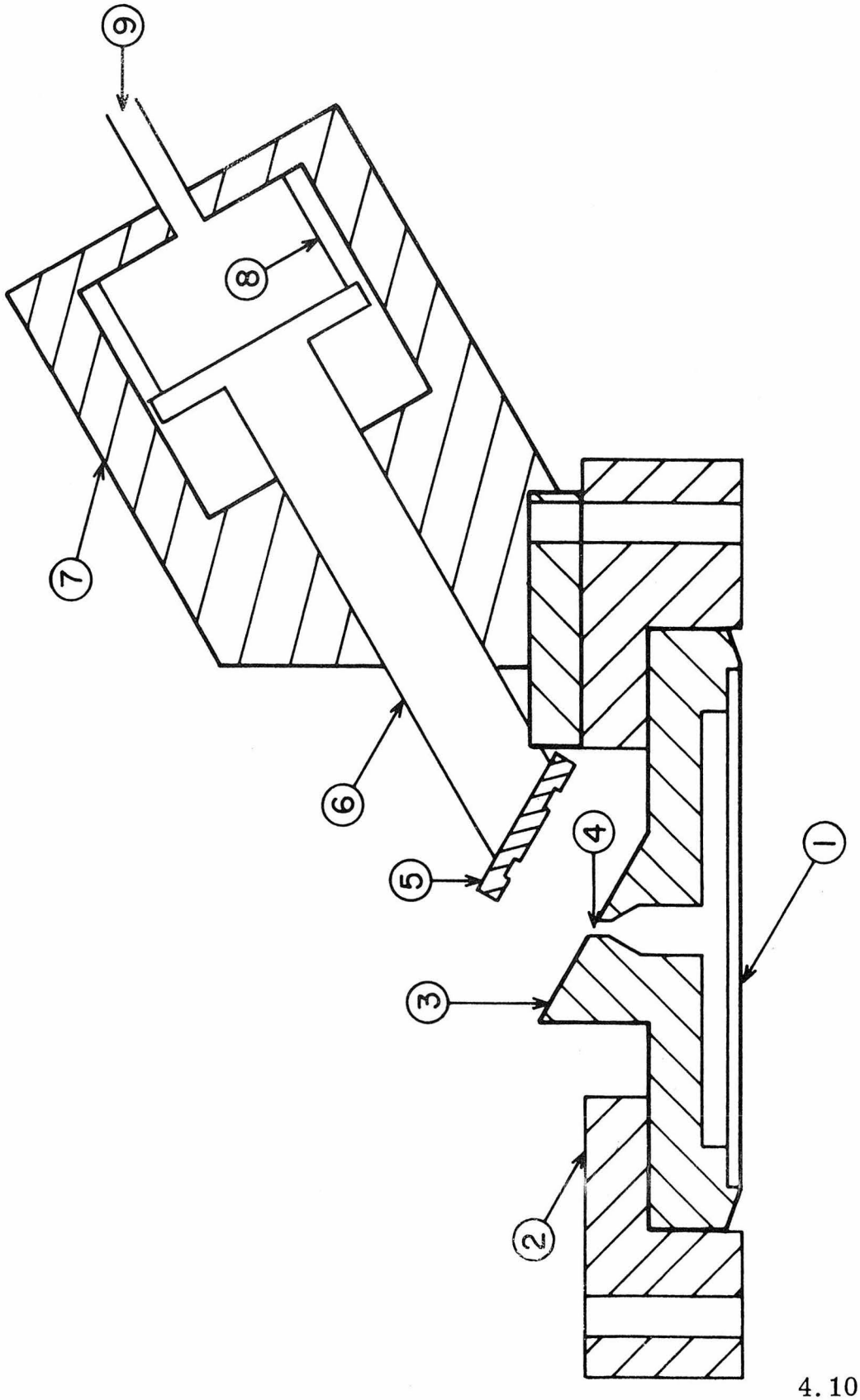

4.10

includes the 2" diameter lower arm piece. This arm, equipped with a 5" long cooling jacket, forms a titanium sublimation pump. Access to the pump is by a 4" conflat flange on the rear of the tube. A Ceramaseal medium current two conductor electrical feedthru is attached to the mating 4" flange, and forms the support for a single titanium filament of the type used in the main chamber sublimator. Also attached to this flange is a General Electric miniature ionization gauge tube. The tube is actually welded to a separate flange which seals to its mate by a gold wire O-ring. A small internal shield is provided to prevent titanium from being deposited on the ion gauge. Power for the sublimator filament is 10 volts DC at 40-50 A. During operation, this filament is only flashed periodically, rather than used in a continuous mode.

The second internal differential chamber comprises the remainder of the detector housing. A 0.25" diameter opening in the bulkhead is the only connection between this chamber and the first. As shown in Figure 4.9, three flanges are located along the top of this chamber. The front and rear openings are both 4" inner diameter, while the center opening is 1" I.D.

In its current configuration, the rear flange supports an NRC model 204 orbion pump. This type of pump, first developed by Herb et al. [30-32], combines both electrostatic and titanium sublimation methods. Two small tungsten filaments mounted on an upper flange of the pump body emit electrons in a downward direction. With an 8000 VDC potential between the pump body and a central electrode running the length of the pump, the electrons will traverse spiral paths in the

resulting electric field. As a result of their very long paths, these electrons have a high probability of ionizing residual gas within the pump. Such positive ions are accelerated toward the grounded outer pump wall. Eventually, the electrons will strike the central electrode which holds two $\frac{1}{4}$" diameter $\times$ 1" long titanium slugs. This electron bombardment heats these slugs sufficiently to cause sublimation of the titanium. This material will be continuously deposited on the cooled outer walls of the pump. This action provides an active getter surface which effectively removes both the ions and any chemically reactive gases. The nominal speed of this pump using water to cool the outer wall is given as 400 ℓ/sec. However, use of liquid nitrogen cooling has increased this value by at least a factor of ten.

Since it has been found necessary to bake the mass spectrometer housing to achieve the desired ultimate pressure, a means had to be provided to allow the large quantities of vapor to be removed from the chamber. While the entrance aperture remains open, its small area was not adequate, and for this reason, an all stainless steel bellows operated 3" diameter O-ring sealed valve was constructed. This bake out valve (BOV), shown in Figure 4.11 is mounted on the small central flange of the housing. The unit actually consists of two valves in series. The first, inner valve, is provided for future use (see below), and remains fixed in the open position. The upper valve is opened during bake out by evacuation of the bellows. In the open position, the O-ring is raised completely off the sealing surface, and thereby not subjected to excessive heating. The bellows and O-ring

Figure 4.11: Cutaway view of the bake out valve. Auxiliary pumping port (1) may be used to connect the mass spectrometer chamber to an external pump (see text). The upper O-ring sealing plate (3) is operated by the bellows (5) assembly via the pressure/vacuum line (4). Access to the O-ring is provided by gold wire sealed flanges (2). (6) and (9) are 6 VCR female Cajon fittings, one for an ion gauge, the other for a by-pass connection to the helium cryopump (see text). The lower O-ring sealing plate (10) is actuated by another bellows assembly (8) and control line (7) fitted with a 2 VCR female Cajon connection. The entire unit mounts onto the mass spectrometer housing (Figure 4.9) by a $2\frac{3}{4}$" Varian flange.

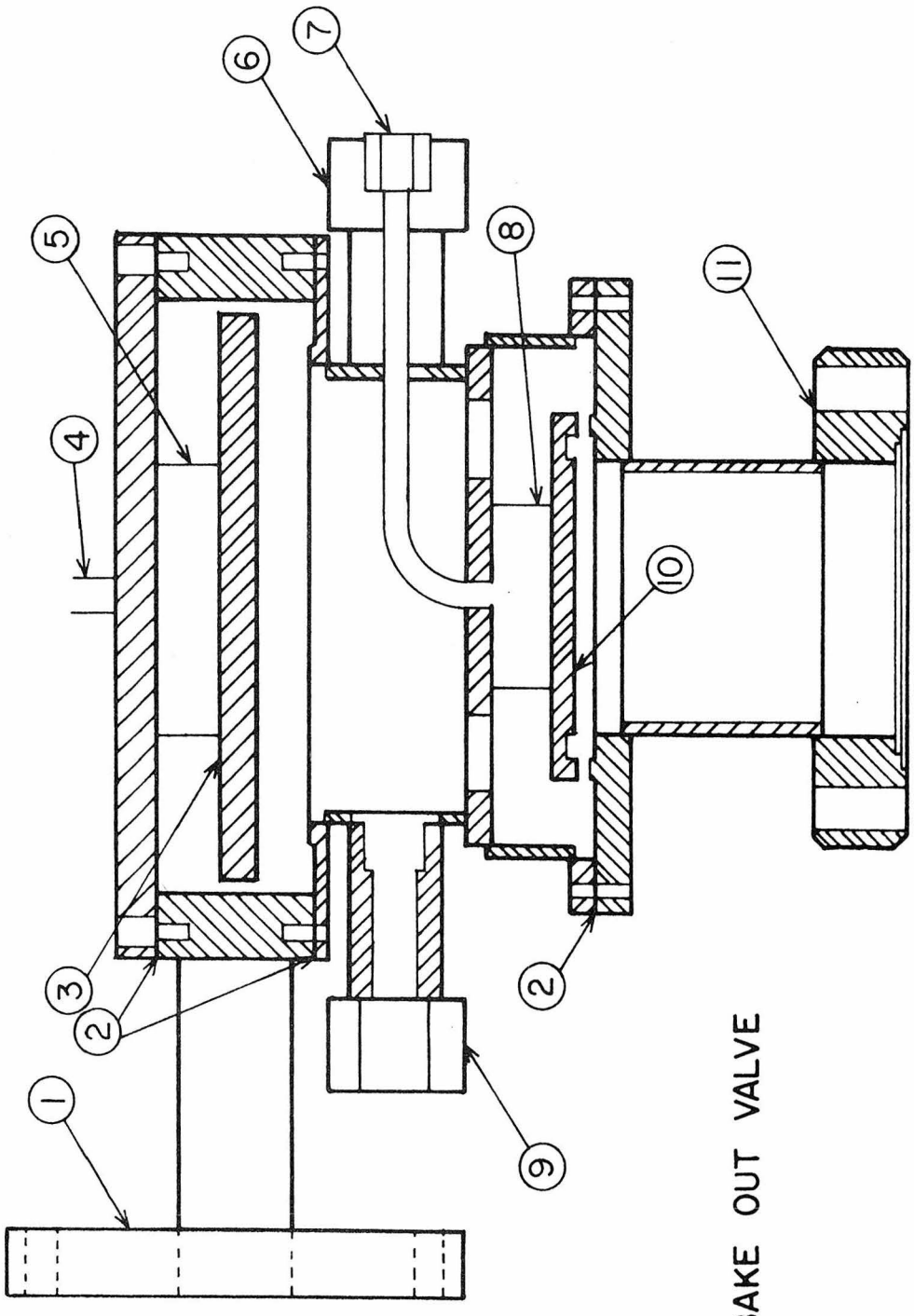

BAKE OUT VALVE

4.11

retainer plate are mounted on the valve body using a gold wire gasket. In addition to the O-ring seal, a second, metal-to-metal, seal is made by the two raised surfaces on either half of the valve. This second seal is between the O-ring and the inner chamber, and protects the mass spectrometer from "seeing" the O-ring which may outgas at very low pressures.

Located just below the sealing surface is a $\frac{3}{4}$" Cajon fitting, to which is attached a Bendix model G1C-028-3 ionization gauge tube. This gauge is used to establish the operating pressure in the mass spectrometer ionizer region.

Between the BOV assembly and the conflat flange on the housing, a 1" diameter Tee adapter is mounted. On the side arm, an Ultek 5 ℓ/sec ion pump is attached. The purpose of this pump is to allow the mass spectrometer housing to be maintained under vacuum continuously, even when the rest of the apparatus is vented. This mode of operation is essential to reduce the background gas pressure in the detector. The combination of the front gate valve and the BOV serve to isolate completely the mass spectrometer chamber. Since neither the side arm sublimator titanium pump nor the orbion pump can operate without liquid nitrogen cooling, which cannot be circulated when the system is at atmospheric pressure, a pump capable of continuous operation was necessary. With the small residual gas load, and because of weight restrictions, a small ion pump was selected to accomplish this. Due to its small size, this ion pump cannot be operated at pressures above 2×10^{-6} torr, however, it operates continuously once this pressure has been reached.

Prior to the installation of the ion pump, an alternate system of maintaining the spectrometer under vacuum was attempted. This system involved using mercury pump number 1 connected to the detector housing via a 2" diameter flex line attaching to the side flange on the BOV (see Figure 4.11). This method required that the front gate valve and the BOV maintain at least 1×10^{-6} torr in the spectrometer while the main vacuum system was vented and the bell jar raised so that the flex line could be attached. During the 10 minutes needed for this operation, the pressure would rise to $\sim 1 \times 10^{-3}$ torr. The failure of this method led to the use of the ion pump which can be operated even during the venting period.

The entire mass spectrometer detector, including the ion source, quadrupole filter, particle detectors and preamp (see next section) is rigidly mounted on a blank Varian 8" flange which mates onto the rear of the housing with a copper gasket. All electrical connections for the spectrometer are passed into the housing by means of a number of feedthrus welded to the back flange. A diagram of this flange showing the locations of the feedthrus is given in Figure 4.12. The RF, high voltage and pulse signal feedthrus are all Ceramaseal type 804C3887-68 units. All feedthrus are electrically insulated from the back flange, except for pin 1 of each octal type which is internally grounded. An optically flat view port is located in the center of the flange, and is used for alignment purposes, as described in Section 4.4.1.

Liquid nitrogen cooling for the lower arm sublimator, the orbion outer wall as well as the outer jacket on the liquid helium

Figure 4.12: Arrangement of feedthrus on the mass spectrometer rear flange. (1) R. F. and DC power inputs to the quadrupole; (2) -HV for the descrete dynode electron multiplier; (3) pulse output signal from the Spiraltron continuous dynode multiplier; (4) -HV for the Spiraltron; (5) Pyrex view port; (6) octal feedthru for the internal preamp power and output signal; (7) spare octal feedthru; (8) octal feedthru for ionizer and electrostatic lens voltages.

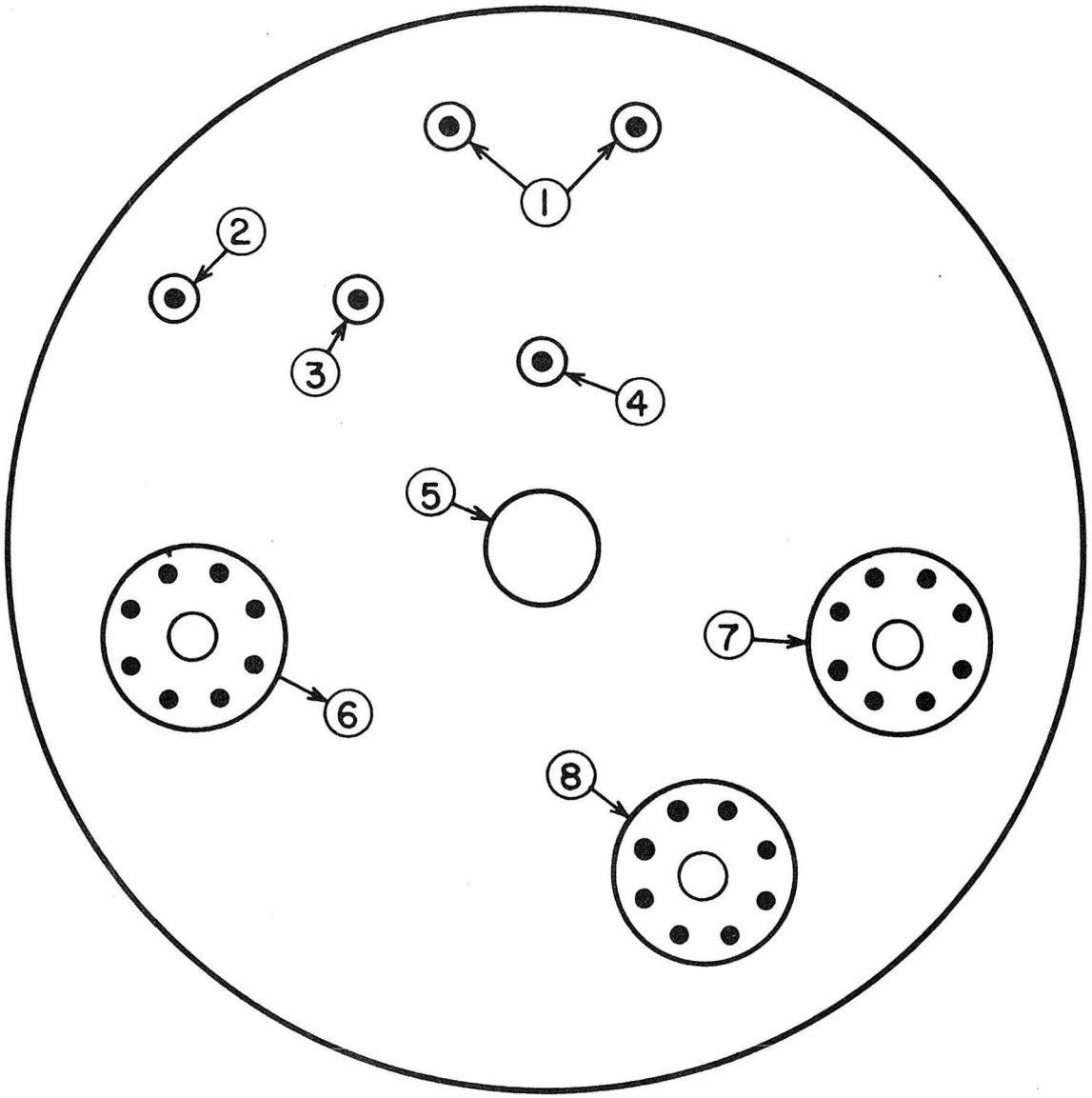

MASS SPECTROMETER

REAR FLANGE

4.12

cryopump (see below) is provided by a series of $\frac{1}{2}$" O.D. flex lines interconnected with Cajon fittings. Liquid nitrogen, introduced through the vacuum wall from a 160 ℓ pressurized dewar, enters near the bottom of the cryopump jacket, exits near the top, enters the bottom of the orbion pump, and travels from the top through the sublimator arm. The discharge end of the sublimator jacket enters the bottom of the large main chamber titanium sublimator pump, before being vented to the outside of the vacuum system.

Bake out of the mass spectrometer is accomplished by passing current through two 600 watt Briskheat type BIH-61 heater tapes. One tape is wound tightly around the orbion pump, while the second encircles the main spectrometer housing including the lower arm. The tapes are carefully mounted to prevent any overlap and to give uniform heating. Power is from a 220 volt variac, delivering about 5 amps to the parallel wired heaters. Six iron-constantan thermocouples, fabricated from 26 AWG wire are located around the housing to indicate bake out temperatures. Readout is by means of a calibrated meter and a Leeds and Northrup thermocouple switching unit.

Recently a liquid helium cryopump was constructed and mounted on the front 6" flange of the mass spectrometer housing. This pump, shown in Figure 4.13, consists of an outer liquid nitrogen jacket, and an inner liquid helium dewar. The inner dewar is supported only by a thin neck which includes a 2" section of uranium glass to minimize heat loss. An optically dense chevron baffle is located below the dewar and cooled by conduction from the liquid nitrogen jacket. Helium is

Figure 4.13: Cutaway view of the liquid helium cryopump. (1) inlet helium transfer line surrounded by a separate vacuum jacket (2) and (6); (3) $2\frac{3}{4}$" Varian flange which allows removal of the transfer line assembly; (4) vent line (terminates in 4 VCR Cajon fitting); (5) 1" diameter glass heat insulator; (7) outer liquid nitrogen jacket; (8) 1 liter capacity liquid helium dewar; (9) mounting plate for optional baffle; (10) 6" diameter NRC flange, which mates to the mass spectrometer housing (see Figure 4.9).

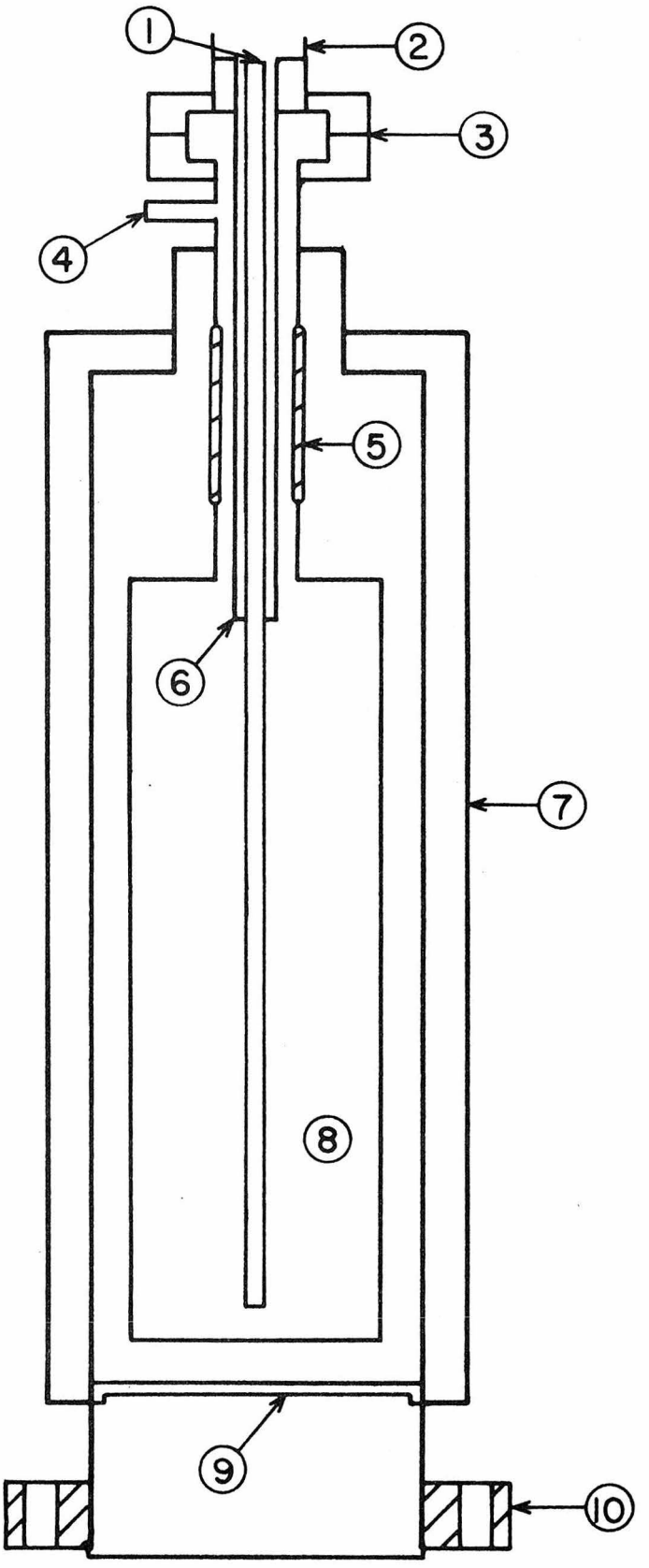

4.13

transferred with a double-walled transfer line which passes through the vacuum wall. The outer half of the line is a flexible type manufactured by Janis Research Company. The part within the vacuum chamber is rigid except for a 12" flexible section which allows motion of the dewar along with the spectrometer.

The helium pump is positioned directly above the ionizer of the spectrometer, and is intended to reduce greatly the pressure in this region by cryopumping [33-37]. If future requirements demand, the ionizer may be dismounted from the quadrupole unit and isolated in a third differential chamber which would only be pumped by the cryopump. Under these circumstances, when the cryopump was not operating, very little pumping speed would be available in this chamber through the two small beam inlet and exit apertures. To overcome this, an auxilary pumping line bored through the base of the cryopump flange and attached to the space between the two valves of the BOV unit would be added. When in standby operation, the inner bellows valve in the BOV would be open, and so the third chamber would be connected with the second chamber. In operation, the inner bellows valve would be closed, thereby again isolating the ionizer chamber. In that case, the Bendix ionization gauge would indicate the pressure in the cryopump chamber.

4.2.4.3 Quadrupole Mass Spectrometer

The detector used throughout these studies was a quadrupole mass spectrometer equipped with an electron bombardment ionizer and a 14 stage Cu-Be electron multiplier. The entire unit, with the exception of the multiplier, but including all the control electronics was

manufactured by Extranuclear Laboratories Incorporated (ELI). The following is a brief description of both its theoretical and actual operation.

A small percentage of the scattered (or background) molecules which enter the high efficiency ion source are ionized, and then extracted and focused by a series of electrostatic lenses. This ion beam then enters the filter region, where only ions with a specific charge-to-mass ratio are passed. These transmitted ions are again accelerated, this time onto the first dynode of an electron multiplier. Thus the output current of the multiplier is a direct measure of the number of molecules which, when ionized, have a given charge-to-mass ratio.

The ELI high efficiency ionizer is of the Weiss type space charge focused design [15]. Electrons emitted from a rectangular array of filaments are accelerated toward the center of the array, through which the neutral beam passes. Stable emission currents as high as 50 ma. can be achieved with this arrangement. The electron impact energy can be varied up to a maximum of 100 eV. Ions formed in this region are repelled by the same field used to establish the electron emission and further accelerated by a biased extractor plate. Three Einzel type cylindrical electron lenses follow the extractor, and serve to focus the ions onto the entrance of the quadrupole filter region.

The filter section consists of four stainless steed rods ($\frac{3}{4}$" diameter and 9" long) arranged in a square array. Boron nitride insulators hold the rods in position with a high degree of dimensional

stability. This design is essentially that due to Paul and co-workers [16-18]. Both a static DC voltage and a superimposed RF voltage are applied to the rods so that opposite rods are at the same potential, while adjacent rods are at the same potential but with reversed polarity. If the rods were hyperbolic rather than circular, the electrostatic field along the rods would be,

$$\phi(t) = (V_1 + V_0 \cos \omega t)(x^2 - y^2)/r_0^2 \quad , \tag{14}$$

where r_0 is the radius of a circular inscribed within the rods, V_1 and V_0 are the DC and RF potentials, respectively. While equation (14) is for hyperbolic rods, it is adequate for describing the real system with circular rods. If a charged particle is injected into this field, it will experience forces given by,

$$F_x = -e \frac{\partial \phi}{\partial x} = -e(V_1 + V_0 \cos \omega t) \frac{2x}{r_0^2} \tag{15a}$$

$$F_y = -e \frac{\partial \phi}{\partial y} = e(V_1 + V_0 \cos \omega t) \frac{2y}{r_0^2} \tag{15b}$$

$$F_z = -e \frac{\partial \phi}{\partial z} = 0 \tag{15c}$$

The resulting equations-of-motion describing the ion trajectory through the filter are,

$$m \frac{d^2x}{dt^2} + \frac{2e}{r_0^2} (V_1 + V_0 \cos \omega t)x = 0 \tag{16a}$$

$$m \frac{d^2y}{dt^2} - \frac{2e}{r_0^2} (V_1 + V_0 \cos \omega t)y = 0 \tag{16b}$$

$$m \frac{d^2z}{dt^2} = 0 \tag{16c}$$

As a consequence of equation (16c), the ions will suffer no axial acceleration, and hence traverse the filter section in a time governed by their injection energy. Equations (16a) and (16b) determine the actual transverse ion trajectory in the quadrupole field, and are of the Mathieu form. Solutions have been found by several investigators [38], and the trajectories plotted and used to determine the range of parameters which yield stable flight paths. Basically, it is found that for a given V_0 and V_1, ions of a specific e/m will pass through the filter with stable trajectories, while all other ions will be accelerated to the point where they strike one of the rods and hence be removed. Quantitatively expressed, the selected mass is given by,

$$m = 0.136\ V_0 (r_0 f)^{-2} \tag{17}$$

where V_0 is in volts, r_0 in cm, $f (= \frac{2\pi}{\omega})$ in MHz and m in amu.

The resolution of a quadrupole filter, that is the range of masses passed for a fixed set of parameters, expressed as $m/\Delta m$ is

$$\frac{m}{\Delta m} = \frac{0.126}{0.16784 - V_1/V_0} \quad . \tag{18}$$

Theoretically, infinite resolution is possible by setting the ratio V_1/V_0 to 0.16784. In reality, of course, infinite resolution cannot be achieved due to instabilities in both the electronics and the dimensions of the device. The ELI system does, however, provide voltages which remain in this ratio throughout the mass range. Mass selection is performed by fixing the RF frequency f, and varying the magnitude of V_0 and V_1. Provision is made for slightly altering the ratio of V_1 and V_0 to

compensate for changes in the resolution, and to operate the filter in a constant Δm mode.

The oscillation frequency is determined to a large extent by the internal capacitances of the filter unit and the RF power leads, but is generally in the range from 1.5 to 4.0 MHz. This frequency in turn establishes the range of voltages used and the maximum value of e/m which can be tuned by the filter. The limit of the ELI unit is in excess of 300 amu. However, in its current configuration, a practical limit of 75 is found due to the excessive lead capacitance.

All measurements reported here were made using a 14 stage descrete dynode Bendix electron multiplier. However, a Spiraltron [39] continuous dynode multiplier has been recently added. These two multipliers are mounted behind the filter section, on either side of the ion beam, and somewhat below its path. This provision allows for optical sighting along the length of the mass spectrometer (see Section 4.5.1), and also prevents photons and excited neutrals from striking the multipliers. Separate power supplies allow the multipliers to be operated independently. The strong negative voltage on the entrance (-2500 VDC for the multiplier, -3200 VDC for the Spiraltron) serves to focus and accelerate the ion beam to the appropriate device.

Despite its gain of $\sim 10^6$, the signal from the electron multiplier is weak and susceptible to noise pickup. Therefore, a small bakeable Nuvistor preamplifier is included in the spectrometer directly behind the multiplier. A 10^8 ohm input resistor generates a voltage pulse, which is amplified by the multistage preamp having a gain of

~130. The amplified output signal is then fed outside the spectrometer housing, and finally out of the main vacuum enclosure.

The entire mass spectrometer unit is approximately 16" long, including a completely enclosed RF shield around the multipliers. It is supported on a reinforced stainless steel channel mounted rigidly to the back flange of the spectrometer housing described above. All electrical connections are passed through the back flange, and consist of 3/32" diameter stainless steel rods with quartz insulators to prevent internal short circuits.

Performance characteristics and a typical background spectrum will be given later.

4.2.5 Data Acquisition Systems

The previous section describes how signals are generated within the mass spectrometer detector by either the descrete dynode multiplier or the Spiraltron; however, these signals must be further processed. Two different modes, the current mode and the counting mode, will both be described in turn. The final results from either mode represents the raw data, the reduction and handling of which will be covered in the section on results.

4.2.5.1 Current Mode

In this configuration, the output current pulses from the 14-stage multiplier are first converted into voltage pulses and subsequently amplified by the internal preamp, as discussed in the previous section. While the resultant output is in fact a voltage pulse, the

electronics are sufficiently slow, and the input signal pulses are so numerous that a nearly continuous output is generated. This is the same result as if a continuous input current were present rather than individual pulses. Hence this mode is referred to as the current mode.

The output of the internal preamp is fed directly into a second ELI amplifier. The first half of this unit is a straight DC coupled amplifier, and serves to monitor the large scale voltages associated with very intense signals, as near a beam source. The output of this stage drives the y-axis of an oscilloscope which also generates the mass sweep ramp voltage. Thus, the resultant display is a mass scan. The DC output is also passed on to the second half of the ELI unit, which is an AC tuned amplifier. Since the signal has been modulated, the information is now contained in the AC portion of the signal voltage. Two modes of AC filtering are available, a notch mode and a tuned mode. The notch mode rejects the selected frequency, while the tuned mode rejects all frequencies other than the tuned one. The latter mode is used, with a variable bandpass set by a "Q" adjustment. This amplified, tuned, signal is passed along to a phase sensitive lock-in amplifier for demodulation. The lock-in used in a Princton Applied Research (PAR) model HR-8. Since its function is of central importance to the data system, it will be described in some detail.

A lock-in amplifier is basically an AC device which is capable of extracting small signals from a large noise background. Since the signal to be measured, i.e., the flux of particles scattered into the detector, is inherently a DC signal with slight aperiodic fluctuations,

some means must be found to produce periodicity. The reason for transforming to an AC signal is that, with the exception of threshold discrimination, no effective means exist to distinguish noise from signal in a DC level. On the other hand, narrow band pass filters can easily remove non-coherent noise from an AC signal.

There are many sources of noise in a molecular beam experiment, including beam intensity fluctuations, background pressure changes, variations in detection efficiency and electronic type noise. These noise sources generally fall into two categories based on their power spectrum. One type is frequency independent white noise, while the other varies as 1/f. The former is more difficult to eliminate, but the latter, most severe at low frequencies, can be greatly attenuated by moving the DC signal away from zero frequency. This shift in signal frequency is easily accomplished by modulating one or both of the beams. This is equivalent to multiplying the DC beam by a square wave, or some other periodic signal. The function of the lock-in then is to use the frequency and phase information contained in the modulated signal to extract the original DC information. The technique is actually a form of correlation analysis in that the cross correlation of random noise with a fixed frequency signal tends to zero, while cross correlation of a modulated signal with a time delayed (phase shifted) signal of the same frequency is a constant.

The first stage of the PAR lock-in amplifier (see Figure 4.14) is a variable gain, wide band AC amplifier. This stage affords little noise rejection, except for blocking any DC signals. The output of this

amplifier is passed on to a tuned AC amplifier, whose center frequency f_0 is set equal to the modulation frequency, and whose bandwidth is adjusted by a "Q" control. With a Q of 10, the FWHM of the bandwidth would be 0.2 f_0, so that substantial noise rejection would result. The output signal is applied to the input of a balanced mixer, often referred to as a synchronous rectifier. Functionally, this circuit is a double pole, double throw switch which reverses the polarity of the signal at exactly the center frequency, f_0. This is accomplished by using the reference modulation waveform to drive the demodulator. Because of this, a reference signal must be supplied to the PAR which exactly matches the chopping function. As described before, the reference signal in the molecular beam is derived from a light and photocell system mounted on the chopper unit itself. This reference signal is passed through a tuned amplifier, tuned to the same frequency, f_0, as the input amplifier. Since some time delay exists between the chopping of the beam and its detection due to the finite molecular velocity, some means must be provided to vary the time relationship between the reference signal and the input signal. A simple variable phase shift network in the reference channel allows for this adjustment. The actual reference signal applied to the balanced mixer is always a square wave, whose on and off periods are exactly equal, regardless of the form of the input reference waveform. The output of the mixer stage is a DC level, equal to the RMS amplitude of the input AC signal. One important difference exists between this DC level and that which would have been generated without modulation--a great deal of non-coherent random noise

has been eliminated. A simple RC integrator on the output of a wide band amplifier following the mixer allows variable smoothing of the output signal. The actual integration time constant is 1/4 RC, and reflects the rate at which fluctuations in the DC output can occur.

The exact degree of S/N improvement will depend on many factors. However, three orders of magnitude can easily be achieved. While increases in both the Q of the input amplifier and the time constant τ can reduce the noise level, practical limits exist on both settings. Higher Q values reduce the bandwidth, and hence cause rejection of some of the signal which has a finite bandwidth itself. Longer time constants greatly increase the time necessary to obtain data. Thus, a compromise is usually reached with a Q of ~ 10 and a τ between 3 and 30 sec.

The PAR lock-in amplifier produces a 10 volt DC full scale output which is used as the actual recorded signal level. This voltage is periodically sampled by a Raytheon model ADC-24 analog-to-digital (AD) converter having 14 bit resolution, corresponding to a ± 0.6 mV accuracy. The digital signal produced by the AD is read into the memory of a Scientific Control Corporation (SCC) 4700 computer. This 16 bit, 8K system also reads in various input parameters from an ASR-33 teletype unit. After an appropriate sampling time, the computer prints out the average signal levels with the secondary beam on and off, their standard deviations, the net scattered (difference) signal and its standard deviation. The actual sequence of events will be covered in Section 4.4.5.

Figure 4.14: Block diagram of the PAR lock-in amplifier. An analysis of the circuit operation is given in the text.

Figure 4.15: (Overleaf). Block diagram of the digital synchronous counter. The operation of this unit is discussed in the text and in Appendix B.

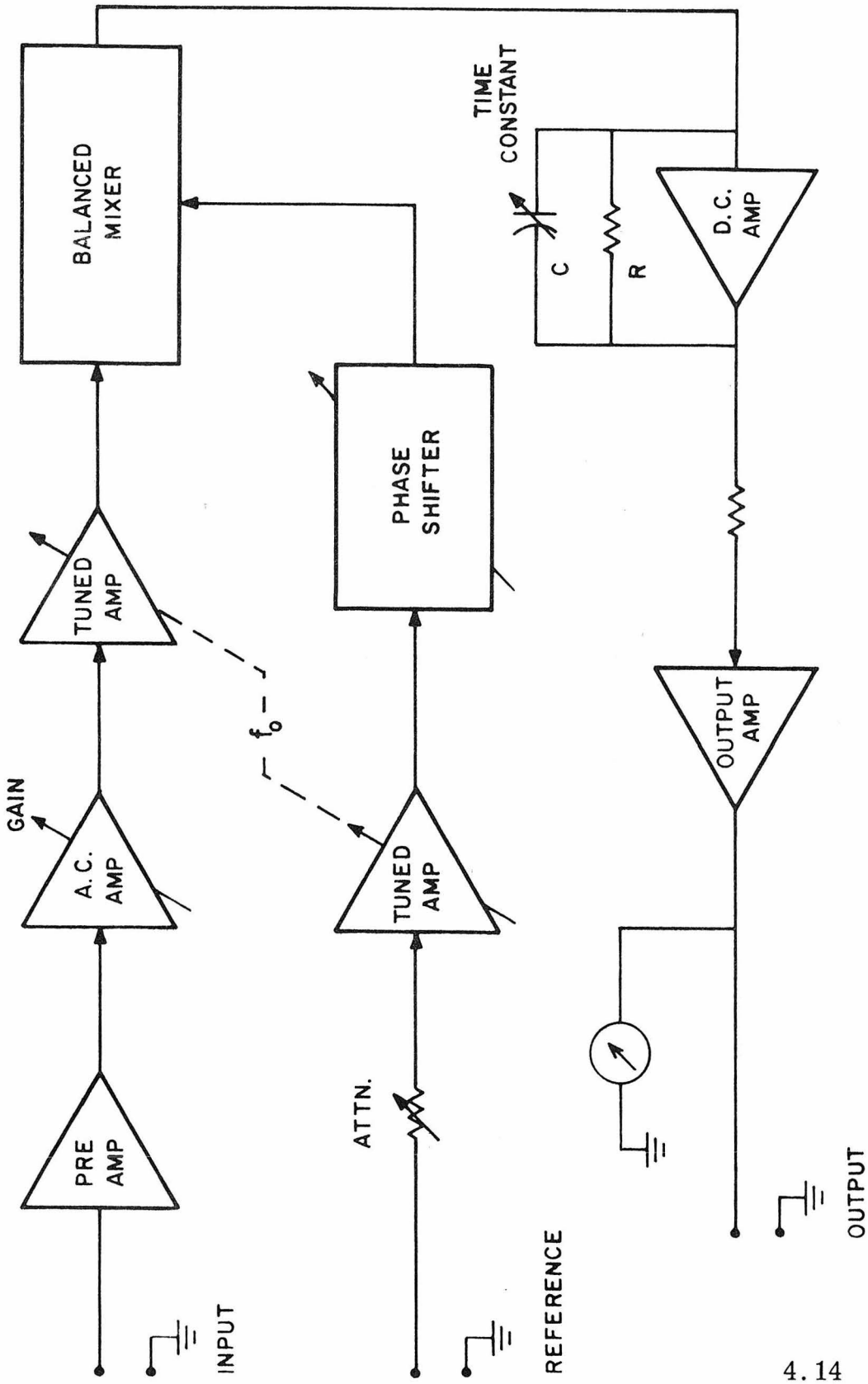
BALANCED MIXER
TIME CONSTANT
C
R
D.C. AMP
PHASE SHIFTER
TUNED AMP
f_o
GAIN
A.C. AMP
OUTPUT AMP
PRE AMP
ATTN.
TUNED AMP
INPUT
REFERENCE
OUTPUT

4.14

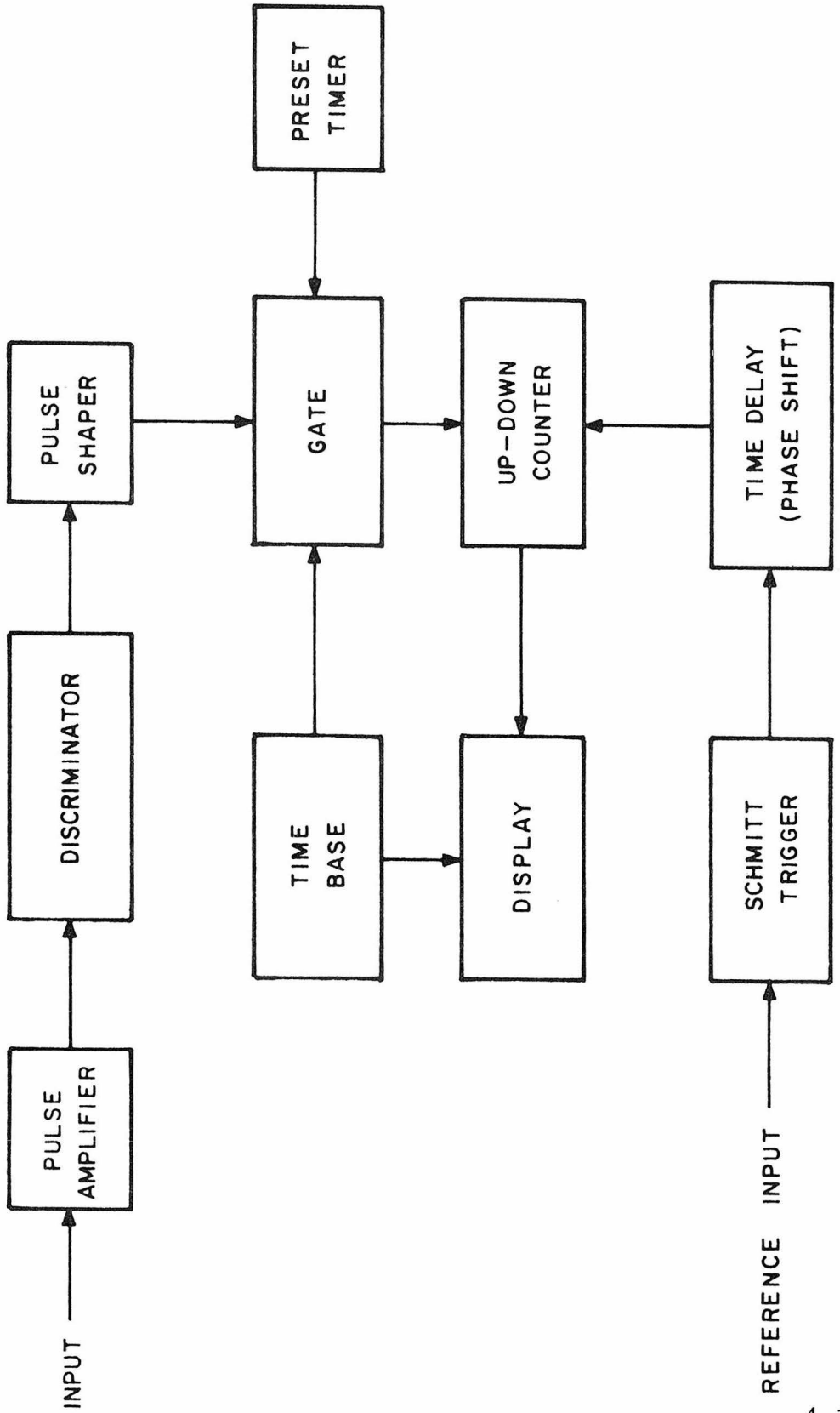
PRESET TIMER
PULSE SHAPER
GATE
UP-DOWN COUNTER
TIME DELAY (PHASE SHIFT)
DISCRIMINATOR
TIME BASE
DISPLAY
SCHMITT TRIGGER
PULSE AMPLIFIER
INPUT
REFERENCE INPUT

4.15

4.2.5.2 Counting Mode

The current mode just described is best suited to large signal levels, and in fact, has a practical lower limit corresponding to approximately 10^5 detected ions per second. Below that flux, it becomes possible to actually count the individual pulses generated by the detected ions. Unfortunately, the electron multiplier which works well in the current mode generates output pulses which are too broad to be accurately counted. In addition, the preamp used with this multiplier does not have a sufficiently wide bandwidth to be used in counting. As a result, a device especially suited to ion counting is employed, that is a continuous dynode Spiraltron multiplier. With a gain of 10^7, an upper limit of 10^6 counts/sec, and a "dark" current background of a few counts/min, this unit is ideal for pulse counting techniques.

Charge pulses generated by the Spiraltron are passed out of the vacuum chamber by a carefully shielded lead. They are then amplified and discriminated by a prototype pulse amplifier [40]. Basically, pulses which pass the discriminator are shaped and made TTL compatible by a Schmitt trigger. The upper limit for this system is approximately 1 MHz, which provides a one decade overlap with the current mode lower limit.

Since the output of the detector in this mode is a series of pulses rather than an AC or DC voltage, we cannot make use of an analog device such as a lock-in amplifier. Also, because some measure of S/N improvement arises because of the statistical nature of the pulsed

signal, any type of digital-to-analog converter would discard this improvement. The best solution is to use the digital equivalent of a lock-in amplifier. Such a unit was designed and constructed for use in pulse counting experiments, and while no data has been obtained with this system as yet, it will be described here and in Appendix B.

An overall block diagram of the digital phase-sensitive detector is shown in Figure 4.15, where some similarities with the PAR can be seen. Rather than use a synchronous driven switch to rectify the signal, such a switch is used to either add or subtract counts from a register. By adjusting the time delay (phase), the added counts will correspond to the signal + background, while the subtracted counts will correspond to background signal only. At the end of a fixed counting period, the counts accumulated in the buffer represent the signal, which is visually displayed. A complete description including circuit diagrams is given in Appendix B.

4.3 Systems Performance

In this section some performance results are given for five of the most important systems of the molecular beam apparatus. These systems include: (1) vacuum system, except the mass spectrometer chamber, (2) primary beam, (3) secondary beam, (4) velocity selector and, (5) mass spectrometer, including vacuum system. Many of these systems have been repeatedly checked and calibrated over the course of several years. However, only the more recent results will be given, which generally correspond to the current configuration. In some

cases, especially with pumping speed measurements, some degree of variation is expected from time to time due to pump conditions, contamination, ion gauge changes, and outgassing. Excessive variations in performance will be noted where appropriate.

4.3.1 Vacuum System

Earlier in this chapter the molecular beam vacuum system was described in some detail. Operation of the system (see next section, 4.4.1) routinely produces vacua well within the range required to perform experimental measurements. In its standby configuration, an ultimate main chamber pressure of 2×10^{-6} torr is achieved [41]. Approximately this vacuum is maintained when both beam sources are placed in operation. Using standard vacuum techniques and formulas, it is possible to calculate the expected performance of this system, and compare these results with the experimentally measured results.

One of the most easily measured quantities of interest in a vacuum system is the pumping speed of any device used to lower the system pressure. For our purposes, the speed can be defined as

$$S(\ell/\text{sec}) = Q(\text{torr } \ell/\text{sec})/P(\text{torr}) \tag{19}$$

where Q is the leak rate into the system, and P is the ultimate pressure. There are a number of means available for measuring the speed, S. One method involves measuring the rate at which a pump can reduce the pressure in a known volume. S is found as

$$S = \frac{\Delta P}{\Delta t} \frac{V}{P_0} \quad . \tag{20}$$

Several difficulties are encountered with this method, including an accurate record of ΔP vs Δt. A more straightforward method is to use a calibrated leak to establish a known Q into the system, and measure the resultant P_0. Several variations of this technique were used to measure the pumping speed of the eight vapor diffusion pumps comprising the vacuum system. The procedures followed were based on the American Vacuum Society standard AVS-4.1 [42].

With all pumps operating, the main chamber was allowed to reach a steady base pressure. For these tests, both sections of the primary beam differential chamber were open to the main system. Using only the eight diffusion pumps, a base pressure of $\sim 1 \times 10^{-7}$ torr was achieved and maintained after several hours. At this point, dry nitrogen gas was admitted to the chamber at a known leak rate. This rate was established using the secondary beam gas inlet and regulation system described in Section 4.2.3, and measured with a Hastings type LF-20 controller and type F-20M sensor head. After a stable leak rate was achieved ($\sim$ 15 minutes), the main chamber pressure was monitored (usually by two Veeco RG-75 ion gauges) and recorded on a strip chart recorder. The value of the established ultimate pressure P_1 is taken as the asymptotic limit of the recorded readings. As long as P_1 is at least 10 times P_0, equation (19) may be used with $P = P_1 - P_0$. The total leak rate Q was varied from $\sim 5 \times 10^{-3}$ tℓ/sec to 5×10^{-2} tℓ/sec, and the new ultimate pressures determined each time. The values of Q, P_1 and S are listed below in Table 4.1. The average speed is found to be $\sim$ 6100 ℓsec.

The above method yields only the total pumping speed, so that this procedure must be repeated using only one diffusion pump at a time in order to obtain the individual speeds. Column one of Table 4.2 lists the average results for these tests. The sum of 6330 ℓ/sec is within 5% of the previous total. One additional comparison test may be made which involves measuring the various speed ratios of each pump with respect to one particular pump. The speed of oil pump number 8 was accurately measured for this purpose. With only this pump open, the ultimate pressure P was found, then number 8 was valved off and one of the other pumps allowed to pump the system to P′. The ratio of these pressures, P/P′, is just the ratio of the speeds S/S(8). The results of these tests are given in column two of Table 4.2.

Based on the approximate leak rate of the secondary beam in operation of 5×10^{-3} tℓ/sec, and the combined pumping speed (excluding numbers 1, 3, and 4), the main chamber pressure during operation is predicted to be $\sim 1 \times 10^{-6}$ torr. This value is within a factor of 2 of the actual experimental value.

The results of these and other pumping speed measurements indicate that all vapor diffusion pumps are operating at approximately their rated nominal speed. Occasionally, one or more of these pumps will show a marked drop in speed, and this condition generally requires removal, cleaning and recharging of the pump.

Also located within the main chamber, is a large titanium sublimation pump. The pumping method here is chemical gettering of active gases on freshly layered titanium metal surfaces. The operation

Table 4.1

Total Pumping Speed Measurements With

$P_0 = 1.1 \times 10^{-7}$ torr (Base Pressure)

Run No.	Q (tℓ/sec)	P_1 (torr)	S (ℓ/sec)
1	5.3×10^{-3}	8.7×10^{-7}	6010
2	8.1	1.37×10^{-6}	5920
3	11.6	1.85	6300
4	23.0	3.75	6120
5	35.5	5.81	6050
6	50.1	8.10	6180
		Average =	6100

Table 4.2

Individual Speed Measurements

Pump No.	Speed (ℓ/sec)	
	Leak Rate	Ratio
1	120	130
2	125	115
3	120	140
4	1150	1120
5	1200	1150
6	1280	1210
7	1100	1080
8	1235	(1235)
Total =	6330	6180

of this pump has been somewhat limited due to its often erratic behavior. On some occasions, large increases in pressure occurred upon heating of the titanium filaments, presumably due to outgassing. Continued heating seemed to have little effect. On the other hand, dramatic results were often found after only several minutes of operation, with order of magnitude pressure drops occurring in seconds. During the latter periods, the speed for this pump could be estimated, again using the known (measured) speed and base pressure before sublimation pumping, and the base pressure after. Typically, with all pumps running ($S \cong 5000$ ℓ/sec) and a base pressure of 1×10^{-7}, the sublimation would reduce the pressure to 2×10^{-8}, hence yielding a speed of 25,000 ℓ/sec. Speeds of this magnitude are typical for titanium sublimation of active gases [21]. The occasional failure of this pump may be due to filament contamination or lack of adequate liquid nitrogen cooling in the surrounding coils.

A discussion of the vacuum characteristics associated with the mass spectrometer differential housing will be deferred until Section 4.3.5.

4.3.2 Primary Beam

A large number of tests have been performed with the primary beam in an effort to obtain maximum performance. With a differentially pumped supersonic source such as the one used here, a number of parameters may be varied including: nozzle size, skimmer size, nozzle–skimmer (N-S) distance, and operating pressure. Some of the desired characteristics can be predicted based only on simple

considerations [43]. For example, higher operating pressures should result in greater center line intensities and narrower velocity distributions, while a smaller skimmer opening will reduce the intensity without affecting the velocity distribution. The purpose of these tests was not, therefore, to verify these characteristics, but rather to determine if an optimum operating pressure, skimmer size, etc., could be found for a particular source configuration.

Several nozzle-skimmer size combinations were first compared on the basis of their velocity distributions, intensity vs pressure and intensity vs N-S distance characteristics. Two nozzle sizes, 70μ and 100μ were used, and four skimmer sizes (throat diameter), 0.202", 0.100", 0.052", and 0.025". Not all possible combinations were tested, but rather only the extreme combinations (70μ + 0.202", 70μ + 0.025", 100μ + 0.202", 100μ + 0.025") and a few intermediate combinations (70μ + 0.100", 70μ + 0.052"). Using the 70μ nozzle size, very little variation was seen in performance with each skimmer, although the smallest combination, with the 0.025" skimmer, gave very high intensity at a comparatively low operating pressure (200-300 torr). The larger nozzle and skimmer combinations resulted in too large a gas throughput into the velocity selector chamber, and so were not considered further. As a result of this series of tests, the 70μ diameter nozzle and 0.025" diameter skimmer were selected for further characterization.

Using the system described previously (see Section 4.2.2.1) for remotely varying the N-S distance, the affect of this parameter was

determined. Operating at 100 torr with H_2, the intensity showed a very broad plateau with respect to the N-S distance. The maximum occurred at approximately 150 nozzle diameters, and fell only 25% over the range from 90 to 300 nozzle diameters. No change in the velocity distribution was found as a function of the N-S distance. Increasing the H_2 pressure to 350 torr caused the intensity dependence to be a little more sharply peaked with respect to the N-S distance. Here, a 40% drop was found over the same range of distances, with a peak occurring at 135 nozzle diameters ($\sim$ 0.95 cm).

Setting the N-S distance at its optimum position, the intensity was measured as a function of operating pressure. Results of this test indicated that up to 800 torr, the intensity increased linearly. Since the pressure in the nozzle chamber remained nearly constant at 1×10^{-4} torr, no evidence of gas buildup leading to self-scattering and lower intensities was found. Unfortunately, the pressure in both the second buffer chamber and the main vacuum chamber began to rise at the higher operating pressures. Similarly, the background pressure in the mass spectrometer also increased. These restrictions placed a practical limit of 350-400 torr on the primary beam operating pressure.

The effect of pressure on both the beam divergence and the velocity distribution was also studied. As might be expected, the source pressure had little effect on the beam's angular spread, which is mainly determined by the skimmer and outer collimator dimensions (see Appendix A). In the range from 100 torr to 450 torr, only a 0.1° increase in the primary beam profile could be measured. With the

nominal operating pressure of 350 torr, this angular spread was approximately 1.4° FWHM. In contrast to this, the width of the velocity distribution was narrowed significantly as the pressure was increased from less than 20 torr (essentially effusive) to 350 torr (fully supersonic). For H_2, the Mach number at 100 torr was ~11, increasing to ~15 at 350 torr, while for D_2 the terminal Mach numbers were ~ 10 and ~13, respectively. The higher final Mach number achieved by H_2 results from its effective specific-heat ratio being slightly larger than for most diatomics [44]. At pressures much above 400 torr, the Mach number no longer increased as rapidly, so that 350 torr was chosen as an optimum operating pressure.

During several experiments the primary beam nozzle was cooled to liquid nitrogen temperature. Under those conditions, keeping the same nozzle and skimmer sizes and the same N-S distance, the optimum operating pressure was determined to be ~48 torr. The beam intensity was quite sensitive to this pressure, and would fall 20% if a ±10 torr change was made. The velocity distribution did suffer somewhat, increasing to 16% FWHM.

In summary then, the optimized primary beam configuration consisted of a 70μ diameter nozzle aperture placed 0.90 cm from a conical skimmer with a 0.063 cm (0.025") diameter throat. Operating at 350 torr with H_2, a 12.75% FWHM velocity distribution was obtained, which peaked at 2519 m/sec. When combined with a second aperture of 0.2 cm diameter located 6.9 cm downstream, a beam width of 1.4° was achieved. All experimental scattering data given in the next

chapter were obtained using this source configuration and operating parameters.

4.3.3 Secondary Beam

The determination of the operating characteristics of the capillary array secondary beam source was somewhat simplified, in that no skimmer was involved, and the velocity distribution was of no real concern. Based on the predictions and experience of Pritchard et al. [45], the two most important characteristics of a capillary array beam, its intensity and angular spread, can be expressed as,

$$I(0) \propto A \frac{\epsilon}{(L)^{\frac{1}{2}}} a^{\frac{1}{3}} \tag{21}$$

$$\theta_{\frac{1}{2}} \propto \frac{a}{(L)^{\frac{1}{2}}} \tag{22}$$

where L is the thickness of the array, a is the capillary radius, ϵ is its transparency, and A the total area of the source. Equation (21) would indicate that a small L/a ratio (the aspect ratio) is needed along with large area and a high transparency to maximize the center line intensity, I(0). On the other hand, a small aspect ratio will give a beam with a substantial angular spread as predicted by equation (22). Clearly then, a compromise must be reached in the choice of an array size. In general, it was felt that $\theta_{\frac{1}{2}}$ was the more important consideration, so an array of minimum pore size was selected.

Even though these considerations were made ahead of time, several array sizes were first tested to verify these predictions, at

least qualitatively. Arrays supplied by Bendix Mosaic Fabrication (formerly Permeonics Corporation [25]) had pore diameters of 2μ, 10μ, and 25μ. The thickness (L) of the arrays was fixed at 0.05 cm for the smallest, and 0.10 cm for the larger two. The fixed aspect ratios were then 250, 100 and 40, respectively. The only shortcomings of the 2μ array were its transparency (ϵ) of 50% as compared with 74% for the other two sizes, and the need for more careful physical handling. As expected, the behavior of the arrays in producing beams followed closely that predicted by equations (21) and (22). Using the 2μ array with O_2, the FWHM of the angular distribution varied from 2.5° at 2.45 torr to 3.5° at 5.77 torr.

To further characterize the secondary beam produced by the 2μ capillary array, it was mounted temporarily in the primary beam chamber in order to measure velocity distributions. Even though the operating conditions were not identical to the normal situation, only a rough idea of the distribution was desired. With operating pressures in the 2-5 torr region, the beams were essentially effusive, having distributions with 70-90% widths, indicating only slight acceleration ($M \approx 0.6$).

In order to maximize the beam intensity at the scattering center, the secondary array was placed as close as possible to that point without physically interfering with the primary beam. This distance was chosen as 0.40 cm, and the resulting configuration was capable of producing a 5% attenuation of the primary beam using a secondary source pressure of 3.0 torr.

4.3.4 Velocity Selector Calibration

Characterization of the beam velocity distributions were performed using the slotted disk selector mentioned in Section 4.2.2.1. The design parameters of this unit were chosen to give a transmission of 1.6% at the peak velocity of 10.66 ω m/sec (ω is the rotor angular velocity in Hz), with a resolution of 4.6%. To ensure accuracy in future measurements, the relation between the peak velocity, v_0 and the rotor velocity was redetermined using a simple calibration procedure. For beams of sufficiently high pressure, the peak velocity can be found from equation (10). For an atomic beam, the peak velocity is given by [5],

$$v_0 = \left(\frac{2kT}{m}\right)^{\frac{1}{2}} \left(\frac{5}{6}\right)^{\frac{1}{2}} M \left(1 + \frac{M^2}{3}\right)^{-\frac{1}{2}} \left(1 + \frac{12}{\gamma M^2}\right)^{\frac{1}{2}} . \qquad (23)$$

Using beams of helium, neon, and argon at pressures of ~ 100 torr, the velocity distributions were accurately measured. The widths of these distributions were used to determine the final Mach numbers in each case, and then equation (23) was applied to find v_0. The rotor velocity (frequency) corresponding to v_0 was measured using a Hewlitt-Packard model 5216A electronic counter to find the motor excitation frequency. The rotor velocity was also directly measured using the light/photocell system described in Section 4.2.2.1. The results of several calibration runs gave an average value of $v_0 = 10.66\ \omega$ m/sec. In view of the very good agreement with the predicted value, the calibration has not been repeated, and all subsequently measured velocities were assumed to be accurate to $\pm$ 100 cm/sec.

4.3.5 Mass Spectrometer System

With the bake out valve closed, the pumping in the mass spectrometer housing is provided by the titanium getter pump in the buffer chamber and the orbion and ion pumps in the spectrometer region. The liquid helium cryopump also pumps on this latter region (see below).

While no speed measurements were made on the titanium sublimator, briefly operating this pump produces dramatic pressure reductions. Application of full power (40 A, 12 VDC) for 5-10 minutes often reduces the pressure from 5×10^{-7} torr to 8×10^{-10} torr, as indicated by the uncalibrated GE ionization gauge in the buffer chamber. This pressure would be maintained for many hours with only liquid nitrogen cooling.

In the spectrometer region, the combination of the 5 ℓ/sec Ultek ion pump and the 400 ℓ/sec (nominal) NRC orbion pump were capable of reducing the pressure to 2×10^{-9} torr, after which the orbion could be switched off and the ion pump and liquid nitrogen cooling maintained. The nominal speed of the orbion is given as 400 ℓ/sec using water to cool the outer jacket, however, using liquid nitrogen, this value should increase by at least a factor of ten.

Limited testing of the helium cryopump has also been carried out. Charging of the dewar was accomplished by inserting the external dip tube of the flexible transfer line (see Section 4.2.4.2) into a 25 ℓ liquid helium dewar. This dewar was pressurized with cold He gas at between 2 and 4 lbs/sq.in. The rate of transfer was monitored using

two silicon diode cryogenic temperature sensors [46] mounted on the bottom of the cryopump dewar and near the top of its transfer line. Temperature verses voltage (at a constant current of 10μ A) curves were determined for each sensor so that an accurate measure of the liquid helium level could be made during and after transfer. Approximately 2-3 liters of liquid helium were needed to completely fill the 1 liter inner cryopump dewar. In tests using a solid copper plate in place of the optical baffle (see Figure 4.13) to reduce the heat load on the dewar, a full 1 liter charge lasted in excess of 20 hours. During this test, no pressure measurements were possible to verify the cryopumping action. With the plate removed and the blackened baffle replaced, similar storage times were found. However, no significant cryopumping action was observed either as a reduction in the total chamber pressure or as a reduction in any of the background masses as monitored by the mass spectrometer. Further testing with the baffle completely removed did show a pressure reduction by a factor of ~ 2, however, the retention time was limited to approximately 4-6 hours with the ionizer filament off, and only 2-3 hours with the filament in operation. Additional liquid nitrogen shielding of the ionizer source is needed to reduce the direct heat load on the dewar during operation. Since much of the residual gas load in the mass spectrometer chamber is H_2, continued pressure reductions beyond $\sim 1 \times 10^{-9}$ torr may not be possible without the use of chemical cryosorption materials [33, 35].

Since the mass spectrometer was set at either mass 2 (H_2) or 4 (D_2) for the majority of these experiments, there was no need to

maximize the resolution or mass peak shape. As a result, the nominal resolution of 600-1000 for mass 28 was never duplicated, however, the nominal ionization and detection efficiency of 10^{-3} at a resolution of 40 and m/e 28, was approximately duplicated. This represents about 100 A/torr of N_2, which is quite high for a quadrupole unit of this size. In general, the mass spectrometer controls were adjusted for a maximum signal at the mass of interest, without reducing the resolution to the point where contributions were obtained from higher and lower masses. Those controls which were varied included the ion and electron energies, the total emission current, and the resolution and ΔM settings.

To record background spectra, the system would be tuned to give sharp peaks with a flat base line over the range of interest. The x and y signals normally applied to the oscilloscope were used to drive an X-Y recorder. The scan speed of the oscilloscope ramp generator was slowed sufficiently to obtain an even recording. A typical background mass scan taken with a total ionizer region pressure of $\sim 4 \times 10^{-9}$ torr is shown in Figure 4.16. This figure was actually computer generated using the measured peak heights and the approximate Gaussian peak shapes. The partial pressure scale was estimated from the integrated peak intensities and the total pressure. Despite several bake outs, the presence of hydrocarbon fragments, H_2O, N_2, and CO_2 is indicated. The anomolous peak at mass 19 appears to be real, and may either result from the formation of H_3O^+ in the ion source, or from residual F^+ formed from the SF_6 used in several experiments. At

Figure 4.16: Typical background mass spectrum from m/e 0 to 44. Emission current = 10 m A, electron energy = 75 eV, ion energy = 9.5 eV.

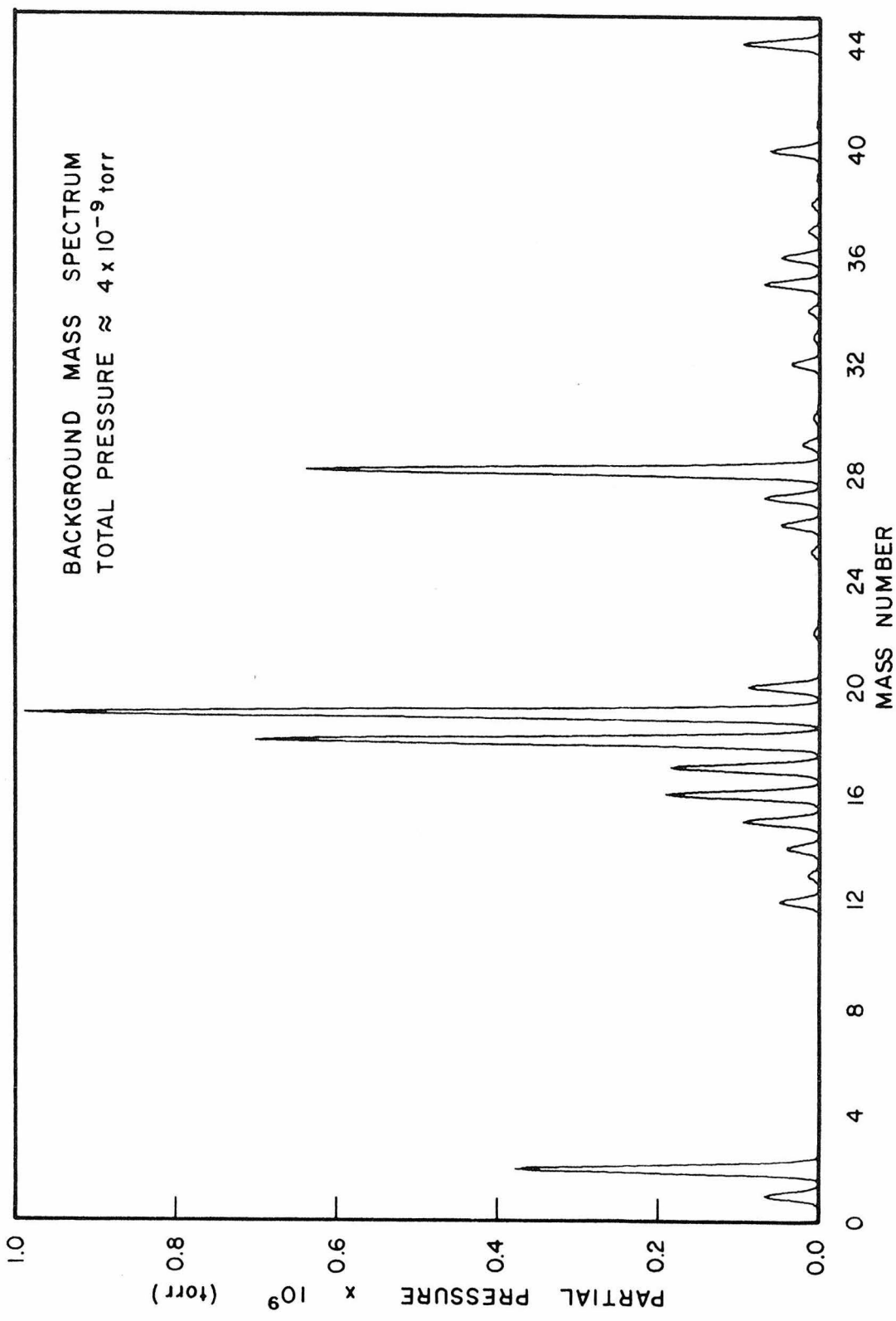
BACKGROUND MASS SPECTRUM
TOTAL PRESSURE ≈ 4 x 10⁻⁹ torr
PARTIAL PRESSURE x 10⁹ (torr)
MASS NUMBER
0.0
0.2
0.4
0.6
0.8
1.0
0
4
8
12
16
20
24
28
32
36
40
44

4.16

higher pressures (5×10^{-8} and above), this peak is very small, and is only apparent at the lower pressures, thus indicating a nearly constant partial pressure.

4.4 System Operation

In the course of setting up the molecular beam system to obtain differential elastic scattering data, several standardized procedures were established and followed. In this section, several of the most important of these procedures are described, including beam and detector alignment, pump down, bake out and liquid nitrogen cooling, and the actual data taking method.

4.4.1 Alignment

An essential aspect of the scattering experiment is the assumption that the detector not only moves exactly in the plane of the two beams, but also that it always remains focused at the scattering center. To ensure this, an accurate system is needed to align the two beam sources and the detector. The starting point for the alignment is the location of an accurate reference point or plane. In the molecular beam apparatus, the front edge of the primary beam chamber has been machined flat and located exactly parallel (± 0.001") to the axis of the secondary beam, and hence perpendicular to the desired primary beam path.

The actual alignment is carried out using a Wild 3N precision optical level mounted on a rigid, variable height, stand. The optical

level is roughly placed in line with the secondary beam, about 8 feet from the scattering center. The exact height is established by sighting the top of a precision machined pin which is mounted on the end of the quadrant arm bearing shaft. This shaft normally holds the gear used to drive the horizontal angle indicator, and is by definition the exact center of rotation of the detector. This pin not only establishes the height, but is also one point needed to locate the secondary (or primary) beam axis. For the secondary beam, two other points are determined by suspending 0.003" steel plumb lines from brackets fixed to the machined face of the primary beam chamber. By locating the optical level in line with these two wires and the pin, the cross hairs in the level establish the secondary beam axis.

At this point, the mass spectrometer housing is moved into position along the secondary axis. The front entrance aperture can now be placed exactly in the center of the cross hairs. By sighting through the glass port on the rear of the mass spectrometer it is then possible to center the ionizer aperture by adjusting the tightening of the rear gasket bolts. Since the ionizer is very nearly in the center to begin with, only small adjustments are needed. Once this is complete, all that remains is to align the primary beam so that it is perpendicular to the secondary axis.

The primary beam axis is found by first removing the locating pin and replacing the gear, then using the angle readout device to move the mass spectrometer through 90°. By rotating the optical level without altering its position, and sighting along the newly established mass

spectrometer axis with the aid of a mirror placed just behind the rear of the detector, the primary beam axis is located. After this step, the locating pin is replaced. If the pin, the entrance aperture, and the ionizer aperture still lie along a line, then it can be assumed that the mirror is accurately placed, and further that the quadrant arm has not tilted in moving through 90°. If these points fail to line up, then the source of misalignment must be determined and corrected before this procedure can be repeated. Using this line, the exit aperture of the primary beam chamber can be located. With a bright light source located behind the primary beam nozzle and skimmer, this unit can be moved into exact alignment with the optical axis.

The last step is to place the secondary beam at the correct height and distance from the scattering center. The optical level is returned to the secondary axis, and the secondary beam source height is adjusted until it is in the center of the cross hairs. Lateral motion of the source is prevented by the optical bench upon which it is located. The distance of the source to the scattering center is measured and set at 0.10" with a caliper, using the aligning pin as reference.

4.4.2 Vacuum System Pumpdown

Operation of the vacuum system described in Section 4.2.1 is straightforward. After the bell jar has been lowered into position and the O-ring compressed sufficiently to provide a good seal (~ 20% compression), roughing can begin. If the two mercury diffusion pumps used in standby condition are operational, their backing valves are

closed by switching off the manifold valve power. All four bypass valves, above pumps 1-4, are opened slowly. After the pressure in the roughing line has dropped to 500μ, the diffusion pump backing valves can be again opened. If these diffusion pumps have not been operating, they can now be started. Once the indicated pressure in the main chamber is below 50μ, the roughing valves are closed and diffusion pump 2 is slowly opened to the system. As the pump begins to work, and the pressure in the chamber falls, the gate valve can be fully opened, as can the gate valve above pump 3.

If the system is leak tight, the pressure as indicated by the Veeco nude ionization gauge should fall to a base pressure of 2×10^{-6} torr within 10-12 hours. If this pumpdown is carried out with the mass spectrometer sealed under vacuum, it may remain so until an experiment is performed. If on the other hand, the spectrometer is not under vacuum, the BOV is left opened so that the pressure in this chamber will also fall to the low 10^{-6} torr region. At this point, the mass spectrometer filament is placed in standby using the voltage regulation option on the filament control unit. Approximately one watt of power is passed through the filament.

The apparatus may be maintained in this condition indefinitely so long as a supply of liquid nitrogen is available, and the clock-based trap filling system is kept in operation.

If the pumpdown has started from full atmospheric pressure, that is, the mass spectrometer has not been kept under vacuum, then a bake out must be performed.

4.4.3 Bake Out

When evacuated from atmospheric pressure, the mass spectrometer shows background peaks at most masses from 12 to 70 plus masses 1 and 2. The largest components are H_2, H_2O, N_2, CO_2, with organic materials also in evidence. If the pressure in the detector is lowered by circulating liquid nitrogen, operating the ion pump and orbion pump, and flashing the buffer chamber titanium sublimator pump, a base pressure of only 1×10^{-8} torr can be reached. The major background components are still present as before. In order to reduce further the pressure, it has been found necessary to subject the mass spectrometer system to an extensive bake out.

With the BOV and the front gate valve open, the oil diffusion pumps are put into operation to help remove the outgassed material. With these pumps working, the base pressure will fall to the mid 10^{-7} torr range or better. At this point, bake out power is applied to the two heater tapes. With 100 volts applied, the pressure will rise rapidly in the main chamber, often to 10^{-5} torr, where it will remain briefly. Once the pressure has fallen again, the heater power is increased to 200 volts. Again, the pressure will rise and fall, after which full power (260 volts, 4.5 A) is applied. Temperatures around the mass spectrometer housing are monitored by six thermocouples located on the front flange, the sublimator arm, the front housing area, the rear housing area, the top of the BOV, and the orbion body. Typically, the latter location reaches the highest indicated temperature of approximately 240°C. Bake out is usually continued for 8-20 hours,

depending on how quickly the pressure drops in the main chamber. Generally, the longer times provide the best results although they tend to cause hardening of the main bell jar O-ring due to heating. During the last 30 minutes of the bake out, the mass spectrometer Bendix ionization tube is degassed (this gauge remains off during all bake out operations). The oil diffusion pumps are left on for several hours after the completion of the bake out. Also, air is blown through the liquid nitrogen lines to help cooling and to heat the cryopump and main chamber sublimator which are not baked.

After 18-24 hours of cooling, it is safe to begin circulating liquid nitrogen through the system. The first cool down period will lower the pressure into the 10^{-8} torr region. The BOV may be closed prior to this cool down, or between cool down periods. The orbion and sublimator pumps may be operated with the system cold, and the ion pump started and left on. Following several days of this procedure of cooling the system and operating the orbion pump, the pressure in the mass spectrometer will fall to 2×10^{-9} torr with only liquid nitrogen and the ion pump running. At this point, the system is ready to record useful elastic scattering results.

4.4.4 Data Accumulation

Once the molecular beam system has been prepared as described above, a typical procedure for taking data would be as follows.

Several hours prior to starting the data accumulation operation, the system, which is in standby, is activated by starting the oil

pumps and the liquid nitrogen flowing through the mass spectrometer. Once the diffusion pumps are opened, the primary and secondary beam gases are admitted. Their pressures are adjusted and allowed to stabilize. If the primary beam is to be cooled, this cooling would begin at this time. During this period, the mass spectrometer electronics are switched on, and a background scan observed. If the peak to be monitored (i.e., the mass of the primary beam) is large, operation of the orbion pump for a short period will often reduce its magnitude greatly.

Approximately one hour is required for both the main chamber and mass spectrometer pressures to stabilize at 1×10^{-6} and 2×10^{-9} torr, respectively. This time is also sufficient for the beams to stabilize. The mass spectrometer is positioned near the primary beam, and the chopper is activated. The mass spectrometer, the preamp and the PAR are all adjusted to give a maximum signal level at the output of the lock-in amplifier. At this point, a velocity distribution may be measured, and the exact center of the primary beam established to calibrate the angular scale.

The actual data accumulation is performed by the computer controlled system mentioned in Section 4.2.5.1. To operate this system, three programs must be loaded into the computer from magnetic tape. These routines are: (1) MBDA10, the main control program; (2) SATOD, the subroutine which samples the output of the AD; (3) ATIME, which provides a printout of the time of day.

The main I/0 device, the ASR-33 teletype is physically located in the molecular beam laboratory while the SCC4700 is in a remote

location. Several input parameters are first requested by the computer. They are: (1) ANGLE, used only for the operators reference, (2) COMMENTS, also for reference only, (3) PAR, the input sensitivity of the lock-in amplifier in units of millivolts, (4) AC, the gain of the ELI preamplifier unit, this must be either 0.01, 0.1, 1.0, or 10.0, (5) TAU, the time constant of the PAR in seconds, (6) TIME, corresponding to the number of seconds duration of each on-off period, (7) FLAGS, the number of secondary on-off periods. A typical input sequence would be,

```
ANGLE    = 3.5
COMMENTS = "reference angle"
PAR      = 200
AC       = 1.0
TAU      = 3
TIME     = 30
FLAGS    = 6
START
```

When S, or start, is entered, the computer immediately prints out the time of day (accurate to 1 sec) and then begins sampling the AD at a fixed rate of 60 Hz. After 30 seconds (= TIME), a computer activated relay tilts the secondary beam out of the scattering plane. Simultaneously, the computer begins a waiting period of 15 seconds (5 × TAU) to allow the lock-in amplifier time to establish its new level. Another 30 second integration period then begins. At the conclusion of the first

two flags, the measured difference signal is printed out. Another waiting period begins, and the process is repeated for the preset number of FLAGS. After the last difference signal (here, the third) is printed out, the time of day is again given. The total number of sample points taken with the beam on and off (60 × TIME × FLAGS/2) is printed out. The average on and off signals, their standard deviations and the average difference value and its standard deviation are all listed. At this point, the system is ready to accept more input parameters. The output signal values are all normalized using the PAR and AC parameters so that the raw data is already scaled.

Two additional features of the computer system are a remote indicator light and a remote abort control. The former indicates whether the system is awaiting input parameters, taking data, or waiting during the 5τ period. The latter control allows the user to terminate the data taking sequence at any time.

Normally, the signal is first measured at a reference angle (between 2° and 4°) and recorded along with the midtime determined from the printed start and stop times. Next, the scattering at another angle is similarly measured. Typically, data is taken at each half angle from 2° to 25°. After each point is measured, the spectrometer is returned to the reference angle, and the signal remeasured. Using the time history of the reference signal, it is possible to correct each data point for the long term system drift. Data taken on successive days is simply normalized using the first days reference value. In this way, data is reproducible to ± 5%.

Reduction of the raw data and the determination of the intermolecular potential will be discussed in the next chapter.

References

1. N. F. Ramsey, "Molecular Beams," Oxford University Press, Oxford, 1956.
2. E. H. Kennard, "Kinetic Theory of Gases," McGraw-Hill, New York, 1938.
3. A. Kantrowitz and J. Grey, Rev. Sci. Instr. 22, 328 (1951).
4. A. Kantrowitz and W. P. Slichter, Rev. Sci. Instr. 22, 333 (1951).
5. J. B. Anderson and J. B. Fenn, Phys. Fluids 8, 780 (1965).
6. J. B. Fenn and J. B. Anderson, in "Rarefied Gas Dynamics," J. A. Laurmann, ed., Academic Press, New York, 1963, pp. 497-515.
7. J. L. Kinsey, Rev. Sci. Instr. 37, 61 (1966).
8. A. E. Grosser, Rev. Sci. Instr. 38, 257 (1967).
9. L. T. Crowley, M. A. D. Fluendy, and K. P. Lawley, Rev. Sci. Instr. 41, 666 (1970).
10. H. U. Hostettler and R. B. Bernstein, Rev. Sci. Instr. 31, 872 (1960).
11. Y. T. Lee, J. D. McDonald, P. R. LeBreton, and D. R. Herschbach, Rev. Sci. Instr. 40, 1402 (1969).
12. L. T. Crowley, M. A. D. Fluendy, D. S. Horne, and K. P. Lawley, J. Phys. E 2, 1021 (1969).
13. R. W. Bickes and R. B. Bernstein, Rev. Sci. Instr. 41, 759 (1970).
14. J. B. Taylor and I. Langmuir, Phys. Rev. 44, 423 (1933).
15. R. Weiss, Rev. Sci. Instr. 32, 397 (1961).
16. W. Paul and M. Raether, Z. Physik 140, 262 (1955).

17. W. Paul, H. P. Reinhard, and V. von Zahn, Z. Physik 152, 143 (1958).

18. W. Paul and H. Steinwedel, Z. Naturforsch. 8a, 448 (1953).

19. J. B. Cross, Ph.D. Thesis, University of Illinois, 1966.

20. O. H. Crawford, Ph.D. Thesis, University of Illinois, 1966.

21. R. G. Herb, T. Pauly, R. D. Welton, and K. J. Fisher, Rev. Sci. Instr. 35, 573 (1964).

22. Pelco, Inc., Tustin, California.

23. E. L. Knuth, private communication.

24. J. G. King and J. R. Zacharias, Advan. Electron. Electron Phys. 8, 1 (1956).

25. Permeonics Corporation, Southbridge, Massachusetts.

26. Collimated Hole Structures, Brunswick Corporation, Chicago, Illinois.

27. (a) K. C. Wang and P. G. Wahlbeck, J. Chem. Phys. 47, 4799 (1967); (b) P. G. Wahlbeck and T. E. Phipps, J. Chem. Phys. 49, 1603 (1968); (c) J. Q. Adams, T. E. Phipps, and P. G. Wahlbeck, J. Chem. Phys. 49, 1609 (1968); (d) K. C. Wang and P. G. Wahlbeck, J. Chem. Phys. 49, 1617 (1968).

28. R. H. Jones, D. R. Olander, and V. R. Kruger, J. Appl. Phys. 40, 4641 (1969).

29. D. R. Olander, J. Appl. Phys. 40, 4650 (1969).

30. W. G. Mourad, T. Pauly, and R. G. Herb, Rev. Sci. Instr. 35, 661 (1964).

31. R. A. Douglas, J. Zabritski, and R. G. Herb, Rev. Sci. Instr. 36, 1 (1965).

32. J. C. Maliakal, P. J. Limon, E. E. Anden, and R. G. Herb, J. Vac. Sci. Technol. 1, 54 (1964).

33. S. A. Stern, J. T. Mullhaupt, R. A. Hemstreet, and F. S. DiPaolo, J. Vac. Sci. Technol. 2, 165 (1965).

34. J. P. Dawson and J. D. Haywood, Cryogenics 5, 57 (1965).

35. S. A. Stern, R. A. Hemstreet, and D. M. Ruttenbur, J. Vac. Sci. Technol. 3, 99 (1966).

36. J. P. Hobson, J. Vac. Sci. Technol. 10, 73 (1973).

37. P. M. Kobzev, Y. V. Kholod, and V. B. Yuferov, Sov. Phys.-Tech. Phys. 14, 424 (1969).

38. See, for example, N. McLacken, "Theory and Applications of Mathieu Functions," Oxford University Press, Oxford, 1947.

39. Bendix Corporation, Electro-Optics Division, Sturbridge, Massachusetts.

40. O. A. Mosher, Ph.D. Thesis, California Institute of Technology, 1975.

41. All pressure readings are uncalibrated ionization gauge measurements.

42. See J. Vac. Sci. Technol. 8, 664 (1971).

43. E. L. Knuth, Appl. Mech. Rev. 17, 751 (1964).

44. The very large vibrational and rotational spacings in molecular hydrogen are the cause of this behavior.

45. J. C. Johnson, A. T. Stair, Jr., and J. L. Pritchard, J. Appl. Phys. 37, 1551 (1966).

46. Lake Shore Cryotronics, Incorporated, Eden, New York, Model DT-500.

5. RESULTS AND DISCUSSION

In order to carry out a systematic study of the nature of the intermolecular forces acting between various diatomic and small polyatomic molecules, a number of differential elastic scattering measurements were made. The systems studied included: $H_2 + O_2$, SF_6, CO, NH_3, CH_4, H_2O and $D_2 + O_2$, SF_6, NH_3, H_3O. These studies were performed using room temperature beams, thus giving relative collision energies of ~ 0.10 eV. Three additional experiments were performed using liquid nitrogen temperature beams of hydrogen: $H_2 + SF_6$, $H_2 + NH_3$, and para-$H_2 + SF_6$. These studies had a relative collision energy of ~ 0.03 eV. As indicated by equation (44) in Section 3.3, the angular spacing of the rapid quantum oscillations (if resolvable) in the differential cross section (DCS) for elastic scattering depends upon three parameters, σ, μ, and v. The choice of the systems studied here allows for the independent variation of each of these parameters; σ varies with the differing target molecules and the same incident hydrogen isotope, μ varies with the choice of hydrogen isotope and the same target molecule, and v is altered by repeating two experiments using different collision energies. Thus, the three parameters σ, μ, and v were varied over a wide range of values, which in turn allowed for a better determination of the nature of the intermolecular potentials involved. The actual effects of these parameters on the measured DCS can be seen in the results shown later.

The raw data were obtained as outlined in Section 4.4.4. Normally, data points were measured at each half degree from

approximately 2° to 20° (in the laboratory frame) depending upon the prevailing signal-to-noise ratio. After a complete DCS was obtained, the same system was repeated at least once, and often twice to ensure reliability. Generally, a simple average was taken of the measured values at each angle obtained from different runs. Single data points were omitted only when they were completely outside the range of the error limits established for that particular angle. These error limits were determined using the standard deviations for each point as calculated by the on-line computer (see Section 4.4). The standard procedure was to obtain three consecutive, independent measurements of the scattered signal by integrating the signal with the secondary beam on, then subtracting the corresponding signal with the beam off, then repeating this sequence twice. The average of these three values was taken as the scattered signal, and the standard deviation calculated (including all the points in the six integration periods) by the computer was then used to establish the error limits. After analyzing these error limits for a number of experimental runs, it was found that a rather simple relationship existed between the calculated error bars, and the angle at which they were determined. As a result, it was possible to assign error bars to any data point measured by simply making use of this relationship. In practice, a second order polynomial was fitted to the calculated error bar-angle function to facilitate further analysis (see below). Since the relative signal-to-noise ratios for H_2 and D_2 experiments were different, two error bar functions were needed, one to characterize each system. As more data were

accumulated, the validity of these functions was tested, and in all cases, the predicted error bars were found to be no smaller than the actual calculated limits. Thus, the use of such a method to generate error bars associated with any scattering measurement appears fully justified.

In addition to the raw data points obtained from each experimental run, several other parameters had to be determined for each system before a thorough analysis could be performed. This information consisted of various velocity distribution parameters associated with both the primary (H_2 or D_2) and the secondary beams. Specifically, the Mach number M, the specific heat ratio γ, and the temperature of each beam was needed. These were obtained by carefully measuring the velocity distributions associated with each of the primary gases and secondary gases (see Section 4.3). The measured distributions were fitted to the functional form,

$$P(v) = Nv^2 e^{-M^2(v-z)^2/\alpha_0^2} \qquad (1)$$

where $\alpha_0 = (2kT_0/m)^{\frac{1}{2}}$, T_0 is the beam temperature, z is $\gamma\alpha_0$, and M is the final Mach number. Typical values for these parameters are listed in Table 1. Several other parameters relating to the ratios of primary and secondary velocities are also needed in the data analysis, however, these are calculable from the information in Table 1 (see below).

Table 1

Velocity Distribution Parameters

	H_2[a]		D_2	O_2[b]
T_0 (K)	285	77.5	285	185
α_0 (m/sec)	1534.6	800.3	1085.1	383.6
γ	1.62	1.62	1.57	1.3
z (m/sec)	2486.1	1296.4	1801.3	498.8
M	15.05	14.2	8.5	1.05

[a] Values are given for both the room temperature beam, and the cooled beam.

[b] These values for O_2 are typical of those for all secondary gases, except for α_0 and z which vary as $m^{-\frac{1}{2}}$.

5.1 Data Analysis

One of the basic aims of these studies was to determine the validity of the central-field approximation for describing the elastic scattering of hydrogen molecules by various other non-spherical molecules. Hence, the analysis of the data was performed using central-field potentials, with the resulting degree of success taken as a measure of the validity of this assumption. As discussed previously (see Chapter 3), the only method available for the analysis of scattering results such as these (exhibiting only rapid quantum oscillations) is a best-fit procedure in which variable parameters of a model potential function are determined. Since model functions can be somewhat restrictive in their flexibility, several types were used, in the hope that any insensitivity to the exact mathematical form of the model could be interpreted as partial justification of the central-field assumption.

The models chosen were simple two, three, and four parameter functions. By fitting a comparatively few parameters, it should be possible at least to determine well that part of the potential sampled by the scattering experiments. In the present studies, a Lennard-Jones (n, 6) potential was used, where the repulsive exponent n was either fixed at 12 or 20, or was allowed to vary as a free parameter. Also, a Morse-cubic spline-van der Waals potential (Section 2.3) was used in analyzing some systems. For each type of potential, a standard method of analysis was carried out to determine the best values for the variable parameters. Although the details vary as a function of the model used, the basic method remains the same, that is, a least-

squares technique is used to reduce the deviations between the measured and calculated scattering. A detailed description of this method is given below as it applies to the fixed n Lennard-Jones potential, with some note given to the MSV case.

5.1.1 Fitting Procedure

The information accumulated from the experiments outlined above forms the input for a computerized least-squares analysis routine which yields from it the best fit potential parameters. The basic workings of that computer routine, written in Fortran IV, will be discussed here, although not necessarily in the exact order in which the program performs each function.

The program begins by reading in the raw data as ordered pairs of points, $(\theta, I(\theta))$. The velocity information relating to both beams is read in, including those parameters needed to reconstruct the velocity distributions according to equation (1), and also the measured ratio of the peak velocities of each distribution. The Lennard-Jones potential exponents are read in next. These are fixed values, but not necessarily integers. Initial guesses for the two potential parameters are expressed as $A (= k\sigma)$ and $K = (E/\epsilon)$, where k is the wavenumber and E the total energy. Since computation of the theoretical DCS need only be performed over a limited range of angles which span the experimentally measured region, the first and last angle of this range of computation are read in, along with $\Delta\theta$ the spacing between calculated points. A number of control parameters are also read in, which

indicate the following: whether fitting the potential parameters will be done in the center-of-mass or the laboratory frame; inclusion of angular averaging using either a rectangular or a triangular resolution function, and whether the width of that function should be fixed (at some specified value) or varied as a parameter; the number of velocities to be included in the energy averaging scheme; and several plotting options. With these input parameters specified, the program must first evaluate the degree of "fit" between the experimental points and the properly scaled and averaged theoretical DCS. This degree of fit is measured by calculating the sum of the squares of the deviations between the two sets of numbers,

$$S = \sum_{i=1}^{n} g_i \left[\langle I(\theta_i) \rangle - \hat{y}_i \right]^2 \quad . \tag{2}$$

Here, n is the number of experimental points, $\langle I(\theta_i) \rangle$ is the averaged (velocity and angular) theoretical intensity at θ_i, $\hat{y}_i$ is the observed intensity at θ_i, and the g_i are weights assigned to each measurement. These weighting parameters are necessary because the magnitude of the $\hat{y}_i$ may span several orders of magnitude as θ varies from 2° to 25°, and also the uncertainty associated with large angle data is greater than for the small angle data. As a result, these weights are taken as,

$$g_i = \frac{s_i^{-2}}{\frac{1}{n} \sum_{i=1}^{n} s_i^{-2}} \quad , \tag{3}$$

where s_i is the measured standard deviation of $\hat{y}_i$. These s_i are directly related to the error bars discussed above. Having established the value of S by means of (2) and (3) using the initial guesses for the potential parameters, this value (designated S_0) becomes the reference against which any other value of S will be compared in the course of the fitting procedure. Thus, if an increase in the ϵ parameter yields a larger value of S, then clearly the degree of fit has been degraded, whereas a smaller S indicates an improvement in fit. Therefore, it is the minimization of S (with respect to the initial S_0) that is the goal of this fitting procedure.

In the evaluation of (2), it is essential that both the $\langle I(\theta_i)\rangle$ and the $\hat{y}_i$ be expressed in the same framework, that is as center-of-mass intensities (and angles), or as laboratory quantities. Since the $I(\theta_i)$ calculated are automatically in the center-of-mass, and the $\hat{y}_i$ are naturally measured in the laboratory frame, one or the other must be transformed. As will be seen later, it is much more feasible to construct a theoretical DCS in the laboratory frame than it is to back transform the laboratory experimental data to the center-of-mass. The major consideration here is the nature of the velocity averaging which must be included in the calculated $\langle I(\theta)\rangle$. This averaging must be included regardless in which direction the transformation is carried out. Since there is no way to remove the effects of velocity averaging from the measured results (even velocity selected experiments are not monoenergetic), they must be included in the theoretical calculations. For these reasons, the $\langle I(\theta_i)\rangle$ used in (2) are obtained by velocity (and angle)

averaging the transformed (CM → LAB) intensities calculated as described below.

The first major task of the program, then, is to calculate the $\langle I(\theta_i)\rangle$ so that S_0 may be evaluated. Since this procedure is repeated (four times) in the actual fitting of the potential parameters, it will be outlined here in some detail:

(a) Because the effects of velocity averaging must be included from the beginning, a relative velocity distribution must be calculated for use in the averaging procedure. Using the input information on the primary and secondary beam velocity distributions, and equation (1), a single distribution function, $P(v_{rel})$ is constructed. From this distribution, five (nine) velocities are chosen if the primary beam is H_2 (D_2). The center velocity of the five (or nine) is always taken as the most probable relative center-of-mass velocity (u_{mp}), while the other four (eight) velocities are chosen in a somewhat more complicated manner. First, the velocities whose probabilities, P(u), are 1% of the probability associated with the center velocity ($P(u_{mp})$) are found. These velocities are taken as the extremes of the distribution function. Since in general, the distribution will not be symmetric about u_{mp}, one of these two extreme velocities (designated u_0) will lie farther from u_{mp} than the other. The additional four (eight) velocities are now found as,

$$u_i = (|u_{mp} - u_0|)x_i + u_{mp} \quad , \qquad i = 1, 2, 4, 5(\ldots 9) \quad , \tag{4}$$

where the x_i are the appropriate Gaussian moments for a five (or nine) point integration [1]. This procedure ensures that the velocities chosen

will span the widest possible range of the relative velocity distribution. The use of the Gaussian moments in (4) is important only if the theoretical cross section is not transformed to the LAB (i.e., the fitting procedure is performed in the center-of-mass frame), in which case the velocity averaging is done by Gaussian quadrature. In that case, the experimental points are transformed to the CM system by means of the fixed velocity approximation (FVA) which simply assumes that the two beams were monoenergetic for the purposes of the transformation. The theoretical cross section $I(\theta, v_{rel})$ is then averaged as (see equation (6), Section 4.1),

$$\langle I(\theta)\rangle = \int_0^\infty \int_0^\infty I(\theta, v_{rel})\, P_1(v_1)\, P_2(v_2)\, dv_1 dv_2 \quad , \tag{5}$$

where the $P_i(v_i)$ are given by (1). In the FVA, the double integral can be reduced to a single integral over the distribution $P(v_{rel})$, given by,

$$P(v_{rel}) = \int_0^\infty dv_1 \int_0^\infty dv_2\, P_1(v_1)P_2(v_2)\, \delta\left[v_{rel} - (v_1^2 + v_2^2)^{\frac{1}{2}}\right]$$

$$= v_{rel} \int_0^\infty (v^2 - v_1^2)^{-\frac{1}{2}}\, P_1(v_1)P_2\left[(v^2 - v_1^2)^{\frac{1}{2}}\right] dv \quad . \tag{6}$$

In this way, (5) becomes

$$\langle I(\theta)\rangle = \int_0^\infty I(\theta, v)P(v)\, dv \quad . \tag{7}$$

However, since the velocities at which $I(\theta, v)$ are calculated have been chosen according to the Gaussian moments x_i, then (7) reduces to

$$\langle I(\theta)\rangle = \sum_{i=1}^{n} I(\theta, v_i)P(x_i)\, w_i \qquad n = 5\,(9) \quad , \tag{8}$$

where the w_i are the Gaussian weights associated to the x_i [1].

The above discussion applies only for a center-of-mass fitting procedure, whereas in the case of a properly transformed (LAB) fitting method, another averaging method must be used. In this case, the fact that the u_i given by (4) were chosen according to the Gaussian moments is not important, and will not be utilized. For the remainder of the discussion, it will be assumed that the fit is being carried out for an H_2 system in the LAB frame.

With the five velocities ($u_1 - u_5$) chosen, the program next calculates $I(\theta_j, u_i)$. The differential cross section is evaluated by the standard partial wave method (see Section 3.2),

$$I(\theta_j, u_i) = \frac{1}{k_i^2} \left| \sum_{\ell=0}^{\infty} (2\ell+1)(e^{2i\eta_\ell} - 1)P_\ell(\cos\theta_j) \right|^2 \qquad i = 1, \ldots, 5 \quad . \tag{9}$$

The η_ℓ in equation (9) are the phase shifts of the partial waves, each corresponding to a classical impact parameter

$$b = (\ell + \tfrac{1}{2})/k_i \qquad \ell = 0, \ldots, \infty; \quad i = 1, \ldots, 5 \quad . \tag{10}$$

The subscript on the wave number k signifies that the η_ℓ are also functions of the velocities, u_i. For $u_i = u_1$, the phase shifts needed for (9) are calculated using the JWKB approximation (see Section 3.2.1) by the method of Munn and Smith [2]. An accuracy of 0.002 radians

(as determined by convergence of the Gauss-Mechler quadrature [3]) was obtained for $\eta_\ell \geq 0.01$ radians. Beyond this point, the high energy eikonal method [4] was used for $0.01 \geq \eta_\ell \geq 0.001$ radians. Phase shifts smaller than 0.001 radians were not included, so that typically 150 JWKB plus 75 eikonal phase shifts were included in (9). A savings of about 20% in computation time was achieved with insignificant loss in accuracy by evaluating every fifth phase shift for $\ell > 5$, and then interpolating over ℓ by a 5th order polynomial method. Once the phase shifts have been determined, equation (9) is evaluated at each θ_j ($j = 1, \ldots, n$) needed to span the angular range of interest. Since these θ_j are independent of the u_i, the values of $P_\ell(\cos\theta_j)$ are calculated once and then stored for use in each successive evaluation of equation (9). Subsequent to the calculation of $I(\theta_j, u_1)$, the procedure is repeated for each u_i, thus yielding $I(\theta_j, u_i)$, $i = 1, \ldots, 5$, $j = 1, \ldots, n$. At this point, the theoretical cross sections are contained in an $n \times 5$ matrix with each entry corresponding to the center-of-mass intensity at the j^{th} angle and the i^{th} relative velocity.

(b) The next step in the procedure is the transformation of the intensities calculated above to the LAB system, and the subsequent velocity averaging. In performing the velocity averaging, equation (5) must be used without any approximation such as the FVA. Hence, the double integral is performed by chosing seven values of v_1 and seven values of v_2, and then making use of,

$$\langle I(\theta)\rangle = \frac{1}{N} \sum_{i=1}^{7} \sum_{j=1}^{7} P_1(v_{1_i}) P_2(v_{2_j})\, I(\theta, (v_{1_i}^2 + v_{2_j}^2)^{\frac{1}{2}}) \quad , \tag{11}$$

where

$$N = \sum_{i=1}^{7} \sum_{j=1}^{7} P_1(v_{1_i}) P_2(v_{2_j}) \tag{12}$$

is the total probability associated with the combined primary and secondary velocities. The 14 velocities are chosen such that the 49 relative velocity vectors which can be formed as $(v_{1_i}^2 + v_{2_j}^2)^{\frac{1}{2}}$ all lie between the limits u_1 and u_5. In this way, the differential cross section at relative velocity v_{ij} may be found simply by interpolation using the matrix of values determined above. This procedure then increases the $n \times 5$ matrix to an $n \times 49$ matrix, with the important difference that not only is the relative velocity v_{ij} known for each point, but also the two velocities v_i and v_j that gave rise to v_{ij}. This point is essential, since any transformation from the CM to the LAB can only be performed if these velocities are known separately. Specifically, the effective Jacobian for the CM-LAB transformation of the scattered primary beam intensity is given by [5],

$$I_{LAB}(\theta, v_1, v_2) = \frac{m_2}{m_1 + m_2} \frac{v_i}{u_i} \frac{1}{|\cos \gamma|} I_{CM}(\theta, v_{ij}) \quad , \tag{13}$$

where γ is the angle between the velocity vectors $(\vec{u}_i, \vec{v}_i)$, and m_i is the mass of particle i. The determination of the angle γ is purely a geometric problem for elastic scattering, and is facilitated by reference

to the Newton diagram shown in Figure 5.1. This kinematic diagram also indicates the relationship between the center-of-mass scattering angle, χ_{CM}, and the corresponding laboratory scattering angle, θ_{LAB}. Using these geometric relationships and (13), each of the n × 49 points is transformed to the LAB frame, that is,

$$I_{CM}(\chi_{CM_j}, v_i) \rightarrow I_{LAB}(\theta_{LAB_j}, v_1, v_2) \qquad i = 1, \ldots, 49;\ j = 1, \ldots, n \ .$$

The application of equation (11) is now straightforward, with the resulting $\langle I(\theta_j)\rangle$ representing the properly transformed and velocity averaged laboratory scattering intensity at each angle θ_j.

(c) Two further corrections must be applied to $\langle I(\theta)\rangle$ before a comparison can be made with the experimental data. First, the effects of finite angular resolution must be included, and second the calculated cross section must be scaled to match the experimental points.

As noted before, the effects of the apparatus angular resolution are accounted for by an integral over either a rectangular or a triangular function $h(\theta, \theta')$ (see Section 4.1), that is,

$$\langle\langle I(\theta)\rangle\rangle = \int_{\theta - w/2}^{\theta + w/2} \langle I(\theta)\rangle\, h(\theta, \theta')\, d\theta' \qquad (14)$$

where w is the FWHM of the distribution $h(\theta, \theta')$. Since $h(\theta, \theta')$ is a simple function, (14) could be evaluated without difficulty by summation. An optimized value for w was determined by allowing it to vary as a free parameter in some of the initial trial calculations. The average

Figure 5.1: Elastic scattering Newton diagram. The vectors $\vec{V}_1$ and $\vec{V}_2$ represent the LAB velocities of the primary (detected) and secondary beams. $\vec{V}_{CM}$ is the center-of-mass velocity which divides the relative velocity vector into $\vec{U}_1$ and $\vec{U}_2$. For a LAB scattering angle θ, the corresponding CM scattering angle is χ. The angle γ is used in the CM to LAB transformation, see equation (13).

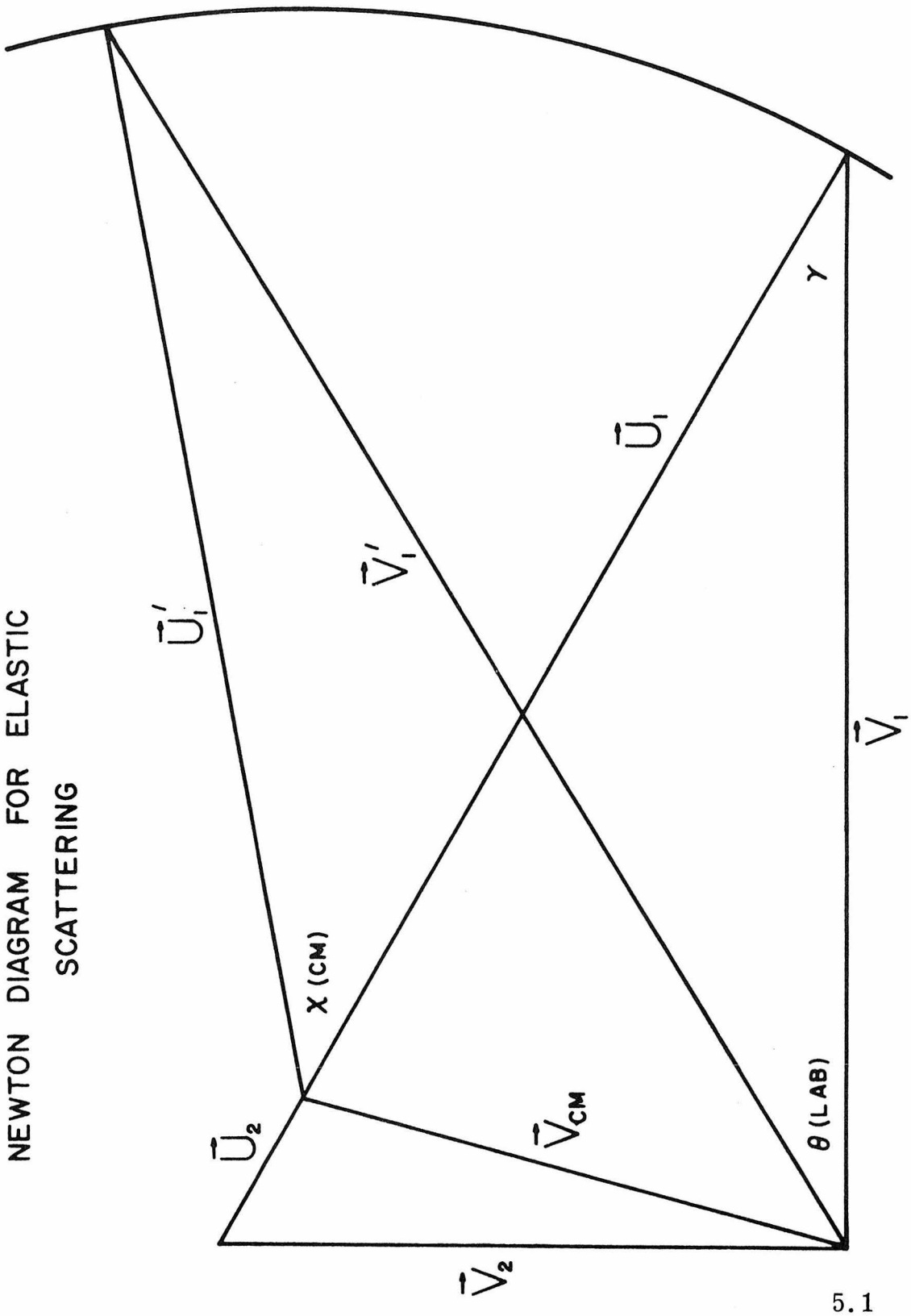
NEWTON DIAGRAM FOR ELASTIC SCATTERING
$\vec{U}_i'$
$\vec{V}_i'$
$\vec{U}_i$
$\vec{V}_i$
$\vec{U}_2$
$\vec{V}_{CM}$
$\vec{V}_2$
χ (CM)
θ (LAB)
γ

5.1

value thus determined was 2.0° with a maximum variation of ± 0.25°. This value of w = 2.0° was used in conjunction with the triangular function in all subsequent fits.

Finally then, the values of $\langle\langle I(\theta)\rangle\rangle$ computed from equation (14) must be scaled by a constant multiplicative factor (α) to bring the experimental and theoretical cross sections into vertical register with one another. The scaling parameter α is found by a simple least-squares technique using the weights given by equation (3).

The net result of steps (a) - (c) is to generate an array of points, $\langle I_{LAB}(\theta_j)\rangle$ given by

$$\langle I_{LAB}(\theta_j)\rangle = \alpha \langle\langle I_{LAB}(\theta_j)\rangle_{\Delta v}\rangle_{\Delta\theta} \quad . \tag{15}$$

The final step is the evaluation of S_0 using equations (2) and (3) and the points $\langle I_{LAB}(\theta_j)\rangle$.

Up to this point, the type of potential being fitted has not affected the procedure, except for the calculation of the phase shifts. However, the next step involves the actual variation of potential parameters and the subsequent optimization of those parameters. For the two parameter Lennard-Jones potential, a Newton's method [6] is used, while for the three parameter LJ (n, 6) and the four parameter MSV potentials, the method due to Marquardt [7] is used. The latter method is based on a non-linear estimation of parameter corrections, while the former method uses a linear approximation.

(d) The fitting of the parameters ϵ and σ for a Lennard-Jones potential is carried out by repeating steps (a) - (c) above, using

four sets of parameters; $(\epsilon, \sigma + \Delta\sigma)$, $(\epsilon, \sigma - \Delta\sigma)$, $(\epsilon + \Delta\epsilon, \sigma)$, and $(\epsilon - \Delta\epsilon, \sigma)$. The corresponding values of S ($S_1, \ldots, S_4$) are each compared with S_0 to determine the magnitude and sign of the corrections to ϵ and σ which will minimize the overall S. In general, three to four iterations of this procedure were sufficient to obtain convergence to within $\sim 1\%$ for all the fitted parameters.

The uncertainties in the fitted parameters can be estimated from the theory of linear regression [6]. From the linear theory, the joint uncertainty of all the fitted parameters is given by the hyper-ellipsoid [8],

$$S(\underset{\sim}{\beta_0} + \underset{\sim}{\Delta\beta}) = S(\underset{\sim}{\beta_0})\left[1 + \frac{p}{n-p} F(p, n-p, \alpha)\right] \quad , \tag{16}$$

where $\underset{\sim}{\beta_0}$ is the set of optimized parameters, $\underset{\sim}{\Delta\beta}$ is the deviation from $\underset{\sim}{\beta_0}$, p is the number of fitted parameters, n is the number of points used in the comparison (= number of experimental points), and $F(p, n-p, \alpha)$ is the Fisher variance ratio [9] for a confidence level of α. For example, if n = 25, p = 2, and α = 95%, F = 2.76. The variances of the individual parameters are given by,

$$\sigma_\lambda^2 = (M^{-1})_{\lambda\lambda}\, \sigma_T^2 \quad , \tag{17}$$

where λ is the fitted parameter, $(M^{-1})_{\lambda\lambda}$ is the diagonal element of the inverse of the variance-covariance matrix, and $\sigma_T^2 = (n-p)S$. In the present case, $\langle I_{LAB}(\theta)\rangle$ is a non-linear function of $\underset{\sim}{\beta}$, and (16) and (17) are not strictly applicable. However, for small deviations $\underset{\sim}{\Delta\beta}$ about the best fit $\underset{\sim}{\beta_0}$, $\langle I_{LAB}(\theta)\rangle$ may be a nearly linear function of $\underset{\sim}{\Delta\beta}$,

and the predictions of the linear theory may be accurate. In practice, $S(\underset{\sim}{\beta_0} + \underset{\sim}{\Delta\beta})$ was calculated using a truncated Taylor expansion,

$$S(\beta_0 + \Delta\beta) = \sum_{i=1}^{n} [(f_i - \hat{y}_i) f_{AA} + f_{A^2}] g_i \Delta^2 A$$

$$+ \sum_{i=1}^{n} [(f_i - \hat{y}i) f_{KK} + f_{K^2}] g_i \Delta^2 K$$

$$+ \sum_{i=1}^{n} [(f_i - \hat{y}_i) f_{AK} + f_A f_K] g_i \Delta A \Delta K \quad , \qquad (18)$$

where $f_i = \langle I_{LAB}(\theta_i) \rangle$, and $f_{xy} = \partial^2 f_i / \partial x \partial y$. Repeated test calculations showed that the terms involving f_{AK} could be ignored with no serious loss in the accuracy of the uncertainty estimates. Using (18), the two dimensional ellipse representing the joint uncertainties in A (= $k\sigma$) and K (= E/ϵ) was plotted for each fit, and it was generally found to be unskewed, implying that A and K were statistically independent parameters.

The computer routine employing the Marquardt method included internal routines to estimate both the individual and the joint uncertainties of each of the fitted parameters.

Extensive testing of all phases of the computer fitting routines for each type of potential was carried out. Each iteration using the two parameter Newton's method required approximately 180 seconds of IBM 370/165 CPU time, while a corresponding four parameter Marquardt method iteration required approximately 250 seconds. The

results of all these calculations for the systems studied here are given and discussed in the following section.

5.2 Analyzed Results

Each of the twelve differential elastic scattering cross sections measured in this study were subjected to a LJ (12, 6) analysis following the scheme just outlined. In addition, most of the systems were also subjected to an LJ (n, 6) and MSV analysis. The results of these studies (except for the H_2, $D_2 + H_2O$) have been reported previously [10-13], with the most comprehensive report reproduced in Appendix D [14]. Several of the figures from that report (Figures 3-10) and updated versions of Tables 1 and 2 are reproduced in this section, along with the previously unreported results of the H_2 and $D_2 + H_2O$ systems.

Table 2 lists the derived potential parameters for all of the Lennard-Jones type potentials used for describing the scattering. Included in that table are the values of ϵ and σ (including their 95% confidence levels), the value of n the repulsive exponent, the de Broglie wavelength, and also the estimated total cross section. This latter value was obtained from the partial wave analysis, making use of the standard relationship (see Section 3.2, equation (30)) between σ_{total} and the phase shifts η_ℓ. Two systems $H_2 + CO$ and $H_2 + CH_4$ were not subjected to the variable (n, 6) potential analysis because these systems were measured with least accuracy and so were judged less suitable for the multi-parameter analysis.

Table 3 contains the corresponding fitted parameters for the MSV potential. Here, the reported parameters are ϵ, r_m (the location

Table 2

Lennard-Jones (n, 6) Potential Parameters and Total Cross Sections

System	n	σ (A)	ϵ (meV)	λ (A)	Q (A^2)
$H_2 + O_2$	12	3.38 ± 0.03	7.7 ± 0.9	0.84	208 ± 15
	13.2	3.40 ± 0.04	7.2 ± 0.9	"	182 ± 12
	20	3.46 ± 0.04	7.6 ± 1.2	"	169 ± 15
$D_2 + O_2$	12	3.5 ± 0.2	7.3 ± 0.6	0.61	270 ± 21
	13.6	3.5 ± 0.3	7.0 ± 0.7	"	251 ± 20
	20	3.6 ± 0.2	6.7 ± 0.9	"	222 ± 20
$H_2 + SF_6$	12	4.05 ± 0.06	10.4 ± 0.5	0.81	380 ± 41
	16.2	4.12 ± 0.04	10.4 ± 0.3	"	361 ± 30
	20	4.15 ± 0.04	10.4 ± 0.8	"	335 ± 31
	12	4.15 ± 0.08	9.6 ± 0.3	"	326 ± 31
	16.3	4.18 ± 0.05	10.0 ± 0.2	"	325 ± 28
	20	4.14 ± 0.04	10.5 ± 0.2	"	313 ± 19
$D_2 + SF_6$	12	4.2 ± 0.4	10.3 ± 0.6	0.58	380 ± 32
	19.1	4.2 ± 0.2	10.3 ± 0.3	"	331 ± 30
	20	4.2 ± 0.2	10.3 ± 0.4	"	334 ± 31
$H_2 + NH_3$	9.1	3.34 ± 0.07	9.6 ± 1.2	0.87	225 ± 15
	12	3.45 ± 0.06	9.8 ± 1.4	"	260 ± 18
	9.1	3.34 ± 0.09	10.3 ± 0.7	0.56	256 ± 17
	12	3.34 ± 0.08	10.3 ± 0.8	"	255 ± 17
$D_2 + NH_3$	9.2	3.39 ± 0.08	9.1 ± 0.8	0.65	250 ± 21
	12	3.26 ± 0.07	9.1 ± 0.7	"	245 ± 21
$H_2 + H_2O$	9.6	3.50 ± 0.09	13.4 ± 0.8	0.87	235 ± 20
	12	3.48 ± 0.08	13.4 ± 0.8	"	239 ± 18
$D_2 + H_2O$	9.5	3.51 ± 0.08	13.1 ± 1.0	0.65	252 ± 20
	12	3.46 ± 0.07	13.2 ± 0.9	"	261 ± 21
$H_2 + CO$	12	3.5 ± 0.1	6.9 ± 1.5	0.84	210 ± 18
$H_2 + CH_4$	12	3.7 ± 0.2	9.9 ± 1.4	0.87	317 ± 26

Table 3

Morse-Spline-Van der Waals (MSV) Potential Parameters and Total Cross Sections

System	σ (A)	r_m (A)	ϵ (meV)	β	C_6 (eVA^6)	λ (A)	Q (A^2)
$H_2 + O_2$	3.34 ± 0.05	3.86 ± 0.05	7.2 ± 0.6	5.2 ± 0.4	64.8 ± 0.7	0.84	213 ± 19
$D_2 + O_2$	3.5 ± 0.2	4.03 ± 0.2	6.9 ± 0.9	4.8 ± 0.4	63.1 ± 0.6	0.61	291 ± 26
$H_2 + SF_6$	4.14 ± 0.02	4.63 ± 0.02	10.0 ± 0.2	6.5 ± 0.5	57.2 ± 0.3	0.81	396 ± 33
	4.16 ± 0.03	4.64 ± 0.03	10.2 ± 0.2	6.3 ± 0.6	55.9 ± 0.5	1.52	325 ± 31
$D_2 + SF_6$	4.2 ± 0.2	4.62 ± 0.2	10.4 ± 0.8	6.6 ± 0.6	54.6 ± 0.5	0.58	389 ± 38
$H_2 + NH_3$	3.42 ± 0.05	3.80 ± 0.05	9.7 ± 0.5	4.9 ± 0.4	58.2 ± 0.6	0.87	288 ± 21
	3.32 ± 0.05	3.88 ± 0.05	10.2 ± 0.5	4.8 ± 0.4	59.2 ± 0.7	1.56	242 ± 20
$D_2 + NH_3$	3.23 ± 0.05	3.77 ± 0.05	9.0 ± 0.8	4.9 ± 0.4	59.8 ± 0.7	0.65	258 ± 18
$H_2 + H_2O$	3.44 ± 0.06	3.92 ± 0.06	13.3 ± 0.9	6.12 ± 0.5	50.4 ± 0.8	0.87	253 ± 25
$D_2 + H_2O$	3.45 ± 0.06	3.88 ± 0.06	13.2 ± 0.6	6.14 ± 0.5	51.1 ± 0.8	0.65	247 ± 18

of the minimum, see Section 2.3, equation (19)), β, C_6, the de Broglie wavelength and the total cross section, determined as above.

Each of the measured systems will be discussed below.

5.2.1 $H_2, D_2 + O_2$

The measured differential elastic scattering for molecular hydrogen and deuterium by molecular oxygen are shown in Figure 5.2. The error bars are those determined experimentally based on the standard deviations measured by the on-line computer. The $D_2 + O_2$ results have been arbitrarily shifted downwards by one decade. The solid curves are the MSV theoretical cross sections, while the dotted curves are the variable n Lennard-Jones fits. Included in the $H_2 + O_2$ case is the standard LJ(12, 6) fit. The fit provided by each of these potentials is quite good over the entire angular range, with the possible exception of the 7° region in the LJ(n, 6) fit to $H_2 + O_2$. The ordinate scales (in A^2/sr) on the right of the figure were determined from the partial wave summation using the MSV potentials.

The effects of changing the reduced mass (de Broglie wavelength) are apparent in the two cross sections. While the amplitude and location of the rapid oscillations have been altered, the changes are adequately described by the fitted potentials. Thus, the change in de Broglie wavelength appears to be the only cause of these effects.

Often, the extent of agreement between the theoretical and the experimental results is difficult to assess from the logarithmic plots such as in Figure 5.2. To overcome this difficulty, the data have been replotted in Figure 5.3 by multiplying the measured intensity $I(\theta)$ by $\theta^{7/3}$, where θ is the scattering angle in radians. This has the effect of removing much of the steep angular dependence in the data, and greatly magnifying the ordinate scale without distoring the abscissa scale. The curves shown are the cross sections calculated from the LJ(12, 6) potentials. As a result of the magnified ordinate scale, some of the data points appear to be fit quite poorly. However, the deviations are usually within the error limits. The important point to notice is the accuracy with which the positions of the extrema are located. This high degree of accuracy is reflected in the confidence level associated with the value of σ in each case.

Figure 5.4 shows a comparison between the potentials determined for the H_2 and $D_2 + O_2$ systems. The curves are shown only over the range of distances actually sampled by the experiments. This range was determined by an analysis of the semi-classical deflection function. Despite the very different appearances of the differential cross sections for these two isotopes, and the very different de Broglie wavelengths, the potentials are quite similar. If, in fact, the range of uncertainties in each of the parameters were included in the plots, the resulting "bands" would overlap over the entire range shown (see Figure 5.9). Therefore, to within the experimental uncertainties, the potentials governing

Figure 5.2: Plot of the scattered intensity $I(\theta)\sin\theta$ against θ in the laboratory frame for $H_2 + O_2$ and $D_2 + O_2$. The lower curves have been shifted downwards by one decade. The points are experimental results including error bars, while the curves are theoretical fits. The solid curves are the MSV fits, and the corresponding potentials were used to establish the outer and inner ordinate scales for the $H_2 + O_2$ and $D_2 + O_2$ results, respectively. The upper dashed curve is the LJ(12, 6) fit, and the dotted curves are the LJ(n, 6) fits.

Figure 5.3: Plot of the scattered intensity $I(\theta)\theta^{7/3}$ ($\theta^{7/3}$ in radians) against θ in the laboratory frame for $H_2 + O_2$ and $D_2 + O_2$. The points correspond to the experimental data points in Figure 5.2, while the curves are the LJ(12, 6) fits. The vertical scale has been scaled arbitrarily, with the value at 1° set to 0.2.

Figure 5.4: Comparison of the intermolecular potentials over the range of distances sampled for $H_2 + O_2$ (λ = 0.84A) and $D_2 + O_2$ (λ = 0.61A), determined from the data in Figures 5.2 and 5.3.

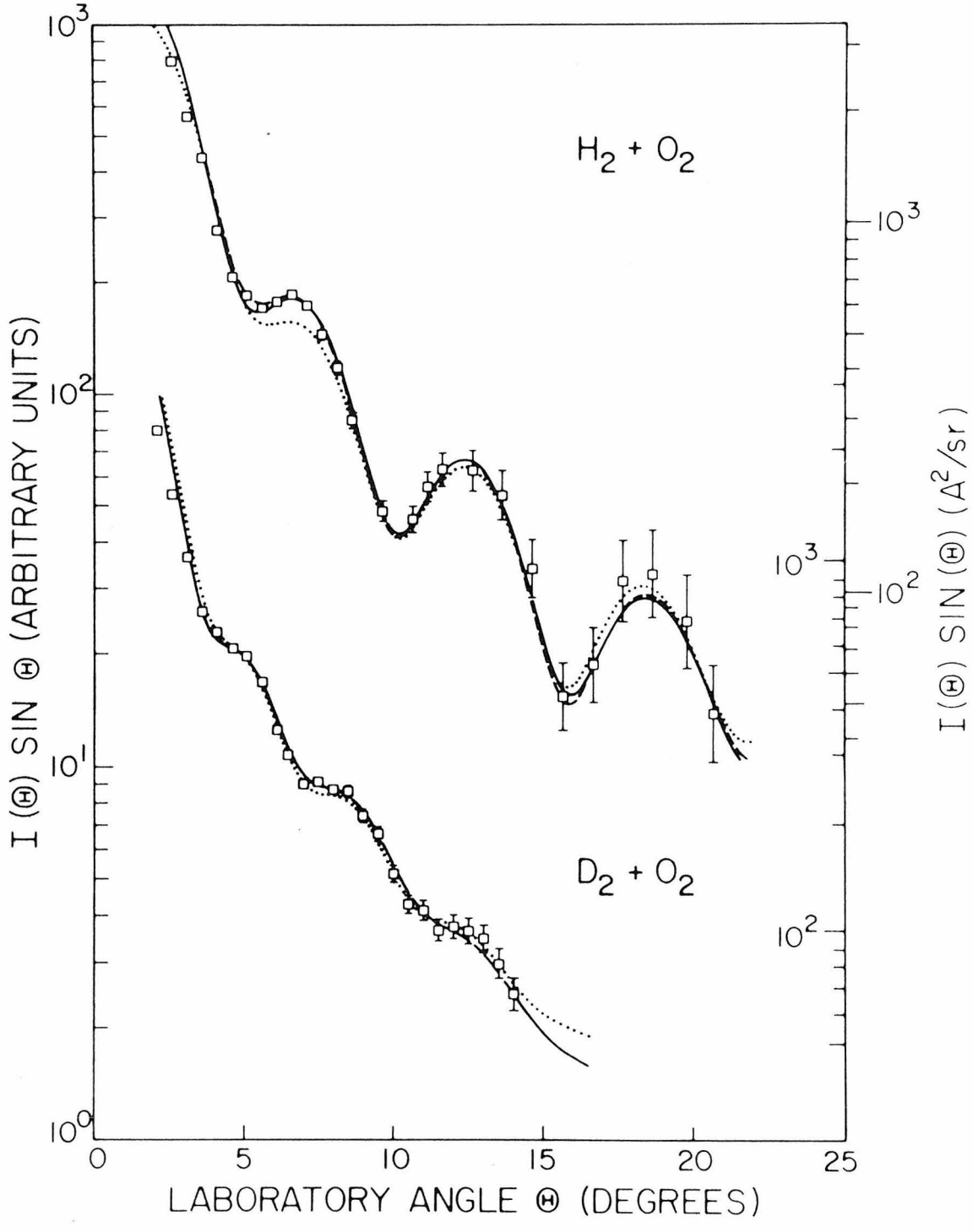
$H_2 + O_2$
$D_2 + O_2$
$I(\Theta)$ SIN Θ (ARBITRARY UNITS)
$I(\Theta)$ SIN (Θ) (A^2/sr)
LABORATORY ANGLE Θ (DEGREES)
10^0
10^1
10^2
10^3
0
5
10
15
20
25

5.2

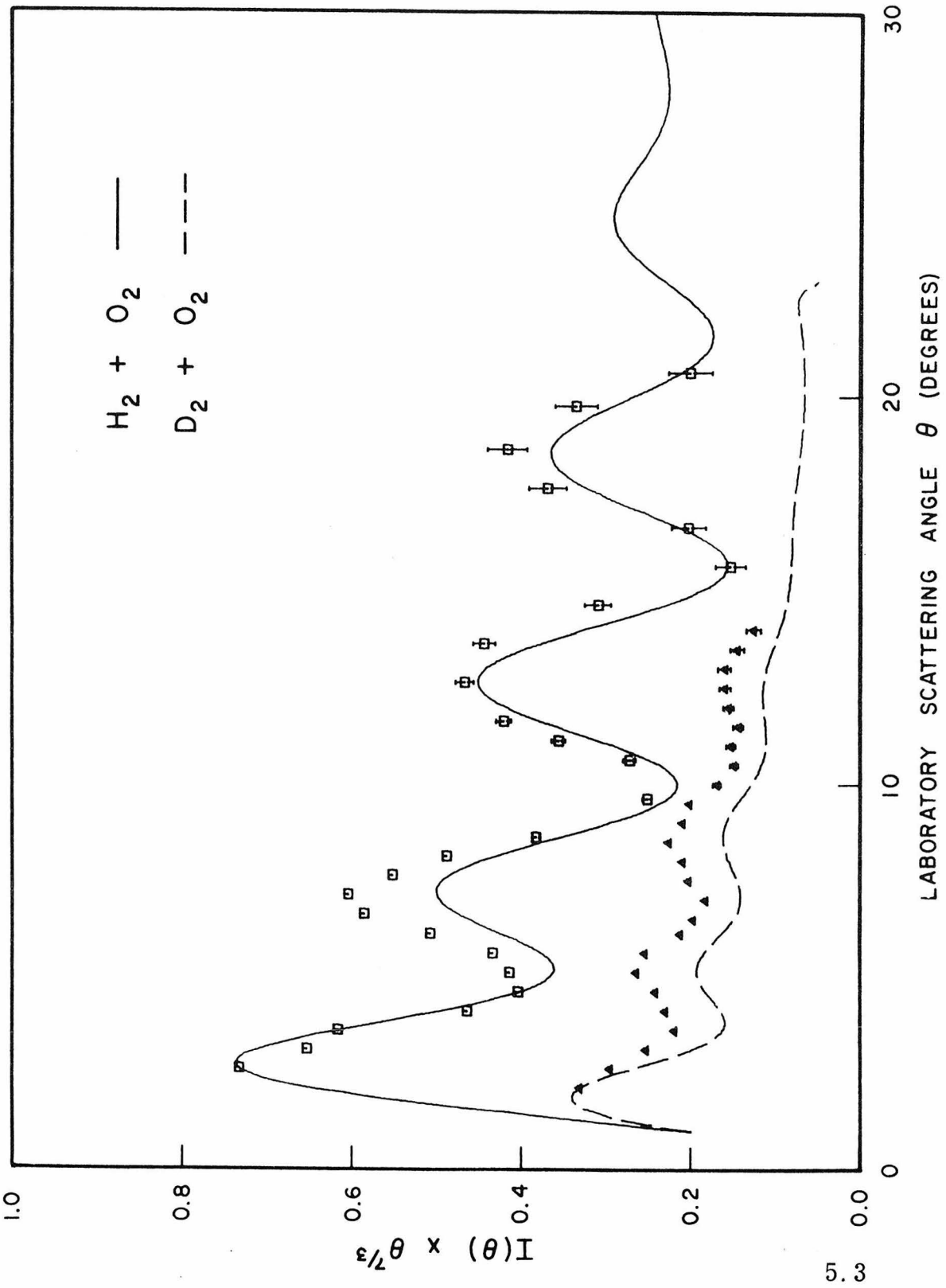
$H_2 + O_2$
$D_2 + O_2$
$I(\theta) \times \theta^{7/3}$
1.0
0.8
0.6
0.4
0.2
0.0
0
10
20
30
LABORATORY SCATTERING ANGLE θ (DEGREES)

5.3

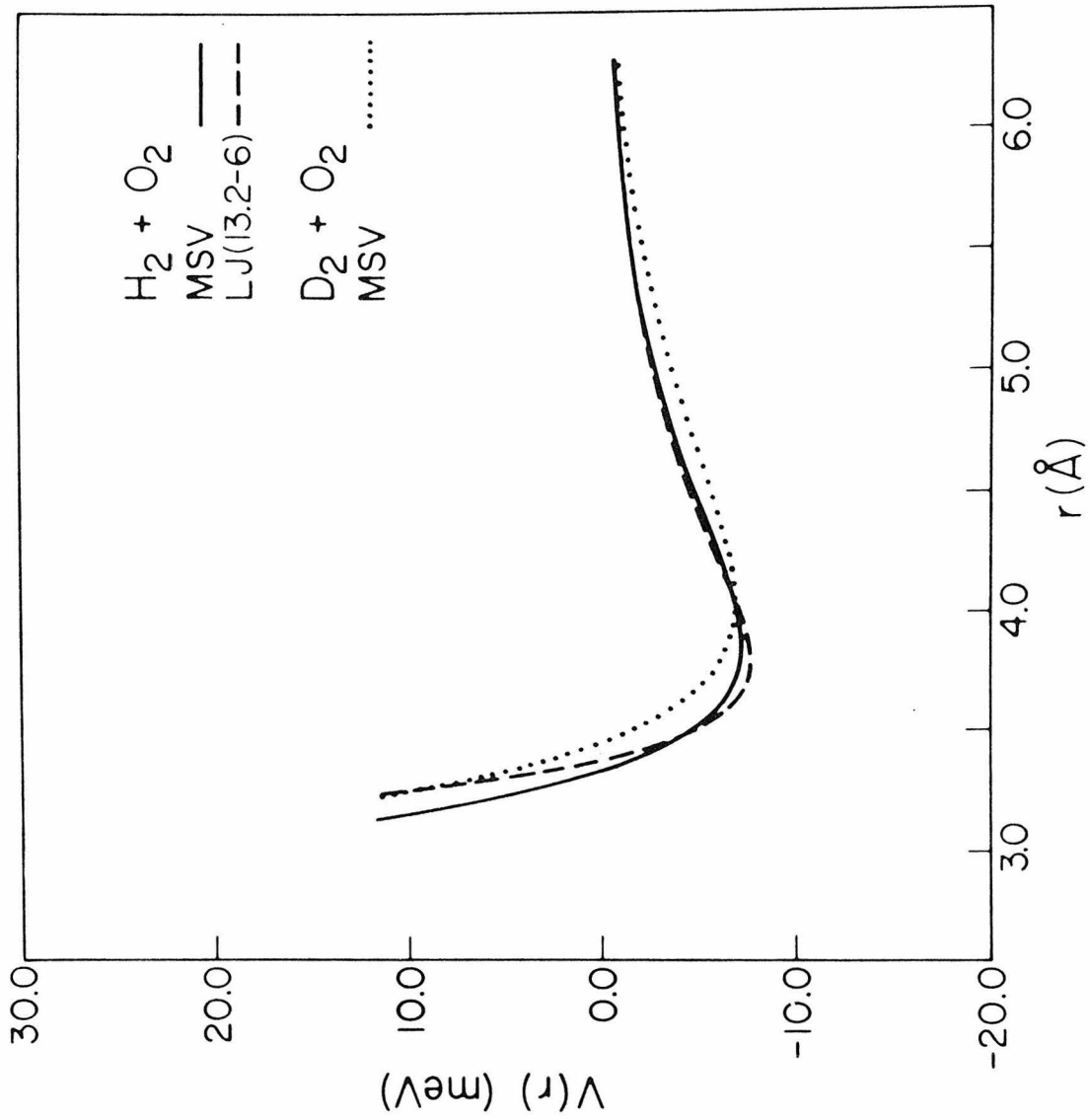
$H_2 + O_2$
MSV
LJ(13.2-6)
$D_2 + O_2$
MSV
V(r) (meV)
r(Å)
30.0
20.0
10.0
0.0
-10.0
-20.0
3.0
4.0
5.0
6.0

5.4

the scattering of H_2 and D_2 by O_2 are the same. Moreover, there is a general lack of sensitivity to the exact mathematical form of the potential used, which lends the results a higher degree of reliability.

5.2.2 H_2, D_2 + SF_6

Figure 5.5 shows the measured and calculated elastic scattering of SF_6 by H_2 and D_2. Again, the two isotopes yielded considerably different differential cross sections. As with the scattering of O_2, these results were adequately described by the several potentials used in the analysis. The reduced cross sections shown in Figure 5.6 confirm that even the LJ(12, 6) potential is capable of locating the extrema in the cross sections to within a few degrees. In addition to these results obtained using a room temperature beam of H_2, the elastic scattering of H_2 by SF_6 was also determined using a low temperature hydrogen beam. These results are shown in the lower half of Figure 5.7, and in reduced form in Figure 5.8. The effect of a 90% increase in the de Broglie wavelength is very dramatic, as the well resolved oscillations apparent at the higher energy are greatly spread out at the lower energy. In spite of this change, the same potential parameters are found to fit both cross sections equally well.

One further experiment was performed using these two collision partners. A beam of low temperature (77°K) pure para-H_2 was scattered by SF_6 under the same conditions as the above mentioned experiment. Since para-H_2 at this temperature is

essentially 100% in the J = 0 ground notational state, it is an exactly spherical molecule. The results of this study were identical with the results of the normal -H_2 + SF_6 scattering, and so are not shown separately.

Figure 5.9 displays the various potentials determined from the H_2 and D_2 + SF_6 data. The cross hatched area represents the band generated when the parameter uncertainties are included in the plot of the H_2 + SF_6 MSV potential. If the corresponding bands were plotted for each of the potentials, they would overlap over the full range of distances sampled by these experiments.

5.2.3 H_2, D_2 + NH_3

The results of the elastic scattering of thermal H_2 and D_2 by NH_3 are given in Figure 5.10. These results appear similar to the H_2, D_2 + O_2 cross sections, although the amplitudes of the rapid oscillations in the D_2 + NH_3 data are more pronounced. Also of interest is the inability of any of the potentials to account for the reduced amplitude of the first oscillation at about 5° in both the H_2 and the D_2 data.

As with the SF_6 system, the scattering of NH_3 was also measured using a low temperature beam of hydrogen molecules. The results of that study are shown in the upper half of Figure 5.7. Once again, a dramatic change in the differential cross section is apparent as a result of the ($\sim$80%) increase in the de Broglie wavelength. The reduced cross sections for both the room temperature H_2 and D_2 scattering are depicted in Figure 5.11,

Figure 5.5: Differential scattering results for (room temperature) $H_2 + SF_6$ and $D_2 + SF_6$ collisions. Explanation of the curves is the same as Figure 5.2.

Figure 5.6: Reduced differential cross section plots for (room temperature) $H_2 + SF_6$ and $D_2 + SF_6$. Explanation of the plot is the same as for Figure 5.3.

Figure 5.7: Low temperature results for $H_2 + NH_3$ and $H_2 + SF_6$ collisions. Explanation of the curves is given in Figure 5.2. The LJ(n, 6) curve for $H_2 + NH_3$ was indistinguishable from the MSV curve, and was not plotted. Results using para-hydrogen + SF_6 were identical to those shown for normal-hydrogen.

Figure 5.8: The reduced cross section results corresponding to to the lower curve in Figure 5.7 for the low temperature $H_2 + SF_6$ scattering. Explanation is as for Figure 5.3.

Figure 5.9: Potential plots comparing LJ and MSV results over the range of distances sampled. The curves determined from the $H_2 + SF_6$ with $\lambda = 0.81$A and $\lambda = 1.52$A were indistinguishable to within plotting accuracy. The cross hatching indicates the range of error of the $H_2 + SF_6$ MSV potential as determined by the parameter accuracies.

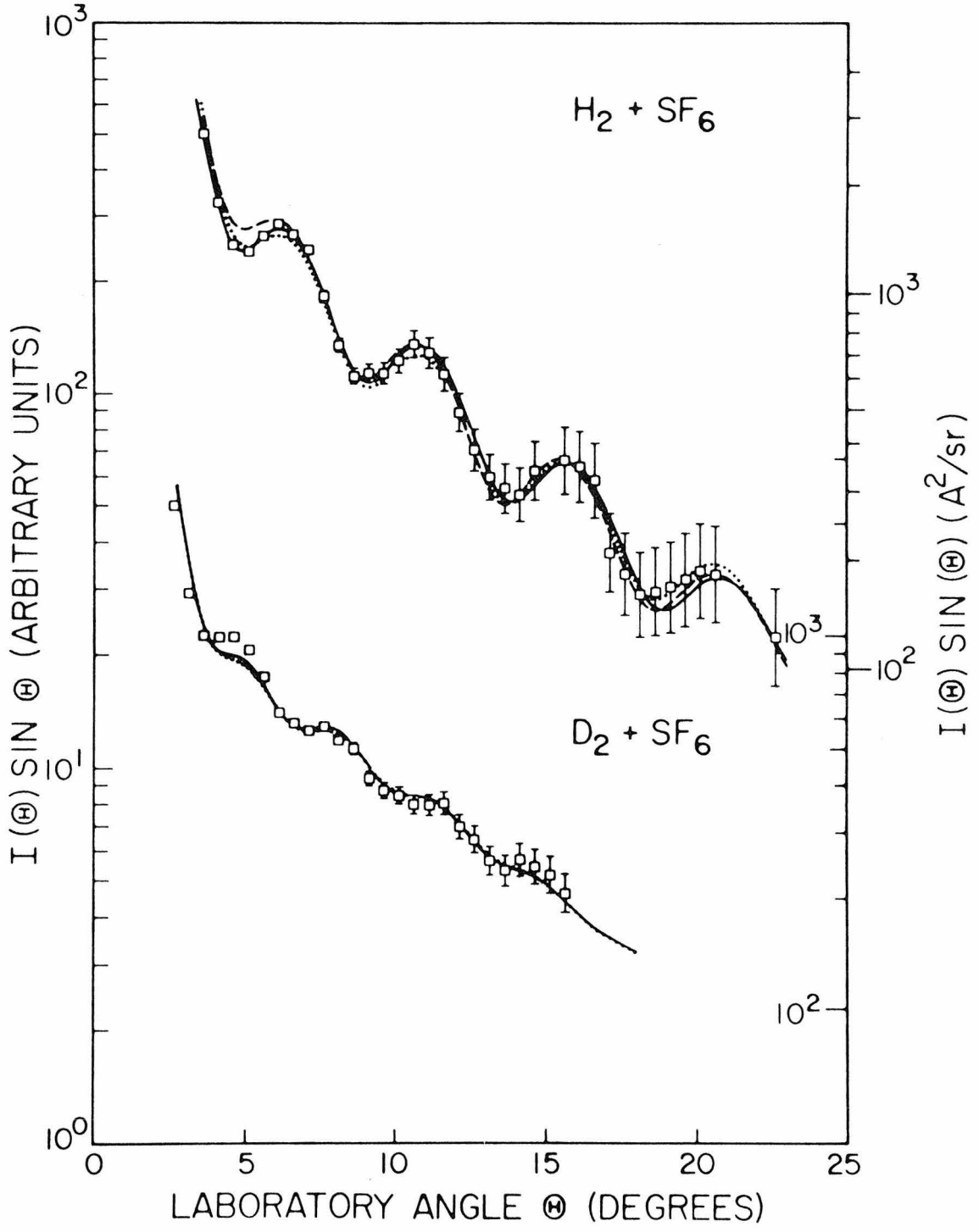
$H_2 + SF_6$
$D_2 + SF_6$
$I(\Theta) \sin \Theta$ (ARBITRARY UNITS)
$I(\Theta) \sin(\Theta)$ (A^2/sr)
LABORATORY ANGLE Θ (DEGREES)
10^3
10^2
10^1
10^0
0
5
10
15
20
25

5.5

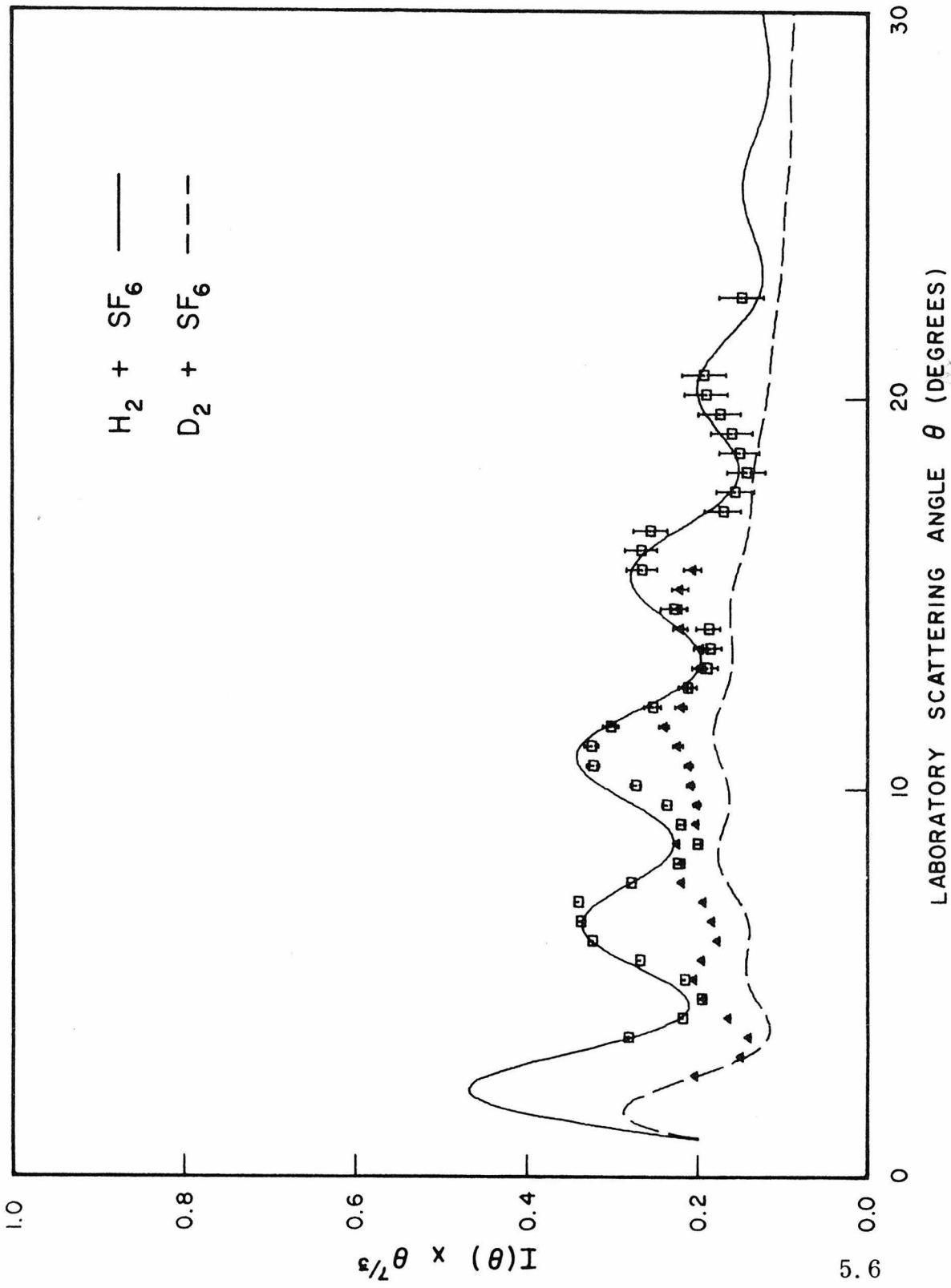
H_2 + SF_6 ——
D_2 + SF_6 – – –
$I(\theta) \times \theta^{7/3}$
1.0
0.8
0.6
0.4
0.2
0.0
0
10
20
30
LABORATORY SCATTERING ANGLE θ (DEGREES)

5.6

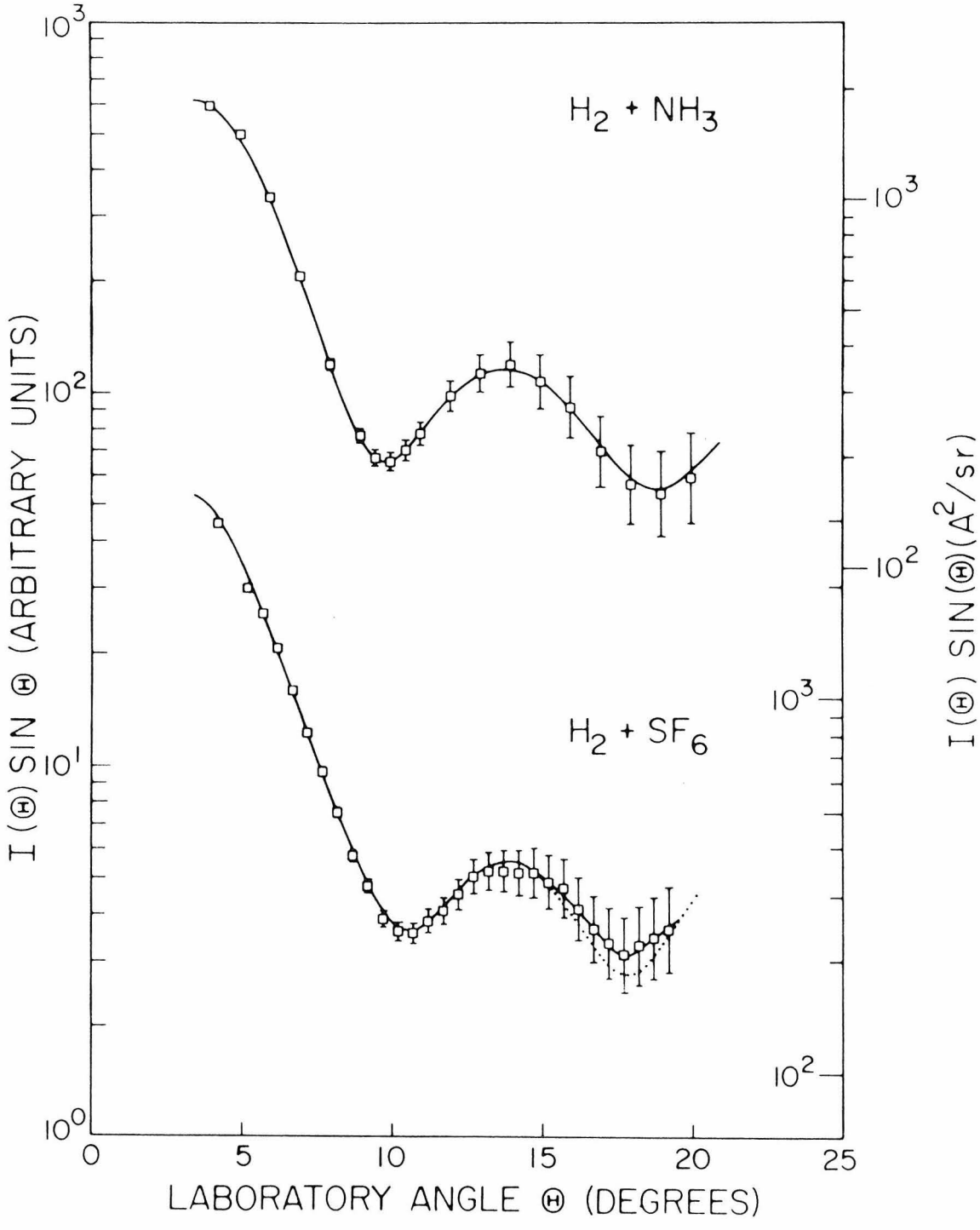
$H_2 + NH_3$
$H_2 + SF_6$
$I(\Theta) \sin \Theta$ (ARBITRARY UNITS)
$I(\Theta) \sin(\Theta)(A^2/sr)$
LABORATORY ANGLE Θ (DEGREES)
10^0
10^1
10^2
10^3
0
5
10
15
20
25

5.7

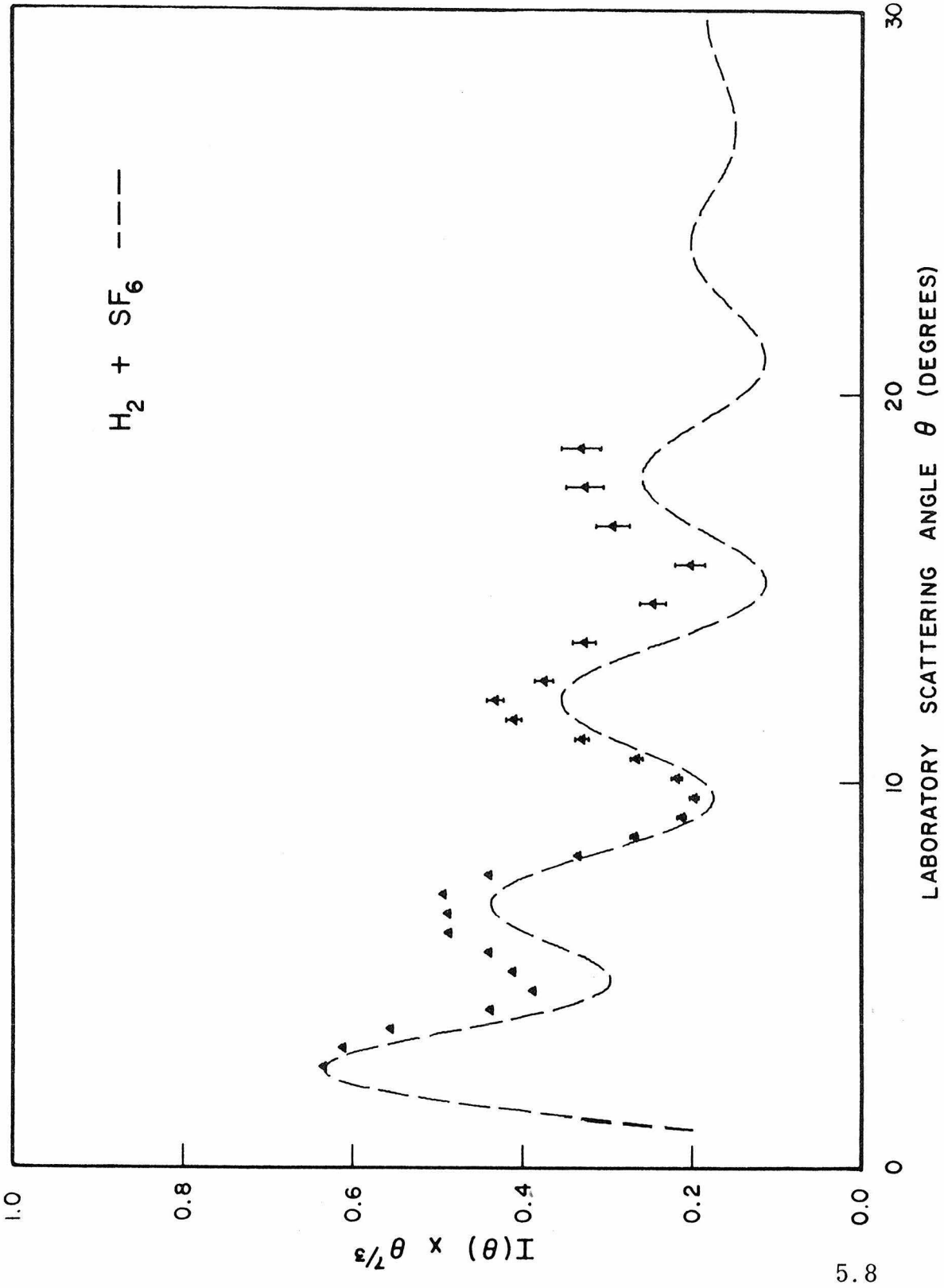
$H_2 + SF_6$ ---
$I(\theta) \times \theta^{7/3}$
1.0
0.8
0.6
0.4
0.2
0.0
0
10
20
30
LABORATORY SCATTERING ANGLE θ (DEGREES)

5.8

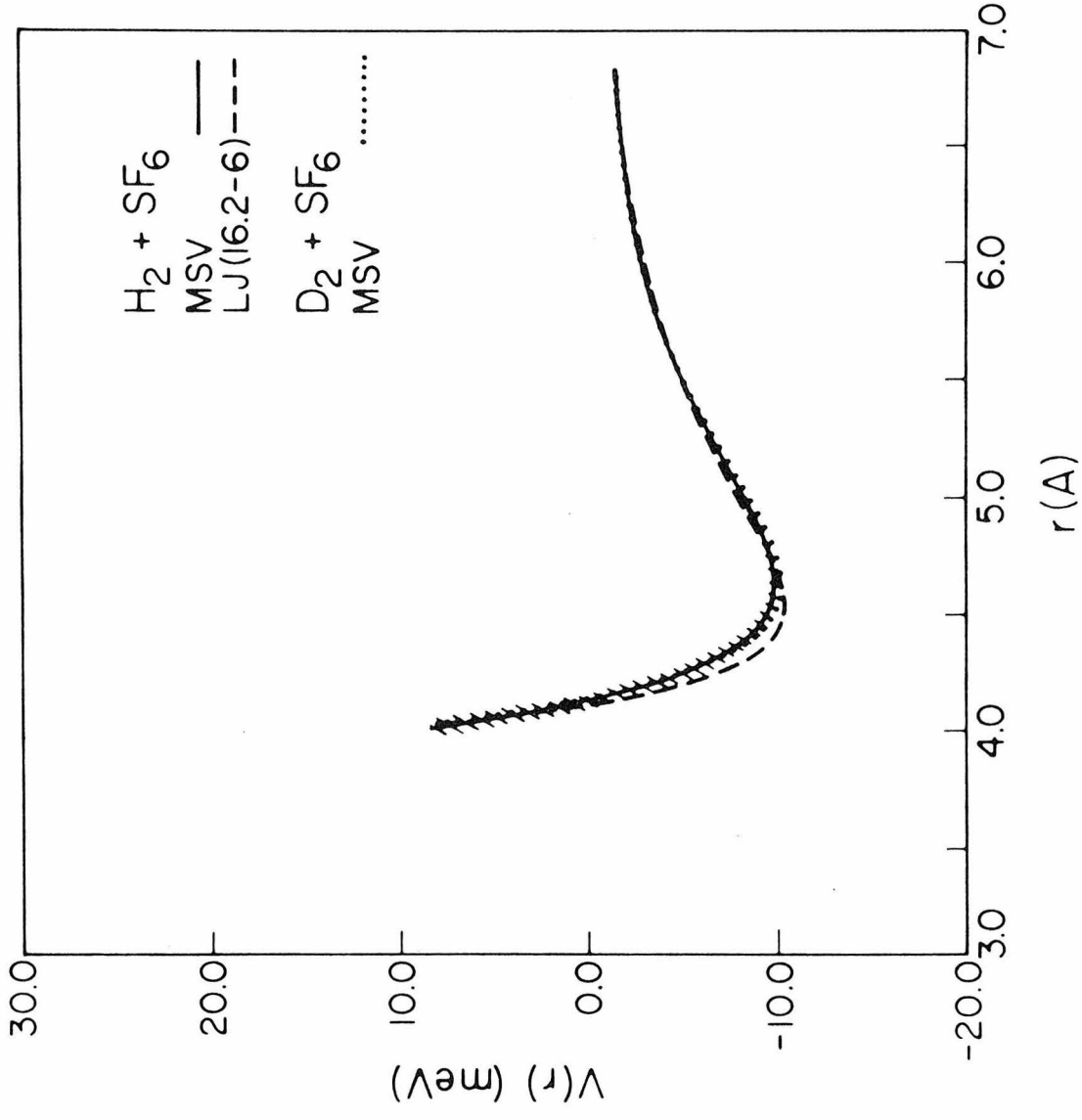
H_2 + SF_6
MSV
LJ(16.2-6)
D_2 + SF_6
MSV
V(r) (meV)
30.0
20.0
10.0
0.0
-10.0
-20.0
3.0
4.0
5.0
6.0
7.0
r(A)

5.9

while the corresponding low temperature results are shown in Figure 5.12. The simple LJ(12, 6) potential continues to provide a good fit between the experiment and theory so far as the extrema positions are concerned.

Three of the fitted potential curves are compared in Figure 5.13, where they are seen to be in reasonable agreement. The potentials determined from the low temperature scattering results were indistinguishable from those found by analyzing the thermal data.

It is worth noting that ammonia has a permanent dipole moment of approximately 1.5D. While the rate of inversion of the nitrogen through the plane is rapid ($\tau \approx 4 \times 10^{-11}$ sec), the collision time between a thermal velocity H_2 molecule and NH_3 is much shorter ($\tau \approx 10^{-13}$ sec). Hence, the effective potential between these two molecules may exhibit additional long-range attractive contributions.

The system $H_2 + NH_3$ has recently been studied by Bickes et al. [15] using a slightly different scattering geometry. An out-of-plane detector is employed to measure the scattering as a function of ϕ, with θ fixed at 0° (see Figure 1, Appendix D). Their measurements cover the angular region from 2° to 24° (in the laboratory frame), and show a good overall qualitative agreement with the present results. Their attempts at using a LJ(12, 6) potential to characterize the measured scattering met with only limited success. While a potential with $\epsilon \cong 8.6$ meV and $\sigma \simeq 3.31$A gave the proper extrema locations, no combination of parameters

Figure 5.10: Differential scattering results for (room temperature) $H_2 + NH_3$ and $D_2 + NH_3$ collisions. Explanation of the curves as for Figure 5.2. The LJ(12, 6) fits were indistinguishable from the LJ(n, 6) ones, and were not plotted.

Figure 5.11: Reduced cross section results corresponding to the data shown in Figure 5.10. See Figure 5.3 for an explanation of the curves.

Figure 5.12: Reduced cross section results for the low temperature $H_2 + NH_3$ scattering shown in the upper curve of Figure 5.7. Note the vertical scale change.

Figure 5.13: Comparison of the intermolecular potentials for $H_2 + NH_3$ (λ = 0.87A) and $D_2 + NH_3$ (λ = 0.65A). Explanation of the curves is given in Figure 5.4. The corresponding curves for $H_2 + NH_3$ at λ = 1.56A are identical to those at λ = 0.87A.

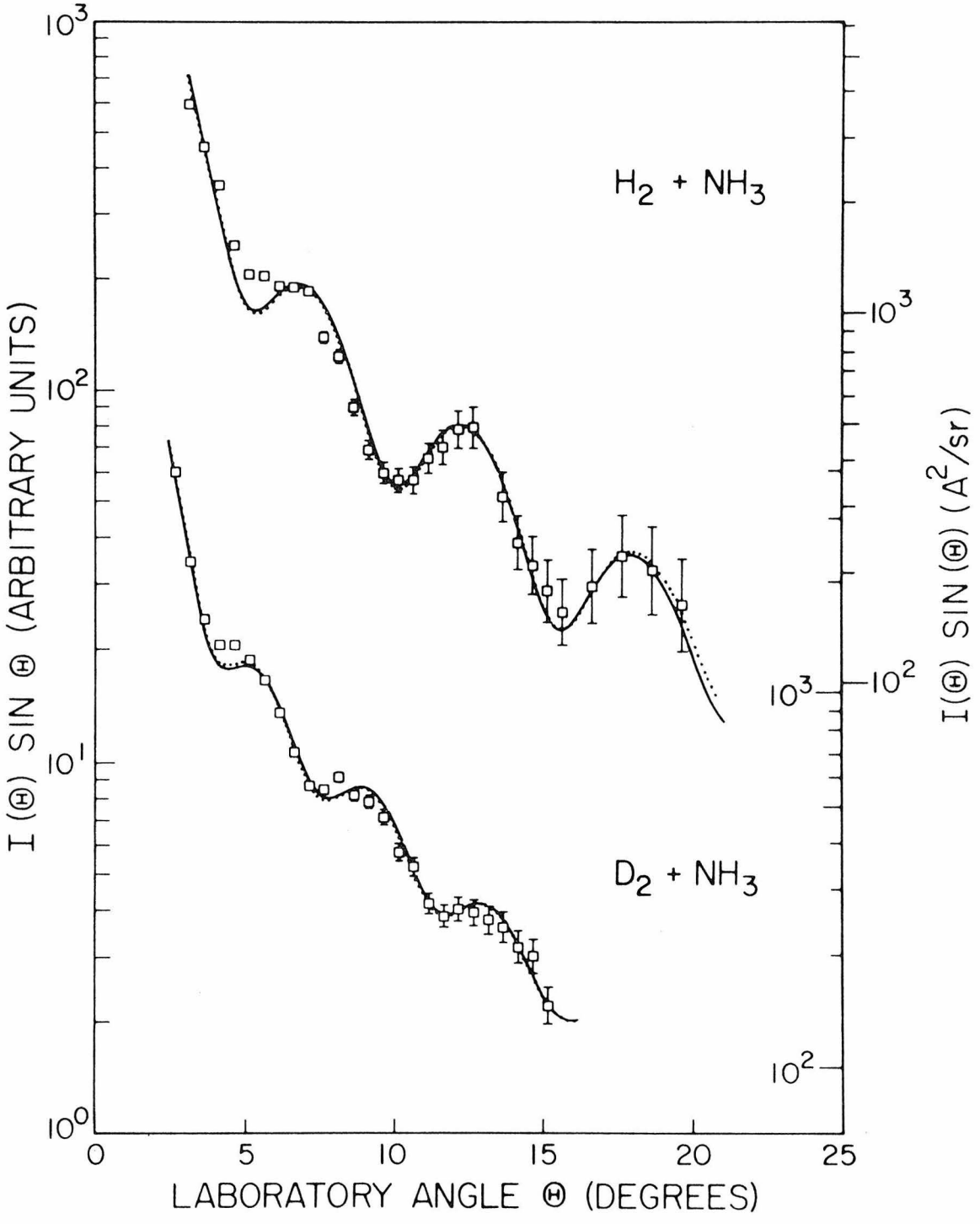
$H_2 + NH_3$
$D_2 + NH_3$
I (Θ) SIN Θ (ARBITRARY UNITS)
I(Θ) SIN (Θ) (A^2/sr)
LABORATORY ANGLE Θ (DEGREES)
10^3
10^2
10^1
10^0
0
5
10
15
20
25

5.10

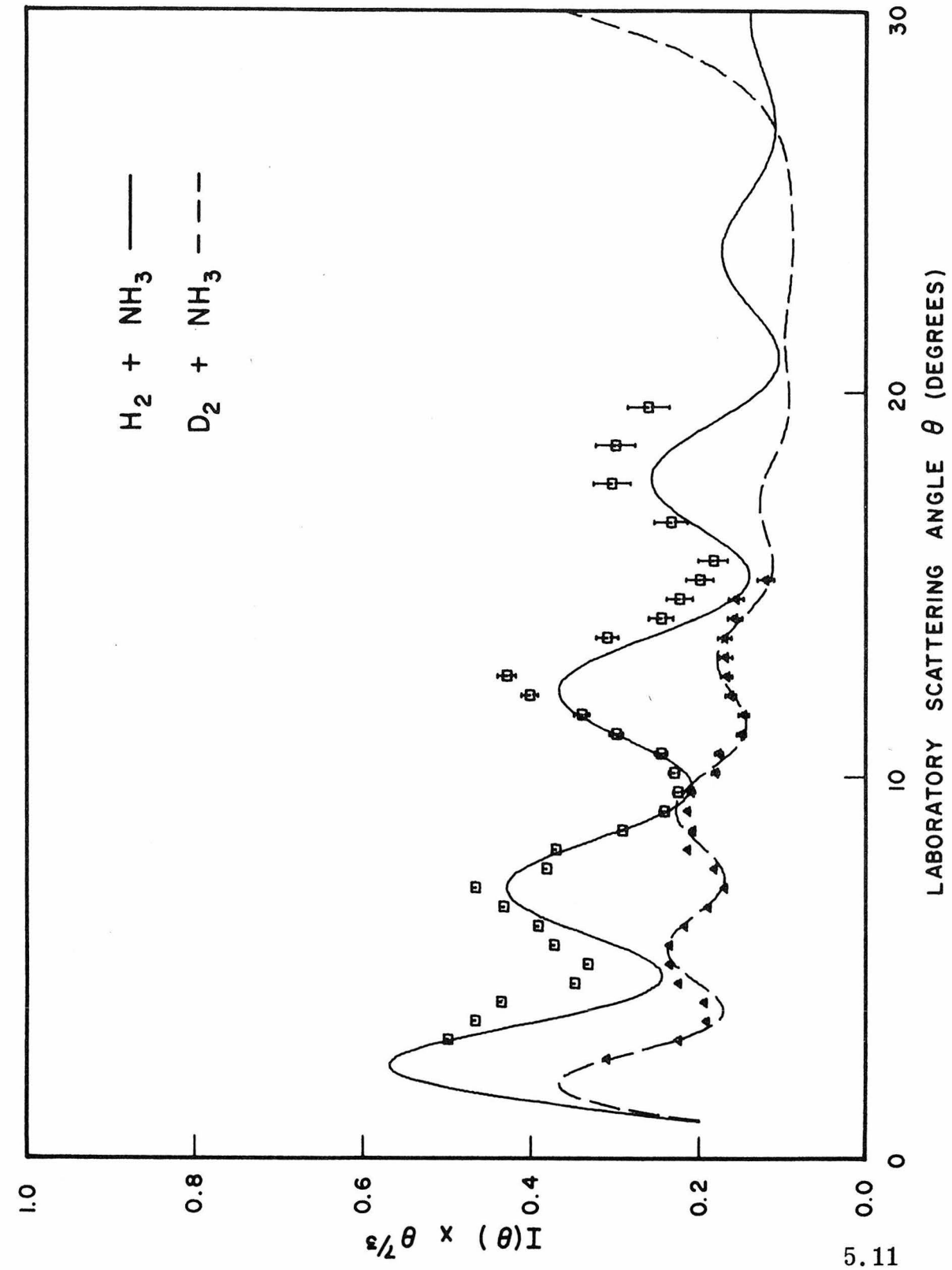
$H_2 + NH_3$ ——
$D_2 + NH_3$ – – –
$I(\theta) \times \theta^{7/3}$
1.0
0.8
0.6
0.4
0.2
0.0
0
10
20
30
LABORATORY SCATTERING ANGLE θ (DEGREES)

5.11

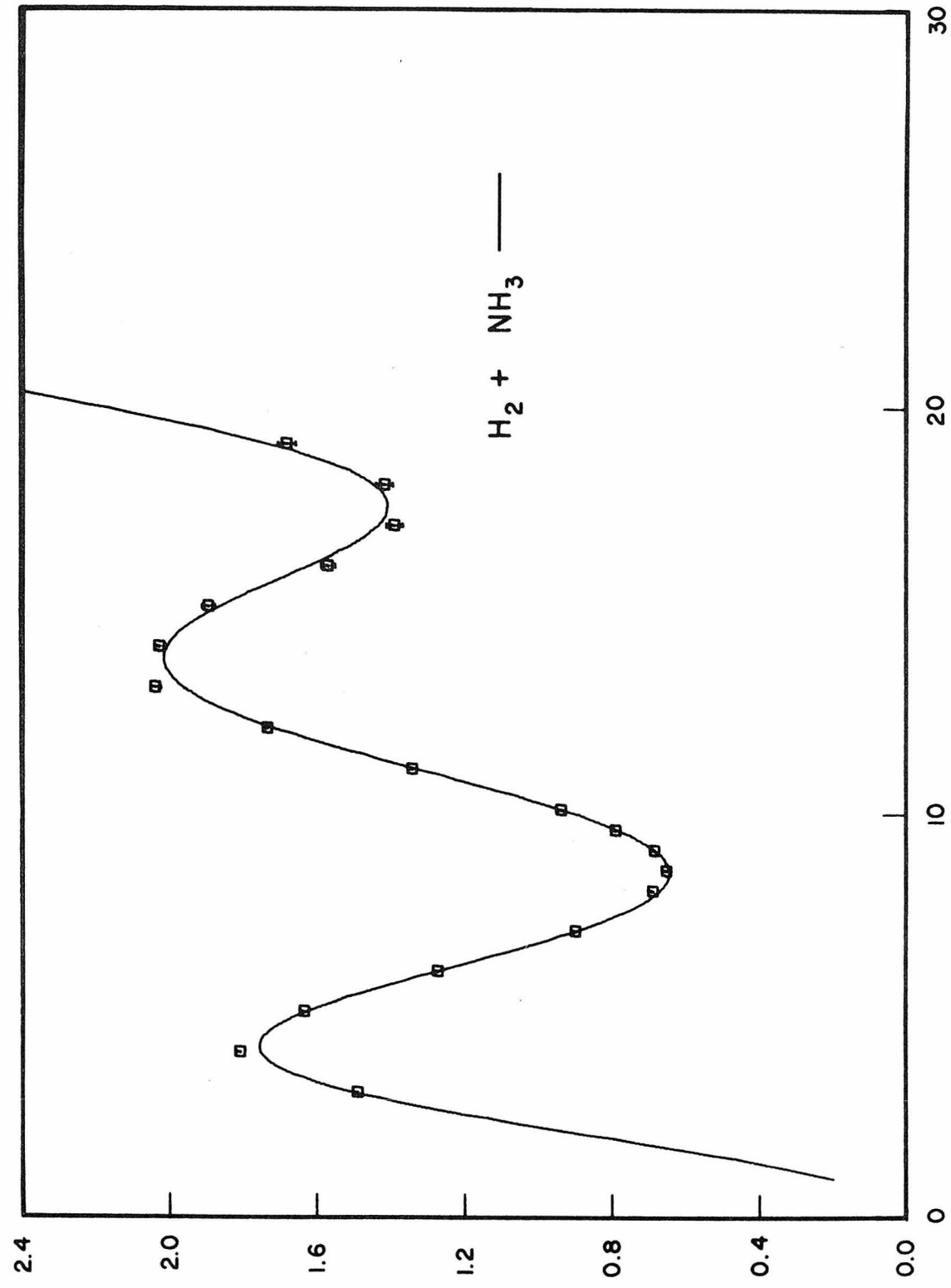
$H_2 + NH_3$ ——
$I(\theta) \times \theta^{7/3}$
2.4
2.0
1.6
1.2
0.8
0.4
0.0
0
10
20
30
LABORATORY SCATTERING ANGLE θ (DEGREES)

5.12

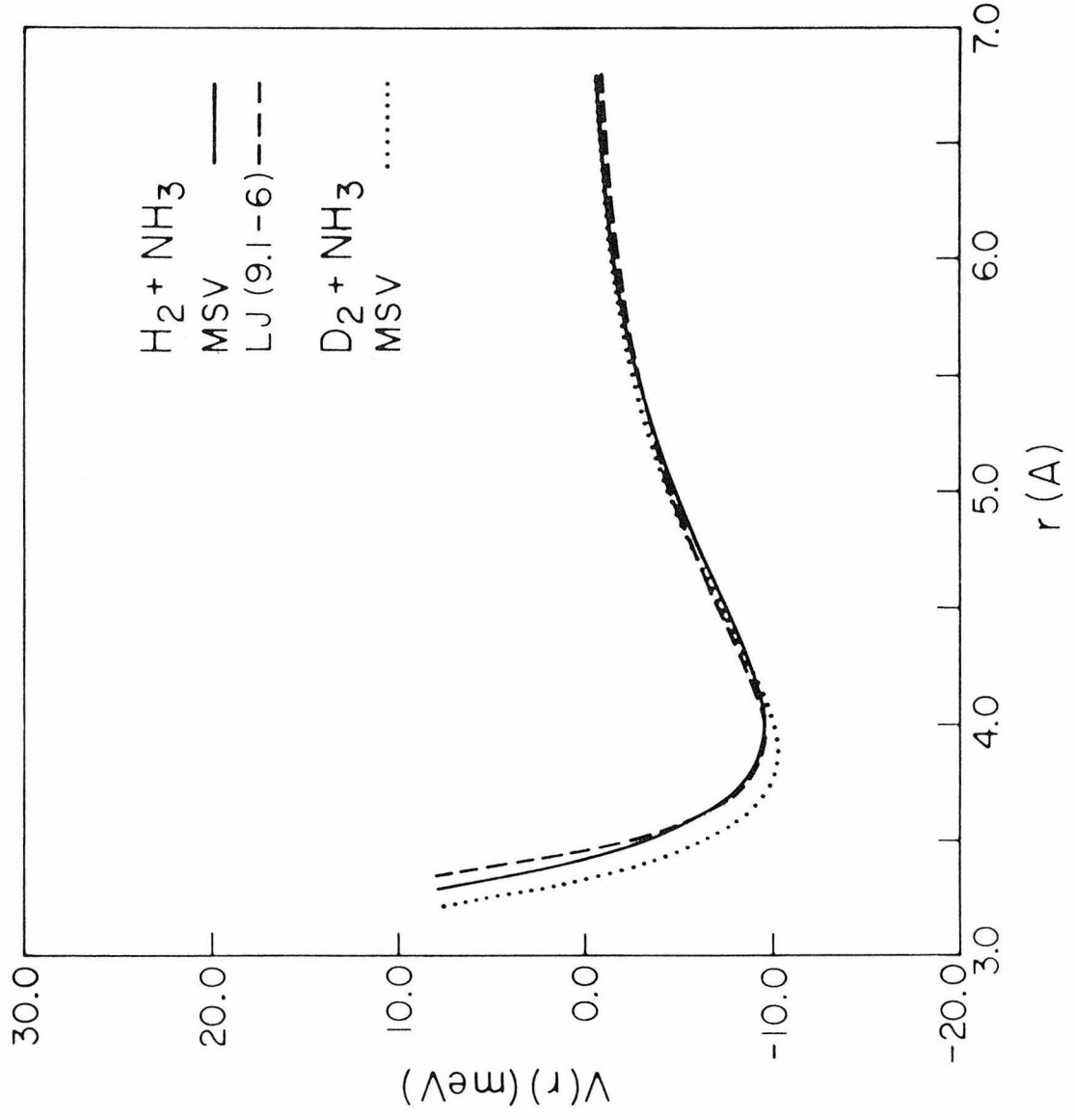
H_2 + NH_3
MSV
LJ (9.1-6)
D_2 + NH_3
MSV
V(r) (meV)
30.0
20.0
10.0
0.0
-10.0
-20.0
3.0
4.0
5.0
6.0
7.0
r (A)

5.13

was found that could adequately match the observed amplitudes. Bickes et. al. do not speculate as to the reason for this failure of a spherically symmetric potential to describe their data, especially in the light of the present success with the same system.

5.2.4 H_2, D_2 + H_2O

Figure 5.14 shows the results of the differential elastic scattering measurements made of H_2 and D_2 with H_2O. Despite the very nearly identical reduced masses of the H_2O and NH_3 systems, the observed scattering is clearly not the same. This would indicate that marked differences exist in the intermolecular potentials governing the collisions of the two systems. The studies of Bickes et. al. [15] show the H_2O and NH_3 results to be very similar, especially as regards the spacings of the rapid oscillations. A comparison of the reduced cross sections for the H_2O systems shown in Figure 5.15 with those of the NH_3 system (Figure 5.11) strongly contradict that result (the present results on the H_2 + H_2O system may be in some doubt, see Section 5.4). As shown by the results in Tables 2 and 3, the potentials for the H_2O systems have both larger σ values (also r_m) and larger ϵ values than do the corresponding NH_3 systems.

The derived potentials for the H_2 and D_2 + H_2O interactions are shown in Figure 5.16. As in all previous cases, the several potentials plotted are in close agreement with one another, and to within the measured accuracy, are the same for the H_2 and D_2

isotopes. When compared with the NH_3 potentials, it is clear that some important differences exist. These differences are not unexpected, as H_2O has a larger dipole moment, 1.85D, and is also of considerably different dimensions and geometry.

In spite of their importance in the understanding of solubilities and liquid state behavior, little is known about the intermolecular potentials involving water [17, 18]. Studies of the $H_2O + H_2O$ scattering by Bickes et. al. [16] have given some preliminary indications that the water molecule interactions may be more complex than assumed here. Specifically, anomalous low angle behavior is evident which cannot be accounted for by any simple theoretical model. Further investigations of this and other H_2O systems are needed to remove much of the present uncertainty.

5.2.5 $H_2 + CH_4$, CO

The final two systems studied were $H_2 + CH_4$ and $H_2 + CO$. Neither of these systems was studied using D_2, principally because of an unexplained lack of reproducibility in the measured H_2 data. This lack of reliability was also the reason that only LJ(12, 6) fits were attempted in the analysis. Both cross sections are shown in Figure 5.17, with the reduced $H_2 + CH_4$ and CO cross sections given in Figures 5.18 and 5.19, respectively. The lack of quality in the data is also reflected in the range of uncertainties associated with the LJ(12, 6) parameters given in Table 2.

These two systems have been studied in total cross section experiments [19, 20]. The results of the total cross section

Figure 5.14: Differential elastic scattering results for $H_2 + H_2O$ and $D_2 + H_2O$. Explanation of the curves is given in Figure 5.2.

Figure 5.15: Reduced cross section results corresponding to the data of Figure 5.14. The plotted curves are explained in Figure 5.3.

Figure 5.16: Comparison of the intermolecular potentials for $H_2 + H_2O$ (λ = 0.87A) and $D_2 + H_2O$ (λ = 0.65A). Explanation of the curves is given in Figure 5.4.

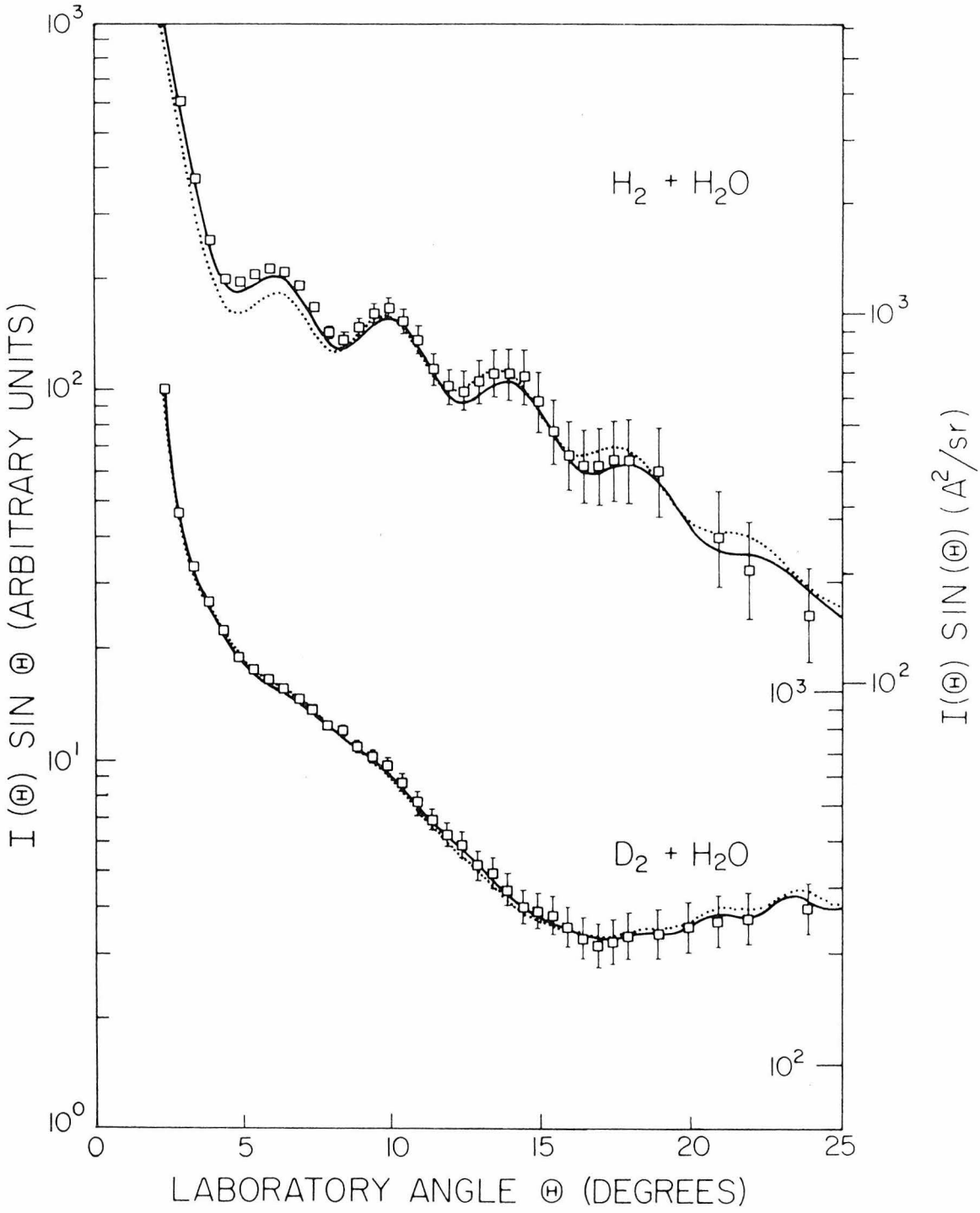
$H_2 + H_2O$
$D_2 + H_2O$
10^3
10^2
10^1
10^0
10^3
10^2
0
5
10
15
20
25
I (Θ) SIN Θ (ARBITRARY UNITS)
I(Θ) SIN(Θ) (A^2/sr)
LABORATORY ANGLE Θ (DEGREES)

5.14

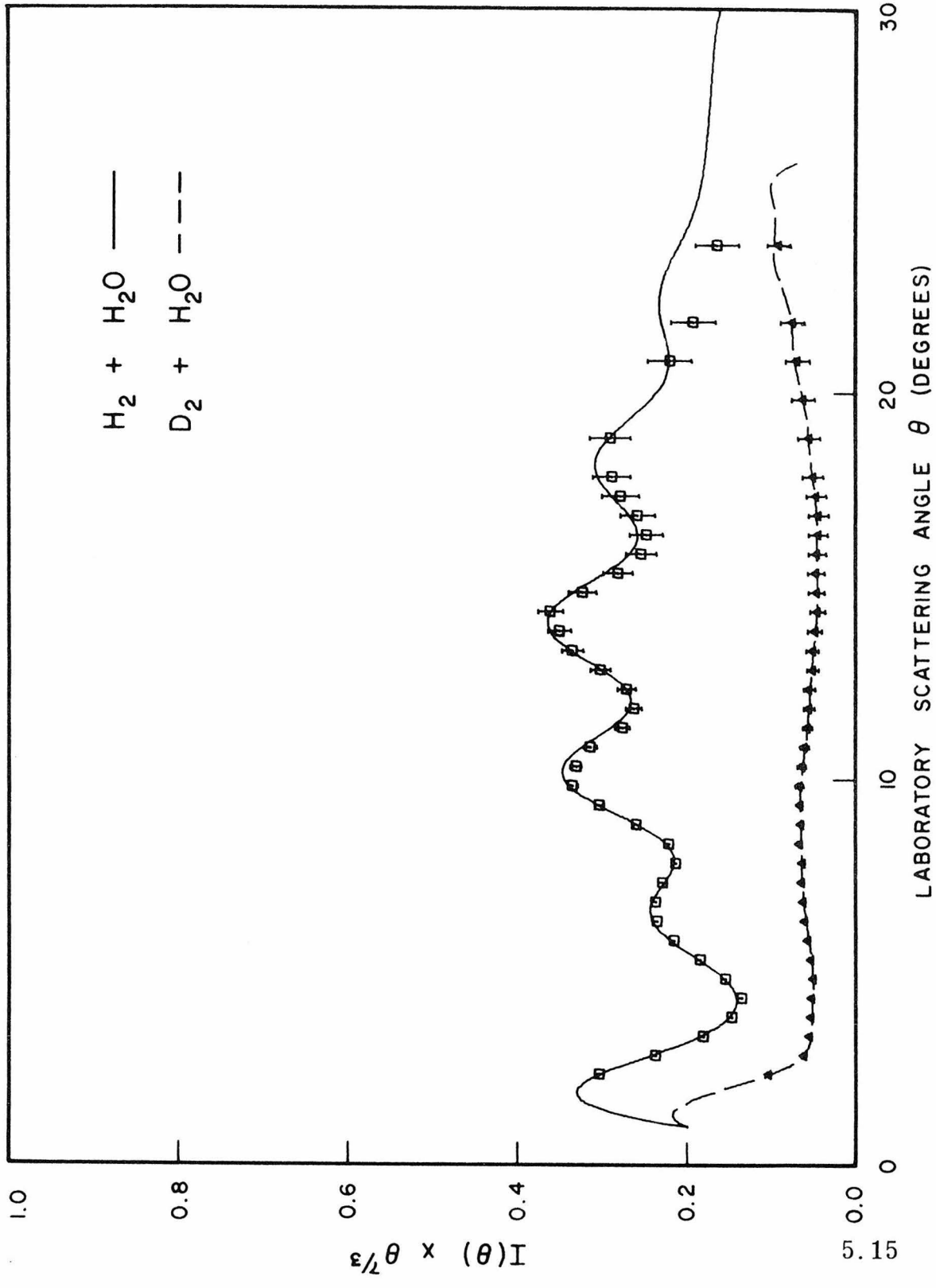
$H_2 + H_2O$ ——
$D_2 + H_2O$ – – –
$I(\theta) \times \theta^{7/3}$
1.0
0.8
0.6
0.4
0.2
0.0
0
10
20
30
LABORATORY SCATTERING ANGLE θ (DEGREES)

5.15

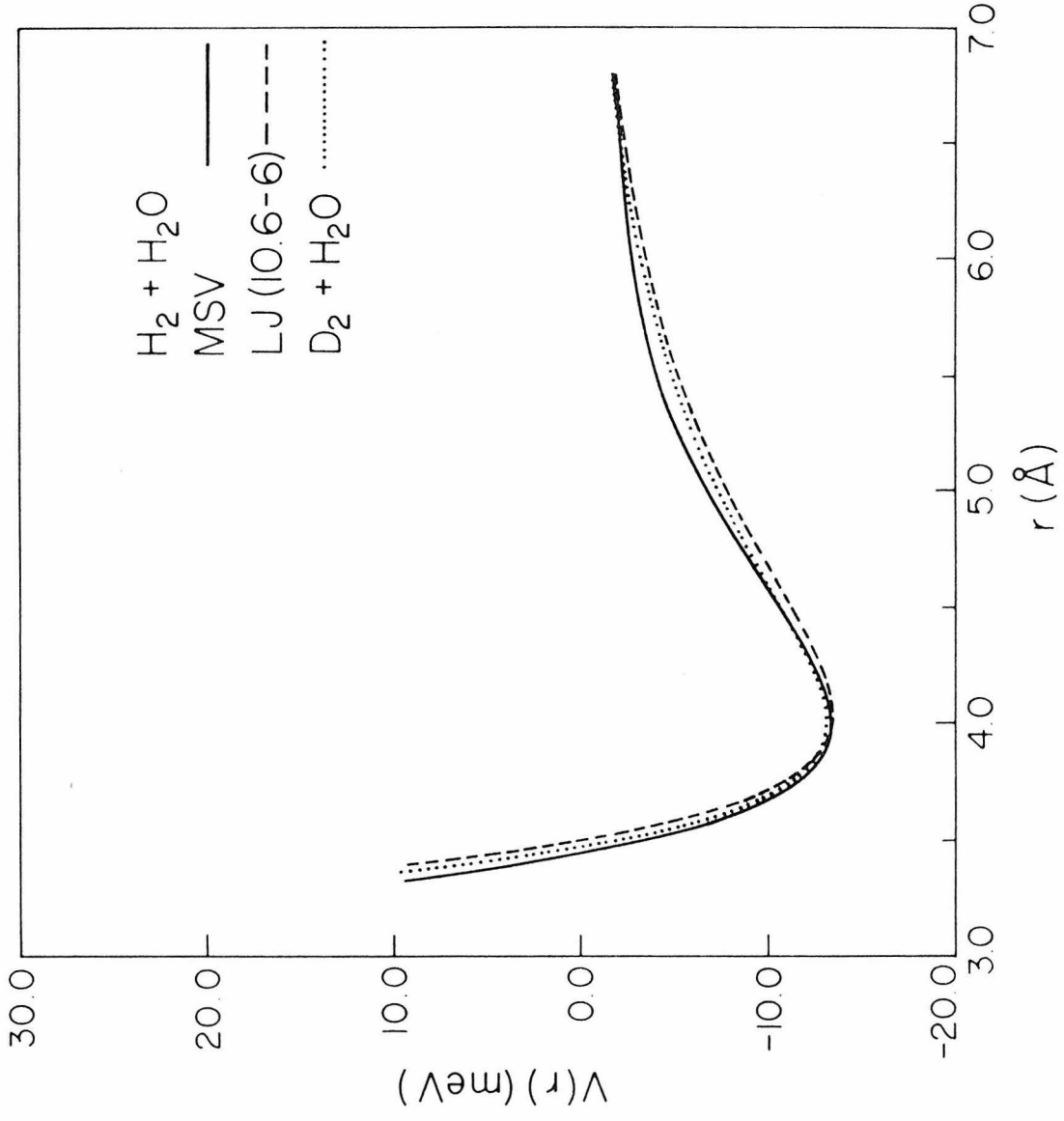
$H_2 + H_2O$
MSV
LJ (10.6-6)
$D_2 + H_2O$
V(r) (meV)
r (Å)
30.0
20.0
10.0
0.0
-10.0
-20.0
3.0
4.0
5.0
6.0
7.0

5.16

Figure 5.17: Differential scattering results for the $H_2 + CH_4$ and $H_2 + CO$ collisions. Only LJ(12, 6) fits were attempted, and they are shown by the solid curves.

Figure 5.18: Reduced cross section plot of the $H_2 + CH_4$ scattering results given in the upper half of Figure 5.17.

Figure 5.19: Reduced cross section plot of the $H_2 + CO$ scattering results given in the lower half of Figure 5.17.

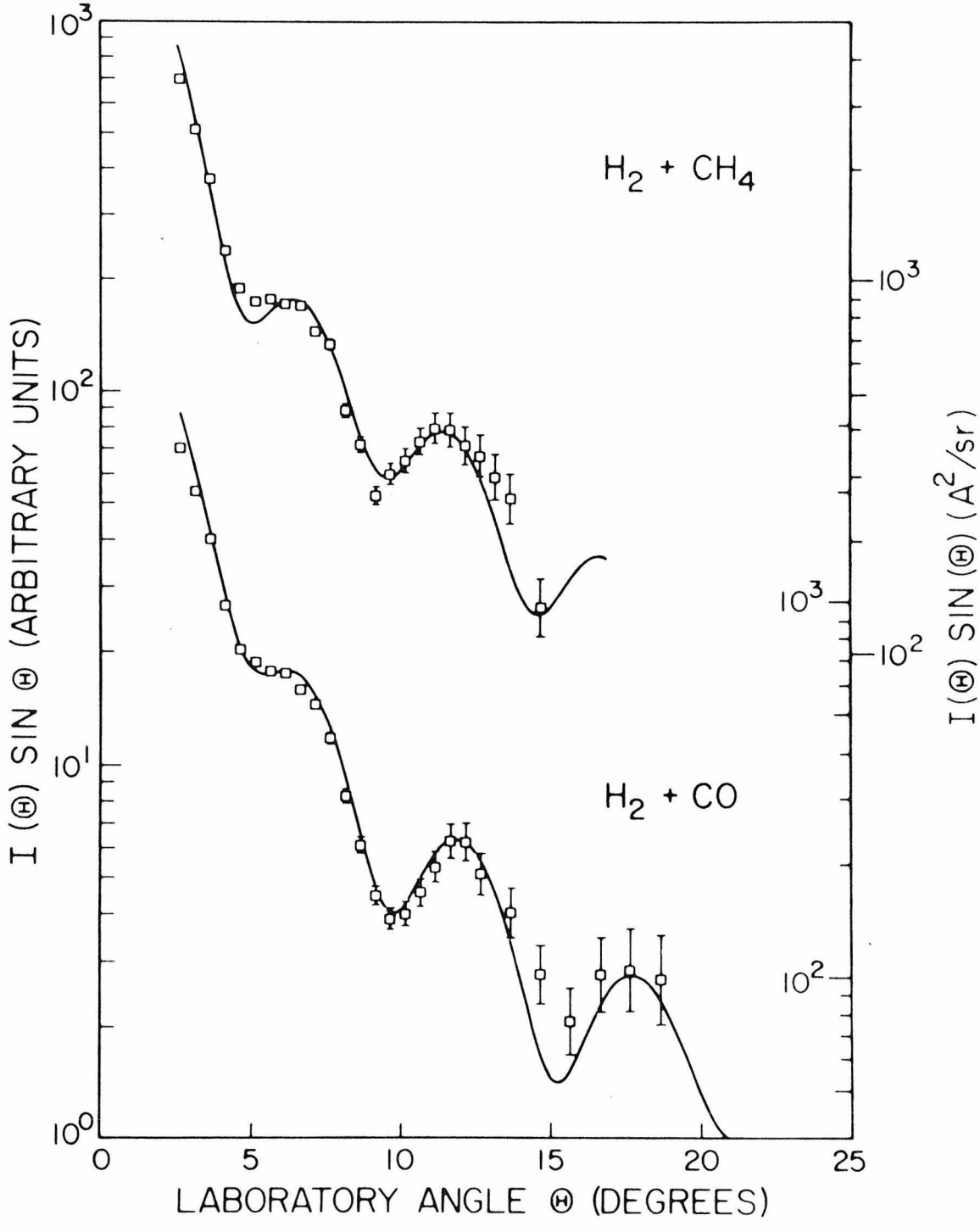
10^3
10^2
10^1
10^0
$H_2 + CH_4$
$H_2 + CO$
I (Θ) SIN Θ (ARBITRARY UNITS)
I(Θ) SIN (Θ) (A^2/sr)
0
5
10
15
20
25
LABORATORY ANGLE Θ (DEGREES)

5.17

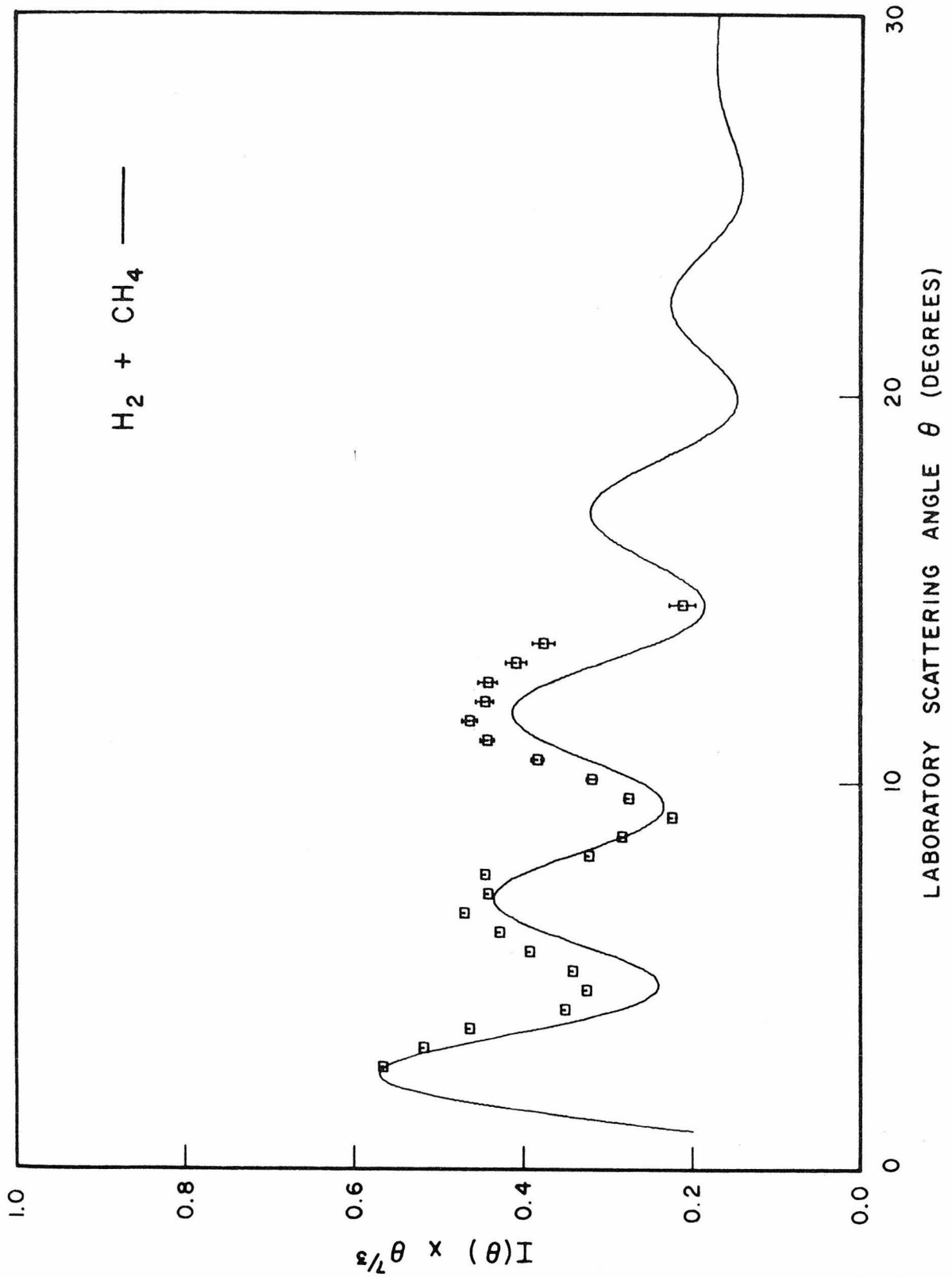
$H_2 + CH_4$ ——
$I(\theta) \times \theta^{7/3}$
1.0
0.8
0.6
0.4
0.2
0.0
0
10
20
30
LABORATORY SCATTERING ANGLE θ (DEGREES)

5.18

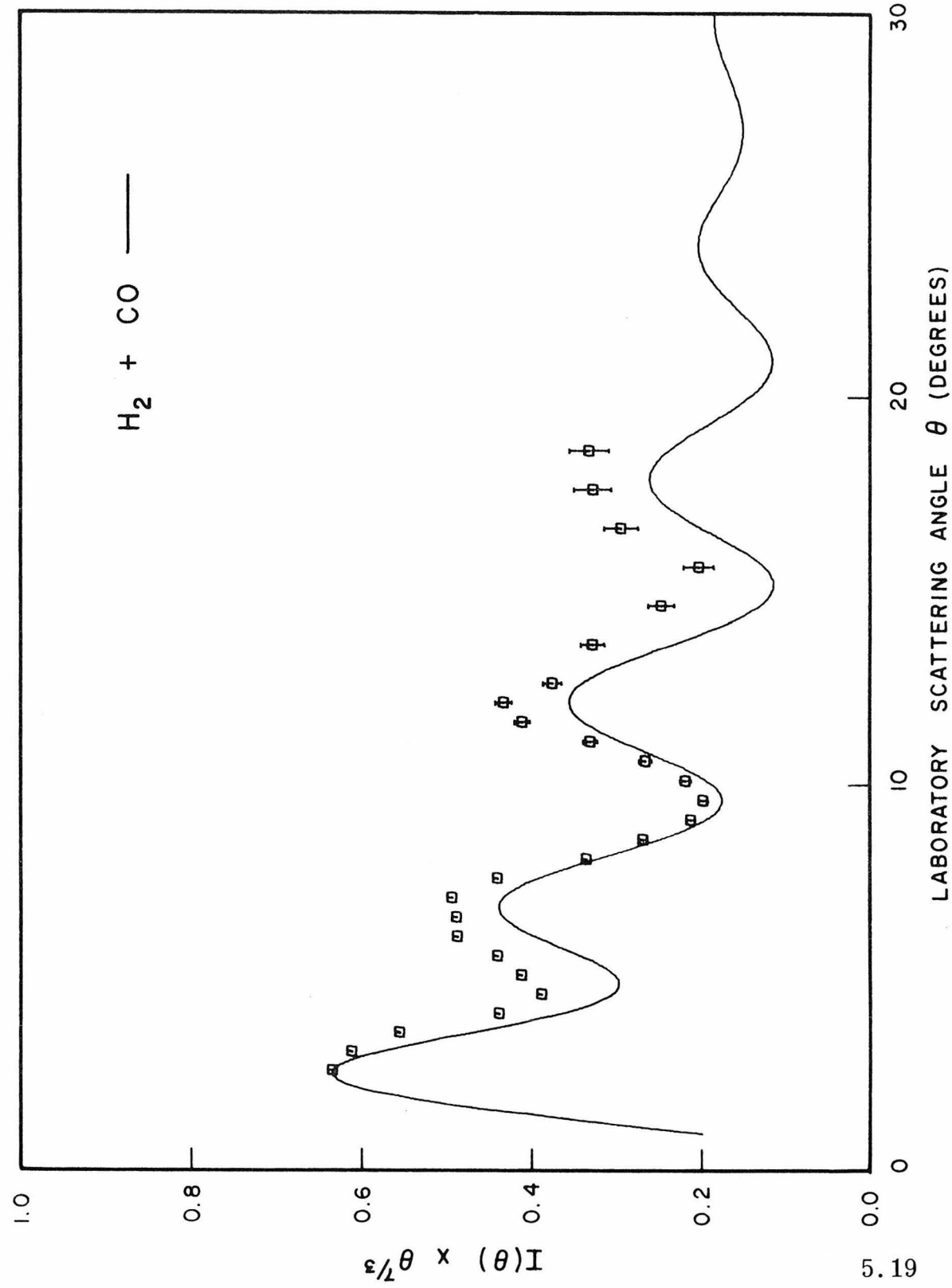
H_2 + CO ——
$I(\theta) \times \theta^{7/3}$
1.0
0.8
0.6
0.4
0.2
0.0
0
10
20
30
LABORATORY SCATTERING ANGLE θ (DEGREES)

5.19

measurements yield reliable estimates of the $\epsilon\sigma$ product (see Section 1.2.1). However, individual parameter estimates are much more unreliable. A comparison of these total cross section results with the present results is presented in Table 3 of Appendix D.

5.3 Discussion of Results

Based upon the results presented above (and in Appendix D), several conclusions may be drawn: (1) the potentials derived from the elastic scattering measurements are independent of the mathematical form used; (2) there is no evidence in any of the measured cross sections of a correlation between the amplitude of the oscillations and the symmetry of the secondary molecule. This result would not be expected if the potential anisotropy had a significant effect on the scattering; (3) the scattering produced by H_2 and D_2 are very different, and yet the derived potentials for these two isotopes and a common scattering partner were always the same to within the experimental error; (4) as evidenced by the $H_2 + SF_6$ and NH_3 systems (studied at two different collision energies) the potentials derived are insensitive to the de Broglie wavelength. This lack of sensitivity to λ is a necessary condition for the validity of the central-field assumption; (5) the experiments involving the para-$H_2 + SF_6$ gave the same results as the normal-H_2 + SF_6 studies, thus indicating an insensitivity to the initial distribution of H_2 rotational states. A more complete discussion of these points is to be found in Appendix D.

It may be concluded from these results that for H_2- or D_2-molecule elastic scattering (measured over the range of angles studied here), a purely central-field potential provides an adequate description of the interactions involved in that scattering. Thus, no effects of anisotropy could be found in any of these systems studied, either as a result of inelastic scattering or quenching of the rapid quantum oscillations. Again, Appendix D contains a further discussion of these conclusions.

5.4 Comparison with Previous Results

It was noted in the previous section that only a few of the systems studied here have been measured and reported by other workers. As a result, it is difficult to confirm either the results or the conclusions presented here. One comparison which can be made, however, is based upon the use of the well-known (albeit non-rigorous) combining rules [21]. The combining rules provide a simple and intuitive means of determining the intermolecular potential parameters for a system such as A + B from the parameters appropriate for A + A and B + B. The simplest combining rules for a LJ(12, 6) potential are just,

$$\sigma_{AB} = (\sigma_{AA} + \sigma_{BB})/2 \tag{19a}$$

$$\epsilon_{AB} = (\epsilon_{AA}\epsilon_{BB})^{\frac{1}{2}} . \tag{19b}$$

Equation (19a) is based on the assumption that the molecules interact as hard spheres, and hence the effective collision diameter

is just the sum of the radii due to each species. Equation (19b) is somewhat better founded in the assumption that the strength of the interaction is proportional to the dispersion forces of each species as determined by the individual polarizabilities (see equations (2)-(5), Chapter 2). In either case, however, the rules are only empirical, and so some care must be exercised in their use.

While equation (19) applies only to the interactions of non-polar molecules, a set of combining rules has been developed for use in determining the potential parameters between a polar and a non-polar molecule. These rules are given by Hirschfelder, Curtiss, and Bird [21] as,

$$\sigma_{np} = \tfrac{1}{2}(\sigma_n + \sigma_p)\xi^{-\frac{1}{6}} \tag{20a}$$

$$\epsilon_{np} = (\epsilon_n \epsilon_p)^{\frac{1}{2}} \xi^2 \tag{20b}$$

where,

$$\xi = [1 + \tfrac{1}{4}\alpha_n^* \mu_p^{*2} (\epsilon_p/\epsilon_n)^{\frac{1}{2}}]. \tag{20c}$$

Here, the subscripts n and p refer to the non-polar and the polar species, respectively. In addition, the reduced polarizability α_n^* is defined as α_n/σ_n^3, while the reduced dipole moment is given by $\mu_p/(\epsilon_p \sigma_p^3)^{\frac{1}{2}}$. Equation (20) is obtained by assuming a LJ(12, 6) interaction which includes additional terms of the type given by equation (3), Chapter 2.

With the exception of the rare-gases [22], equation (19) has not been tested extensively due to a general lack of data on mixed molecule-molecule systems. In general, results obtained by application of equations (19) and (20) are used to calculate virial and diffusion coefficients for mixed systems. Table 3.6-3 of reference [21] gives a comparison of the second virial coefficients for a number of non-polar molecule-molecule systems calculated using (19). For the most part, the results are in reasonable agreement with experimentally determined values.

Recently, Smith [23] has introduced a new type of combining rule based on a model of atomic distortion. For atoms and simple molecules, the repulsive potential $V_{AB}(R)$ is given by

$$V_{AB}(R) = \tfrac{1}{2}\left[V_{AA}(2r_1) + V_{BB}(2r_2) \right], \tag{21}$$

where r_1 and r_2 $(= R-r_1)$ are determined from,

$$\left[dV_{AA}(R)/dR\right]_{R=2r_1} = \left[dV_{BB}(R)/dR\right]_{R=2r_2} . \tag{22}$$

When compared with the simple combining rules given by (19), Smith's equations proved more accurate for the repulsive regions of rare-gas mixture potentials [24]. Extending these ideas, Kong [25] has developed a set of rules for combining both Lennard-Jones potentials and Morse potentials. The equations appropriate to the LJ(12, 6) potential are;

$$\epsilon_{AB}\sigma_{AB}^{12} = (\epsilon_{AA}\sigma_{AA}^{12}/2^{13})\left[1 + (\epsilon_{BB}\sigma_{BB}^{12}/\epsilon_{AA}\sigma_{AA}^{12})^{1/13} \right]^{13} \tag{23a}$$

$$\epsilon_{AB}\sigma_{AB}^{6} = (\epsilon_{AA}\sigma_{AA}^{6}\epsilon_{BB}\sigma_{BB}^{6})^{\frac{1}{2}} \quad . \tag{23b}$$

Equation (23b) just represents the attractive C_6 coefficient as $(C_{AA}C_{BB})^{\frac{1}{2}}$. Kong has used these equations to calculate the potential parameters for unlike rare-gas atom pairs. These calculated values agreed reasonably well with the experimentally determined parameters.

Using the experimental results given in the previous section for the $H_2 + O_2$, NH_3, SF_6, H_2O, CH_4, and CO systems, these various combining rules have been compared. In Table 4, the necessary values of $\sigma_{H_2\text{-}H_2}$, $\epsilon_{H_2\text{-}H_2}$ and the other LJ(12, 6) parameters for each of the pair potentials are given. These values have been independently determined from bulk properties, and in general are known to ±20%. Also given in Table 4 are experimental values of the static polarizabilities, the dipole moments, and the ionization potentials of each molecule. These values will be used below in the calculation of the various C_6 coefficients.

Table 5 lists the results of applying equations (19) and (23) to each system, and equation (20) where appropriate. Also given are the experimentally determined results taken from the previous section. In general, the results show reasonable agreement in both the ϵ and σ parameters, with the exception of the $H_2 + H_2O$ σ value. Since the diffusion coefficient has been measured for that system [26], an additional comparison can be made of the σ value. Using the experimental value of $D_{12} = 1.02$ (cm^2/sec) and the present ϵ result of 13.4 meV, the $\sigma_{H_2\text{-}H_2O}$ parameter was

found from [21],

$$\sigma = \left[\frac{(2.628 \times 10^{-3})[T^3(m_1+m_2)/(2m_1m_2)]^{\frac{1}{2}}}{\Omega^{(1,1)*}(T^*)\, D_{12}} \right]^{\frac{1}{2}}. \qquad (24)$$

Here, T is the temperature in Kelvin, the m's are the molecular weights, $T^* = kT/\epsilon$ and $\Omega^{(1,1)*}(T^*)$ is a reduced collision integral (see Section 1.2.2, equations (3)-(5)). For a temperature of 373K, $T^* = 1.976$, and using Table I-M of reference [21], $\Omega^{(1,1)*}(1.976) = 1.079$. The resulting value for σ is 2.75A. Since this value is the same as calculated from the combining rules, and much lower than the presently determined experimental value, the latter result must be viewed with some suspicion.

One further measure of the validity of the combining rules given here is a comparison of the C_6 parameters. Table 6 shows the experimental values ($= \epsilon\sigma^6$) compared with those calculated using the parameters found from equations (19), (20), and (23). In addition, the C_6 fitted parameter obtained from the MSV potential analysis for each system is also given. Finally, using the polarizabilities, dipole moments and ionization potentials from Table 4, the induced dipole-induced dipole dispersion constants (equation (2), Chapter 2) and the dipole-induced dipole constants have been calculated and tabulated.

It is interesting to note that while the experimental and calculated values of C_6 are in reasonable agreement (except for the $H_2 + H_2O$ system), the results obtained using the combining rules

are always lower. Also, the C_6 contants obtained from the MSV fits are not very sensitive to the individual system, since they only vary by ±20%. This lack of sensitivity may just reflect the fact that the use of a four parameter potential function such as the MSV model is not justified by the accuracy of the data. Alternately, the C_6 parameter may simply not be well determined by the scattering data used here.

As above, the experimental and calculated results for the $H_2 + H_2O$ system are in disagreement, here by over a factor of two. Since it is unlikely that the ϵ value is too large by this amount, it seems more reasonable to assume that the experimentally determined σ value is too large. At present, no firm explanation for this anomaly can be advanced, although the possible existence of high concentrations of water dimers is being investigated.

Table 4

Like Pair Potential Parameters, Polarizabilities, Dipole Moments, and Ionization Potentials

	ϵ (meV)[a]	σ (A)[a]	α (A^3)[a]	μ (D)[d]	I.P. (eV)[c]
H_2	5.143	2.827	0.79	-	15.427
O_2	9.19	3.467	1.60	-	12.99
NH_3	12.6[b]	3.441	2.26	1.47	10.50
SF_6	17.30[b]	5.128[b]	6.56[c]	-	19.3
H_2O	32.7	2.641	1.44	1.82	12.69
CH_4	12.80	3.758	2.60	-	12.5
CO	7.90	3.69	1.95	0.13	14.01

[a]R. C. Reid and T. K. Sherwood, "The Properties of Gases and Liquids," McGraw-Hill, (New York, 1966).

[b]Ref. 21.

[c]Ref. 27.

[d]A. L. McClellan, "Tables of Experimental Dipole Moments," Freeman, San Francisco, 1963.

[e]R. W. Kiser, "Tables of Ionization Potentials," Kansas State University Press, 1960.

Table 5

Comparison of Lennard-Jones (12, 6) Potential Parameters

	ϵ (meV)				σ (A)			
	expt.	eqn. (19)	eqn. (23)	eqn. (20)	expt.	eqn. (19)	eqn. (23)	eqn. (20)
$H_2 + O_2$	7.7	6.87	6.29	-	3.38	3.15	3.18	-
NH_3	9.8	8.05	7.29	8.14	3.45	3.13	3.17	3.13
SF_6	10.4	9.43	4.88	-	4.05	3.98	4.25	-
H_2O	13.4	12.97	12.76	13.29	3.50	2.74	2.74	2.73
CH_4	9.9	8.11	5.02	-	3.7	3.29	3.53	-
CO	6.9	6.37	5.60	6.37	3.5	3.26	3.30	3.26

Table 6

Comparison of C_6 Parameters (eV A^6)

	expt.	eqn. (19)	eqn. (23)	eqn. (20)	MSV	Dispersion[a]	Dipole[b]
$H_2 + O_2$	11.4	6.71	6.47	-	16.2	13.37	-
NH_3	16.52	7.57	7.40	7.65	14.5	16.73	1.06
SF_6	45.89	41.3	28.74	-	14.3	46.53	-
H_2O	24.6	5.67	5.40	5.50	12.6	11.88	1.63
CH_4	25.4	12.5	9.72	-	-	21.27	-
CO	12.68	8.28	9.23	8.28	-	16.96	0.008

[a]Calculated from equation (2), Chapter 2.

[b]Contribution from the dipole induced-dipole dispersion force; equation (3), Chapter 2.

References

1. See for example, A. H. Stroud and D. Secrest, "Gaussian Quadrature Formulas," Prentice-Hall, Englewood Cliffs, N.J., 1966.
2. R. J. Munn and F. J. Smith, Mol. Phys. 10, 163 (1966).
3. Z. Kopel, "Numerical Analysis," Wiley, New York, 1955, pp. 381-384.
4. R. J. Glauber, Lectures Theoret. Phys. 1, 315 (1959).
5. K. G. Anlauf, R. W. Bickes, Jr., and R. B. Bernstein, J. Chem. Phys. 54, 3647 (1971).
6. See for example, N. R. Draper and H. Smith, "Applied Regression Analysis," Wiley and Sons, New York, 1960.
7. D. W. Marquardt, J. Soc. Ind. Appl. Math. 11, 431 (1963).
8. E. M. L. Beale, J. Roy. Stat. Soc. B-22, 41 (1960).
9. See for example, E. Parzan, "Stochastic Processes," Holden-Day, San Francisco, 1962, p. 14.
10. Robert J. Gordon, M. J. Coggiola, and Aron Kuppermann, Abstract of papers, VIIth ICPEAC, North-Holland 1971, p. 552.
11. M. J. Coggiola, R. J. Gordon, and A. Kuppermann, Abstracts of papers, VIIIth ICPEAC, Beograde, 1973, p. 45.
12. M. J. Coggiola, Robert J. Gordon, and Aron Kuppermann, Proceedings of the IVth International Symposium on Molecular Beams, Cannes (1973).
13. Robert J. Gordon, M. J. Coggiola, and Aron Kuppermann, Chem. Phys. Letters 20, 493 (1973).

14. Aron Kuppermann, Robert J. Gordon, and Michael J. Coggiola, Disc. Faraday Soc. 55, 145 (1973).

15. R. W. Bickes, Jr., G. Scoles, and K. M. Smith, Proceedings IVth International Symposium on Molecular Beams, Cannes (1973).

16. R. W. Bickes, Jr., G. O. Este, G. Scoles, and K. M. Smith, J. Phys. B 7, L19 (1974).

17. P. H. Kydd, J. Chem. Phys. 37, 931 (1962).

18. W. R. Snow, J. T. Dowell, J. G. Chervenak, and H. E. Berek, J. Chem. Phys. 58, 2517 (1973).

19. H. P. Butz, R. Feltgen, H. Pauly, and H. V. Vehmeyer, Z. Physik, 247, 70 (1971).

20. V. Aquilanti, G. Luti, F. Vecchio-Cattivi, and G. G. Volpi, Mol. Phys. 21, 1149 (1971).

21. J. O. Hirschfelder, C. F. Curtiss, and R. B. Bird, "Molecular Theory of Gases and Liquids," J. Wiley, New York, 1954.

22. W. Hogervorst, Physika 51, 77 (1971).

23. F. T. Smith, Proc. Roy. Soc. A5, 1708 (1972).

24. C. L. Kong, J. Chem. Phys. 59, 968 (1973).

25. C. L. Kong, J. Chem. Phys. 59, 2464 (1973).

26. F. A. Schwartz and J. E. Brow, J. Chem. Phys. 19, 640 (1951).

27. A. B. Tipton, A. P. Dean, and J. E. Boggs, J. Chem. Phys. 40, 1144 (1964).

Appendix A. Determination of the Angular Resolution

In Chapter 4, it was pointed out that the measured results of differential elastic scattering could be significantly affected by the detector angular resolution. It was also noted that, in general, the a priori determination of the resolution function is not particularly straightforward. Despite this, some simple considerations of collimator sizes and locations can yield qualitative criteria for optimizing the overall resolution. To simplify matters, it will be assumed that only the primary beam makes a significant contribution to the size of the scattering center. For any scattering angle θ, the overall width of the scattering region is just,

$$\Gamma_{sc} = \Gamma_p \cos\theta + \Gamma_s \sin\theta \qquad \text{(A1)}$$

where Γ_p and Γ_s are the FWHM of the primary and secondary beams, respectively. Hence, for small θ, $\Gamma_{sc} \approx \Gamma_p$, so that ignoring the secondary beam width is a good approximation in this case. Under these conditions, the geometry of the system would be as shown in Figure A-1. The top half of this diagram is just that shown in Figure 4.1, with $L_1 = L_{sc}$, $L_2 = L_{cd}$. Now, the FWHM at the scattering center (Γ') will be taken as the width of a source in line with the collimator (w_d) at the entrance of the detector. Using the equations given before, it is now possible to find Γ' and then Γ once L_1-L_4 and w_s, w_c and w_d are known. If we define

$$\lambda = 1 + L_2/L_1 \tag{A2}$$

$$\lambda' = 1 + L_3/L_4 \tag{A3}$$

the resolution Γ will have three different forms depending on the following inequalities,

$$\text{Region I:} \qquad w_c \leq \frac{1}{\lambda} w_d \tag{A4}$$

$$\text{Region II:} \qquad \frac{1}{\lambda} w_d \leq w_c \leq \frac{\lambda}{\lambda'} w_d \tag{A5}$$

$$\text{Region III:} \qquad \frac{\lambda}{\lambda'} w_d \leq w_c \tag{A6}$$

These three regions are mapped out in Figure A-2 as functions of the reduced variables w_d/w_s and w_c/w_s. Using equations (4.3) and (4.4) to first find Γ' in terms of w_s, w_c and λ, the detector resolution function width can be determined. In Regions I and II the widths Γ_1 and Γ_2 are found to be equal,

$$\Gamma_1 = \Gamma_2 = w_d \frac{\lambda'}{\lambda' - 1} \tag{A7}$$

while in Region III,

$$\Gamma_3 = w_c \frac{\lambda}{\lambda' - 1} \ . \tag{A8}$$

Since the usual system variables are w_s, w_c and w_d with λ and λ' fixed, the slopes of the two boundary lines will also be fixed. If a particular choice of w_s, w_c and w_d corresponded to the point a, the method of reducing Γ would be as follows. Any reduction in w_c (holding w_d constant) would correspond to moving to

Figure A-1: Schematic diagram of the molecular beam scattering geometry. The Γs are taken as the average penumbra-umbra distances, as shown. The notation is essentially that due to Ramsey in "Molecular Beams," Oxford Press, London, 1952, p. 17.

Figure A-2: Resultant resolution FWHM plotted as a function of the reduced collimator width (see text).

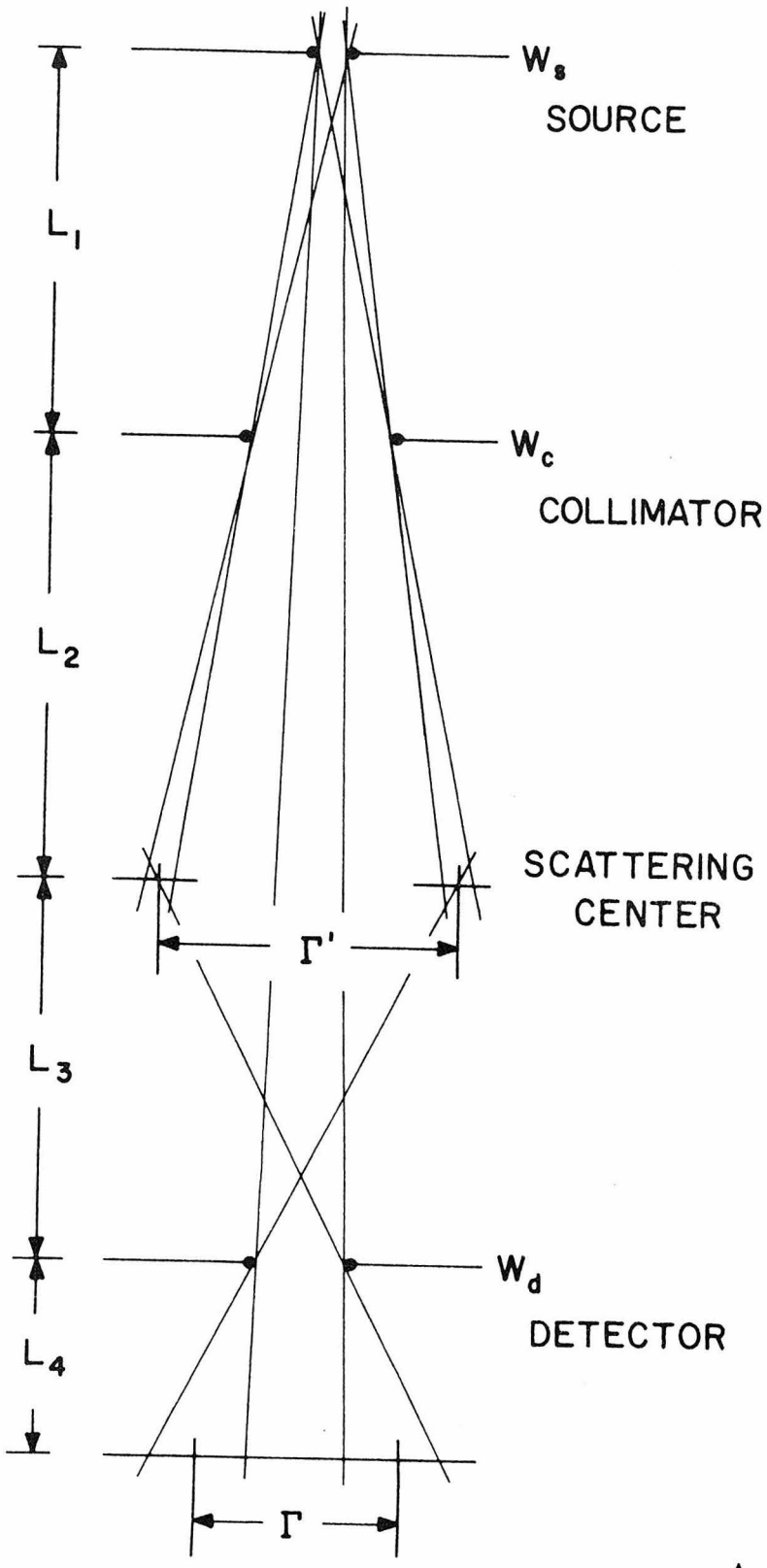
W_s
SOURCE
L_1
W_c
COLLIMATOR
L_2
SCATTERING
CENTER
Γ'
L_3
W_d
DETECTOR
L_4
Γ

A-1

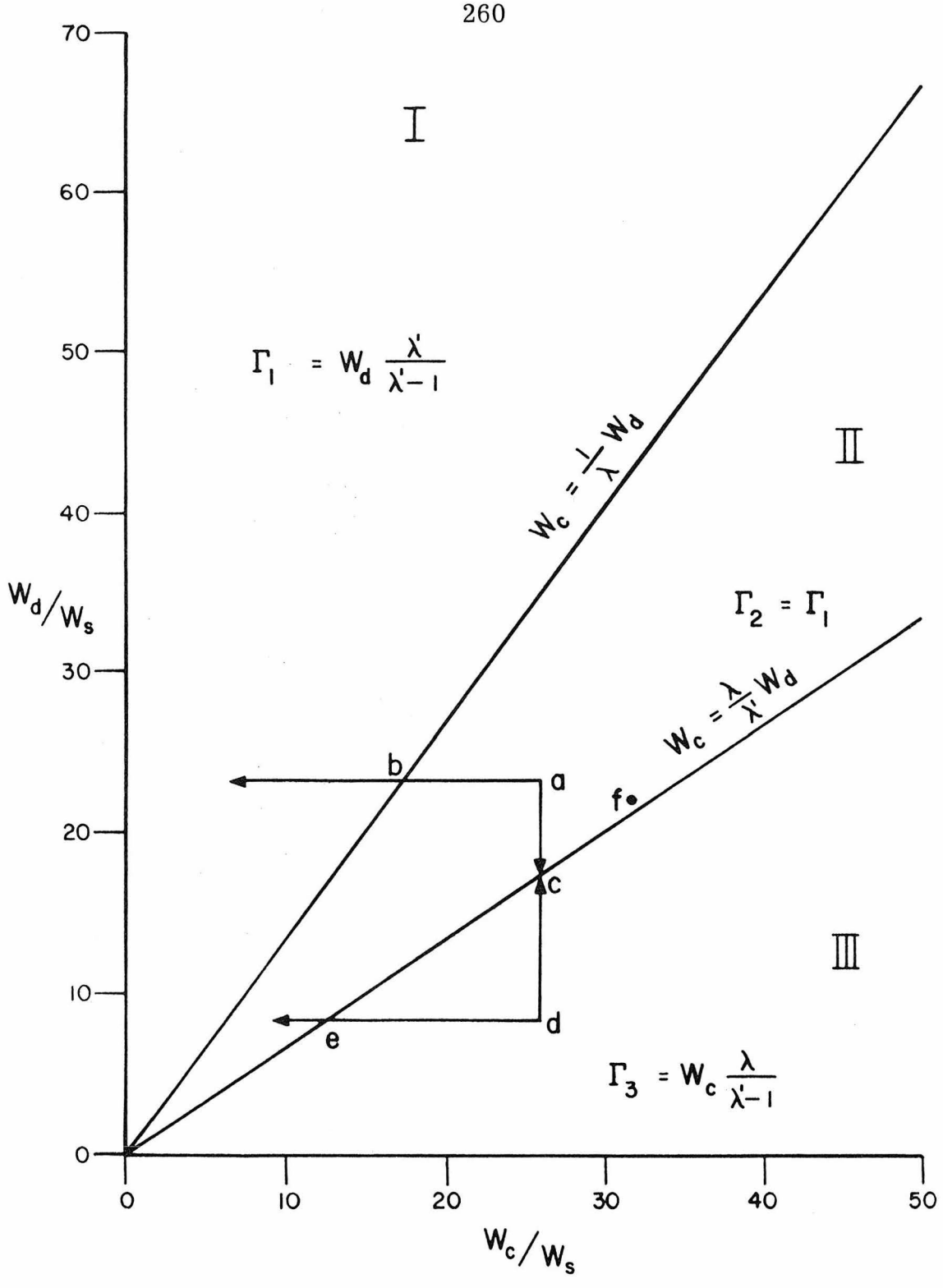
70
60
50
40
30
20
10
0
0
10
20
30
40
50
W_d/W_s
W_c/W_s
I
II
III
$\Gamma_1 = W_d \frac{\lambda'}{\lambda'-1}$
$W_c = \frac{1}{\lambda} W_d$
$\Gamma_2 = \Gamma_1$
$W_c = \frac{\lambda}{\lambda'} W_d$
$\Gamma_3 = W_c \frac{\lambda}{\lambda'-1}$
a
b
c
d
e
f

point b, and would produce no improvement (reduction) in Γ, since in Regions I and II w_c has no effect on Γ. Reducing w_d (w_c constant) will, however, reduce Γ, until the point c is reached. Thereafter, further reduction of w_d will have no effect in Region III. Similar arguments apply if the initial geometry corresponds to point d. Now, reduction of w_c improves the resolution until point c is reached, while no change in the resolution will occur if w_c is fixed and w_d increased until point c is reached. The obvious strategy is to select w_d/w_s and w_c/w_s corresponding to a point along the boundary between Regions II and III. Furthermore, the closer the point lies to the origin, the better will be the resolution. Clearly, $w_c = w_d = 0$ gives infinite resolution but zero signal, hence some compromise must be reached between resolution and intensity as determined by the degree of collimation.

The actual geometry of the molecular beam system corresponds approximately to the point f in Figure A-2. Calculation of Γ by equation (A7) gives an FWHM of $\sim 1.1^\circ$, while that determined experimentally (see Section 5.1.1) is $\sim 2.0^\circ$. From Figure A-2, it is clear that some small improvement ($\sim 13\%$) in the resolution could be realized by a corresponding reduction of w_d. Based on the results shown in Figure 4.2, this change in Γ would not produce a significant enough improvement in the measured differential cross section to compensate for the $\sim 25\%$ loss in signal due to the increased collimation.

While this scheme for determining the FWHM of the detector resolution function is only approximate, it nonetheless

resulted in a reasonable set of conditions for optimizing Γ, and also yielded a satisfactory prediction of the actual resolution.

Appendix B. Digital Synchronous Counter

To take advantage of the sensitivity of pulse counting techniques without losing the S/N enhancement of synchronous lock-in detection, a digital phase sensitive counter was constructed. The principle design work was performed by Oren Mosher of this laboratory. The actual unit can be operated in three modes; (1) counter mode (CM), (2) total count mode (TC), (3) synchronous counter (SC). In the CM, input data pulses are counted for a 1 second period and the results displayed. Each second the display is updated with the current count rate. With a six decade display, the counter has a 1MHz limit. The TC mode will integrate the incoming pulses for a preset time interval. Again, the display is updated at one second intervals; however, the display now represents the accumulated count. Nine totalizing times from 1 second to 1000 seconds are available. As with the analog synchronous detector, the digital SC requires a reference signal input corresponding to the chopping function. In this mode, the reference signal is used to determine two time periods, one associated with the open chopper, the other associated with closed chopper. The first period then represents the interval during which signal + noise is detected, while the latter period corresponds to the interval during which only noise is detected. To obtain the signal value, pulses counted during the first (chopper open) period are added to the accumulator, while pulses counted during the second (chopper closed) period are subtracted from the accumulator. This up-down counting process continues for a preset total

time, after which, the resultant display represents the time averaged signal only. Since there is some time delay between the chopping of the beam and the detection of the signal, a means must be provided to introduce a similar time delay in the reference signal in order to bring the input and reference signals into exact synchronization.

Each of the three modes will be described in more detail by examining the logic diagrams in Figures B-1 - B-4. In the descriptions, a number in square brackets will represent a specific numbered gate on the diagrams. Figure B-5 is a legend indicating the actual type of TTL integrated circuit component used in constructing the counter.

(1) Counter mode. Two types of pulses can be counted by this system, TTL compatible pulses, or any positive going pulse at least 0.1 volt in magnitude. The latter pulses are detected by the comparitor [10] (see Figure B-2) with a variable input threshold. If TTL pulses are to be counted they are applied to [13] after the grounding switch is opened. In either case, the pulses to be counted will appear at the output of [12]. These pulses are passed along to gates [14] and [15]. In the count mode, the CM switch is closed, and hence the output of [20] is always high, regardless of the states of [18] or [19]. As a result, the pulses applied to [14] are passed (actually inverted) to the UP input of the reversible decade counters [42-47] (see Figure B-4). With CM = 0 (switch closed) gate [17] blocks any pulses that may be passed from [12] → [15] → [16] → [17]. The net result of this input channel then, is to apply any input pulses

to the UP input of the actual decade counters. Hence, so long as the counters [42-47] are not cleared (by CC), they will contain the total count. Each time LATCH on the buffer registers [49-54] goes high, the results in the decade counters are entered and displayed by the combination of drivers [55-60] and RCA Numitron incandescent display tubes. In the CM, the LATCH signal is generated each second to display the counts per second, and is immediately followed by a CC clearing pulse, so that the counters [42-47] will start accumulating counts for the next 1 second period. These signals are generated by the timing circuits shown in Figure B-3.

The time base of the unit is derived by counting the 60 Hz line frequency. A full wave rectified signal is applied to [23] after shaping by [21, 22]. The output of the comparator is a 120 Hz signal (since the full wave input peaks twice per cycle). This 120 Hz output is divided down by a combination of a divide by 12 [24] and a divide by 10 [25] counter. The resultant signal is a 1 Hz square wave, which when applied to the retriggerable monostable [26], produces 100 nsec wide pulses at Q (1 Hz) and $\overline{Q}$ (that is the complement of Q, i.e. $\overline{1\,Hz}$). The $\overline{1\,Hz}$ is applied directly to [48], which drives the LATCH at the desired rate. In addition, the 1 Hz signal is applied to another monostable [30] via [28] (and [27] with CM = 0). The output pulse of 70 nsec width from [30] is used to clear the counter (CC). Since the 1 Hz signal will always precede the CC signal, the contents of the counters will always be displayed before they are cleared. So

long as the count mode switch is closed, the counter unit will continue to function as an ordinary counter.

(2) Total count mode. The input pulse path is similar to the CM, except that now, the TC switch is closed (TC = 0). Again, no input pulses will be passed by [17] to the DOWN input of the counters. With TC = 0, the output of [18] will remain high, and the output of [19] will be low so long as GDIT is high. GDIT will be high only during the preselected integration time interval. During that period, the output of [20] is high (CM = 1) and again pulses applied to [14] will be passed on to the UP input of the decade counters. As soon as the counting period ends, GDIT will go low, and hence both inputs to [20] will be high (output low), thus blocking pulses at [14].

As in the CM, the $\overline{1\,Hz}$ signal applied to the LATCH inputs (via [48]) will update the display with the current contents of the counters. Now, however, since CM = 1, no 1 Hz signal will pass [28] or be applied to [30]. As a result, no CC clear pulse will be generated, so that the counters will continue to count up without being reset. These counters must be reset at the start of an integration period, however. The start of the period results from depressing the RESET push button. This action clears flip flop (FF) [41], and on the next 1 Hz pulse (positive edge) causes Q to go high and $\overline{Q}$ to go low. The Q signal is applied to [30], where it generates the necessary CC clear pulse. The $\overline{Q}$ signal ($\overline{RF}$) clears the time interval counters [38-40], clears FF [37] (via [36]) which in turn clears FF [32] (via the $\overline{Q}$ output of [37]). With the first $\overline{1\,Hz}$ pulse, [32] is clocked via [31]. Since [32]

was just cleared, this $\overline{1\,Hz}$ pulse causes $\bar{Q}$ to go low. When combined with $\overline{CM} = 0$ and 1 Hz (gates [33], [34] and [35]), the time interval counters [38-40] will begin to count the 1 Hz pulses. At the point when the total in the interval counters reaches the preset value (according to the setting of the 9 position time switch), FF [37] is clocked. The resulting change in $\bar{Q}$ again clears [32]. As a result, the output of [33] will go low. The net result of this circuit then is to produce a high signal at [33] beginning with the reset pulse, and lasting for the preselected time interval. This signal at the output of [33] is just GDIT.

In summary then, in the total count mode, an integration time is selected, and the counting operation is initiated by the reset push button. The data counters are cleared (CC), the time interval counters are cleared ($\overline{RF}$), and the timing period is started (GDIT goes high). Each second, the accumulated contents of the counters are displayed. At the end of the preselected period, GDIT goes low, and the counting stops, with the final total displayed continuously until another counting period starts.

(3) Synchronous counting. With both TC = 1 and CM = 1, the path of the input pulses is determined by GDIT, UPCNT and DWCNT. Again, GDIT will remain high during the selected counting period, however, the other two signals will alternately be high and low. When $\overline{UPCNT}$ is low (DWCNT will also be low), and GDIT is high, the output of [20] will be high, and hence pulses applied to [14] will again be passed on to the UP inputs of the counters. With DWCNT low, no pulses will pass [15]. However, when $\overline{UPCNT}$ goes high (as does DWCNT), the output of [20] will

go low, thereby blocking pulses at [14]. Now, with both GDIT and DWCNT high, pulses from [12] will be passed by [15], [16] and [17] (since CM = TC = 1), and onto the DOWN input of the counters. The result then is to add pulses to the counter total when $\overline{\text{UPCNT}}$ = 0 and subtract counts from the total when DWCNT = 1. It is, therefore, necessary to generate these two signals of the proper duration and in synchronization with the chopping function. This is accomplished by the reference channel circuit in Figure B-1.

The reference circuit consists of two essentially identical halves, one to generate the $\overline{\text{UPCNT}}$ signal, and one to generate the DWCNT signal. In describing the reference channel, only the latter section will be discussed. As in the TC mode, the RESET button initiates the counting period. In addition to resetting both the display and timing counters and setting GDIT high, a 100 nsec pulse is also generated by monostable [29] via the Q of [41]. This $\overline{\text{RFF}}$ pulse is applied to the clear of FF [9] of the reference channel. This ensures that the first clock input to [9] will set Q high, thus clearing [8] and pulling DWCNT low. The sequence of pulses that follow are shown in a timing diagram in Figure B-6.

The top (and bottom) wave form represents the input from the chopper light/photocell unit, with the rise and fall times somewhat exaggerated. This signal is applied to the comparator [1], whose triggering level (LL) is adjustable (see below). The output of [1] and [2] is the square wave $\overline{\text{LLEX}}$, which is true whenever the lower level (LL) is not exceeded. The width of this period is determined both by the LL setting, and the shape of the

reference signal. The $\overline{\text{LLEX}}$ waveform is applied to the retriggerable monostables [3] and [4]. On the first positive (rising) edge of $\overline{\text{LLEX}}$, a positive going pulse will be generated at the Q output of [3]. The width of this pulse (τ) is adjustable from 10 μsec to 10 msec. This pulse is the clock input to [9], and as noted above, it ensures that DWCNT is low before the counting sequence begins. The $\overline{Q}$ output of [3] (TD3) is a negative going pulse also of duration τ. This pulse will be used to clock FF [8] to pull DWCNT up and begin the first count down segment. However, since the Q and $\overline{Q}$ output pulses are simultaneously generated, they might clock [9] and [8] in either order. That is, if [9] is clocked before [8], the sequence would be correct, if on the other hand [8] was clocked ahead of [9], DWCNT would be first set high, then immediately set low again. To avoid this possible complication, the TD3 signal is delayed by 70 nsec by passing it through a pair of slow (74L05) inverters. The resulting pulse (waveform 5, Figure B-6) TD3D still has width τ. When $\overline{\text{LLEX}}$ falls, it triggers [4], which produces another variable width pulse (TD4) at the $\overline{Q}$ output. The widths of the pulses from [3] and [4] (and the two monostables in the lower half of the circuit) are all controlled by a multisection 10 turn potentiometer. The net effect is to make all these pulses of the exact same width, τ. Both TD3D and TD4 are applied to [7] which inverts and adds the two pulses to give the signal applied to the clock input of [8]. Notice that since both TD3D and TD4 have the same width, the separation between pulses is just T seconds, less 70 nsec due to the delay in TD3D. Since T is generally $\sim$3 msec (160 Hz

reference signal), the 70 nsec delay will be insignificant. The falling edge of the clock pulses applied to [8] will cause the Q output to change state each time, thus generating the DWCNT signal. This waveform is identical to $\overline{\text{LLEX}}$, except that it has been shifted by τ seconds. This time delay is just the phase shift ($= \tau\pi/T$ degrees). In an exactly analogous manner, the lower reference circuit will generate $\overline{\text{UPCNT}}$, which will look similar to DWCNT. It is important that the width T of these two pulses be the same so that the proper amount of background will be subtracted from the signal + background count. These widths are adjusted by setting the levels of the trigger voltages applied to the comparators. If the reference signal is quite asymmetric or has large rise and fall times, it may be necessary to set the levels in such a way that only a fraction of the on and off periods are actually counted. This introduces no problems, so long as the dead periods are equal during the up and down counting segments.

The overall action of the counter in the synchronous mode is, therefore, to alternately add and subtract input pulses from the total in exact phase with the chopping function. The duration of counting is selectable from 1 sec to 1000 sec, with a fixed 1 Hz data display update rate.

Construction of the counter was straightforward. All logic elements were standard TTL integrated circuits, whose type is given by the symbol table in Figure B-4. Two, twenty IC wire wrap boards were used to assemble the circuits. Separate regulated power supplies were provided for the ±15 volt DC (needed by the comparators), +5 VDC for the logic gates, and +5 VDC for

the six display tubes. Front panel controls include a main power on/off switch, the input threshold adjustment, the CM, TC and TTL switches, the time selector switch, the phase shift adjustment, a TTL input jack, the reset button, and a jack for the use of a remote reset control. The pulse input and reference input jacks are located on the rear of the chassis, along with the reference level threshold controls.

To operate the counter in the synchronous mode, a reference signal is applied, and the duration of the UPCNT and DWCNT segments is adjusted using the threshold level controls while observing the signals (via test points) on an oscilloscope. Once these periods are equal the pulses are applied, and the input threshold adjusted. Optimization of the phase shift is by trial and error adjustment until the signal reaches a maximum. After these adjustments have been made, the desired time is selected, the reset button pushed, and the final displayed signal recorded. Recent tests of this system and comparison with commercial units have verified its correct operation in all modes.

Figures B-1 - B-4: Logic diagrams of the reference, input, timing, and display circuits, respectively. Individual gates are numbered for text reference purposes.

Figure B-5: Logic symbol table indicating the actual types of integrated circuit components used in construction of the counter unit.

Figure B-6: Timing diagram corresponding to generation of the DWNCT signal. See text for explanation.

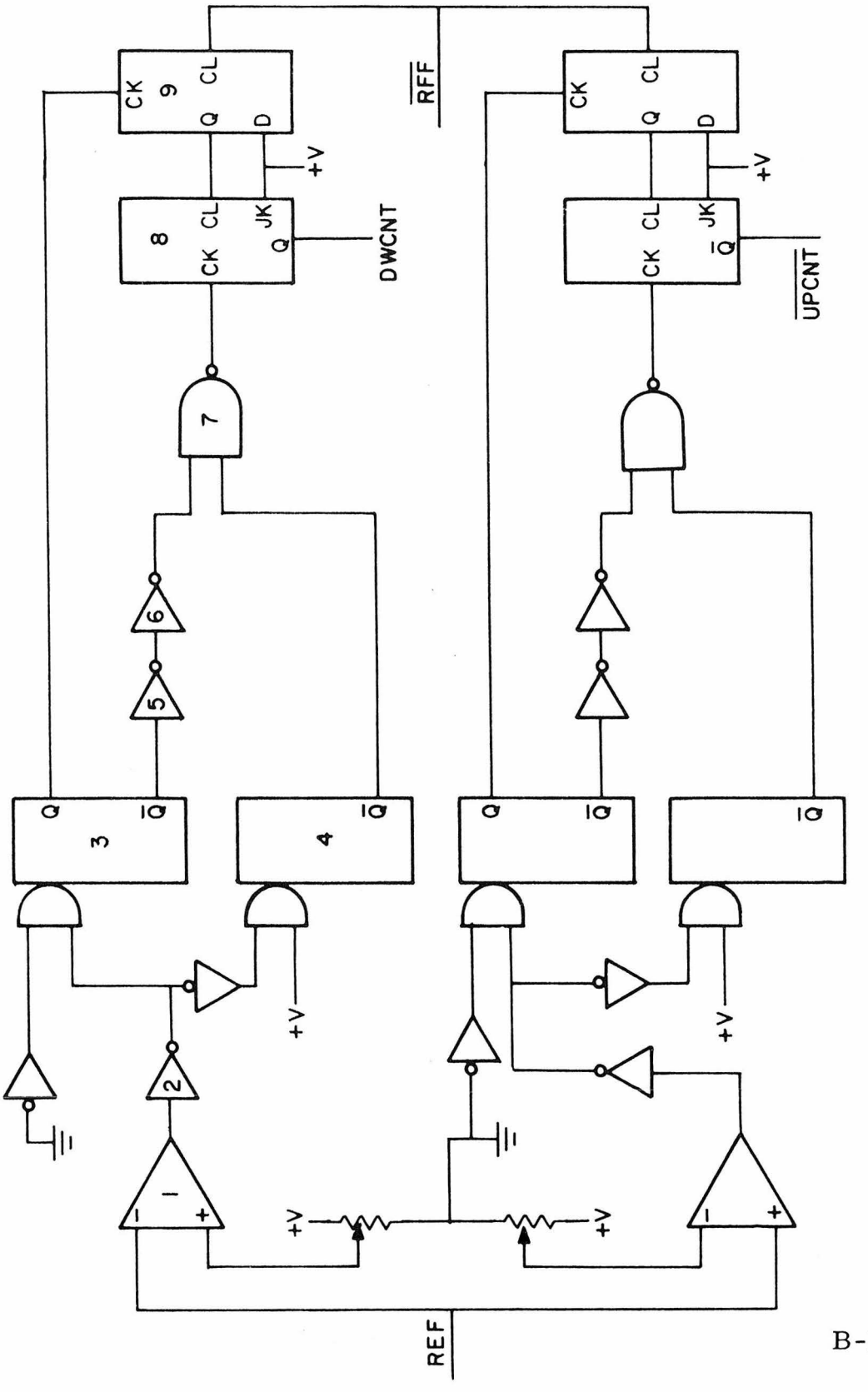
CK
9
CL
Q
D
+V
RFF
CK
CL
Q
D
+V
8
CK
CL
JK
Q
DWCNT
CK
CL
JK
Q̄
UPCNT
7
6
5
Q
Q̄
3
4
Q̄
Q
Q̄
Q̄
+V
+V
2
1
+V
+V
REF

B-1

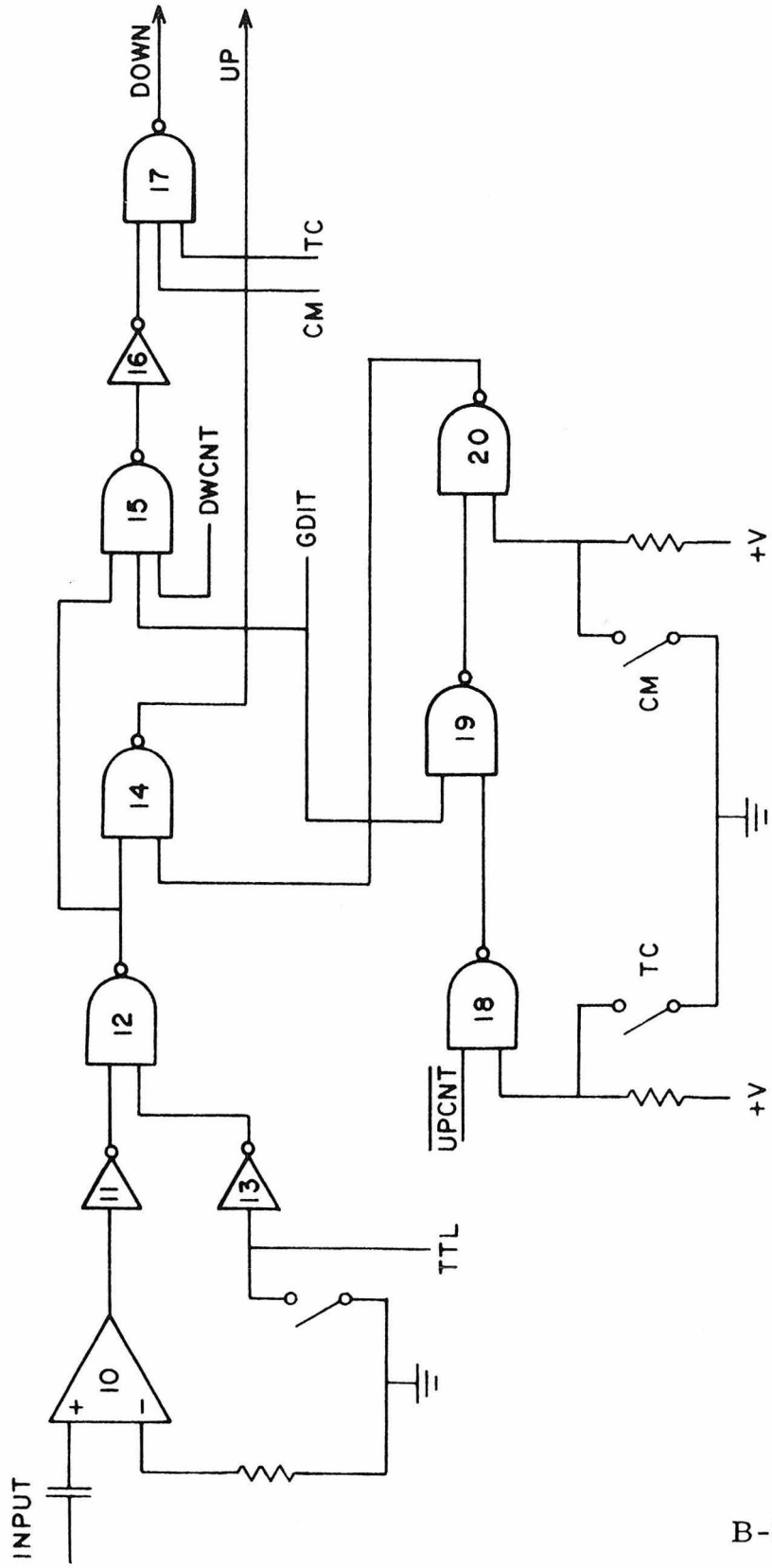
DOWN
UP
17
TC
CM
16
15
DWCNT
GDIT
20
+V
CM
19
14
12
TC
18
UPCNT
+V
11
13
TTL
10
+
-
INPUT

B-2

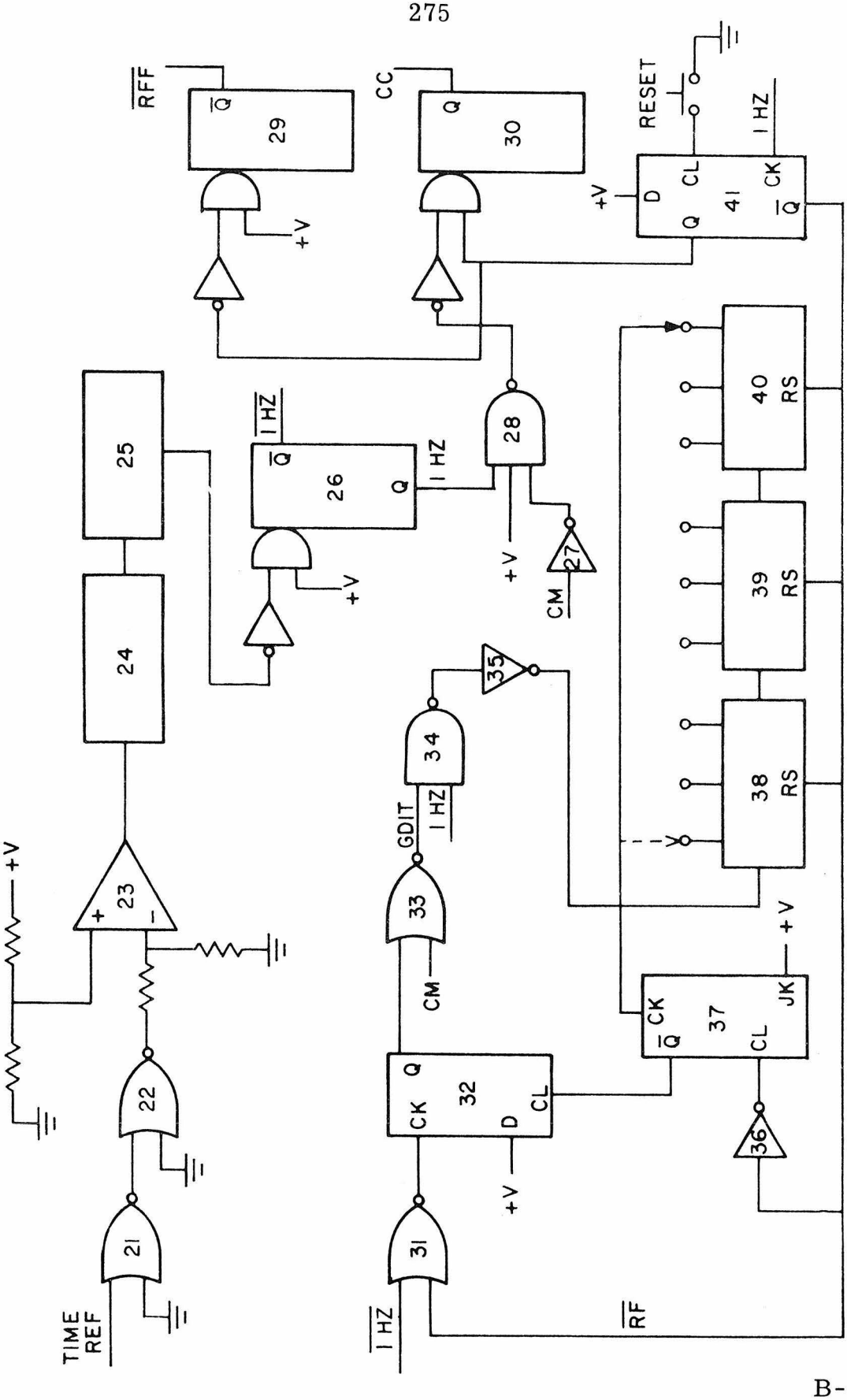
TIME REF
21
22
23
+V
24
25
26
1 HZ
Q
Q
+V
RFF
29
+V
CC
30
28
+V
CM
27
RESET
+V
D
CL
41
CK
1 HZ
Q
Q
40 RS
39 RS
38 RS
35
34
GDIT
1 HZ
33
CM
32
CK
Q
D
CL
+V
31
1 HZ
RF
37
CK
Q
CL
JK
+V
36

B-3

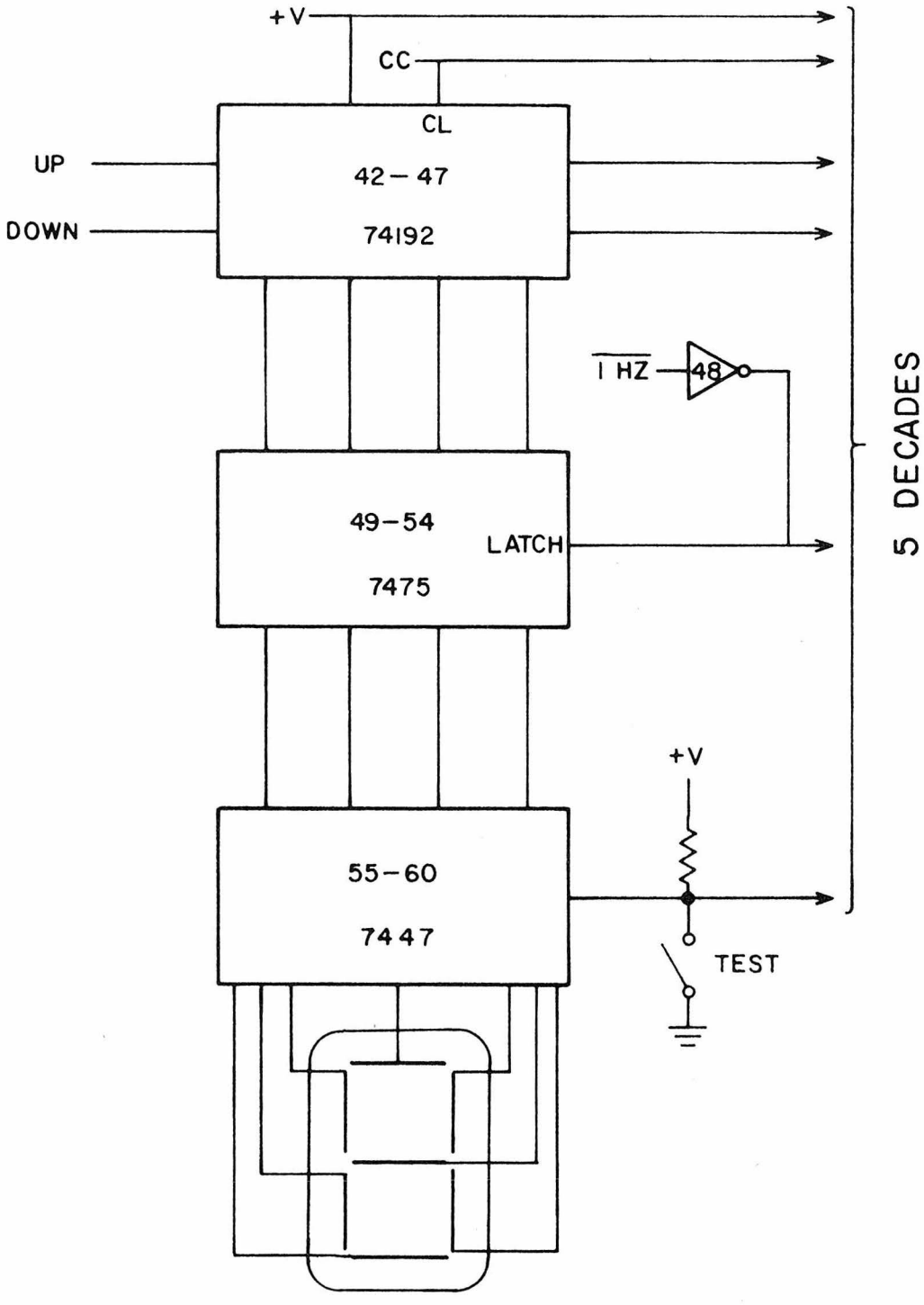
+V
CC
CL
UP
42 – 47
DOWN
74192
1 HZ
48
49–54
LATCH
7475
5 DECADES
+V
55–60
7447
TEST
RCA DR2010
NUMITRON

LOGIC SYMBOL TABLE

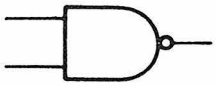

= 1/4 7400

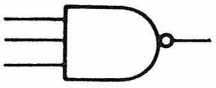

= 1/3 7410

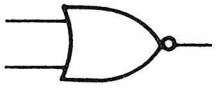

= 1/4 7402

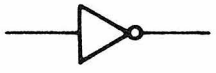

= 1/6 7404

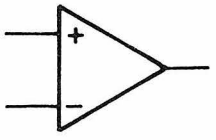

= 1/2 74720

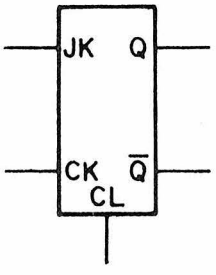

= 1/2 7474

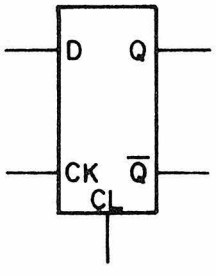

= 1/2 74123

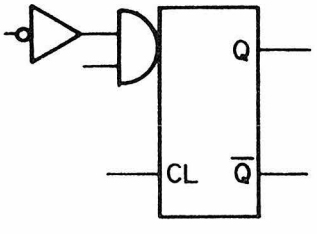

GATE 24 = 7492

GATES 25, 38-40 = 7490

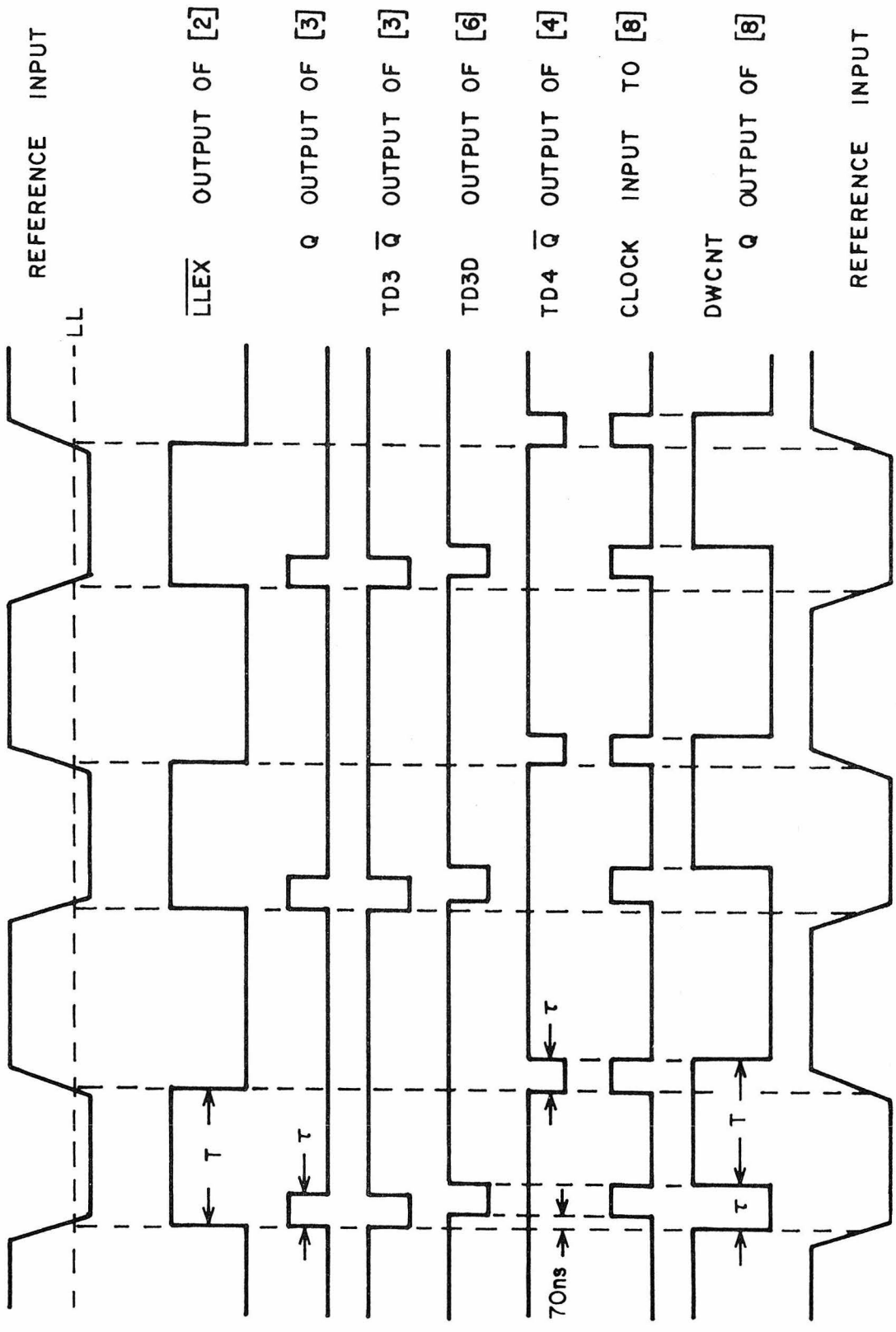
REFERENCE INPUT
LL
$\overline{\text{LLEX}}$ OUTPUT OF [2]
Q OUTPUT OF [3]
TD3 $\overline{Q}$ OUTPUT OF [3]
TD3D OUTPUT OF [6]
TD4 $\overline{Q}$ OUTPUT OF [4]
CLOCK INPUT TO [8]
DWCNT Q OUTPUT OF [8]
REFERENCE INPUT
T
τ
τ
70ns
T
τ

Appendix C. An Arc-Heated Hydrogen Atom Source

In connection with planned experiments involving the inelastic and reactive scattering of hydrogen atoms, a high intensity arc-heated plasma source has been constructed. In order to conduct such experiments, the H-atoms produced must have energies in the chemically interesting region, that is from ~ 0.2 eV to 5 eV. Recently, a number of methods have been developed to produce beams of atoms and molecules in this energy range. These techniques include binary (seeded) gas mixtures [1-3], charge-exchange systems [4-6], and shock-tube nozzle beams [7-9]. While each of these methods has produced beams of a few eV energy, none is well suited to the production of hydrogen atoms. The binary mixture method will only accelerate a species if a lighter gas is used in the mixture, clearly then H atoms cannot be accelerated. Charge-exchange sources cannot, in general, produce beams with energies below ~ 10 eV due to space charge focusing limitations. In the case of H atoms, 10 eV is a great deal of energy, resulting in exceedingly high velocities ($\sim 10^7$ cm/sec). Shock-tube type sources usually have limited operating times, and also provide no simple means of generating H atoms.

The type of source chosen for hydrogen atom production is an arc-heated plasma nozzle system of the type developed by Knuth [10-12]. This source combines the aerodynamic acceleration of a supersonic nozzle source with very high temperatures due to arc-heating. As a result of these high temperatures ($\sim$10-15000 K), the hydrogen gas (molecular H_2) introduced into the arc discharge

will not only be completely dissociated into atoms, but these atoms will attain translational energies up to 1.3 eV. The supersonic nature of the source produces a very high beam intensity with quite good velocity resolution ($\sim 10\%$).

Following the design of Knuth et. al. [12, 13], an arc-heated source was constructed. A cutaway view of the source is shown in Figure C-1. Basically, the source consists of a movable cathode tip and a fixed anode. Gas is introduced into the area between the two, and an arc is struck. Under the proper conditions (see below), the resulting plasma "flame" will move outside the anode (through the nozzle hole in the anode piece) and thus will carry away the great majority of the heat generated. It is this external arc that allows the very high temperatures to be reached without consuming any of the metal source. A water cooled electromagnet surrounding the nozzle produces a field which has the effect of stabilizing the arc discharge [14].

The cathode portion of the source consists of a hollow brass tube with a 1" × $\frac{1}{8}$" dia. tip piece attached. This tip is made from 2% thoriated tungsten rod and can withstand temperatures in excess of 6000 K. The hollow cavity in the cathode tube allows for water cooling of the piece, including the tungsten tip. This tube is fitted inside of a support piece in such a way that it can move $\sim \frac{3}{4}$" with respect to the support. A metal brass bellows is silver soldered between the two to maintain a vacuum tight assembly. The anode segment consists of a large cylindrical piece which has six water cooling channels bored into it, and which holds a copper nozzle. Since much of the heat is generated

Figure C-1: Cutaway view of arc-heated source. (1) Exit aperture, (2) anode housing, (3) water cooling inlet/outlet ports, (4) source gas chamber, (5) O-ring insulator and vacuum seal, (6) cathode support, (7) flexible bellows, (8) cathode, (9) cathode water cooling channel, (10) cathode tip.

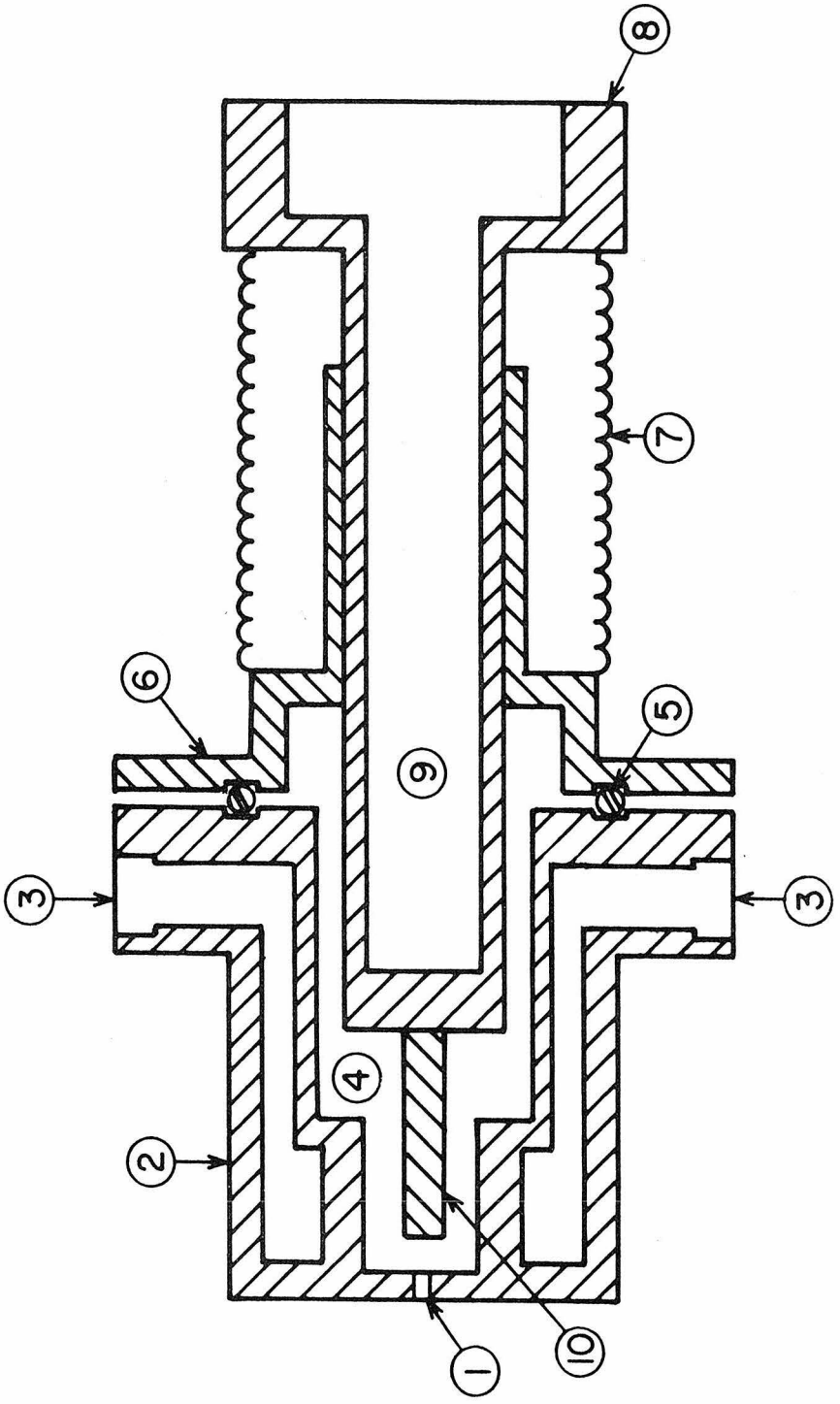

C-1

at or near the exit aperature in the nozzle, this piece is made easily replaceable. When assembled, the anode and cathode are joined with a Viton O-ring. This O-ring both vacuum seals the unit and electrically insulates the two halves. The space between the cathode tip and the anode nozzle forms a small chamber (see figure) into which the gas is introduced. To ensure a uniform flow, the gas is introduced through two holes on opposite sides of the chamber, drilled at sharp angles through the cathode housing. This has the effect of causing the gas to swirl around in the chamber, and seems to produce a more stable arc. Water cooling is provided by $\frac{1}{4}$" dia. copper and polyethylene tubing, the latter to maintain electrical insulation. When assembled, the cathode-anode distance can be adjusted by moving the cathode tube and fixed in place at the appropriate location.

The unit is mounted into the center of the 6" diameter × 1" thick electromagnet. Approximately 450 turns of #10 enameled copper wire produces a 400 gauss magnetic field when 10 amperes of DC current is passed through the coil. The central magnet piece also contains water cooling channels to reduce thermal effects from the arc. The magnet is mounted on a movable rail track so that the source may be moved with respect to the downstream skimmer. This skimmer is a two piece assembly having an aluminum base and a removable copper tip. The overall length of the skimmer is ~11" (9" base + 2" tip) with a 16° interior half angle and 18° exterior half angle. The skimmer aperature is 0.060" dia. The track assembly mentioned above mounts to the

base of the skimmer and thus maintains the nozzle alignment. At present, no water cooling is provided for the skimmer.

In order to test this arc source, a separate vacuum chamber was constructed. As a result of the large quantities of gas that are needed to maintain a stable discharge, a pumping system is required which can provide both high speed and high throughput. Consequently, a 20" dia. oil diffusion pump was used along with a 6" oil diffusion booster pump and a Kinney DVD 8810 mechanical pump [15]. A pumping stand was constructed to provide a moveable base for the pump. The mechanical pump was also mounted on a moveable base, with the two units connected by ~8' of 6" dia. flexible tubing. A 6" ball valve was fitted to the discharge side of the booster pump for isolation. The source test chamber mounted on the 10" I.D. flange of the pumping stand using an O-ring seal. The test chamber itself consists of a 24" long × 10" dia. mild steel TEE. One end of the TEE and the side arm were also fitted with 10" dia. O-ring flanges. The far end of the tube was blanked off leaving only a 6" dia. exit port, equipped with a Varian conflat flange. The skimmer base mounted on this end of the chamber so that the nozzle and skimmer were in alignment with the center of the 6" exit port. Three $2\frac{3}{4}$" conflat sealed feedthrus in the top of the chamber were used to pass electrical power (arc and magnet), cooling water, and gas into the source.

Power for the arc source was provided by a Westinghouse type WS variable current arc welder supply. This unit has an upper limit of 180 amperes, with an open circuit voltage of 90 VDC. The level of the regulated output current could be remotely adjusted

by means of a servo motor built into the power supply. A Westinghouse 0-150 VDC meter was used to monitor the output voltage, while a 0-250 ADC current meter (also Westinghouse) monitored the current.

To protect the various components of the arc heater system from damage or accidental misuse, an interlock-control system was constructed. This unit is designed to shut off the arc power if any failures occur in the other components of the system. Each stage of the interlock is enabled only when the preceding stage is made operational. This sequential control ensures that the arc cannot be started until the system is ready. The first stage controls the Kinney mechanical pump, which will only start if its water cooling is turned on. If the Kinney is operating, and water is flowing through the diffusion pump, then its heater power may be switched on. Both a thermal cut-out switch and an over-pressure switch are provided to protect the diffusion pump. The pressure sensor is a Schulz-Phelps gauge and controller (Granville-Phillips). Once the diffusion pump is on and operating, three additional requirements must be met before the arc will start. These are: (1) cooling water must be flowing, (2) gas must be flowing through source, and (3) the temperature of the cathode tip must be below a preset level. If these requirements are met, the arc power may be applied to the source. To start the arc, a 200 amp lamp starter (Hanovia Model 29912) is used to generate a high voltage pulse. If after the arc is struck, any of the interlock segments fail (such as an overpressure, or a water failure), the arc will immediately be shut off.

At this time, only limited testing of the arc source has been undertaken. In these tests, the source was operated either in air (similar to an inert gas welding torch) or at about 1 torr (produced by the Kinney mechanical only). Starting with a pure argon flow of ~700 torr pressure, the magnetic field was established, and the arc started. A very bright blue-red flame was seen extending 2" to 4" from the nozzle exit. Only the aluminum skimmer base was in place during these tests, and a chromel-alumel thermocouple was placed near where the skimmer tip would be located. A maximum temperature of ~500°C was registered when the outer edges of the arc flame were near the thermocouple.

Some adjustments were needed in the gas flow and operating current to obtain a stable arc. In general, currents of 90-120 amperes and gas pressures of 300 to 500 torr seemed to produce reasonably optimum results. At lower pressures and currents, the arc flame oscillated in intensity and showed variations in the arc voltage (8-15 VDC). This condition often lead to an internal arc being formed which was quickly shut off to prevent damage to the source. A thirty minute run of the source (with a 0.063" dia. nozzle) using only argon produced no discernible erosion of any of the arc pieces, and in fact the entire source was cool to the touch indicating that the arc was operating properly.

As yet, no hydrogen atoms have been produced by the source, although W. C. Stwalley [16] has reported the successful operation of a similar source using hydrogen. Following his experience, the arc will be started using a pure argon beam, and

then slowly switched over to hydrogen. Preliminary attempts to switch to hydrogen have produced a bright yellow flame followed by a loss of the arc discharge. Further testing and characterization of the source is now underway.

Eventually, this source will be installed in the main crossed molecular beam apparatus (see Part I, Section 4). The vacuum system (but not the test chamber) will also be retained for use with the main system.

References

1. J. B. Anderson, R. P. Andres, and J. B. Fenn, in "Advances in Atomic and Molecular Physics," D. R. Bates and I. Estermann, eds., Vol. I, Academic Press, New York, 1965.
2. R. Klinelhofen and P. Lohse, Physics of Fluids 7, 379 (1964).
3. N. Abauf, J. B. Anderson, R. P. Andres, J. B. Fenn, and D. G. H. Marsden, Science 155, 197 (1967).
4. N. G. Utterback, Phys. Rev. 129, 219 (1963).
5. N. G. Utterback and G. H. Miller, Rev. Sci. Instrum. 32, 1101 (1961).
6. N. G. Utterback and G. H. Miller, Phys. Rev. 124, 1477 (1961).
7. G. T. Skinner, Physics of Fluids 4, 1172 (1961).
8. G. T. Skinner and B. H. Fetz, in "Rarefied Gas Dynamics," J. H. deLeeuw, ed., Vol. II, Academic Press, New York, 1966.
9. T. V. Jones, in "Rarefied Gas Dynamics," C. L. Brundin, ed., Vol. II, Academic Press, New York, 1967.
10. E. L. Knuth, Applied Mechanics Rev. 17, 751 (1964).
11. E. L. Knuth, N. M. Kuluva, and J. P. Callinan, Entropie 18, 38 (1967).
12. W. S. Young, W. E. Rodgers, and E. L. Knuth, Rev. Sci. Instrum. 40, 1346 (1969).
13. The author wishes to thank Wayne Rodgers for his assistance in designing the source.
14. W. S. Young, Ph.D. Thesis, University of California, Los Angeles, 1969.

15. The author gratefully acknowledges A. Neubieser and D. Sells of the Caltech synchrotron laboratory for their help in obtaining the diffusion and mechanical pumps.

15. W. C. Stwalley, private communication.

Appendix D

Central-Field Intermolecular Potentials from the Differential Elastic Scattering of $H_2(D_2)$ By Other Molecules*

* This manuscript has been published in Discussions of the Faraday Society 55, 145 (1973).

Central-Field Intermolecular Potentials from the Differential Elastic Scattering of $H_2(D_2)$ By Other Molecules*

ARON KUPPERMANN, ROBERT J. GORDON,† AND M. J. COGGIOLA‡

Arthur Amos Noyes Laboratory of Chemical Physics,§

California Institute of Technology,

Pasadena, California 91109

Received _____

Differential elastic scattering cross sections for the systems $H_2 + O_2$, SF_6, NH_3, CO, and CH_4 and for $D_2 + O_2$, SF_6, and NH_3 have been obtained from crossed beam studies. In all cases, rapid quantum oscillations have been resolved which permit the determination of intermolecular potential parameters if a central-field assumption is adopted. These potentials were found to be independent of both the isotopic form of the hydrogen molecule, and the relative collision energy. As a result of this, and the ability of these spherical potentials to quantitatively describe the measured scattering, it is concluded that anisotropy effects do not seem important in these H_2 (D_2) systems.

INTRODUCTION

The determination of interatomic and intermolecular potentials from molecular beam experiments has received considerable attention over the

*Work supported in part by the U.S. Atomic Energy Commission, Report Code No. CALT-767P4-112.

†Present Address: Naval Research Laboratories, Washington, D.C.

‡Work performed in partial fulfillment of the requirements for the Ph.D. Degree in Chemistry at the California Institute of Technology.

§Contribution No. 4650.

last few years. Early experiments at high energy with various atomic,[1] ionic,[2] and molecular[3] systems yielded essentially structureless total cross sections. In order to determine the scale of the potential from such data, it is essential to have absolute cross sections,[4] which require accurate calibration of beam intensities. It has long been recognized that the calibration problem can be avoided if the cross section has structural features that provide an internal "calibration." Recently, rapid quantum oscillations have been resolved in differential elastic cross sections,[5-9] which provide the necessary calibration. The frequency of such undulations has been related,[10] for central-field potentials, to the range of the potential according to the approximate expression

$$\Delta\theta \approx \frac{\pi\hbar}{\mu v \sigma} \approx \frac{\lambda}{2\sigma} \tag{1}$$

where $\Delta\theta$ is the spacing of the oscillations, μ is the reduced mass, v is the relative collision velocity, σ is a range parameter for the potential (e.g., the zero of the potential), and λ is the de Broglie wavelength. As a result, well resolved rapid oscillations permit the estimation of σ independently of the shape and depth of the potential well. A more quantitative fit of the differential cross sections calculated from an assumed potential to experiment permits one to determine more quantitatively this potential for systems subject to central forces. In particular, information about the depth of the attractive well and the steepness of the repulsive part of the potential can be obtained.

Partly because of the simplicity of interpreting the experiments for central fields, most of the measurements of quantum oscillations have been for atom-atom scattering. The first molecular system found to have

oscillations given by (1) was $D_2 + N_2$, reported by Winicur et al.[6] In the present study, which is a continuation of their work, we have measured the differential elastic cross sections of D_2 and H_2 scattered by O_2, CO, NH_3, CH_4, and SF_6, in order to obtain information about the corresponding intermolecular potentials. The data is discussed from the perspective of a central field approximation. Variation of the relative collision energy and the use of both H_2 and D_2 with the same scattering partner provides a useful test for the validity of this approximation.

Some of the systems reported here have also been studied in total cross section experiments by Butz et al.[11] and by Aquilante et al.[12] Information obtained from total and differential cross section measurements on the same systems are mutually complementary.

EXPERIMENTAL

The crossed molecular beam apparatus is shown schematically in figs. 1 and 2. The main features of the machine are a movable, differentially pumped quadrupole mass spectrometer detector, a differentially pumped supersonic primary beam and a subsonic secondary beam perpendicular to the primary beam, all contained in a bakeable stainless steel 1200 liter main vacuum chamber. The beams intersect the axis of the main chamber at the center of rotation of the detector. The detector chamber is mounted on a semicircular shaped quadrant arm which pivots about the axis of the main chamber, while the detector is free to move along the rim of the quadrant out of the plane of the beams. Thus the detector can scan both colatitudinal and longitudinal angles, although only in-plane measurements were made in the present experiments. Pumping

in the main chamber is by means of four 6" oil diffusion pumps, each having a nominal trapped speed of 1250 ℓ/sec, and a liquid nitrogen cooled titanium sublimation pump, with a calculated speed of 20, 000 ℓ/sec for air. The primary beam source chamber and buffer chamber are pumped by a 6" oil diffusion pump (1250 ℓ/sec) and a 6" mercury diffusion pump (150 ℓ/sec), respectively.

All apertures in the apparatus are circular, with the entrance aperture of the detector housing (0.16 cm in diameter) located 8.05 cm away from the intersection of the beams. The exit aperture of the primary beam chamber (0.21 cm diameter) is located 7.9 cm away from the scattering center, and the secondary effusive source (0.16 cm diameter) is 0.5 cm from the center. The primary beam is formed with the aid of a nozzle-skimmer arrangement giving a measured Mach number of ~15 and an angular FWHM (full width at half maximum) of 1.4°. A jacket surrounding the nozzle tube permits one to cool the entire nozzle assembly to liquid nitrogen temperature.

The secondary beam source consists of a glass capillary array attached to the end of a brass tube, which can be tilted out of the plane of the beams by pumping the air out of a stainless steel bellows attached to this source. When the secondary source is tilted, the two beams do not cross, and the background signal intensity can be measured. This procedure is superior to flagging the secondary beam since the latter method tends to modulate the background as well as the signal. The angular width of the secondary beam is 2.4° FWHM. The FWHM cross section of the beam interesection region in the collision plane has the approximate shape of a rectangle 0.17 cm along the direction of the primary beam and 0.22 cm along the direction of the secondary beam. The angular resolution of the detector is approximately 2°.

The heart of the apparatus is an Extranuclear 324-9 quadrupole mass spectrometer[13] mounted in a bakeable double differentially pumped chamber.

The operating pressure in the ionization region, measured with an uncalibrated Bendix miniature ionization tube, is typically 2×10^{-9} torr with the beams on, whereas in the main chamber, it is about 1×10^{-6} torr under these conditions. To obtain such a large pressure differential, we found it necessary to bake the spectrometer housing and Orbion pump for about 8 hours at approximately 200°C whenever the machine was pumped down from atmospheric pressure. The mass spectrometer chamber is equipped with a bellows activated valve 6 cm in diameter which is kept open to the main chamber during the bake-out period in order to accelerate the removal of background gas.

Particles entering the mass spectrometer chamber pass successively through a high-efficiency electron impact ionizer, a series of electrostatic focusing lenses, and a 23 cm long Paul[14] quadrupole mass filter. Ions are detected by a 14 stage CuBe electron multiplier whose output is amplified by an Extranuclear tuned amplifier followed by a Princeton Applied Research HR-8 phase sensitive detector. The amplified signal is finally converted to digital form by a Raytheon model ADC-24 analog-to-digital converter.

The apparatus is interfaced to an SCC-4700 computer, which serves several functions. First, it tilts the secondary beam in ("on" mode) and out ("off" mode) of the scattering plane. Second, the computer periodically samples and averages the amplified signal and subtracts the background from the total intensity. Third, it calculates the standard deviations for both "on" and "off" modes.

The signal to noise ratio varied from better than 100 at the small scattering angles to a minimum of 10 at the largest one. To correct for long term drift in the signal caused by such factors as fluctuations of beam intensities and gradual build-up of background in the mass spectrometer,

a fixed scattering angle (generally between 3.0° and 5.0°) was chosen as a reference angle. After the measurement of the signal at each scattering angle, the intensity at the reference angle was remeasured to provide a normalization factor. In this way, individual relative intensity points were reproducible to within 5% when remeasured on different days.

RESULTS

The differential cross sections for the systems $H_2 + O_2$, SF_6, CO, NH_3, CH_4 and $D_2 + O_2$, SF_6, NH_3, were all measured using room temperature H_2 and D_2 beams, with a relative collision energy of approximately 0.06 eV. Measurements of the $H_2 + SF_6$ and $H_2 + NH_3$ systems were also made using an H_2 beam cooled to liquid nitrogen temperature, with a relative energy of approximately 0.02 eV. In addition, the SF_6 system was studied using a low temperature beam of para-hydrogen. These experiments scan a wide range in the size, anisotropy and initial relative collision energy of the scattering species, and of the corresponding de Broglie wavelengths. The measured differential elastic cross sections are shown in figs. 3 through 7 along with the on-line computer determined error bars. The various curves drawn through the measured points were fitted to the data as described below.

DETERMINATION OF THE INTERMOLECULAR POTENTIAL

In the interpretation of our data we have assumed that the differential elastic cross sections measured are due to the spherically symmetric part of the intermolecular potentials. The reason for this assumption and the tests of its validity are described in the Discussion section. In our analysis, a model potential function is assumed and the potential parameters are

varied until a least-squares fit of theory to experiment is obtained.

In the present analysis we have used a Lennard-Jones (n, 6) potential, where the repulsive exponent n was either fixed at 12 or 20, or was allowed to vary as a fitted parameter. In addition, a Morse-cubic spline-van der Waals (MSV) potential[15] was used in some systems. The MSV potential is defined by

$$V(r) = \begin{cases} \epsilon \{\exp[-2\beta(r - r_m)] - 2 \exp[-\beta(r - r_m)]\} & r < r_1 \\ \text{cubic spline} & r_1 \leq r \leq r_2 \\ -C_6 r^{-6} & r_2 < r \end{cases}$$

The cubic spline function is a set of five cubic polynomials whose coefficients are chosen to smoothly join the inner and outer branches of the potential. The end points were taken such that $V(r_1) = -0.75\ \epsilon$, and $r_2 = r_1 + 0.2\ r_m$. The fitting parameters were ϵ, r_m, β and C_6. The corresponding differential cross sections were accurately calculated using a partial wave expansion employing both JWKB and high energy eikonal phase shifts, tested against accurate integration of the radial Schroedinger equation to assure the validity of this method. In order to compare the computed cross sections with the data, it is necessary to correct for velocity spread and angular resolution of the apparatus. In trial calculations we found that the former effect tends to dampen the undulations at CM scattering angles $> 15°$ while the latter dampens the small angle scattering to roughly an equal extent. This situation differs from that of Siska et al.[15] who found that under their experimental conditions with both beams supersonic, the effect of angular resolution was dominant at all scattering angles and that they could lump both corrections into a single effective angular

resolution function. Consequently, the calculated cross sections were transformed to the laboratory system and averaged over both the relative collision energy distribution and the detector angular resolution.

The potential parameters were fitted to the data by minimizing the weighted sum of squares of the cross sections calculated as just described and the experimental results, treating the verticle scale coefficient as a fitting parameter. For the Lennard-Jones potentials with n fixed, the fitted parameters ϵ and σ were found using a simple Newton's method. In the case of the MSV (ϵ, r_m, β, C_6) and the three parameter Lennard-Jones (ϵ, σ, n) potentials, a general method due to Marquardt[16] was used. In the following sections, the quoted values for the uncertainties of the potential parameters are those corresponding to a 95% confidence level.

All the systems were initially fitted with an LJ (12, 6) potential. The optimum values of ϵ and σ and their 95% confidence levels are listed in table 1 along with λ, the de Broglie wavelength for each system, and Q the total cross section as calculated from the partial wave expansion. In addition, the results of the LJ (20, 6) and (n, 6) fits are also given in this table. The O_2, SF_6 and NH_3 data were measured with the most accuracy, and hence were chosen for the four parameter MSV fits. The $H_2 + CH_4$ and $H_2 + CO$ data were of poorer reproducibility quality and for this reason not submitted to such fits. The corresponding parameters are listed in table 2 along with the values for λ and Q. Various calculated differential cross sections are shown in figs. 3 through 7. In all cases, the σ thus determined was within 10% of the value predicted by eqn (1). It is worth emphasizing that while the statistical uncertainties in the fitted potential parameters listed in tables 1 and 2 are often quite small, it does not

follow that the "true" values of these quantities (e.g., the actual well depth) must lie within the predicted ranges.

In figs. 8, 9 and 10 are shown fitted LJ and MSV potentials for the O_2, SF_6 and NH_3 data. In each case, the MSV and LJ potential with fitted repulsive parameter are given for the room temperature H_2 system, while only the MSV fit is given for the corresponding D_2 systems. Those potentials not shown, were in general, indistinguishable from those which were plotted. In the case of the SF_6 and NH_3 systems, all three potentials are seen to be in very close agreement, while for the O_2 systems, the agreement is somewhat poorer. In all cases, however, the potentials overlap throughout the range plotted when the uncertainties in the potential parameters are taken into account. Hence, to within the experimental errors, the potentials for the H_2 and D_2 isotopes are the same for a given scattering partner, and the resulting potential is independent of the mathematical form chosen, and of the de Broglie wavelength. It should be noted that agreement of the long range regions of the potentials is expected since both the LJ and MSV forms are chosen to have an r^{-6} dependence, and in addition, the measured scattering is not very sensitive to this region. The range of intermolecular distances sampled in these experiments and depicted in figs. 8 through 10 were approximately estimated by calculating the classical deflection function from the MSV potentials and considering the range of angles in the CM system covered for each system.

DISCUSSION

Ford and Wheeler[17] have shown by semi-classical techniques and for a central-field potential having an overall shape analogous to that of an

LJ (12, 6) potential that when the deflection function has a relative extremum, interference between the attractive and repulsive branches leads to rapid oscillations superimposed on the broader supranumerary rainbow undulations. In the past, oscillations of the sort reported here have been described qualitatively as resulting from such an interference effect. This description is incorrect for our systems because in the quantum limit, where the de Broglie wavelength becomes comparable to the potential range, the Ford and Wheeler analysis is inapplicable. The breakdown of the semiclassical description is seen in at least two ways. First, we have observed strong undulations at angles considerably larger than the rainbow angle, whereas the semiclassical description predicts that the oscillations die out rapidly on the dark side of the rainbow. For example, the LJ (12, 6) fit for the $H_2 + O_2$ system predicts a classical rainbow at 15° in the CM, whereas we see strong oscillations out to 25°. Indeed, the absence of rainbows both in theory and experiment for these systems shows that the semi-classical approach cannot be used here. Second, accurate quantum mechanical theoretical calculations predict oscillations with a spacing given by eqn (1) for purely repulsive potentials with monotonic deflection functions.[18] The Ford and Wheeler analysis, however, reduces to the classical result whenever the deflection function is single-branched, and no undulations are possible. The oscillations in our systems are more accurately described as a diffraction effect produced at the steep repulsive wall of the potential.[19] The presence of an attractive well intensifies the diffraction oscillations and can increase their frequency since in this case the appropriate range parameter to use in eqn (1) is r_m rather than σ. However, since in most cases the van der Waals minimum occurs at a distance r_m only slightly

larger than the zero of the potential, the frequency of the undulations is only slightly affected by the presence of the well.

The intermolecular potentials of the systems we have studied are anisotropic, and consequently the interpretation of our data is more complicated than for atom-atom scattering. One approximate way of coping with this difficulty is to separate the potential into a spherical and an anisotropic part. We then assume that the effect of the latter is unimportant due to a combination of rotational averaging and the likelihood that the decrease of the magnitude of this anisotropy with the intermolecular distance, r, is more rapid than that of the spherically symmetric part making it already sufficiently small for the distance range sampled by the present experiments. A partial wave expansion can then be used to determine the isotropic part of the potential, as was done in the previous section. Such an analysis, however, is not necessarily correct since the anisotropy may dampen or "quench" the oscillations and possibly shift their locations. Rothe and Helbing[20] and Kramer and LeBreton[21] report quenching of the glory undulations in the total scattering cross section of alkali atoms by various large asymmetric molecules. On the other hand, Aquilante et al.[12] find no evidence for quenching in the glory scattering of D_2 by N_2 and several hydrocarbons. Also, Butz et al.[11] were able to fit the glory undulations in the total cross sections of He, HD and D_2 scattered by CH_4, N_2, O_2, NO and CO using a spherical Lennard-Jones (12, 6) potential. Only the CO_2 glories appeared slightly dampened, as compared with their theoretical calculations. Turning to the rainbow maximum, Anlauf et al.[22] found that for Ar + N_2 it was weaker than expected from a Lennard-Jones (n, 6) potential (with best fit obtained for n = 20), and attribute this difference

to quenching. Similarly, Cavallini et al.[23] compared the rainbow of $Ar + N_2$ with that of Ar + Ar and attributed the dampening of its intensity and the shift of its position to higher angles to anisotropy effects. Tully and Lee,[24] after studying the same $Ar + N_2$ system, assume that the shift in the rainbow position to larger angles is negligible, but that the quenching is not, and get a slightly deeper well than Anlauf et al. Stolte[25] measured the total cross section of Ar + NO with the rotational quantum numbers of NO selected to be $J = M_J = 3/2$ on $J = M_J = 5/2$, and found that the anisotropic contribution to the total cross section is less than 1%. Farrar and Lee[26] have seen rapid quantum oscillations in the differential elastic scattering cross section for the $pH_2 + pH_2$ system, and were able to interpret their data using a central-field assumption. Let us now consider the theoretical calculations on anisotropy effects on differential elastic cross sections done so far.

Cross[27] found in an approximate semi-classical calculation, using a potential with an isotropic part similar to that of K + Kr that anisotropy can significantly quench glory, rainbow and "rapid" oscillations. However, Cross' theory, which is based on the Ford and Wheeler treatment of interference between different branches of the deflection function, is inapplicable to our systems where the undulations are produced to a large extent by diffraction at the steep repulsive wall of the potential. Furthermore, they assume that the dependence of the isotropic and anisotropic parts of the potential is identical, an assumption subject to question. Finally, the systems treated in the present paper are more highly quantum than that considered by Cross, and the anisotropic effects are expected to be quantitatively different. Wagner and McKoy,[28] in an exact solution of the

Schroedinger equation for the scattering of Ar + H_2, found no significant quenching or shifting of the rapid quantum undulations. However, their results provide only a lower estimate on these effects since H_2 is more isotropic than other diatomic molecules, and, rotational transitions which play an important role in quenching, are less likely for low energy collisions with H_2.

The range of intermolecular distances sampled in the present experiments, estimated by a semi-classical analysis as described in the previous section, and depicted in figs. 8 through 10, includes part of the repulsive wall and the minimum in the attractive well. We conclude from the present experiments that in this range, and for the hydrogen or deuterium systems considered, effects of anisotropy on the differential cross sections are negligible (within experimental error). This conclusion is based on the following observations. First, the potentials obtained were independent of their assumed mathematical form. Indeed, comparison of the results for the three-parameter LJ(n, 6) potential and the four-parameter MSV potential, as given in figs. 8 through 10, shows that they are nearly equal, even though their mathematical form in the r range sampled by the experiments is substantially different. Second, a variety of different secondary scattering partners were studied. We did not find a correlation between the amplitudes of the observed oscillations and the symmetry of the secondary molecule, as would have been expected for significant anisotropy effects. Third, both H_2 and D_2 were scattered by the same secondary molecule. If quenching and angular shifting of the undulations by the anisotropy in the potential were significant, they would be expected to be sensitive to the relative momentum, or wavelength, of the colliding molecules.

The fitted potential parameters obtained using the central-field assumption for the two isotopes at the same relative collision energy should as a result be different, but as pointed out at the end of the previous section, these potentials are the same to within the experimental errors. Fourth, the potentials for $H_2 + SF_6$ and $H_2 + NH_3$ were determined at two different relative energies (see tables 1 and 2). The fitted parameters are in excellent agreement with each other, a necessary condition for validity of the central-field assumption. Finally, the para-$H_2 + SF_6$ experiments yielded results identical to the normal-$H_2 + SF_6$ scattering at the same relative energy, to within experimental error, thus indicating the insensitivity of the measurements to the distribution of H_2 initial rotational states. In summary, we have found it possible in every case to describe the measured differential elastic scattering cross sections using a spherically symmetric potential which is independent of the de Broglie wavelength λ of the experiment.

Both the position and the amplitude of the rapid oscillations, as well as the overall shape of the cross section are accurately fitted by such spherical potentials, and no effects of anisotropy are observed.

Butz et al.[11] have fitted a LJ(12, 6) potential to their total cross section measurements of $D_2 + O_2$, $D_2 + CO$ and $D_2 + CH_4$. The total cross section results yield the product $\epsilon\sigma$, but do not give reliable estimates for the individual parameters. Aquilante et al.'s results[12] for $D_2 + CH_4$ agree with those of Butz et al. To compare the latter's results with our own, we have used their $\epsilon\sigma$ product values and determined the individual parameters by the Newton's method described in the previous section. Based on our previous conclusions that the H_2 and D_2 isotopes yield the same scattering

potentials, these calculations were done for the $H_2 + O_2$, $H_2 + CO$ and $H_2 + CH_4$ systems in which the quantum undulations are more pronounced. The results of these restricted fits are given in table 3, along with the unrestricted ones, as well as those obtained by Butz et al. from their total cross sections. The corresponding differential cross sections are shown in fig. 11 for $H_2 + O_2$. In addition, our LJ (12, 6) best fit cross section is reproduced for comparison. It is clear that neither the total cross section data, nor the best fit obtained using the constrained product of $\epsilon\sigma$ give as good an agreement as the unconstrained LJ (12, 6) fit. While this is true for all of the systems compared, it should be noted that the results obtained from the constrained fit are in much better agreement with the differential cross section data than are the predictions from the separate parameters obtained from the total cross sections. This emphasizes the value of total cross section measurements in determining $\epsilon\sigma$ product values, while giving less reliable estimates of the separate parameters. In contrast, differential cross section measurements of the type reported here yield a more accurate description of the intermolecular potential, indicating among other things deviations from the LJ (12, 6) expression, as shown from the $H_2(D_2) + O_2$ system in fig. 3.

In concluding, it should be remarked that the lack of anisotropy effects for the $H_2(D_2)$ containing systems described in the present paper, are probably due at least in part to the fact that this molecule is nearly spherical. In addition, rotational excitation processes probably result from small orbital angular momenta and manifest themselves at large scattering angles, in a manner determined mainly by the intermolecular potential at distances shorter than those sampled in the present experiments. One should be extremely cautious in attempting to extend these conclusions to other systems.

REFERENCES

1. See for example, J. Amdur and J. B. Jordan, Adv. Chem. Phys. Vol. X, pp. 29-74 (Interscience, New York, 1966) and references cited therein.
2. A. J. H. Boerboom, H. Van Dop and J. Los, Physica, 1970, 46, 458.
3. Yw. N. Belayev, N. V. Kamyshon, V. B. Leonas and A. V. Smeryagin, Entropie, 1969, 30, 173.
4. The same is true for differential cross sections. See, for example, William H. Miller, J. Chem. Phys., 1969, 51, 3631.
5. U. Buck and H. Pauly, J. Chem. Phys., 1971, 54, 1929.
6. Daniel H. Winicur, A. L. Morsund, W. R. Devereaux, L. R. Martin, and Aron Kuppermann, J. Chem. Phys., 1970, 52, 3299.
7. M. Cavallini, L. Meneghetti, G. Scoles, and M. Yealland, Phys. Rev. Lett., 1970, 24, 1469.
8. D. Auerbach, C. Detz, K. Reed, and L. Wharton, Abstracts from VII ICPEAC (North-Holland, Amsterdam, 1971), pp. 541-542.
9. J. M. Farrar and Y. T. Lee, J. Chem. Phys., 1972, 56, 5801, and earlier papers cited therein.
10. See, for example, Richard B. Bernstein, Adv. Chem. Physics, Vol. X, (Interscience, New York, 1966), John Ross, ed., Eq. (VI.6), with
$$L_a \approx L_o \approx \frac{\mu v b}{\hbar} .$$
11. H. P. Butz, R. Feltgen, H. Pauly and H. V. Vehmeyer, Z. Physik, 1971, 247, 70.
12. V. Aquilante, G. Liuti, F. Vecchio-Cattivi and G. G. Volpi, Molecular Physics, 1971, 21, 1149.
13. Extranuclear Laboratories, Inc., Pittsburgh, Pennsylvania.
14. W. Paul and H. Steinwedel, Z. Naturforsch, 1953, 8a, 448.

15. P. E. Siska, J. M. Parson, T. P. Schafer, and Y. T. Lee, J. Chem. Phys. 1971, 55, 5762.

16. D. W. Marquardt, J. Soc. Ind. Appl. Math., 1963, 11, 431.

17. Kenneth W. Ford and John A. Wheeler, Ann. Phys., 1959, 7, 259.

18. John Adams, Ph.D. Thesis, University of Arkansas, 1969.

19. Robert J. Gordon and Martin Griss, to be published.

20. Erhard W. Rothe and Reinhard K. B. Helbing, J. Chem. Phys., 1970, 53, 2501.

21. H. L. Kramer and P. R. LeBreton, J. Chem. Phys., 1967, 47, 3367.

22. K. G. Anlauf, R. W. Bickes Jr., and R. B. Bernstein, J. Chem. Phys., 1971, 54, 3647.

23. M. Cavallini, M. G. Dondi, G. Scoles and U. Valbusa, Chem. Phys. Lett., 1971, 10, 22.

24. F. P. Tully and Y. T. Lee, J. Chem. Phys., 1972, 57, 866.

25. Steven Stolte, Ph.D. Thesis, Catholic University of Nijmegen, 1972.

26. J. M. Farrar and Y. T. Lee, J. Chem. Phys., 1972, 57, 5492.

27. R. J. Cross, J. Chem. Phys., 1970, 52, 5703.

28. A. F. Wagner and V. McKoy, J. Chem. Phys., 1972, 58.

TABLE 1 - LENNARD-JONES (n, 6) POTENTIAL PARAMETERS AND TOTAL CROSS SECTIONS

System	n	σ (A)	ϵ (meV)	λ (A)	Q (A^2)
$H_2 + O_2$	12	3.38 ± 0.03	7.7 ± 0.9	0.84	208 ± 15
	13.2	3.40 ± 0.04	7.2 ± 0.9	"	182 ± 12
	20	3.46 ± 0.04	7.6 ± 1.2	"	169 ± 15
$D_2 + O_2$	12	3.5 ± 0.2	7.3 ± 0.6	0.61	270 ± 21
	13.6	3.5 ± 0.3	7.0 ± 0.7	"	251 ± 20
	20	3.6 ± 0.2	6.7 ± 0.9	"	222 ± 20
$H_2 + SF_6$	12	4.05 ± 0.06	10.4 ± 0.5	0.81	380 ± 41
	16.2	4.12 ± 0.04	10.4 ± 0.3	"	361 ± 30
	20	4.15 ± 0.04	10.4 ± 0.8	"	335 ± 31
	12	4.15 ± 0.08	9.6 ± 0.3	1.52	326 ± 31
	16.3	4.18 ± 0.05	10.0 ± 0.2	"	325 ± 28
	20	4.14 ± 0.04	10.5 ± 0.2	"	313 ± 19
$D_2 + SF_6$	12	4.2 ± 0.4	10.3 ± 0.6	0.58	380 ± 32
	19.1	4.2 ± 0.2	10.3 ± 0.3	"	331 ± 30
	20	4.2 ± 0.2	10.3 ± 0.4	"	334 ± 31
$H_2 + NH_3$	9.1	3.34 ± 0.07	9.6 ± 1.2	0.87	225 ± 15
	12	3.45 ± 0.06	9.8 ± 1.4	"	260 ± 18
	9.1	3.34 ± 0.09	10.3 ± 0.7	1.56	256 ± 17
	12	3.34 ± 0.08	10.3 ± 0.8	"	255 ± 17
$D_2 + NH_3$	9.2	3.39 ± 0.08	9.1 ± 0.8	0.65	250 ± 21
	12	3.26 ± 0.07	9.1 ± 0.7	"	245 ± 21
$H_2 + CO$	12	3.5 ± 0.1	6.9 ± 1.5	0.84	210 ± 18
$H_2 + CH_4$	12	3.7 ± 0.2	9.9 ± 1.4	0.87	317 ± 26

TABLE 2 - MORSE-SPLINE-VAN DER WAALS (MSV) POTENTIAL PARAMETERS AND TOTAL CROSS SECTIONS

System	σ (A)	r_m (A)	ϵ (meV)	β	C_6 (eVA^6)	λ (A)	Q (A^2)
$H_2 + O_2$	3.34 ± 0.05	3.86 ± 0.05	7.2 ± 0.6	5.2 ± 0.4	64.8 ± 0.7	0.84	213 ± 19
$D_2 + O_2$	3.5 ± 0.2	4.03 ± 0.2	6.9 ± 0.9	4.8 ± 0.4	63.1 ± 0.6	0.61	291 ± 26
$H_2 + SF_6$	4.14 ± 0.02	4.63 ± 0.02	10.0 ± 0.2	6.5 ± 0.5	57.2 ± 0.3	0.81	396 ± 33
	4.16 ± 0.03	4.64 ± 0.03	10.2 ± 0.2	6.3 ± 0.6	55.9 ± 0.5	1.52	325 ± 31
$D_2 + SF_6$	4.2 ± 0.2	4.62 ± 0.2	10.4 ± 0.8	6.6 ± 0.6	54.6 ± 0.5	0.58	389 ± 38
$H_2 + NH_3$	3.42 ± 0.05	3.80 ± 0.05	9.7 ± 0.5	4.9 ± 0.4	58.2 ± 0.6	0.87	288 ± 21
	3.32 ± 0.05	3.88 ± 0.05	10.2 ± 0.5	4.8 ± 0.4	59.2 ± 0.7	1.56	242 ± 20
$D_2 + NH_3$	3.23 ± 0.05	3.77 ± 0.05	9.0 ± 0.8	4.9 ± 0.4	59.8 ± 0.7	0.65	258 ± 18

TABLE 3 - COMPARISON WITH LJ (12,6) PARAMETERS OBTAINED FROM TOTAL CROSS SECTION MEASUREMENTS

System	σ (A)	ϵ (meV)	REF
$H_2 + O_2$	3.38 ± 0.03	7.7 ± 0.9	This work
	2.99	6.3	Ref. 11
	3.37 ± 0.05	5.6 ± 1.2	(a)
$H_2 + CO$	3.5 ± 0.1	6.9 ± 1.5	This work
	3.11	5.7	Ref. 11
	3.41 ± 0.4	5.2 ± 1.5	(a)
$H_2 + CH_4$	3.7 ± 0.2	9.9 ± 1.4	This work
	2.95	7.4	Ref. 11
	3.52 ± 0.3	6.2 ± 2.0	(a)
	3.6	6.0	Ref. 12
	3.53 ± 0.3	6.2 ± 2.0	(a)

(a) These values were obtained by holding the product $\epsilon\sigma$ constant, while allowing σ to vary to give a best fit to the experimental data.

Figure Captions

Fig. 1. Vertical cross section of molecular beam apparatus. N - primary nozzle source, S - skimmer cone, VS - velocity selector, C - primary beam chopper, F - beam flag, CA - secondary beam glass capillary array, IS - electron bombardment ionizer, MF - quadrupole mass filter, EM - electron multiplier, TSP - titanium sublimator pump, OP - Orbion pump, IG - ionization gauge, BV - bellows operated bakeout valve, VP - pyrex view port.

Fig. 2. Crossed beam geometry. Θ is the measured laboratory scattering angle.

Fig. 3. Plot of the product of the scattered intensity I times the sine of the angle Θ against Θ in the laboratory system of reference for $H_2 + O_2$ and $D_2 + O_2$ collisions. The lower curve has been shifted downwards by one decade. Points are experimental, and curves are theoretical fits. The solid curves are the MSV fits, and the corresponding potentials were used to establish the outer and inner ordinate scales for the $H_2 + O_2$ and $D_2 + O_2$ results, respectively. The upper dashed curve is the LJ (12, 6) fit, and the dotted curves are the LJ (n, 6) fits.

Fig. 4. Differential scattering results for (room temperature) $H_2 + SF_6$ and $D_2 + SF_6$ collisions. Explanation of the curves is the same as Fig. 3.

Fig. 5. Differential scattering results for (room temperature) $H_2 + NH_3$ and $D_2 + NH_3$ collisions. Explanation of the curves as for Fig. 3. The LJ (12, 6) fits were indistinguishable from the LJ (n, 6) ones and were not plotted.

Fig. 6. Low temperature results for $H_2 + NH_3$ and $H_2 + SF_6$ collisions. Explanation of curves is given in Fig. 3. The LJ (n, 6) curve for $H_2 + NH_3$ was indistinguishable from the MSV curve and was not plotted. Results using para-hydrogen $+SF_6$ were identical to those shown for normal-hydrogen.

Fig. 7. Differential scattering results for the $H_2 + CH_4$ and $H_2 + CO$ collisions. Only LJ (12, 6) fits were attempted, and they are shown by the solid curves.

Fig. 8. Comparison of the intermolecular potentials over the range of distances sampled for $H_2 + O_2$ (λ = 0.84 A) and $D_2 + O$ (λ = 0.61 A), determined from the data in Fig. 3. The solid curve is the $H_2 + O_2$ MSV potential, while the dashed curve is the $H_2 + O_2$ LJ (n, 6) potential. The dotted curve represents the $D_2 + O_2$ MSV potential.

Fig. 9. Comparison of the intermolecular potentials for $H_2 + SF_6$ (λ = 0.81 A) and $D_2 + SF_6$ (λ = 0.58 A). Explanation of the curves is given in Fig. 8. The corresponding curves for $H_2 + SF_6$ at λ = 1.52 A are indistinguishable from those at λ = 0.81 A, within plotting accuracy.

Fig. 10. Comparison of the intermolecular potentials for $H_2 + NH_3$ (λ = 0.87 A) and $D_2 + NH_3$ (λ = 0.65 A). Explanation of the curves is given in Fig. 8. The corresponding curves for $H_2 + NH_3$ at λ = 1.56 A are indistinguishable from those at λ = 0.87 A, within plotting accuracy.

Fig. 11. Comparison of the differential elastic scattering predicted by total cross section measurements with the experimental $H_2 + O_2$ data from Fig. 3. The solid curve represents the LJ (12, 6) fit given in Table 1. The

dotted curve was determined using the LJ (12, 6) ϵ and σ parameters of Butz et al.[11] given in Table 3, while the dashed curve was fitted to the data using the $\epsilon\sigma$ product determined by Butz et al.

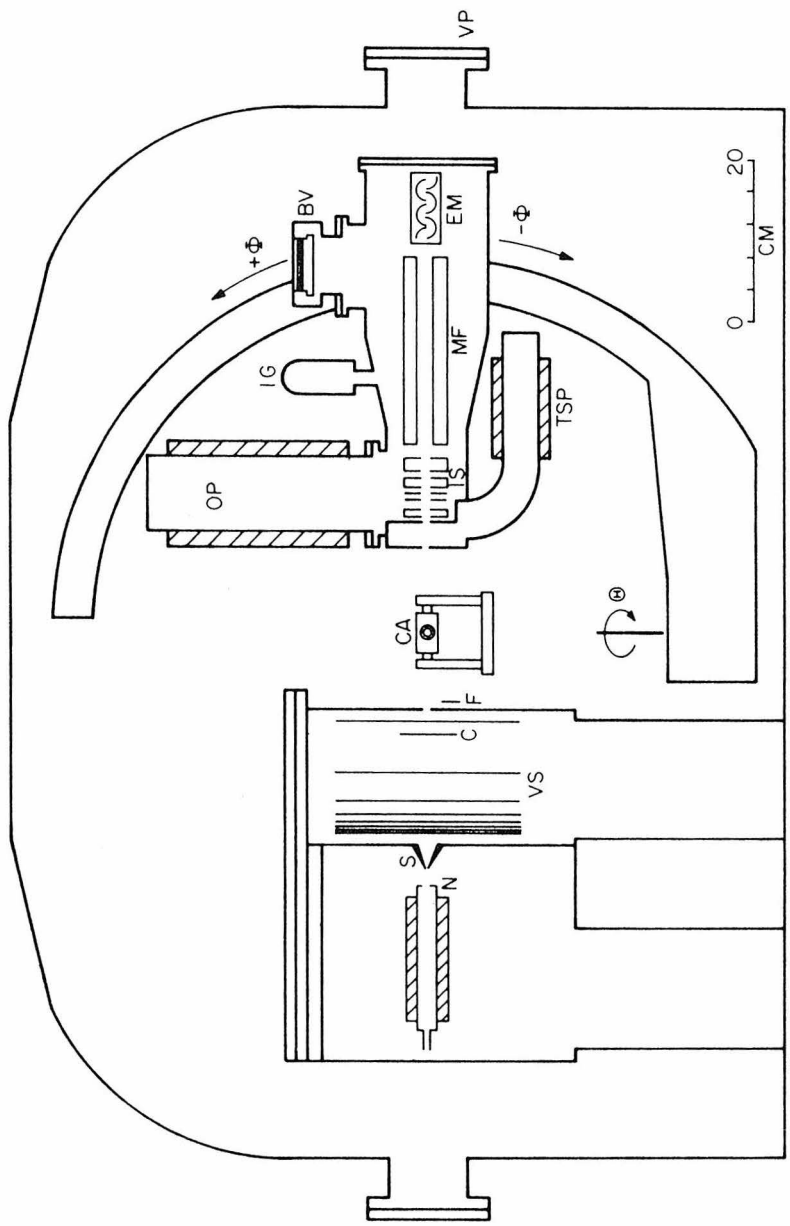

D-1

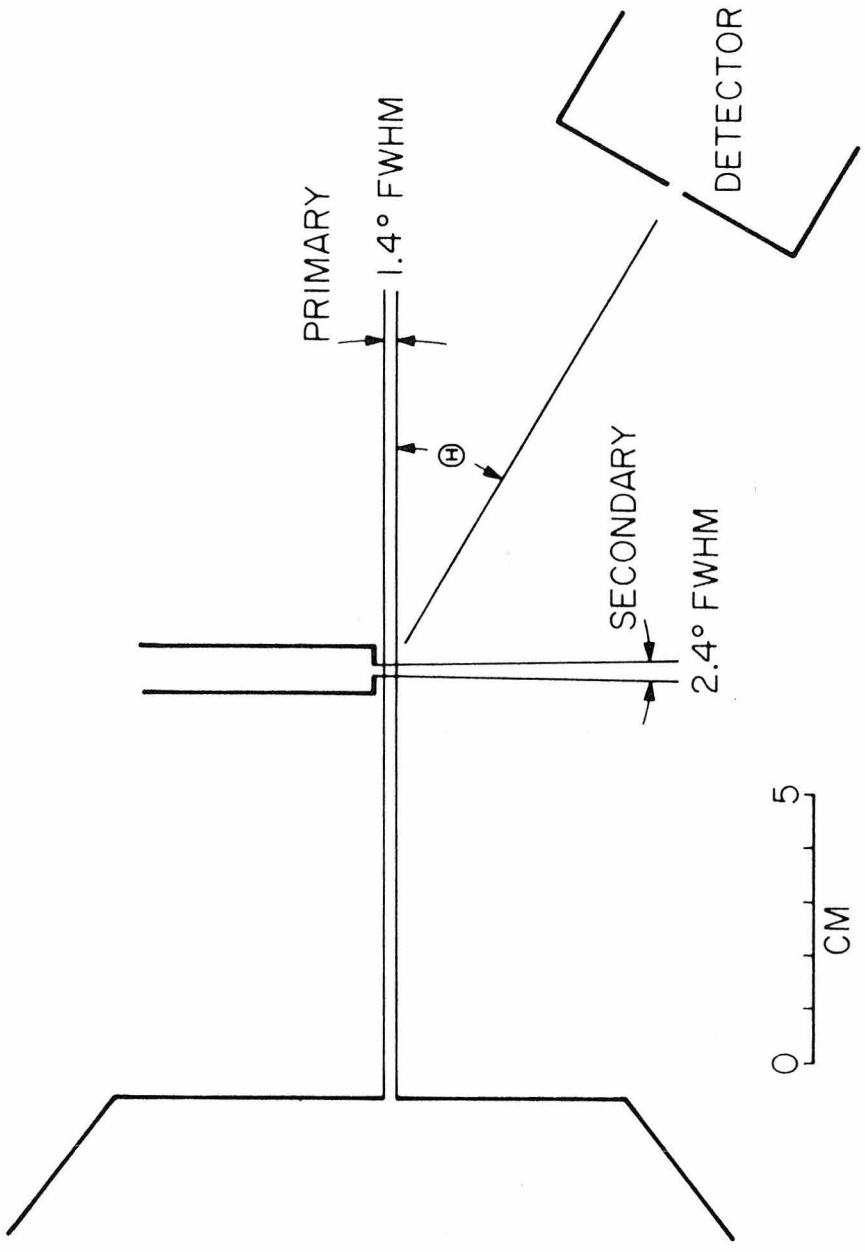

D-2

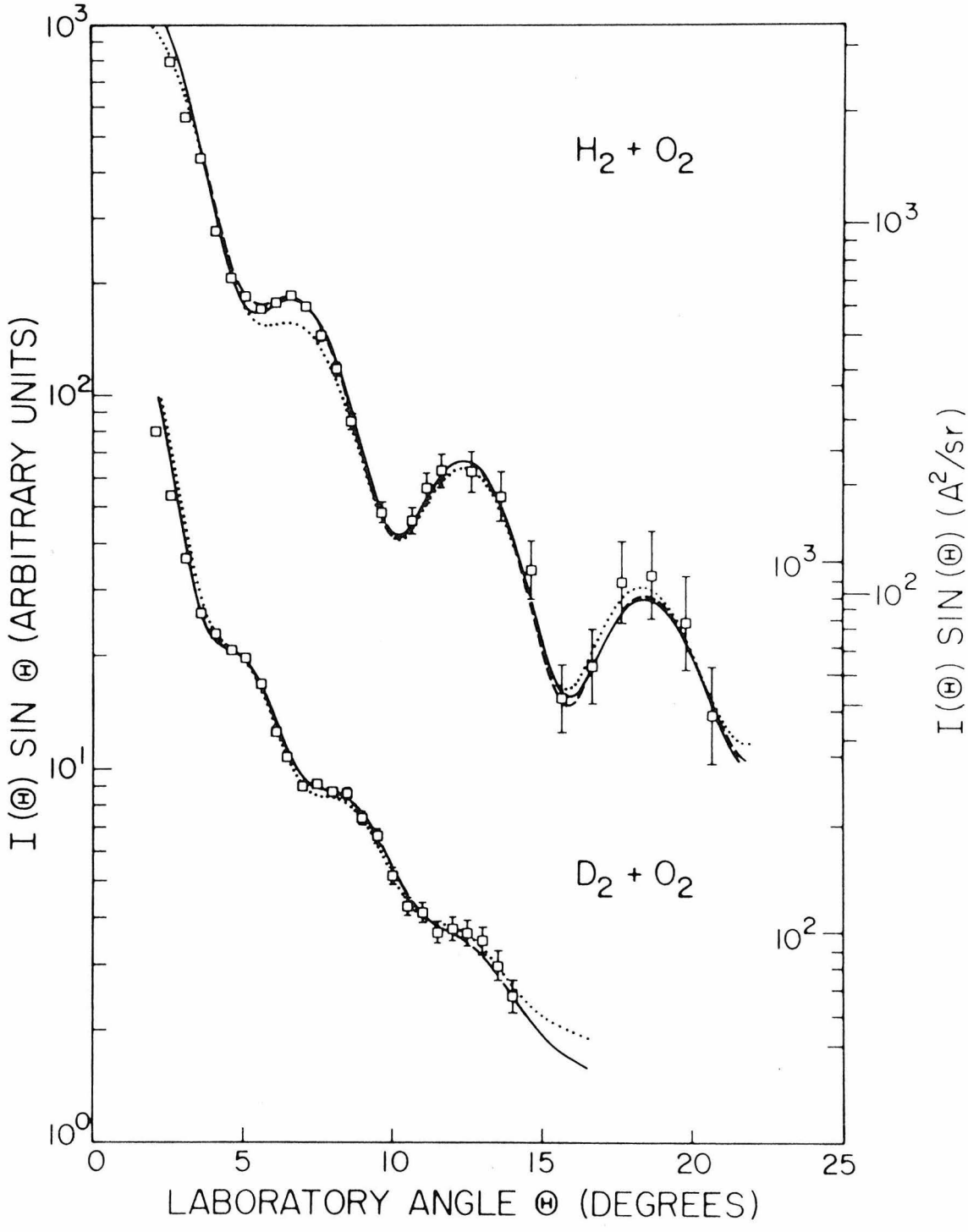
$H_2 + O_2$
$D_2 + O_2$
$I(\Theta)$ SIN Θ (ARBITRARY UNITS)
$I(\Theta)$ SIN (Θ) (A^2/sr)
LABORATORY ANGLE Θ (DEGREES)
10^0
10^1
10^2
10^3
0
5
10
15
20
25

D-3

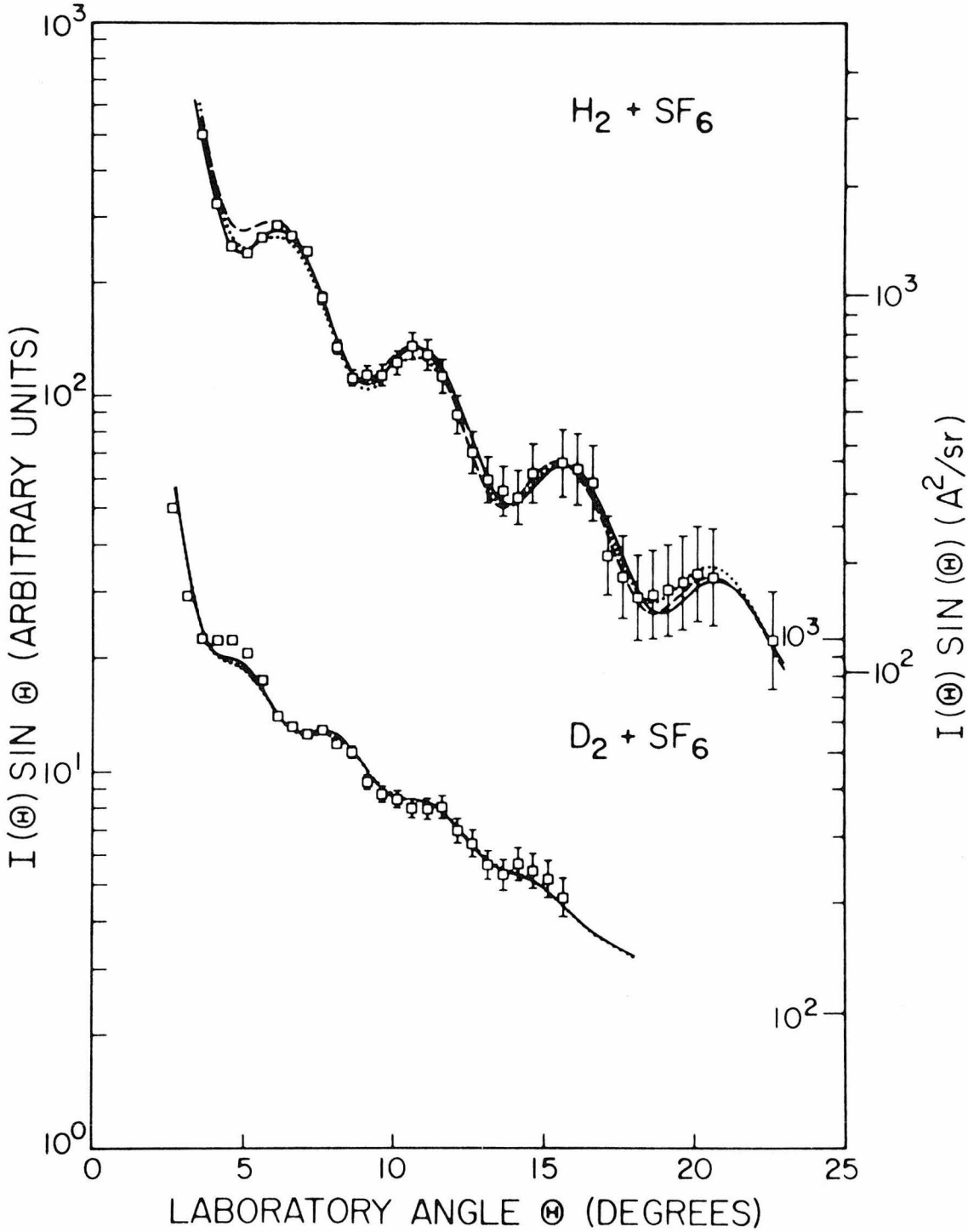
$H_2 + SF_6$
$D_2 + SF_6$
$I(\Theta) \sin \Theta$ (ARBITRARY UNITS)
$I(\Theta) \sin(\Theta)$ (A^2/sr)
LABORATORY ANGLE Θ (DEGREES)
10^3
10^2
10^1
10^0
0
5
10
15
20
25

D-4

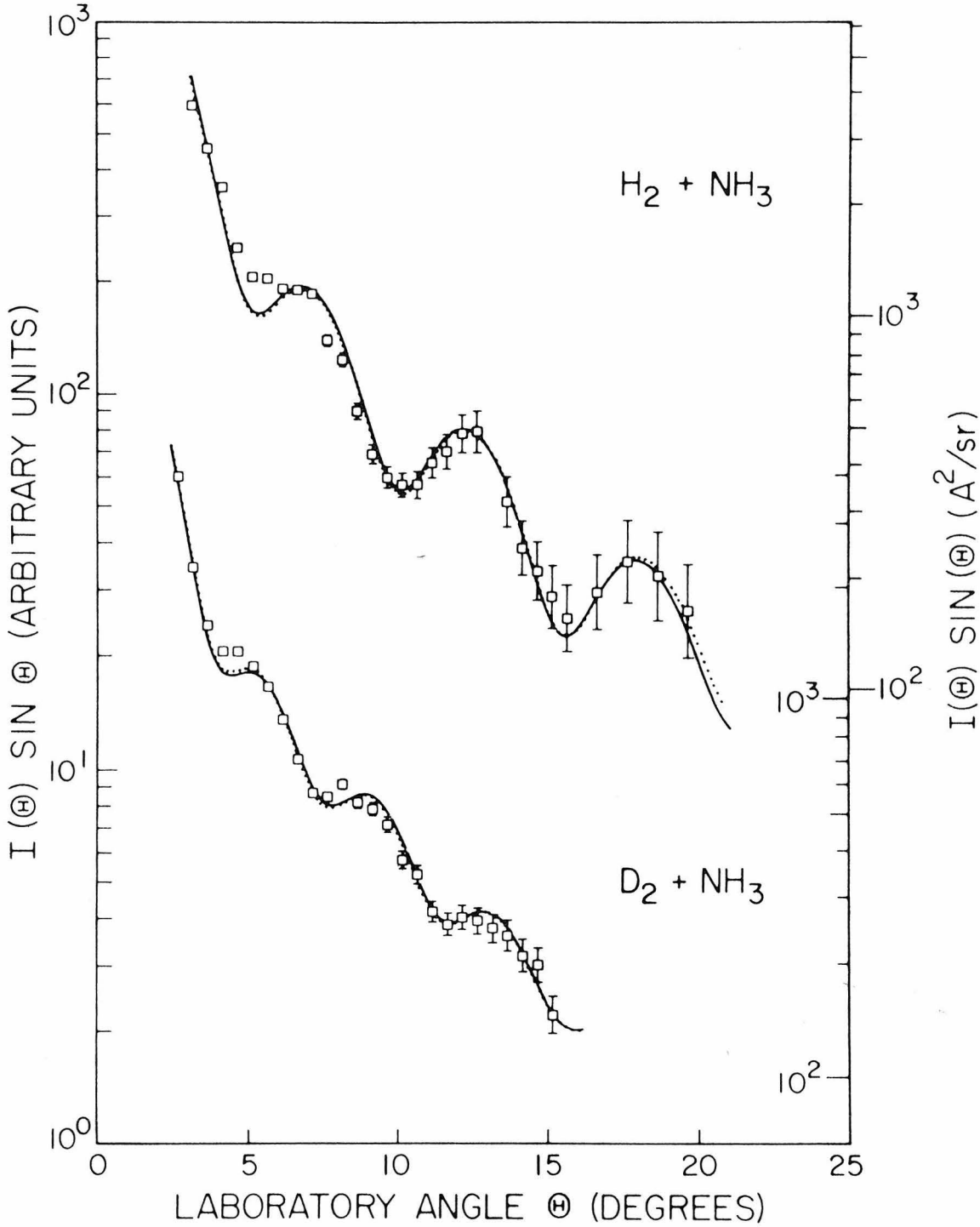
$H_2 + NH_3$
$D_2 + NH_3$
I (Θ) SIN Θ (ARBITRARY UNITS)
I(Θ) SIN (Θ) (A^2/sr)
LABORATORY ANGLE Θ (DEGREES)
10^0
10^1
10^2
10^3
0
5
10
15
20
25

D-5

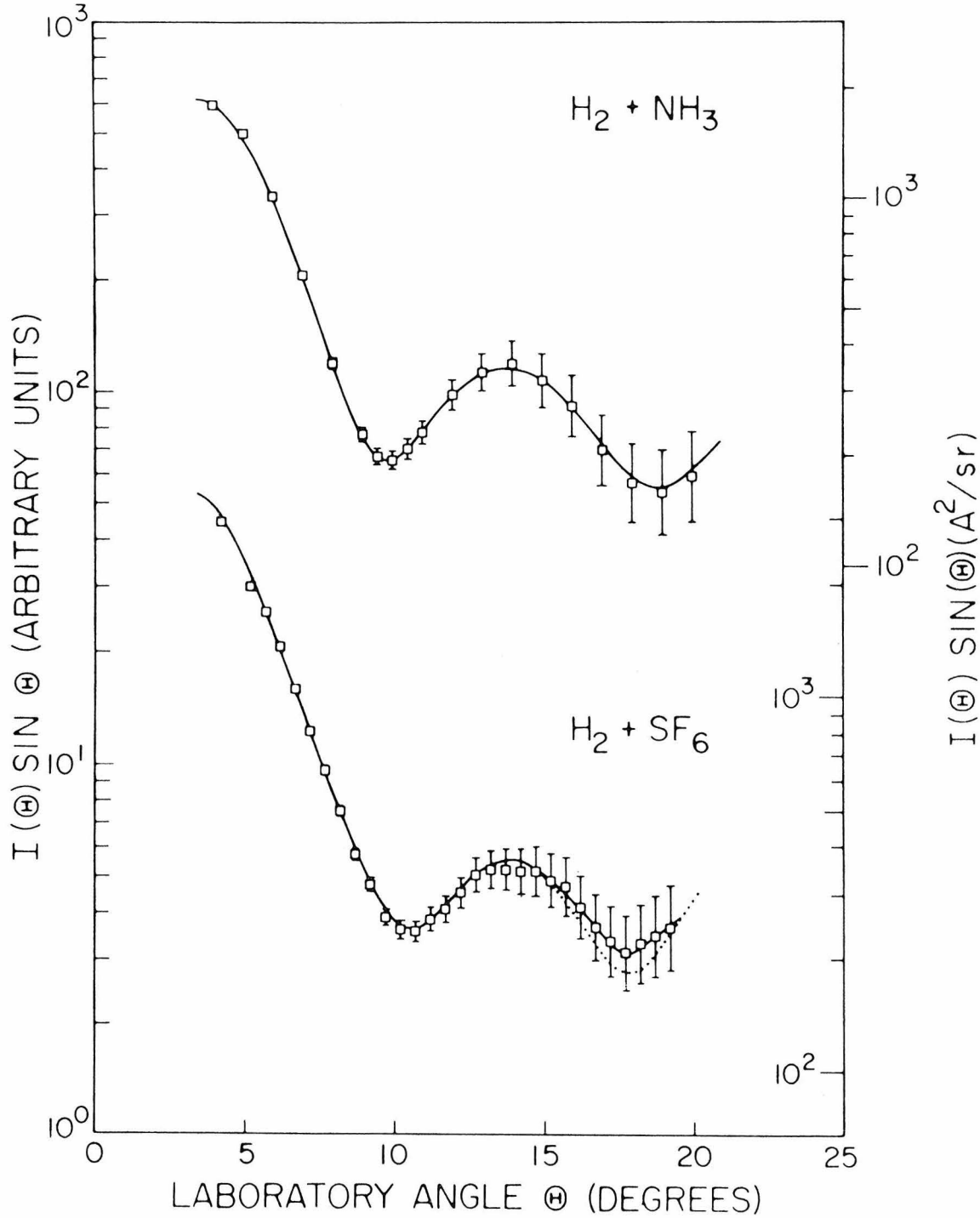
$H_2 + NH_3$
$H_2 + SF_6$
$I(\Theta) \sin \Theta$ (ARBITRARY UNITS)
$I(\Theta) \sin(\Theta)(A^2/sr)$
LABORATORY ANGLE Θ (DEGREES)
10^0
10^1
10^2
10^3
0
5
10
15
20
25

D-6

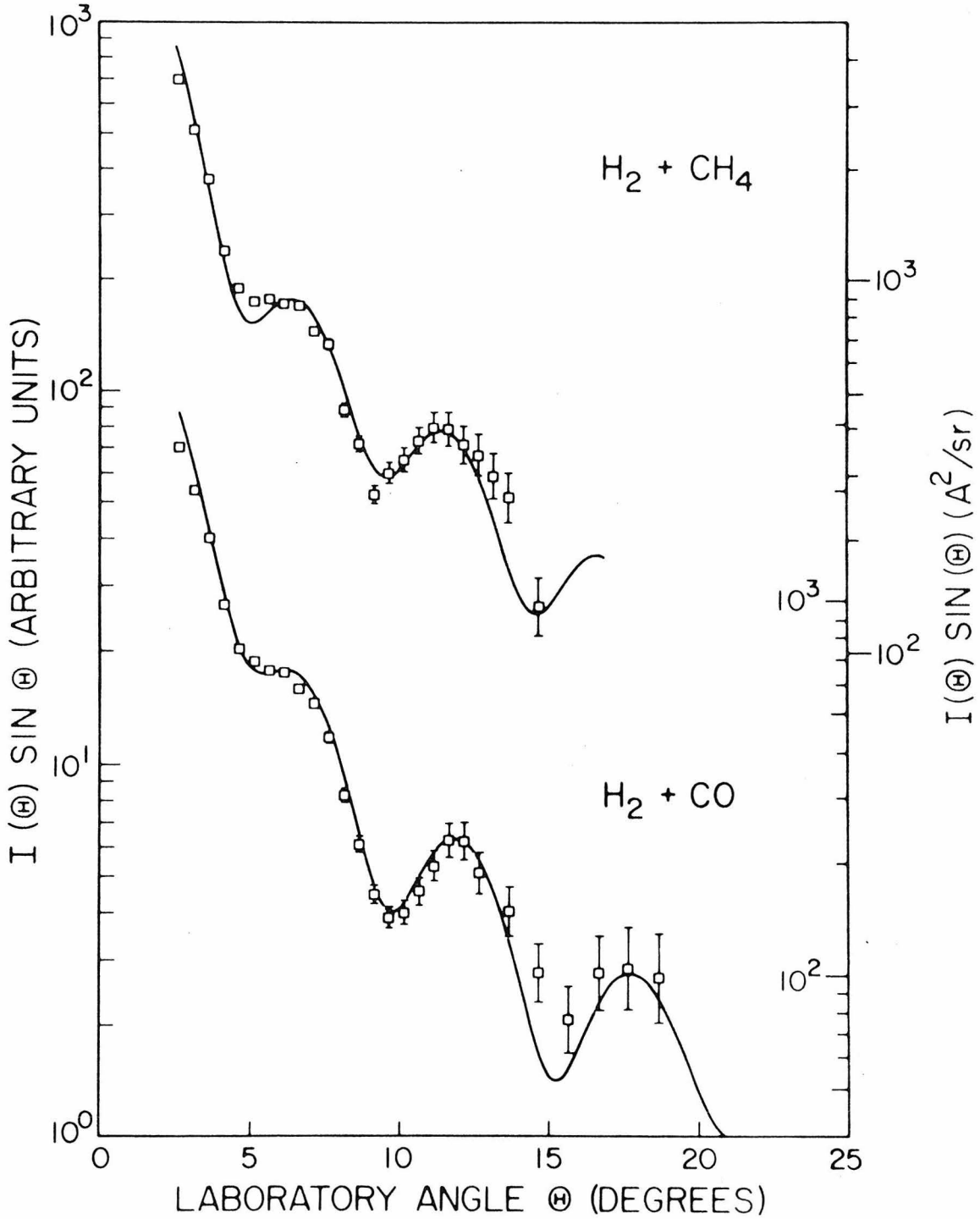
10^3
10^2
10^1
10^0
$H_2 + CH_4$
$H_2 + CO$
I (Θ) SIN Θ (ARBITRARY UNITS)
I(Θ) SIN (Θ) (A^2/sr)
10^3
10^2
10^3
10^2
0
5
10
15
20
25
LABORATORY ANGLE Θ (DEGREES)

D-7

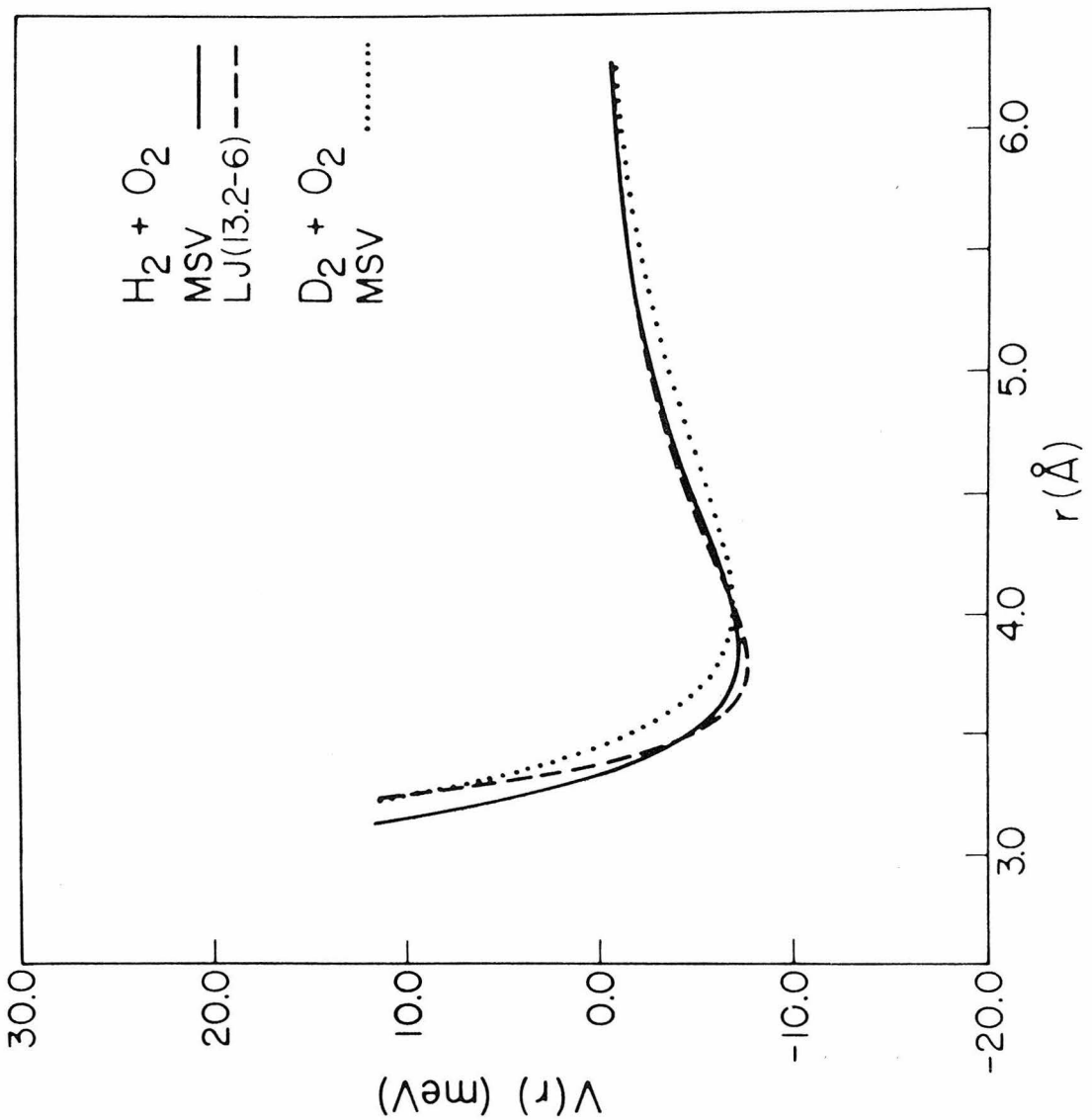
H_2 + O_2
MSV
LJ(13.2-6)
D_2 + O_2
MSV
V(r) (meV)
r(Å)
30.0
20.0
10.0
0.0
-10.0
-20.0
3.0
4.0
5.0
6.0

D-8

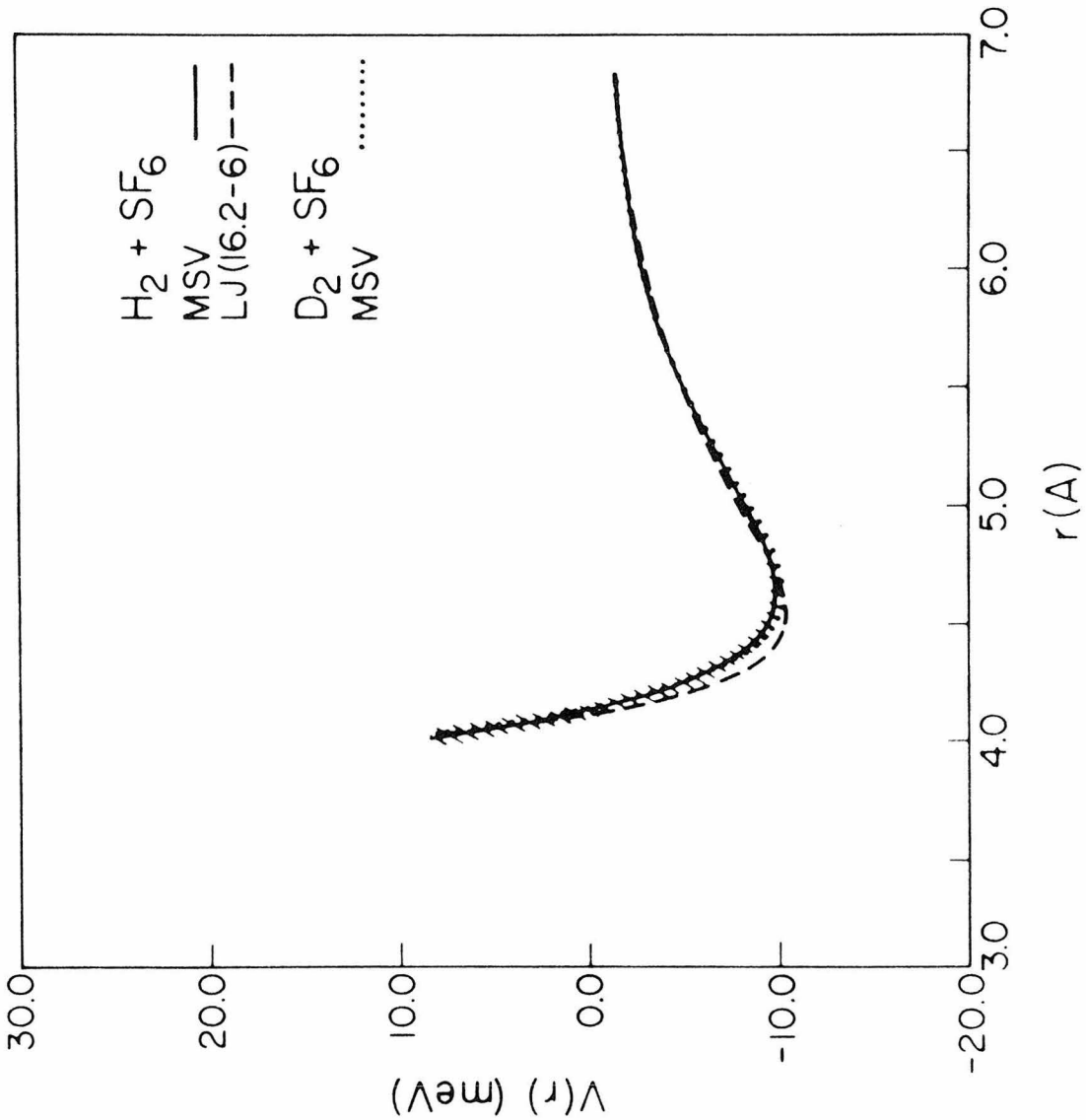
H_2 + SF_6
MSV
LJ(16.2-6)
D_2 + SF_6
MSV
V(r) (meV)
r(A)
30.0
20.0
10.0
0.0
-10.0
-20.0
3.0
4.0
5.0
6.0
7.0

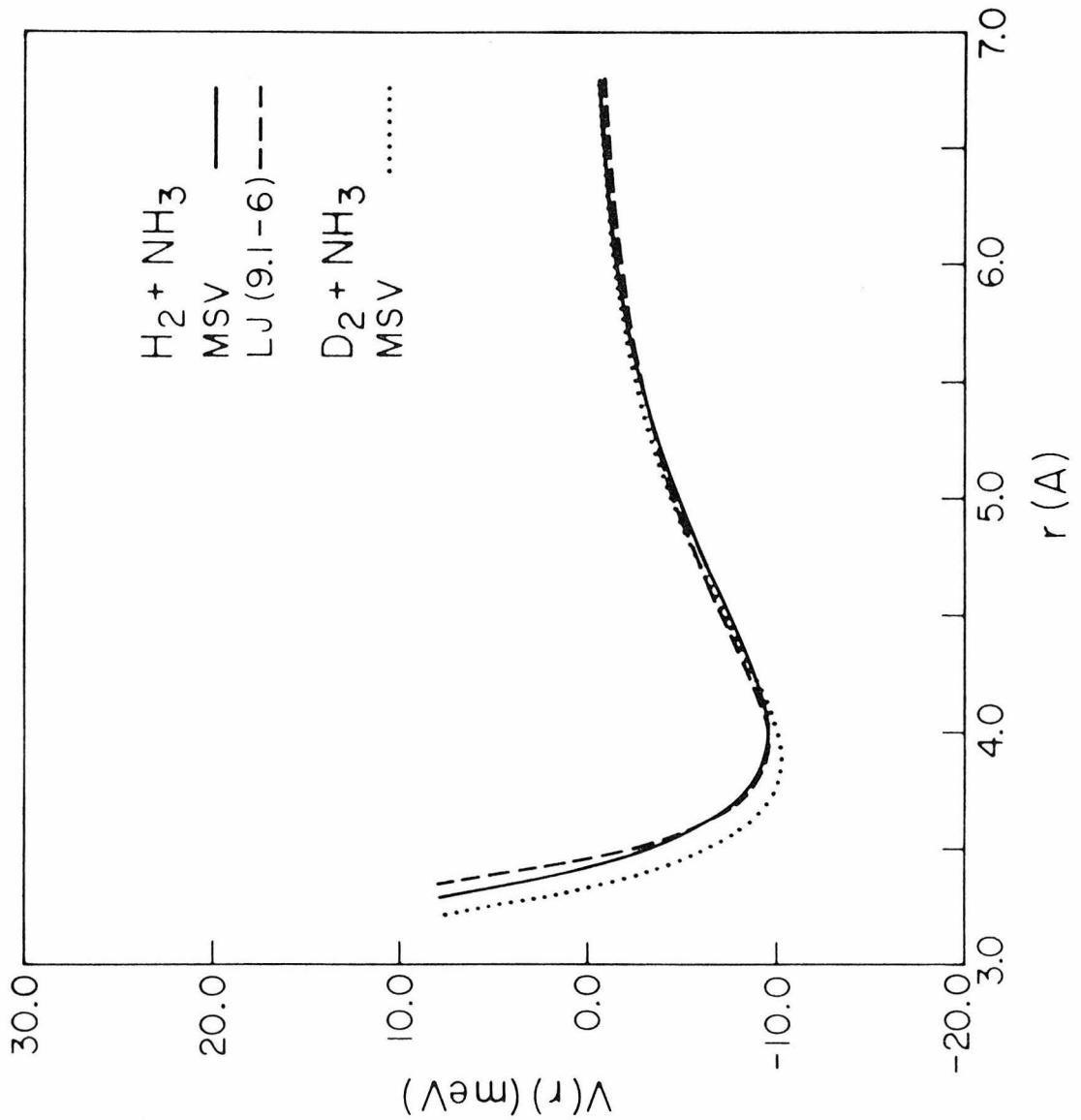
H_2 + NH_3
MSV
LJ (9.1-6)
D_2 + NH_3
MSV
V(r) (meV)
r (A)
30.0
20.0
10.0
0.0
-10.0
-20.0
3.0
4.0
5.0
6.0
7.0

D-10

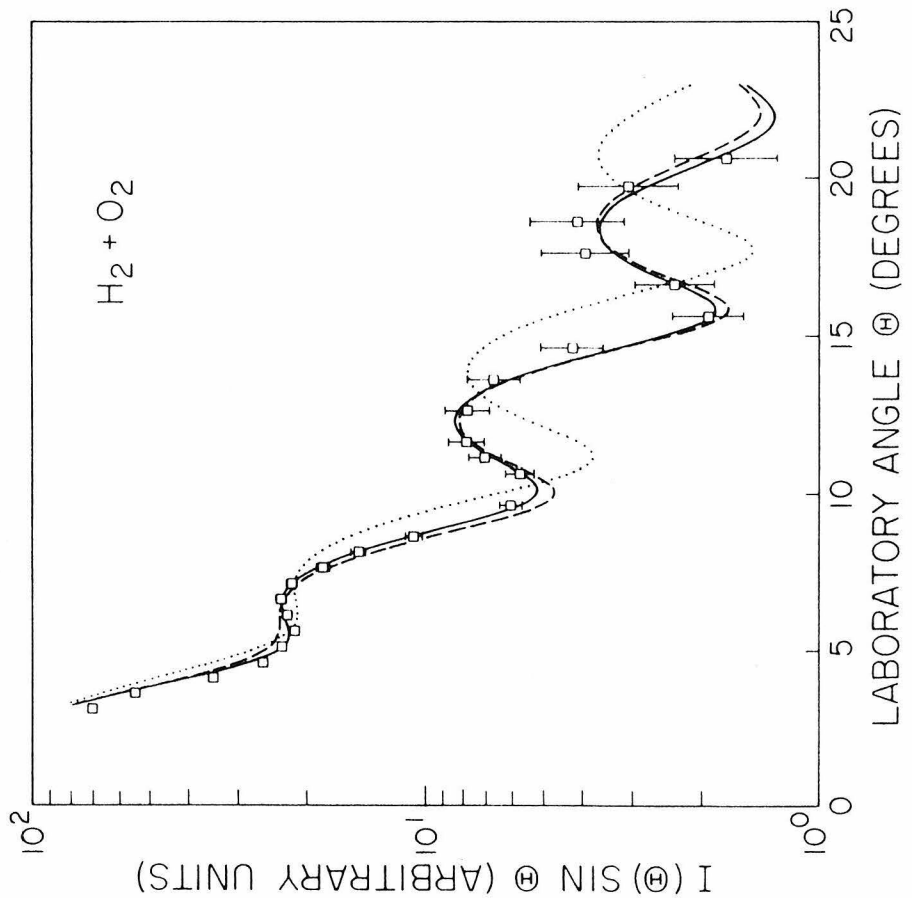
$H_2 + O_2$
I (Θ) SIN Θ (ARBITRARY UNITS)
LABORATORY ANGLE Θ (DEGREES)
10^2
10^1
10^0
0
5
10
15
20
25

PART II

ELECTRONIC EXCITATION SPECTROSCOPY OF THE FLUORINE-SUBSTITUTED ETHYLENE BY ELECTRON IMPACT

1. INTRODUCTION

In contrast to the study of low energy molecule-molecule elastic scattering discussed in Part I, it is the inelastic scattering of low energy electrons from molecules that is of prime interest here. The possible inelastic events include; the internal excitation of the molecule (electronic, vibrational or rotational) either by direct energy transfer or by electron exchange, ionization, electron attachment to form negative ions, fragmentation, or some combination of these. While each of these processes can yield important information regarding various molecular properties, the production of internal electronic excitation of the molecule is particularly valuable. To see this, it is only necessary to envision a simple scattering experiment (similar to the total cross section measurements discussed in part I, Section 2) in which a beam of energy selected electrons passes through a chamber containing the target gas molecules. By detecting the number of electrons that suffer inelastic collisions as a function of their energy-loss (due to the excitation of various electronic transitions within the molecule) it is possible to measure directly the inelastic scattering cross section. Under the proper experimental conditions, this scattering cross section corresponds exactly to the electronic excitation spectrum of the molecule. This technique is known as electron impact spectroscopy.

While it is true that the highly developed field of photon spectroscopy can generate electronic excitation spectra as well, there are several important advantages associated with the use

of electron impact spectroscopy. First, many of the selection rules [1] which govern the possible types of transitions allowed by photon excitation do not hold under electron impact conditions. Specifically, it is known that electrons whose kinetic energy is within a few tens of an electron volt of an excitation threshold can produce spin-forbidden transitions (that is, $S \rightarrow S \pm 1$). These transitions arise via the mechanism of exchange scattering [2] where the incident electron replaces one of the bound electrons in the molecule. Thus, the total spin of the electron + molecule system remains constant, while the spin multiplicity of the molecule changes. Excitations involving symmetry-forbidden transitions can also be produced by electron impact spectroscopy. The cross sections for these normally forbidden transitions are often as large as 5-10% of the cross sections for fully allowed transitions. This behavior is in marked contrast to the case of optical spectroscopy where the intensities of spin-forbidden transitions are reduced by as much as eight orders of magnitude as compared with fully allowed excitations.

A second important advantage of the electron impact technique over the optical method is the range of excitation energies which may be covered. Using a single instrument, features are observed with transition energies from a few tenths of an eV (25000A) to 20 eV ($<$ 600A) with approximately the same sensitivity. This ability allows the simultaneous study of both low-lying excitations and high energy transitions to superexcited states (see Section 3.4.4).

It is principally the lack of high resolution (only 0.060 eV maximum in the present studies) that limits the usefulness of electron impact spectroscopy in the study of the detailed vibrational and rotational spectra of molecules. In addition, the requirement of a gas phase sample in electron scattering experiments may restrict the study of some compounds to optical spectroscopy only.

While much information is available from a study of the total cross sections for molecular excitation by electrons, additional insight and information is available from the study of the differential scattering cross sections. As in the molecule-molecule scattering case, the differential cross section for a process is a measure of the angular distribution of scattered particles. In the case of electron scattering, the wide disparity in the incident and target particle masses results in measurable deflections of the electrons only. If the incident electrons are in the form of a well defined beam, and the target molecules are randomly oriented, then the differential cross section (DCS) for a given process is found by measuring the scattered electron flux as a function of the planar angle θ (with $\theta = 0°$ corresponding to the incident beam direction). Unless the target molecules are oriented with respect to some fixed axis, there will be no azimuthal (ϕ) dependence. Little additional experimental effort is required to make accurate DCS measurements as opposed to total cross section measurements. The additional information gained from DCS studies is, however, substantial.

Fundamentally, there are two mechanisms by which electronic excitation of the target molecule may occur. The first method involves long range Coulombic interactions between the electron and the molecule. In this case, the interaction produces translational → internal electronic energy transfer resulting in kinetic energy loss of the electron and electronic excitation of the molecule. If only energy transfer is involved, then the resulting electronic excitations will be dominated by the optically allowed transitions. Since Coulombic interactions can occur over long distances (large impact parameters), the majority of electrons which cause optically allowed transitions will be only slightly deflected by the scattering process. Thus, it is to be expected that excitations with a strongly forward peaked DCS correspond to fully allowed transitions.

The second excitation mechanism encountered is the previously noted electron exchange scattering. In order for this exchange to occur, the incident electron must have a sufficiently small impact parameter so that formation of the compound negative ion results. Once the ion is formed, all information concerning the incident electron direction is lost. Within 10^{-13} seconds, the extra electron is ejected with a kinetic energy of $(E_0 - E)$, where E_0 is the incident energy and E is the excitation energy of some electronic transition. As important as the ejected electrons kinetic energy, is its angular distribution, which will be very nearly isotropic. Statistically, the probability that this ejected electron will leave the molecule with spin angular momentum opposite that of the incident electron (thus changing the spin

multiplicity of the molecule) is just 50%. As a result, this exchange mechanism is very efficient in producing spin-forbidden transitions which can now be identified by the isotropic distribution of the scattered (exchanged) electron [3, 4].

In addition to the differences expected in the scattered electron angular distributions produced by the two excitation mechanisms, a distinct energy dependence is also evident. Incident electrons of low kinetic energy (15-25 eV) will produce longer interaction times than high energy electrons (45-65 eV), with a resulting enhancement of the exchange scattering. As the energy is increased, only the Coulombic interactions will retain any significant probability of producing an internal excitation in the target molecule. Therefore, cross sections corresponding to spin-forbidden transitions will be larger at the lower incident energies, while those cross sections corresponding to allowed transitions will increase with increasing incident electron energy. In fact, at sufficiently high incident energies ($\sim$ 100 eV) the electronic excitation spectrum will closely resemble the corresponding optical spectrum [5].

In view of these characteristics, a study of the angular and energy dependences of inelastic electron-molecule scattering can provide valuable information on the electronic structure of that target molecule.

A large number of experimental studies have now been performed which exploit these characteristics. Much of the early work involved only total cross section studies or, at most, fixed angle studies of electron-molecule scattering [5]. More

recently, Lassettre and co-workers [6] have studied the low angle ($\leq 20^{\circ}$) and high energy (≥ 100 eV) scattering of many small molecules. The first identification of singlet→triplet spin-forbidden transitions using electron impact spectroscopy was by Kuppermann and Raff [7]. Following that work, others have observed spin-forbidden transitions in many molecules [8-12], so that the general technique is now well established.

The studies reported here involve the application of the electron impact method to the systematic investigation of the electronic structure of a family of molecules, the fluoroethylenes.

References

1. G. Herzberg (a) "Atomic Spectra and Atomic Structures," Dover Publications, New York (1944); (b) "Spectra of Diatomic Molecules," 2nd ed., Van Nostrand, New York, 1950; (c) Electronic Spectra of Polyatomic Molecules," Van Nostrand, Princeton, 1960.
2. J. R. Oppenheimer, Phys. Rev. 32, 361 (1928).
3. S. Trajmar, J. K. Rice, and A. Kuppermann, in "Advances in Chemical Physics," vol. XVIII, I. Prigogine and S. A. Rice, Eds., Interscience, New York, 1970.
4. H. S. W. Massey and E. H. S. Burhop, "Electronic Impact Phenomena," Vols. 1 and 2, Clarendon Press, Oxford, 1969.
5. (a) E. N. Lassettre, Rad. Res. Supplement 1, 530 (1959); (b) E. N. Lassettre, A. S. Berman, S. Silverman, and M. E. Krashow, Phys. Rev. 95, 635 (1954); (c) E. N. Lassettre and S. A. Francis, J. Chem. Phys. 40, 1208 (1964); (d) E. N. Lassettre and E. A. Jones, J. Chem. Phys. 40, 1222 (1964).
6. (a) V. D. Meyer, A. Skerbele, and E. N. Lassettre, J. Chem. Phys. 43, 805 (1965); (b) E. Lassettre, A. Skerbele, and V. D. Meyer, J. Chem. Phys. 45, 3214 (1966); (c) E. N. Lassettre, A. Skerbele, M. A. Dillon, and K. J. Ross, J. Chem. Phys. 48, 5066 (1968).
7. A. Kuppermann and L. M. Raff, J. Chem. Phys. 37, 2497 (1962); Discussion Faraday Soc. 35, 30 (1963).

8. J. A. Simpson, M. G. Menendez, and S. R. Mielczarek, Phys. Rev. 150, 76 (1966).

9. J. K. Rice, A. Kuppermann, and S. Trajmar, J. Chem. Phys. 48, 945 (1968).

10. A. Chutjian, D. C. Cartwright, and S. Trajmar, Phys. Rev. Lett. 30, 195 (1973).

11. A. J. Williams, III and J. P. Doering, J. Chem. Phys. 51, 2859 (1969).

12. I. W. Larkin and J. B. Hasted, J. Phys. B 5, 95 (1972)

2. EXPERIMENTAL

2.1. Apparatus Description

The present experimental studies of the electronic structure of the fluoroethylenes were performed using a variable-angle electron impact spectrometer. This instrument, which is based upon the designs of Simpson and co-workers [1], has been described in detail elsewhere [2, 3], so that only a brief description will be given here. Basically, the apparatus consists of a source of monoenergetic (~ .2% FWHM) electrons which are passed through the target gas contained in a scattering chamber. Scattered electrons are collected at an angle θ° (variable) from the incident electron beam direction, and analyzed for energy loss. Signal pulses from an electron multiplier detector are stored as raw data in a multichannel scaler. The data is subsequently transferred to magnetic tape for computer analysis. The more important features of each of these segments of the system are given below.

The first half of the electron impact spectrometer (see schematic in Figure 2.1) is designed to provide a high flux (current) of energy-selected electrons. The electrons are extracted from a thermionic tungsten filament in the form of a Pierce type gun. Successive accelerating and decelerating lenses allow the beam flux to be increased beyond the normal space change limits. Pairs of deflector plates are positioned coaxially along the electron path to maintain a well directed beam. The use of small diameter apertures in this gun stage result in a well

Figure 2.1: Electron-impact spectrometer block diagram. See text for a more complete description of each section.

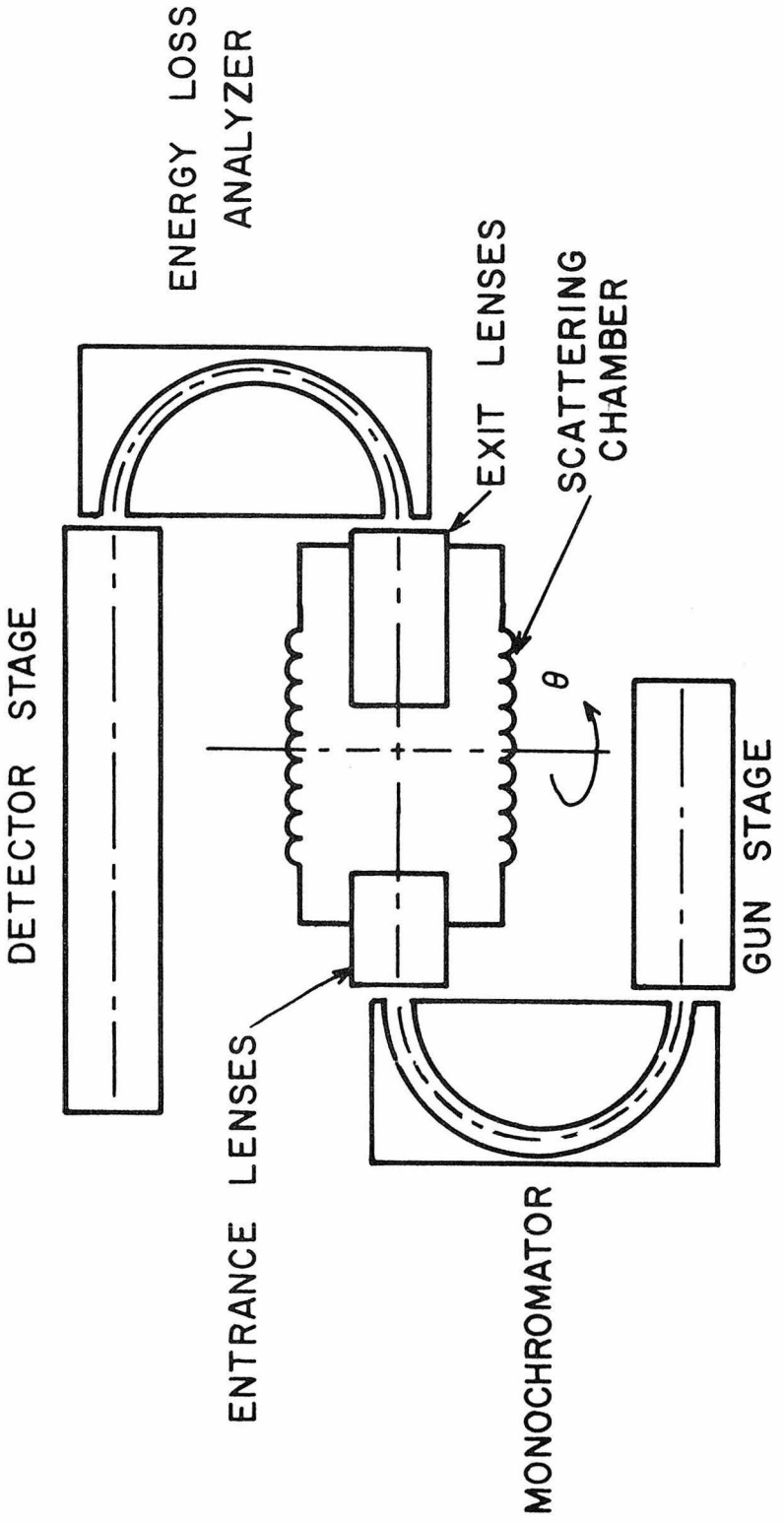

SPECTROMETER BLOCK DIAGRAM

2.1

collimated beam (~ 0.1 rad. divergence). The low energy electron beam (usually around 4 eV) is focused onto the entrance of a 180° hemispherical electrostatic monochromator. With a mean electron path diameter of 3.0", only a small segment of the thermal energy distribution of incident electrons is passed. The width of the transmitted beam energy distribution is typically 0.070 eV to 0.090 eV. These energy selected electrons are then uniformly accelerated to the desired impact energy E_o (from 20 eV to 60 eV) upon entrance into the scattering chamber.

The scattering chamber itself is a welded stainless steel bellows assembly. One end of this unit (the electron entrance) is fixed to the gun stage and monochromator which are in turn mounted on a large diameter rotating gear wheel. The exit end of the scattering chamber and the analyzer and detector stage (see below) are rigidly fixed to the instrument frame. In this way, the scattering angle θ is varied by rotating the entire first half of the spectrometer (gun, lenses, and monochromator) with respect to the second half (analyzer, lenses, and detector), while the scattering chamber flexes between them. The range of θ is approximately -25° to 85°, and is limited by internal interference.

The target gas is admitted into the scattering chamber from a simple gas inlet system. Samples were contained in 300 ml glass bulbs fitted to the inlet manifold with standard taper joints. A Granville-Philips variable leak valve regulated the flow, while a Schulz-Phelps high pressure ionization gauge indicated the scattering chamber pressure. This gauge was located within the spectrometer vacuum housing (see below) to minimize its distance

from the scattering chamber. Stainless steel bellows sealed Nupro valves were used to connect the inlet line to the scattering chamber and the pump out line used to clean the system.

Electrons scattered from the target gas into a small solid angle cone (0.014 steradians) pass through a set of exit lenses. These lenses serve to focus the scattered electrons onto the entrance of a second 180° hemispherical energy analyzer. Using appropriate potentials, only electrons with a preset energy will be passed. As with the monochromator (the two are physically identical), a typical resolution of 0.070 eV to 0.090 eV is obtained. With the analyzer energy fixed to pass electrons of energy E, any detected electrons have lost $(E_0 - E)$ electron volts due to inelastic collisions with the target gas molecules.

Electron detection is by means of a Bendix Spiraltron (type 4219X) continuous dynode electron multiplier. A final set of deflector plates are used to ensure that electrons exiting from the analyzer will strike the entrance cone of the multiplier. The multiplier is supplied with between 3000 and 3200 VDC which provides operation in the plateau region. Output pulses are AC coupled out through a 0.001 μfd. capacitor, resulting in charge pulses of ~ 0.1 μsec FWHM. A prototype pulse amplifier is positioned immediately beyond the output feedthru to reduce stray noise pickup and excessive pulse broadening.

The electron impact spectrometer is contained within an all stainless steel vacuum chamber equipped with a 400 ℓ/sec baffled and trapped mercury diffusion pump. This arrangement gives a base pressure of $\sim 5 \times 10^{-8}$ torr and an operating pressure

(with gas in the scattering chamber) of $\sim 2\times 10^{-7}$ torr. The vacuum chamber is lined with a Mu-metal shield to reduce the magnetic field below ~ 2 milligauss. All sources of stray magnetic fields must be carefully eliminated because of their effects on the low energy electrons used in the spectrometer. As a result, non-magnetic materials are used whenever possible, along with careful degaussing of small magnetic pieces.

Variable voltages for each of the lenses and sets of deflector plates are obtained from either regulated power supplies or batteries. The voltage setting which determines the energy of electrons transmitted through the analyzer must be smoothly varied during an experiment to obtain an energy-loss spectrum. In addition, the detected electrons must be correlated with the energy-loss at which they were transmitted through the analyzer. To accomplish these two requirements, a multichannel scaler and a digital to analog converter are used. The 1024 channel scaler (Nuclear Data Corporation ND-181) produces a digital output signal (corresponding to the currently open channel number) as it advances through its memory. This digital signal is applied to the D to A converter to produce a voltage which is proportional to the scaler channel number. A variable step gain (from X1 to X10) on the D to A allows the full scale output to vary from ~ 1.024 volts to ~ 10.24 volts. This voltage is in turn used to sweep the analyzer voltage and hence to vary the corresponding energy-loss. In operation then, the Nuclear Data unit is placed in the sweep mode, usually with a dwell time (gate time per channel) of 0.1 seconds. The voltage produced by the D to A (as determined by the channel

number) is applied to the analyzer, and any electrons which pass through are counted into that channel. By repeatedly sweeping the memory and continually adding the detected counts, the signal-to-noise ratio of the energy-loss spectrum may be greatly increased. The usual procedure (see below) is to scan energy-loss from $\sim$ -0.3 eV to $\sim$ 9.7 eV, that is, include in the spectrum the elastically scattered electron peak (ΔE = 0.0 eV). Since there is seldom any signal within a few eV beyond the elastic peak, a method has been provided to skip over this region. This jump circuit can be set to skip a variable width segment of the energy-loss region beginning with channel 32, 64, 128, 256 or 512. If each channel corresponded to a voltage span of 0.01 eV (i.e., D to A gain of 10) and a 3.0 volt jump was set at channel 32, then the sequence would be as follows: begin scan with channel 1, voltage = 0.01 eV, advance to channel 2 (in 0.1 sec), voltage = 0.02 eV, . . . channel 32, voltage = 0.320 eV, advance to channel 33 (include jump), voltage = 3.330 eV, . . . channel 1024, voltage = 13.24 eV. Using the jump system, a single spectrum could include the elastic peak (ΔE = 0) and features up to ΔE = 10.24 + δ eV, where δ is the jump voltage. Since the total voltage swing is limited to 10.24 eV, a larger δ would mean that more of the low energy-loss region would be skipped. The beginning channel of a jump and the width of the jump would be determined separately for each spectrum so as to optimize the information content.

2.2. Data Acquisition

The first step in obtaining an electron impact spectrum of a molecule is the sample preparation. All samples used in the present studies were obtained in metal cylinders, and each was transferred to a glass bulb for use. A standard all glass vacuum line was used for the transfer. Sample bulbs were generally filled to 300-400 torr (as measured by a Wallace and Tiernan gauge) and then subjected to repeated freeze-pump-thaw cycles. This procedure removed any impurities that may have been in the original sample.

With the sample bulb attached to the spectrometer inlet system, the target gas was admitted to the scattering chamber. The variable leak valve was adjusted to give ~ 5 microns of pressure in the scattering chamber. The desired impact energy was set and the spectrometer tuned to obtain the best combination of energy resolution and signal intensity. This tuning procedure consisted of carefully adjusting each of the lens and deflector potentials, as well as the sphere (analyzer and monochromator) voltages. To assist in tuning, a Faraday cup could be temporarily inserted into the beam path just beyond the entrance to the scattering chamber. By maximizing the current to the Faraday cup the first half of the spectrometer could be tuned. The second half was then tuned by setting the analyzer for $\Delta E = 0$ eV (elastic peak) and maximizing the detected signal.

Once tuned, the appropriate beginning and ending voltage limits of the sweep were set, including any jump desired. A typical range of voltages would be to start at $\Delta E = \sim -0.3$ eV,

jump at channel 64 ($\Delta E \cong 0.34$ eV) with a width of ~ 3.0 volts and continue from channel 65 ($\Delta E \cong 3.34$ eV) to 1024 ($\Delta E \cong 12.94$ eV). Between 200 and 250 scans were accumulated for each spectrum, depending on the angle and impact energy used. Generally, each molecule was studied at two impact energies and at nine angles (0°, $10^\circ \ldots 80^\circ$). Additional scans were required to obtain higher energy-loss regions (from $\Delta E = 6$ to 16 eV). In general then, some 20 to 25 spectra were obtained for each molecule.

After a spectrum had been completed, the results (stored in memory) were recorded in two ways. First, a hard copy of the spectrum was made using an X-Y recorder. The Nuclear Data multichannel analyzer provides a voltage proportional to the count level stored in each channel, and a voltage proportional to the channel number. This hard copy spectrum is used only as a secondary reference. The primary data recording method involves the generation of a punched paper tape which records the exact count stored in each channel. The punch unit is interfaced to the Nuclear Data system and also to the keyboard of an ASR-33 teletype. The teletype unit is used to punch a heading onto the paper tape, including identification of the sample, impact energy, angle, energy-loss region, jump channel and jump voltages, etc. After the heading is punched, the contents of the memory of the scaler is punched in sequence. The final paper tape then is a self-contained record of the spectrum. For permanent storage, the contents of the paper tape are later transferred to magnetic tape using an SCC4700 computer and a Cipher tape unit. The IBM compatible tape is then used in all subsequent data analysis.

In addition to each of the recorded spectra, the differential elastic cross section of each molecule is measured at each impact energy studied. These DCS measurements are not recorded using the multichannel scaler, since no energy-loss sweep is necessary. The analyzer is set to $\Delta E = 0$ eV, and the count rate (measured by a Hewlett Packard 5216A frequency meter) recorded at each angle for which a full energy-loss spectrum has been measured. The DCS is needed later in the analysis of the data to obtain normalized transition intensity ratios (see below).

2.3. Data Reduction and Analysis

The spectra recorded on magnetic tape are analyzed using a two pass computer program. The first pass of the analysis performs several tasks, including: (1) removal of any large noise spikes generated by occasional high voltage arcs within the detector stage of the spectrometer. The spike (generally only one channel wide) is replaced with an average count rate determined from the neighboring channels; (2) a minor correction is made for ($\sim 1\,\mu$sec) dead time of the multichannel scaler. This dead time correction is most important at very high count rates; (3) a simple multiple channel averaging (smoothing) procedure is applied to the data to reduce the statistical fluctuations often encountered in features with very low count rates. A variable number of channels (3 to 9) may be used in the smoothing; (4) peaks in the spectrum are located, and their voltages calculated relative to the largest peak in the spectrum; (5) the areas under each peak are calculated using approximate upper and lower limits; (6) the smoothed spectrum is

plotted in an optimized manner, with a variable number of decades of multiplication used to display weaker features; (7) the raw spectrum, its smoothed counterpart and all additional heading and identification information is printed.

The principle information which the analysis must provide is the exact peak locations and the accurate areas under each peak. The latter are used to calculate the ratios of transition intensities needed for the identification of allowed and forbidden transition types (see Section 3). This information is provided by the second pass, using the results of the first pass as input information. Specifically, by specifying a channel number in a spectrum corresponding to a peak location (as determined by examination of the results of the first pass), the program will determine the exact voltage of that peak. Also, by specifying the first and last channel to be included in the calculation of a peak area, a more accurate value of that area may be found than the approximate result given by part one. The results of the second pass then include both a listing of peak voltages and peak areas as well as the ratio of peak areas with respect to the longest and second largest features in the spectrum.

An additional feature of the second half of the analysis routine is the deconvolution of overlapping peaks. This feature is generally applied only when a very weak shoulder appears on a much stronger peak. Since the shoulder is most probably due to a forbidden transition, while the main peak is likely due to a fully allowed transition, the latter will be strongest at very low angles, while the former will remain very weak. By subtracting a (scaled)

low angle spectrum from the spectrum with the overlapping peaks, it is often possible to reveal the true band shape of the weak transition, as well as find its peak location and area more accurately. This method was applied to the analysis of a weak singlet → triplet transition observed in monofluoroethylene (see Section 3.4.1).

One final correction must be applied to the area ratios calculated above, that due to the changing scattering volume as a function of angle. This correction is often approximated by $\sin \theta$, however, in the results given later, a more accurate volume correction was made [4]. The results of using this and other corrections noted here on the analysis of the scattering data obtained from the fluoroethylenes are given in section 3.

References

1. (a) J. A. Simpson and S. R. Mielczarek, J. Chem. Phys. 39, 1606 (1963); (b) J. A. Simpson, Rev. Sci. Instru. 35, 1698 (1964); (c) J. A. Simpson, M. G. Menendey, and S. R. Mielczarek, Phys. Rev. 150, 76 (1966); (d) J. A. Simpson and C. E. Kuyatt, Rev. Sci. Instru. 38, 103 (1968).
2. J. K. Rice, Ph.D. Thesis, California Institute of Technology, 1969.
3. O. A. Mosher, Ph.D. Thesis, California Institute of Technology, 1975.
4. S. Trajmar, D. C. Cartwright, J. K. Rice, R. T. Brinkmann, and A. Kuppermann, J. Chem. Phys. 49, 5464 (1968), see also reference 2, pp. 209-211.

3. RESULTS AND DISCUSSION

3.1 Introduction

Spectroscopic measurements on the six fluorine-substituted ethylene molecules provide an opportunity to study the effects of fluorine atom substitution on the electronic structure of the ethylene molecule [1, 2]. The strongest absorption feature in the ethylene spectrum peaks at 7.6 eV [1, 2], and is known as the $N \rightarrow V$ transition. Recent optical studies [3] of the fluoroethylenes have shown that the spectra of five of the molecules are similar to ethylene, but that there is a large hypsochromic (positive) shift in the $N \rightarrow V$ transition energy of tetrafluoroethylene. These experiments have been limited both by the optical selection rules and by the relatively narrow range of transition energies studied (6 eV - 10 eV). As a result, no information has been obtained concerning transitions outside of this energy range. No spin-forbidden, singlet $\rightarrow$ triplet transitions have been observed optically.

While both ion impact [4] and threshold electron impact [5] studies have recently produced evidence for spin-forbidden transitions in several of the fluoroethylenes, no complete study of these excitations is available.

In an effort to overcome these deficiencies, a systematic study of the electronic transitions in the six fluoroethylenes was undertaken using the variable angle electron impact technique. This method provides information on electronic transition energies over a broad energy range (0-16 eV in these studies), and permits accurate identification of each electronic transition as spin-allowed

or spin-forbidden. The suitability of the electron impact technique for obtaining this type of information is well documented [2]. In the present study, excitation spectra were obtained at 40 eV and either 20 eV or 25 eV impact energy (E_o), and scattering angles (θ) from 0° to 80°.

In the following sections, previous experimental and theoretical work is summarized, the pertinent experimental details of this work are given, and the results are presented and discussed. The assignments of various transitions are made with reference to the known states of ethylene in the case of valence type excitations, and by using the term value approach for Rydberg type transitions. A brief discussion of the implications of this work for the photochemistry of the fluoroethylenes is also given.

3.2. Previous Studies of the Electronic Structure of the Fluoroethylenes

3.2.1. Optical Spectroscopy

The only complete optical study of the fluoroethylenes is that due to Belanger and Sandorfy [3]. Their study extending from 2000A (6.2 eV) to 1150A (10.7 eV), revealed a strong $\pi \rightarrow \pi^*$, singlet → singlet transition in each molecule. Most of the maxima were at an energy near that of the N → V transition of ethylene [1], except for that of tetrafluoroethylene, where a large (1.2 eV) blue shift was observed. These singlet → singlet transition energies are listed in Table 1. In each molecule, several Rydberg series were identified as originating from the highest occupied π orbital and converging to the first ionization potential (IP).

3.2.2. Other Spectroscopic Studies

In addition to the optical study cited above, several members of the fluoroethylene series have been studied by ion impact [4] and electron scavenger techniques [5]. In each case, these methods have revealed low-lying absorptions which were attributed to spin-forbidden singlet → triplet transitions.

Using 3 keV He ions, Moore has observed a transition at 4.6 eV in 1,1-difluoroethylene [4]. The absence of this feature in the corresponding H^+ impact spectra suggests that it is excited by an electron exchange process giving rise to a singlet → triplet transition. The peak is assigned to the N → T ($\pi \rightarrow \pi^*$) transition in analogy with the N → T singlet → triplet absorption seen at 4.4 eV in ethylene [2]. An additional peak is observed at 7.6 eV in the energy-loss spectra of both ions, and is therefore assigned as the singlet → singlet transition.

O'Malley and Jennings [5] have also observed a similar transition at 4.4 eV in monofluoroethylene using SF_6 as a scavenger for thermal energy electrons in an ion cyclotron resonance mass spectrometer. The spectrum, obtained at 0.5 eV resolution, shows additional transitions at 7.2 eV and 9.6 eV. The former is presumably the singlet → singlet, $\pi \rightarrow \pi^*$ transition, while the latter is not identified.

The results obtained from both methods are included in Table 1.

3.2.3. Theoretical Calculations

Several theoretical studies [6-10] have made predictions of the effect of fluorine substitution on both the electronic excitation and photoelectron spectra of the parent ethylene molecule. Simple Hückel-type molecular orbital calculations by Landau, et al. [6] have shown that the energy of the electron in the highest occupied π orbital of the fluoroethylenes is close to that of the electron in the unperturbed ethylene π orbital. This finding has been confirmed in the case of monofluoroethylene by Meza and Wahlgren [7] using a simple Gaussian basis set in an SCF calculation. These calculations do not, however, provide any information on the N $\rightarrow$ T or N $\rightarrow$ V transition energies of the fluoroethylenes. Recently, semi-empirical MO-CI calculations for the singlet $\rightarrow$ triplet and singlet $\rightarrow$ singlet transition energies of the fluoroethylenes have been performed by Salahub [9]. Energies were obtained for both the N $\rightarrow$ T and N $\rightarrow$ V transitions, and these values are included in Table 1 for comparison with the experimental results.

3.2.4. Ionization Potentials

The effects of fluorine substitution on the energies of the neutral ground state and the various ionic states of ethylene can be seen in the IPs of the fluoroethylenes. Measurements of the first IP, corresponding to the removal of an electron from the highest occupied π orbital of each of the fluoroethylenes, have been made both by photoionization [10-12] and electron impact methods [13]. The results, listed in Table 2, show only a ± 0.20 eV

variation over the entire series with respect to the 10.51 eV first IP of ethylene [14]. The second IP values, which correspond to σ electron removal, have been measured by several investigators [10, 12] and are also listed in Table 2. In contrast to the first IP values, the second IP increases by 3 eV in going from ethylene to tetrafluoroethylene. A number of different explanations have been advanced to explain these fluorine substitution effects [8, 10, 11, 15], and several theoretical calculations have yielded first IPs in very good agreement with the experimental results [7, 16].

3.3. Experimental

Both the electron impact spectrometer and the data accumulation and reduction methods have been described previously (see Section 2) [17]. An energy selected electron beam is scattered off the target gas contained in a collision chamber. The electrons scattered at a preselected angle are analyzed for energy loss and detected with an electron multiplier and pulse counting system. Peaks in the energy loss spectrum correspond to vibrational or electronic excitations of the target molecules.

Spectra were obtained with an instrumental resolution chosen between 0.06 eV and 0.15 eV as measured by the full width at half maximum (FWHM) of the elastic peak. The gas sample pressure in the scattering chamber was maintained at approximately 5×10^{-3} torr as measured by an uncalibrated Schulz-Phelps ionization gauge.

The monofluoroethylene (vinyl fluoride) and the 1,1-difluoroethylene were both obtained from Matheson Gas Products with stated purities of 99.9% and 99.0%, respectively. All other gas samples were from PCR Incorporated and had 97.0% minimum purity. Each sample was subjected to a liquid nitrogen freeze-pump-thaw cycle before use, and no evidence for impurity absorption was observed in any of the spectra.

The areas under the elastic peak and each of several inelastic features are obtained by numerical integration as described previously [17]. Plots of selected area ratios are shown in Figure 3.1. The differential cross section (DCS) values shown for each molecule have also been measured by a previously described method [18,19]. The elastic scattering DCS was normalized to a value of 1.0 at a scattering angle of 40°. Both the area ratios and the DCS values for each molecule are listed in Tables 3 and 4, respectively.

3.4. Analyzed Results

Table 1 summarizes the principle results of this study [20]. Peak locations determined from the electron impact spectra have an uncertainty of ± 0.05 eV, while that of the Franck-Condon limits of each band is ± 0.1 eV.

3.4.1. Vinyl Fluoride

Figures 3.2 and 3.3 show two energy-loss spectra of vinyl fluoride at scattering angles (θ) of 0° and 40° and an impact energy (E_0) of 40 eV. The first inelastic feature has an

Figure 3.1: Plots of the ratio of the area under the $N \rightarrow T$ transition to that under the $N \rightarrow V$ transition at $E_o = 40$ eV for each of the fluoroethylenes. The curves are identified as follows; (a) monofluoroethylene, (b) 1,1-difluoroethylene, (c) cis-1,2-difluoroethylene, (d) trans-1,2-difluoroethylene, (e) trifluoroethylene, (f) tetrafluoroethylene. Curves (b) - (f) have been shifted vertically from the (a) by successive factors of 5.

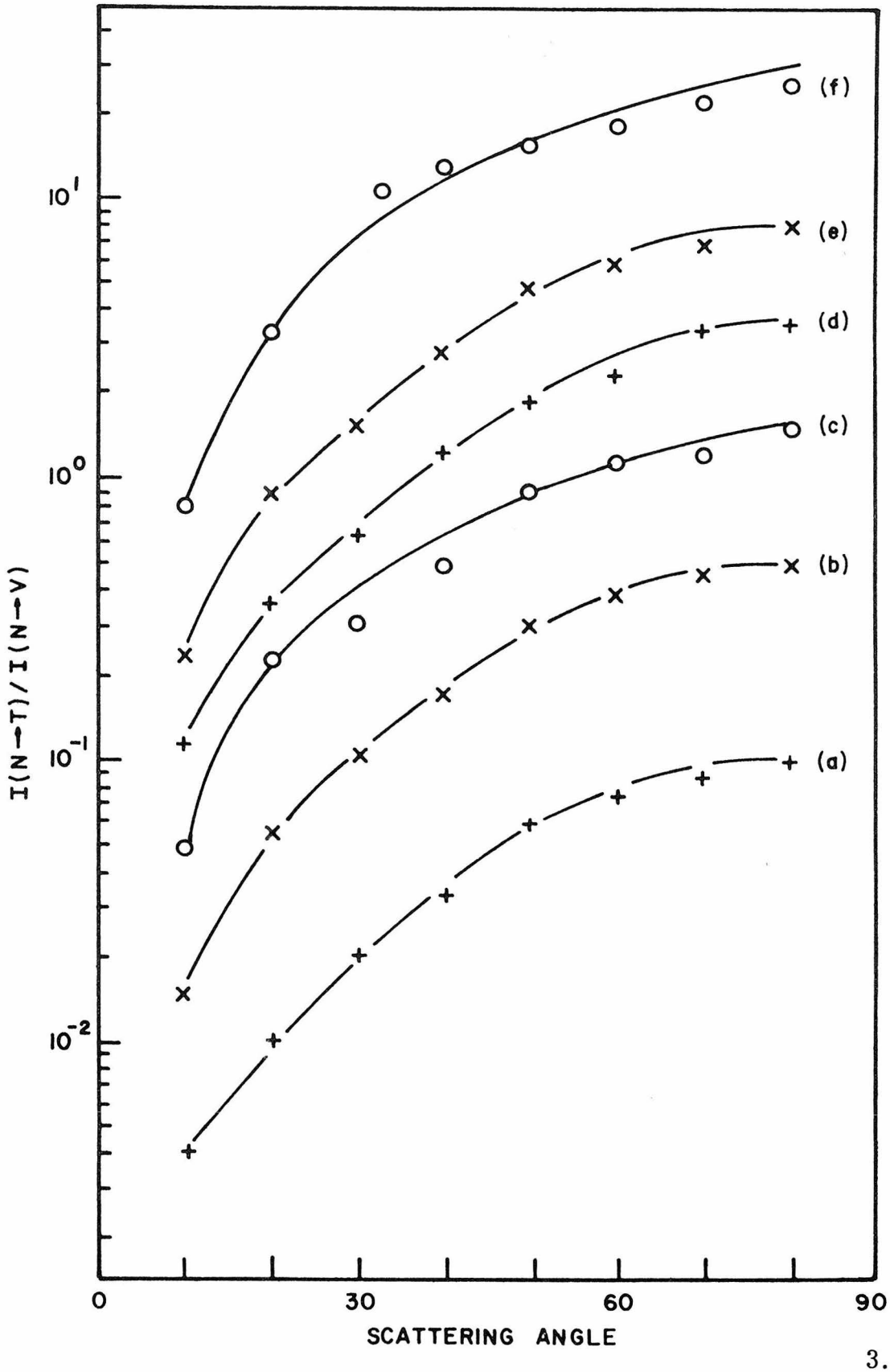

3.1

onset at about 3.4 eV and extends to about 5.4 eV with a peak at 4.40 eV. The ratio of the area under this peak to that under the singlet → singlet absorption at 7.5 eV is shown in Figure 3.1a as a function of the scattering angle for an impact energy of 40 eV. An increase in this ratio by a factor of about 50 over the angular range from 10° to 80° is apparent. In addition, the ratio at 25 eV is larger than that at 40 eV for all scattering angles studied. This behavior is indicative of a spin-forbidden, singlet → triplet transition [2, 17]. The isotropic nature of the DCS curves in Figures 3.4 and 3.5 also supports this conclusion. In analogy with the 4.4 eV $\pi \rightarrow \pi^*$ triplet transition in ethylene, this feature is designated as the N → T transition. The value obtained from the threshold electron impact study is also 4.4 eV.

At scattering angles of 30° and above, a weak feature appears as a shoulder on the low energy side of the 7.50 eV transition. This feature was more prominent at an impact energy of 25 eV than at 40 eV. Using a $\theta = 0^\circ$ and $E_0 = 25$ eV spectrum of vinyl fluoride as a reference, this peak was more accurately located by deconvoluting a $\theta = 40^\circ$, $E_0 = 25$ eV spectrum. The resulting peak, located at 6.45 eV, is shown in Figure 3.6. While a quantitative evaluation of the energy and angular dependences of this feature was not possible due to its weakness, a qualitative examination of its behavior indicates that it is the second singlet → triplet transition. One possibility is that this absorption is the singlet → triplet transition corresponding to the sharp singlet → singlet transition observed at 7.0 eV. The latter transition has been identified as the first member of a $\pi \rightarrow \pi^*$

Figure 3.2: Energy-loss spectrum of vinyl fluoride taken at $\theta = 0^{\circ}$, $E_0 = 40$ eV, resolution = 60 meV, and scattering chamber pressure of 5.4 mtorr.

Figure 3.3: Energy-loss spectrum of vinyl fluoride taken at $\theta = 40^{\circ}$, $E_0 = 40$ eV, resolution = 120 meV, and scattering chamber pressure of 2.6 mtorr.

Figures 3.4 and 3.5: DCS curves for vinyl fluoride at $E_0 = 25$ eV and 40 eV, respectively. Squares (□) = elastic DCS × 0.1, circles (○) = N → V DCS, triangles (Δ) = N → T DCS.

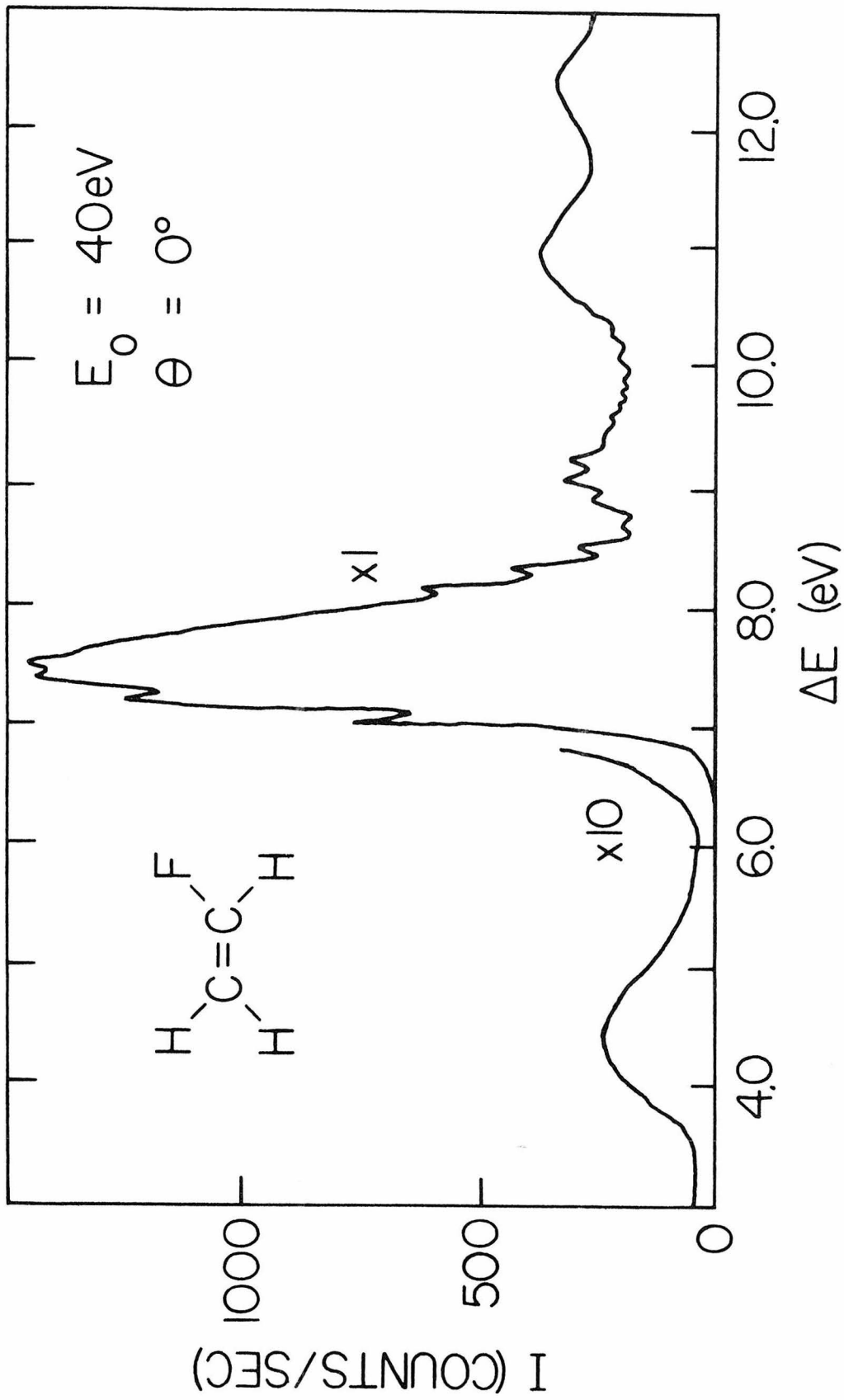
I (COUNTS/SEC)
1000
500
0
4.0
6.0
8.0
10.0
12.0
ΔE (eV)
E_0 = 40eV
θ = 0°
x1
x10
F
H
C=C
H
H

3.2

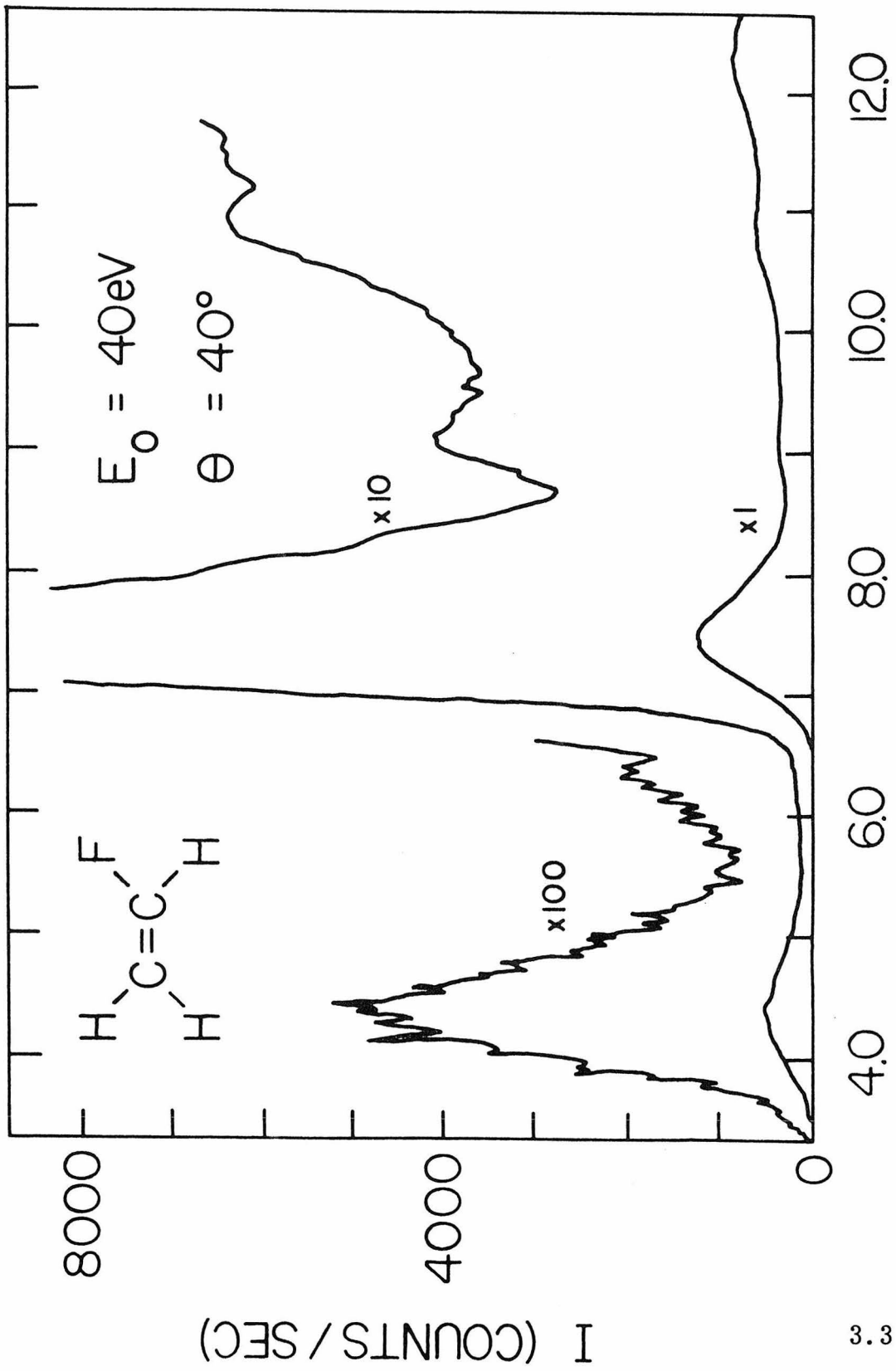
I (COUNTS / SEC)
8000
4000
0
4.0
6.0
8.0
10.0
12.0
ΔE (eV)
E_0 = 40eV
θ = 40°
x10
x1
x100
H
H
C=C
H
F

3.3

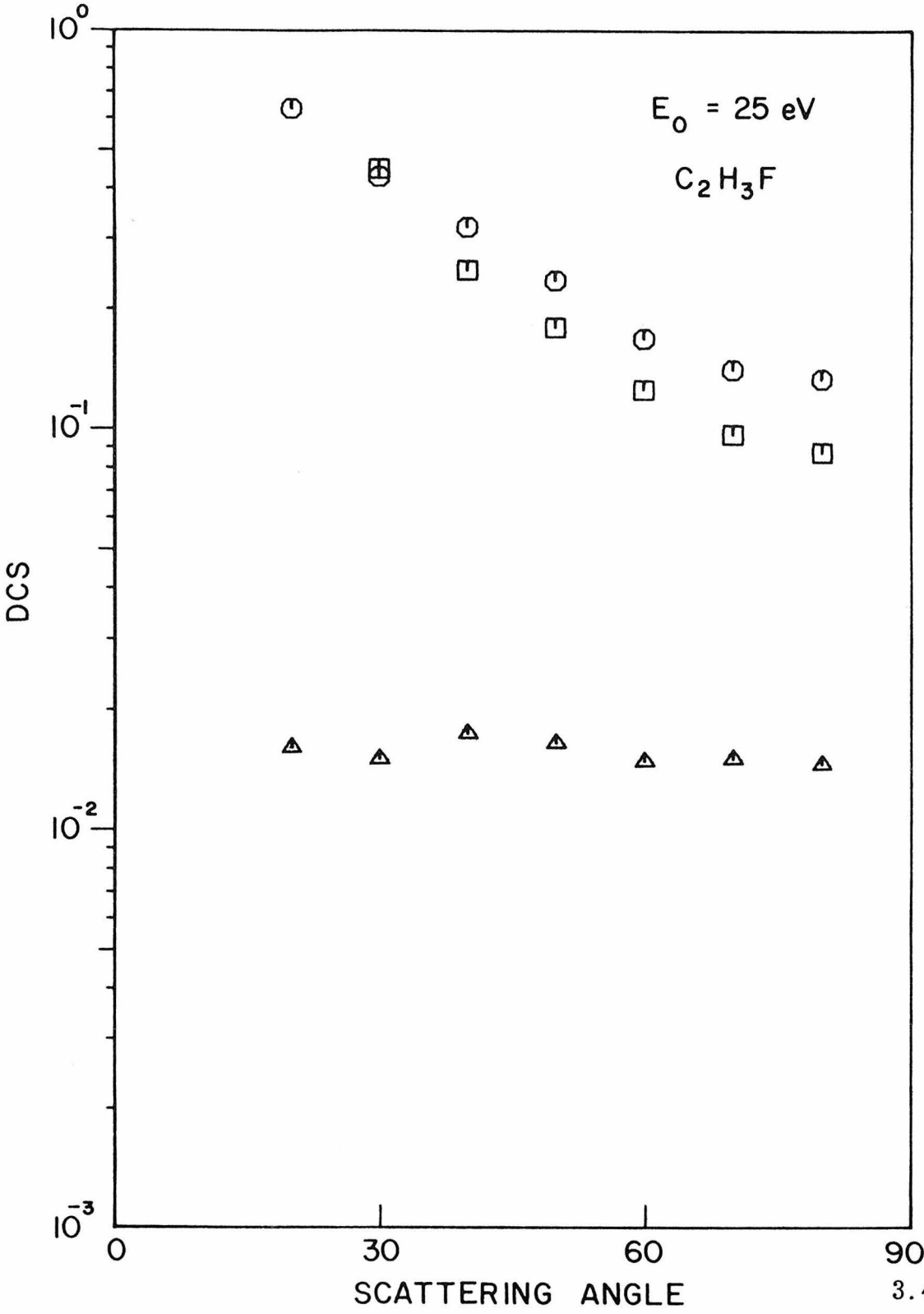

3.4

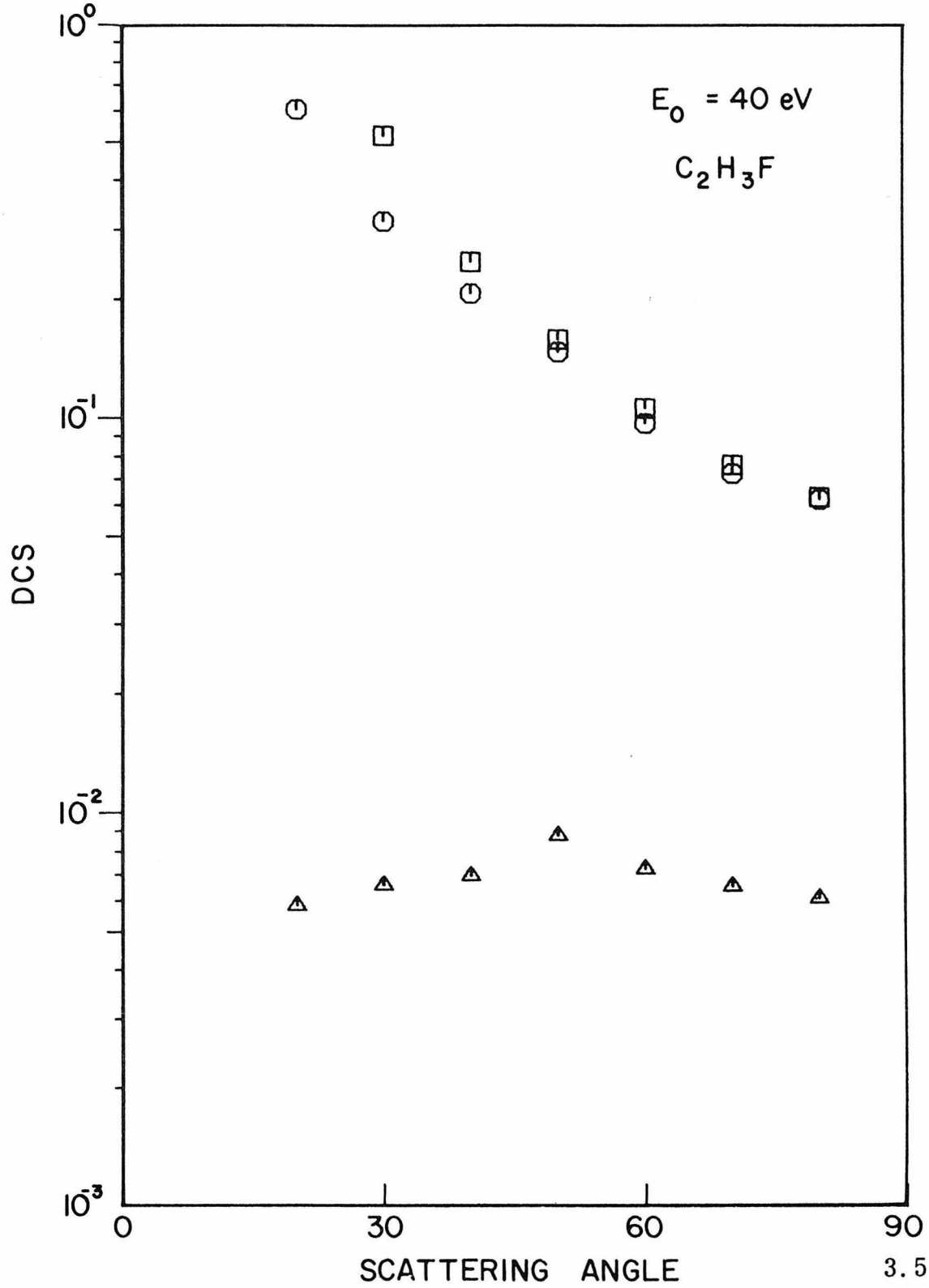

3.5

Figure 3.6: Results of deconvoluting a $\theta = 40^{\circ}$, $E_O = 25$ eV spectrum using a $\theta = 0^{\circ}$, $E_O = 25$ eV spectrum. The dashed line corresponds to the former spectrum, while the solid line shows the band shape obtained from the difference of the two spectra. The peak of this feature was found to be 6.45 eV.

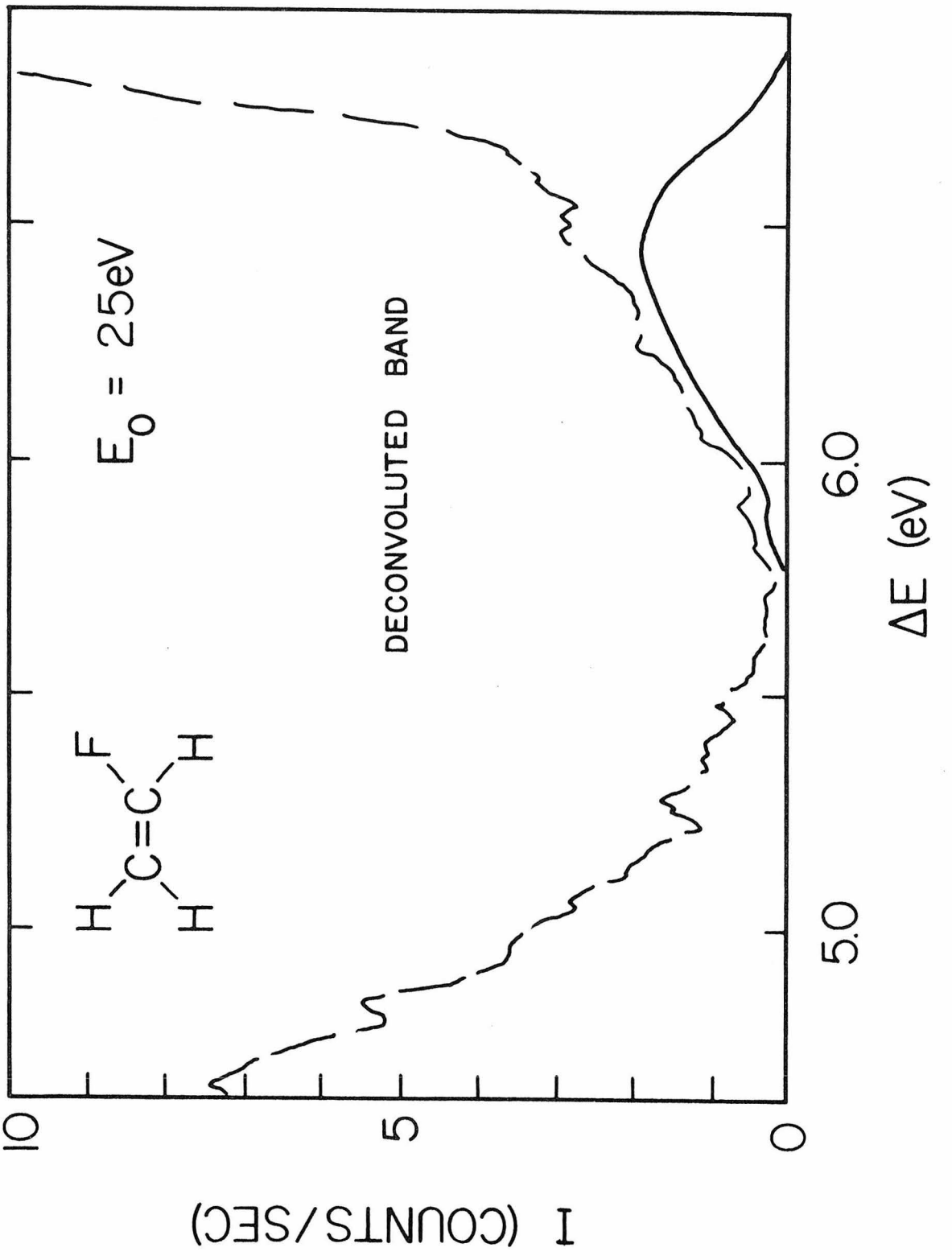
I (COUNTS/SEC)
10
5
0
5.0
6.0
ΔE (eV)
DECONVOLUTED BAND
E_0 = 25eV
H
F
C=C
H
H

3.6

(3s) Rydberg series [3] (see below). The 6.5 eV feature may, on the other hand, be associated with one of the other singlet → singlet transitions above 7.1 eV. Careful examination of all spectra revealed no evidence for this transition in any of the other fluoroethylenes. However, observation of a second triplet excited state in the other molecules would be more difficult because of the increased overlap of the singlet → singlet Rydberg and N → V transitions (see below) in the excitation energy range from 6 eV to 7 eV.

The most intense absorption feature in the vinyl fluoride energy-loss spectrum is the transition at 7.50 eV. The DCS curve shown in Figure 3.5 is sharply forward peaked and this confirms its assignment to a fully allowed singlet → singlet transition. The 7.50 eV peak is designated as the N → V transition in analogy with the corresponding absorption in ethylene at 7.6 eV [1]. Both the optical and threshold electron impact results for the N → V transition energy are in fair agreement with this peak value.

The large number of features observed in the 6 eV - 10 eV region of the energy-loss spectra of vinyl fluoride in Figure 3.2 have also been seen in the optical absorption spectrum, and have been identified as members of various Rydberg series. A more complete analysis of these features will be given in Section 3.4.6. It is also evident from the results in Figure 3.2 that several broad absorption features occur at energies above the first ionization potential of 10.58 eV. The exact nature of the super-excited states involved is not well understood, although it is clear

that they do not consist of temporary negative ions, since the transitions are still observed at impact energies 25 eV above threshold. These superexcited states may either be valence-like states, or members of Rydberg series converging to a higher ionization potential as in the fluoromethanes [21]. In either case, they may lead to autoionization or predissociation of the molecule [22]. Recently, superexcited states have been observed in a number of molecules [21, 23, 24], and their importance in both radiation chemistry [25] and chemical reactions [26] has been discussed.

The peak locations of transitions to the superexcited states are listed in Table 1 and discussed further in Section 3.4.6.

3.4.2. Difluoro- and Trifluoroethylenes

Spectra obtained of 1,1-difluoroethylene for a θ of 10° and 70° and an E_0 of 40 eV are shown in Figures 3.7 and 3.8. As with vinyl fluoride, the first inelastic feature is the N $\rightarrow$ T transition peaking at 4.63 eV with a Franck-Condon region from 3.5 eV to 5.5 eV. The ion impact result of Moore is in good agreement, having a peak value of 4.6 eV [4].

The corresponding N $\rightarrow$ V maximum is found to be 7.50 eV, in agreement with the optical value, while both the ion impact value and the calculated result are somewhat higher (see Table 1).

Spectra of cis and trans 1,2-difluoroethylene are shown in Figures 3.9 through 3.13. For the cis 1,2-difluoroethylene, the N $\rightarrow$ T transition peaks at 4.28 eV with a Franck-Condon region from 3.7 eV to 5.4 eV, while the corresponding transition

Figure 3.7: Energy-loss spectrum of 1,1-difluoroethylene taken at $\theta = 10^{\circ}$, $E_0 = 40$ eV, resolution = 95 meV, scattering chamber pressure ≈ 5 mtorr.

Figure 3.8: Energy-loss spectrum of 1,1-difluoroethylene taken at $\theta = 70^{\circ}$, $E_0 = 40$ eV, resolution = 120 meV, scattering chamber pressure ≈ 3 mtorr.

Figure 3.9: Energy-loss spectrum of cis-1,2-difluoroethylene taken at $\theta = 30^{\circ}$, $E_0 = 40$ eV, resolution = 85 meV, scattering chamber pressure ≈ 5 mtorr.

Figure 3.10: Energy-loss spectrum of cis-1,2-difluoroethylene taken at $\theta = 70^{\circ}$, $E_0 = 40$ eV, resolution = 85 meV, and scattering chamber pressure ≈ 5 mtorr.

Figure 3.11: Energy-loss spectrum of cis-1,2-difluoroethylene taken at $\theta = 10^{\circ}$, $E_0 = 60$ eV, resolution = 125 meV, and scattering chamber pressure ≈ 5 mtorr.

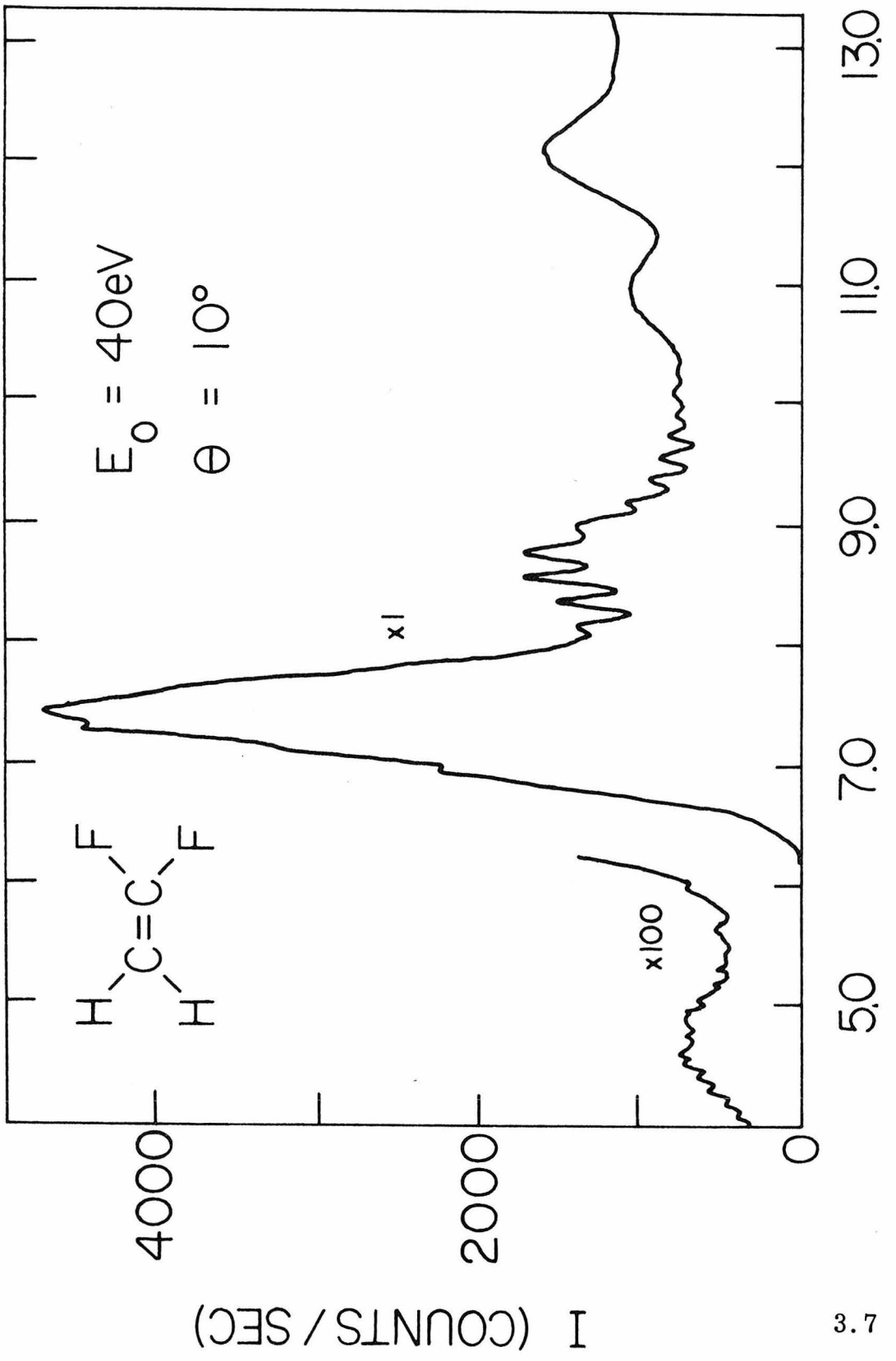
I (COUNTS / SEC)
4000
2000
0
5.0
7.0
9.0
11.0
13.0
ΔE (eV)
E_0 = 40eV
θ = 10°
×1
×100
H
C=C
F
H
F

3.7

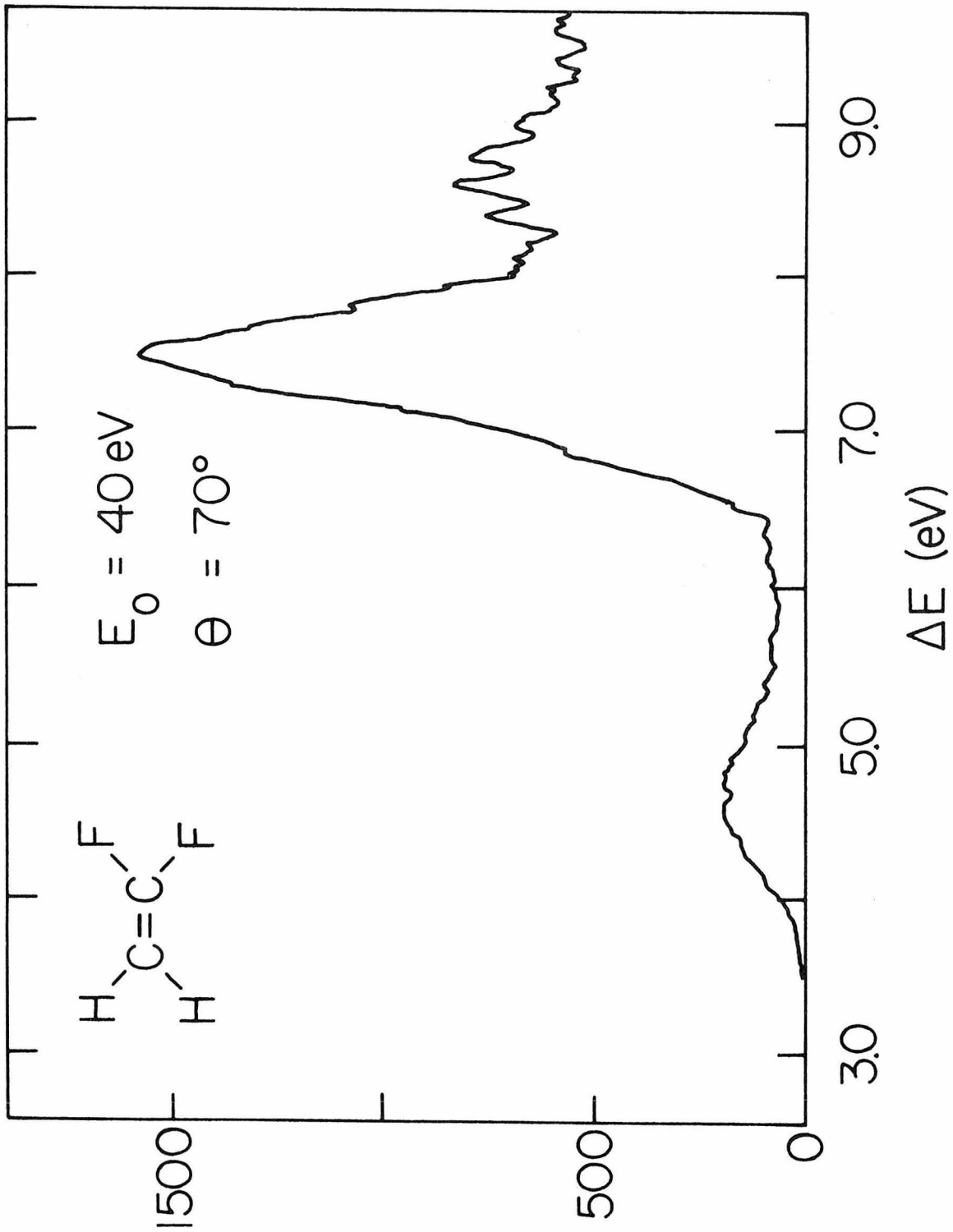

3.8

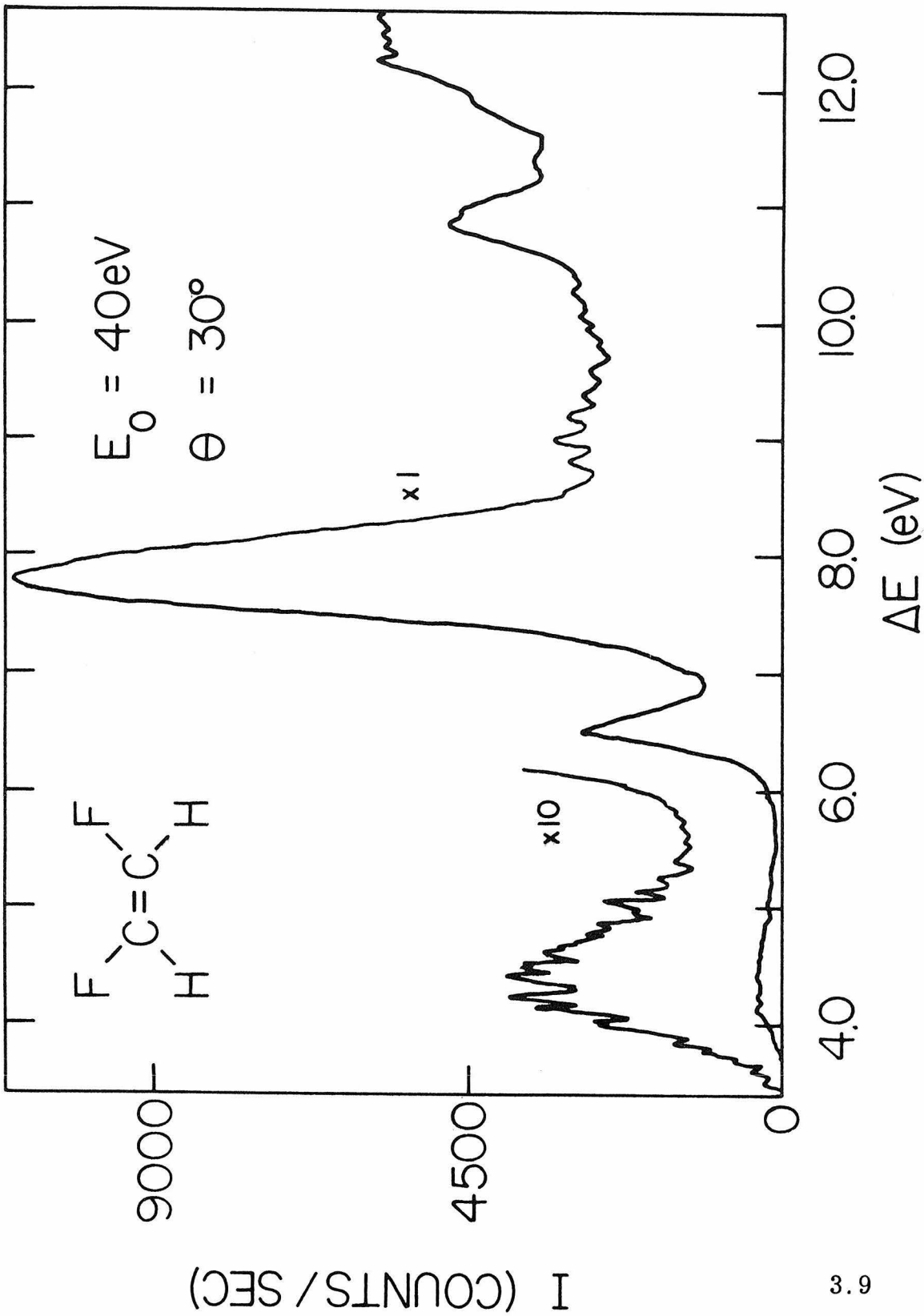
I (COUNTS / SEC)
9000
4500
0
4.0
6.0
8.0
10.0
12.0
ΔE (eV)
E_0 = 40eV
θ = 30°
x1
x10
F
C=C
F
H
H

3.9

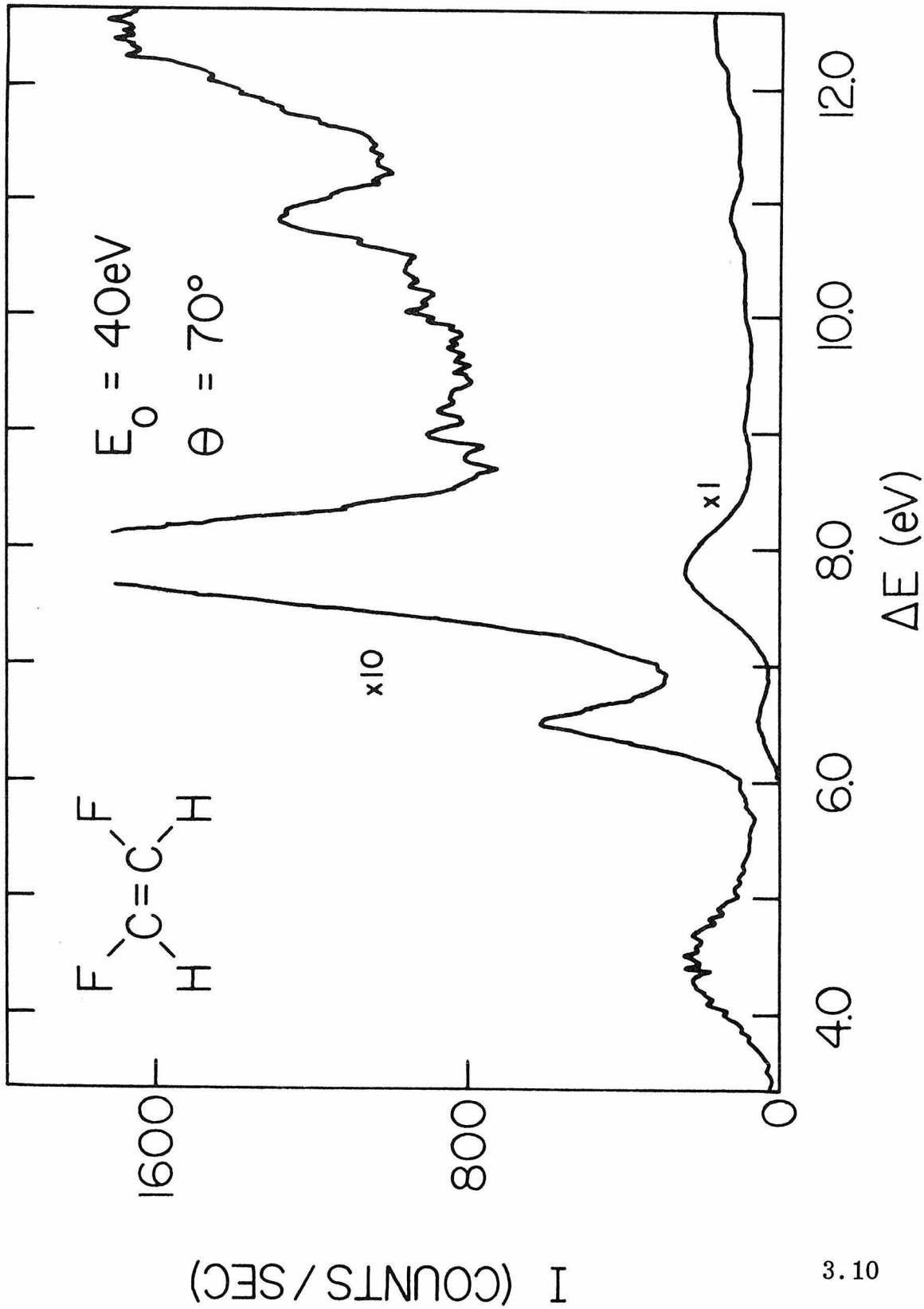
I (COUNTS / SEC)
1600
800
0
4.0
6.0
8.0
10.0
12.0
ΔE (eV)
x10
x1
E0 = 40eV
θ = 70°
F
C=C
H
F
H

3.10

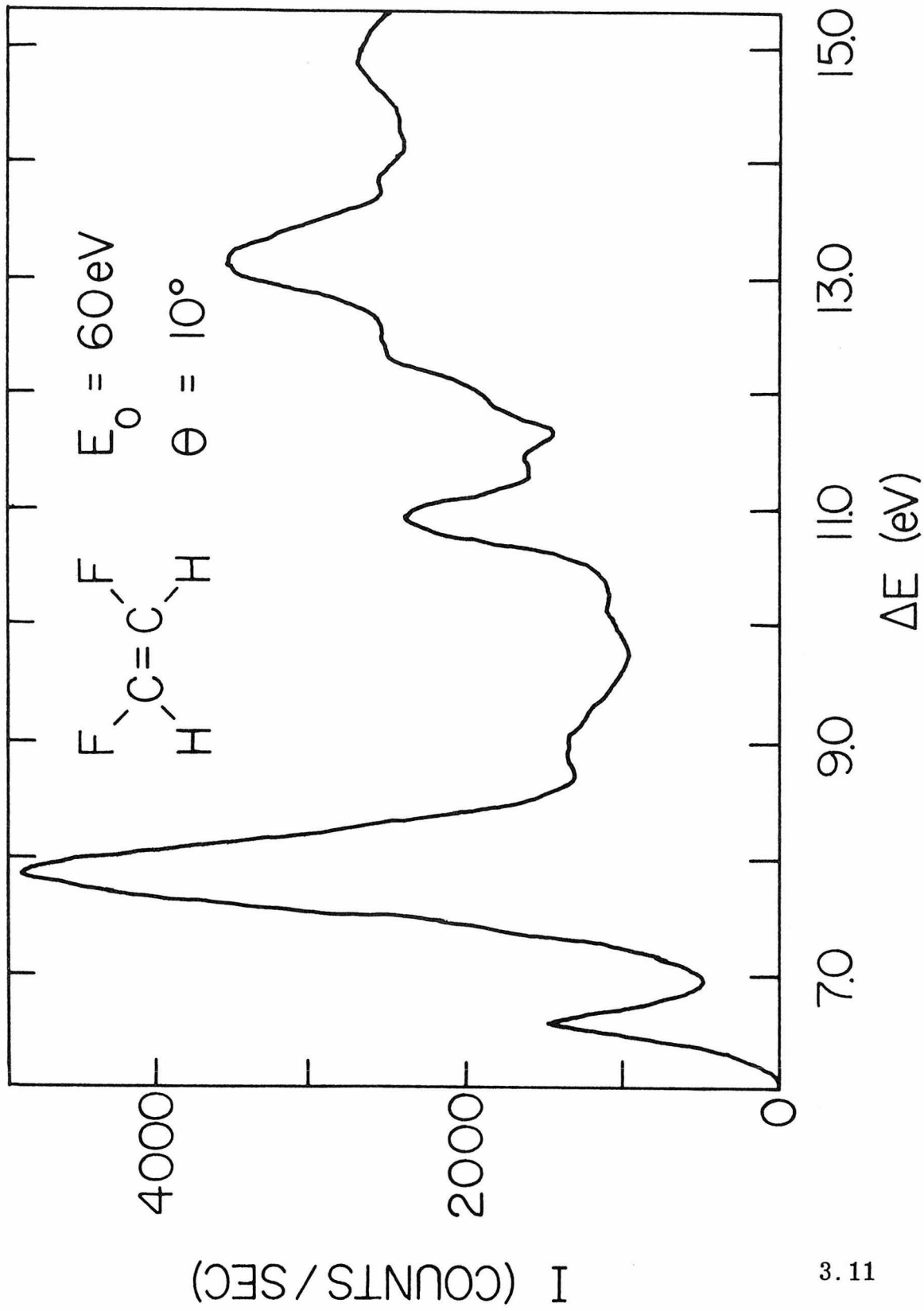
I (COUNTS/SEC)
4000
2000
0
7.0
9.0
11.0
13.0
15.0
ΔE (eV)
E_0 = 60eV
θ = 10°
F
H
C=C
F
H

3.11

Figure 3.12: Energy-loss spectrum of trans-1,2-difluoroethylene taken at $\theta = 5^{\circ}$, $E_0 = 40$ eV, resolution $\simeq$ 100 meV, and scattering chamber pressure = 4.3 mtorr.

Figure 3.13: Energy-loss spectrum of trans-1,2-difluoroethylene taken at $\theta = 70^{\circ}$, $E_0 = 40$ eV, resolution $\simeq$ 140 meV, and scattering chamber pressure = 4.3 mtorr.

Figure 3.14: Energy-loss spectrum of trifluoroethylene taken at $\theta = 0^{\circ}$, $E_0 = 40$ eV, resolution = 70 meV, and scattering chamber pressure = 5.4 mtorr.

Figure 3.15: Energy-loss spectrum of trifluoroethylene taken at $\theta = 60^{\circ}$, $E_0 = 40$ eV, resolution = 125 meV, and scattering chamber pressure = 4.7 mtorr.

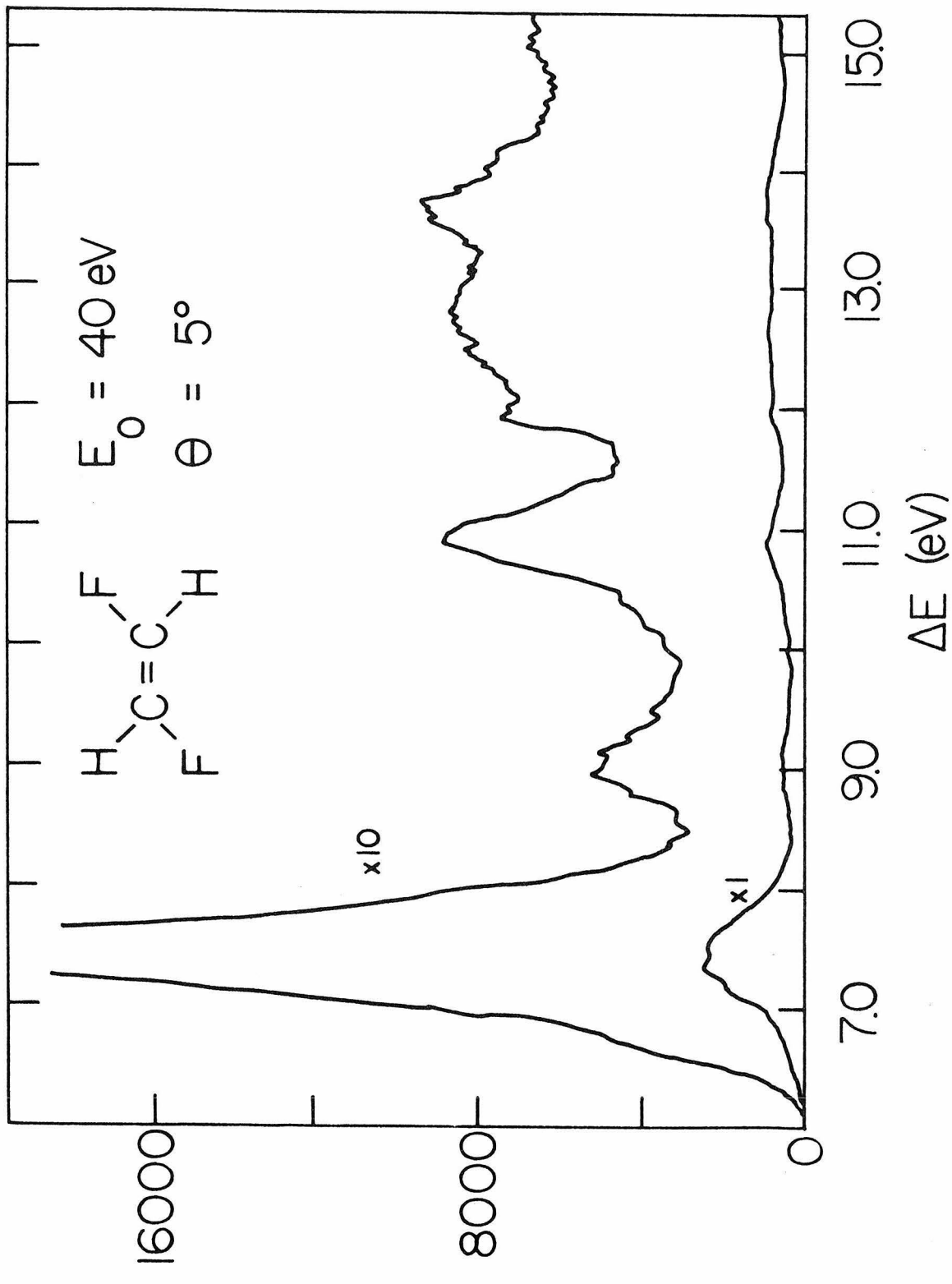
I (COUNTS / SEC)
16000
8000
0
7.0
9.0
11.0
13.0
15.0
ΔE (eV)
x10
x1
E_0 = 40 eV
θ = 5°
H
F
C=C
H
F

3.12

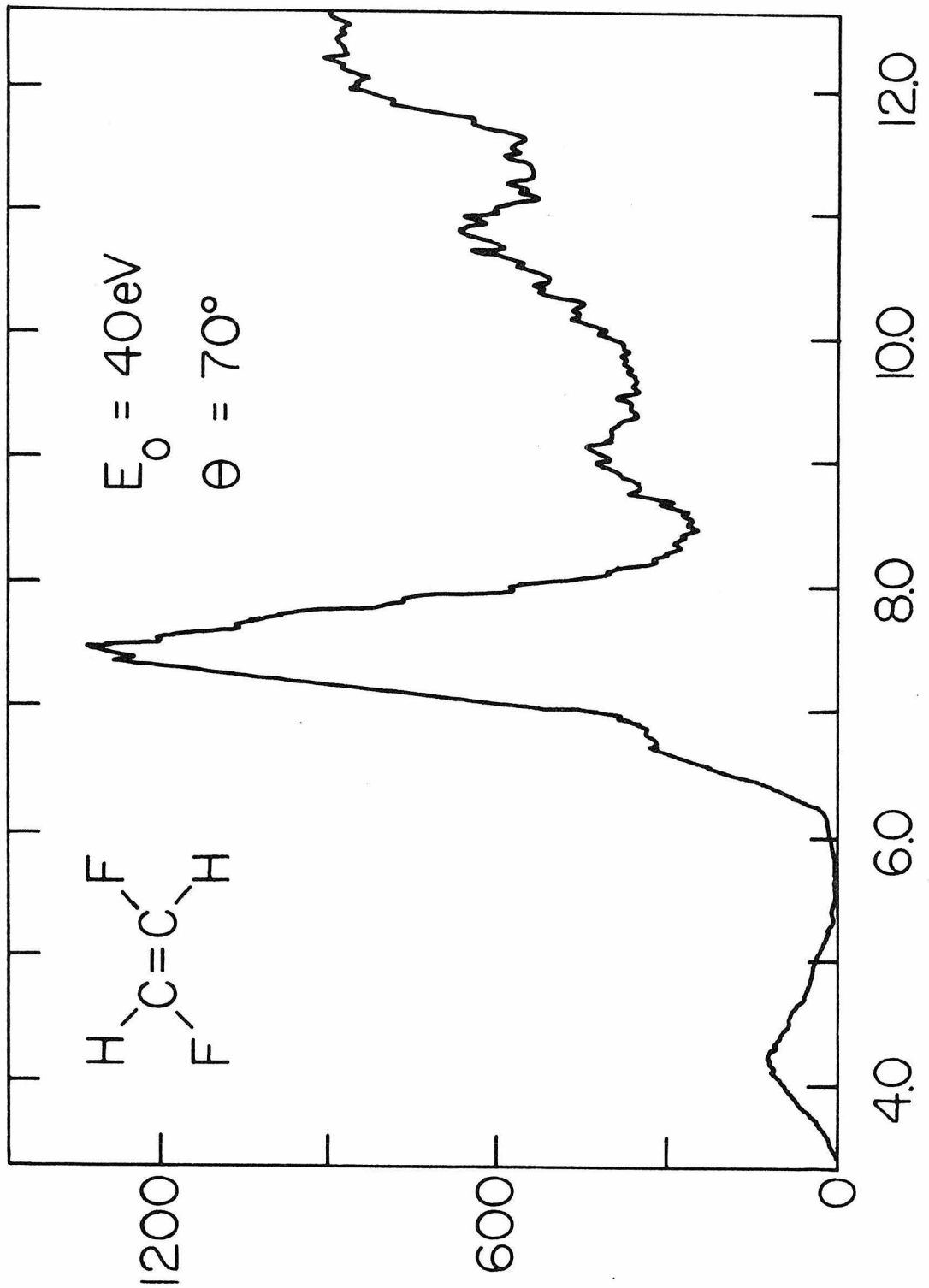

3.13

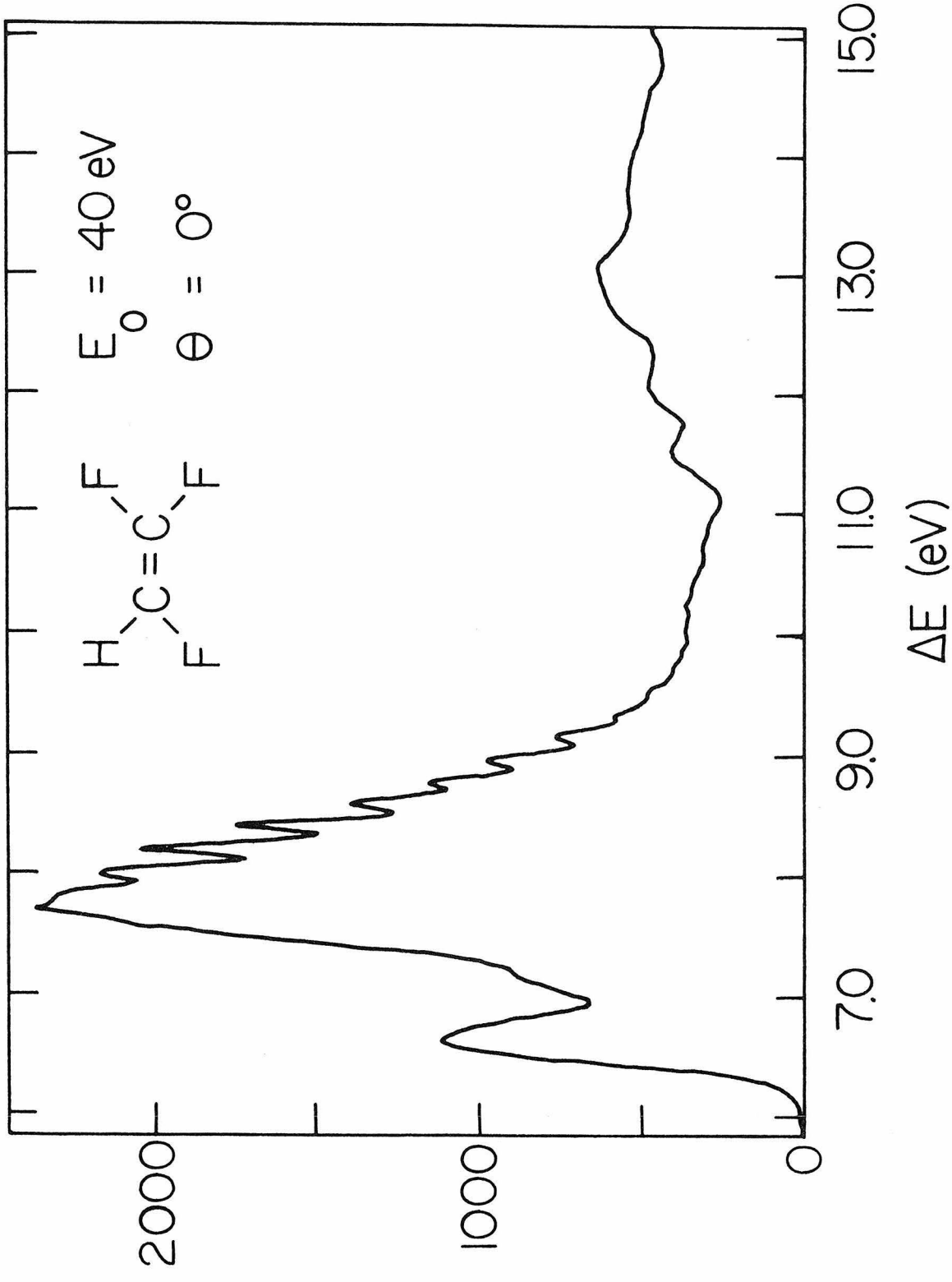
I (COUNTS / SEC)
2000
1000
0
7.0
9.0
11.0
13.0
15.0
ΔE (eV)
E_0 = 40 eV
θ = 0°
H
C=C
F
F
F
F

3.14

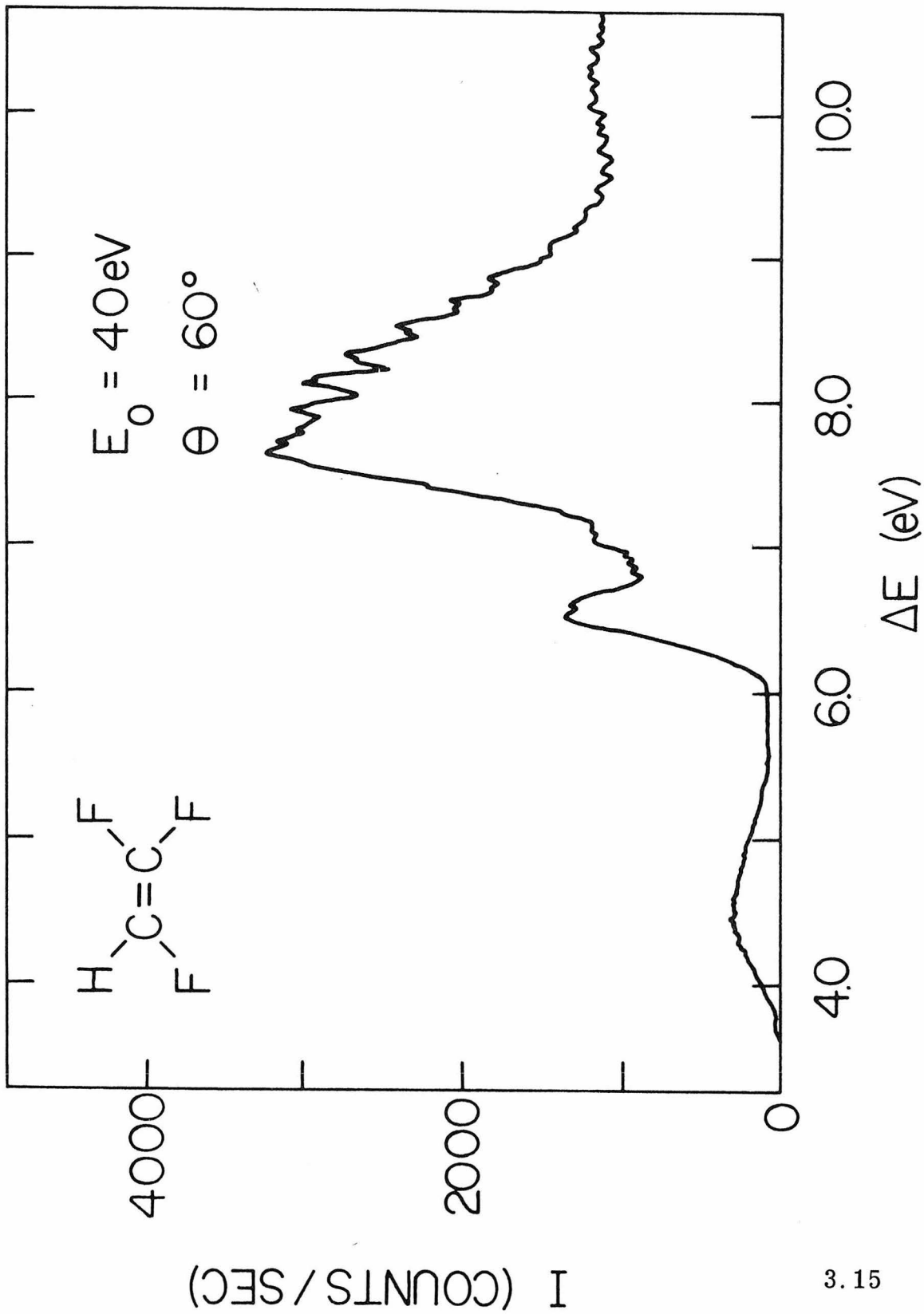

3.15

for the trans isomer occurs at 4.18 eV and has a Franck-Condon region extending from 3.5 eV to 5.4 eV.

In the cis isomer, the N → V transition peaks at 7.82 eV, but occurs at 7.39 eV in the trans isomer. As shown in Table 1, both singlet → singlet peak locations are in agreement with the optical values [3].

Figures 3.14 and 3.15 show the $\theta = 0^\circ$ and 60° energy-loss spectra for trifluoroethylene taken at 40 eV impact energy. For this molecule, the N → T transition has a maximum at 4.43 eV and a corresponding Franck-Condon band from 3.5 eV to 5.4 eV.

The corresponding singlet → singlet N → V transition in trifluoroethylene has a peak value of 7.65 eV, in agreement with the optically determined value. These values are listed in Table 1.

The 40 eV singlet → triplet to singlet → singlet area ratio plots for 1,1-difluoroethylene, cis and trans 1,2-difluoroethylene, and trifluoroethylene are shown in Figures 3.1b-3.1e, respectively. The N → T, N → V, and elastic peak DCS curves for these molecules are given in Figures 3.16-3.23. The well resolved Rydberg features as well as the superexcited states of these molecules are discussed in Section 3.4.4.

3.4.3. Tetrafluoroethylene

The electron impact excitation spectra of tetrafluoroethylene measured for $\theta = 0^\circ$ and 80° using 40 eV incident electrons are shown in Figures 3.24 and 3.25. The peak location of the singlet→triplet N→T transition is at 4.68 eV with a Franck-Condon band extending from 3.6 eV to 5.6 eV. The ratio of the area

Figures 3.16 thru 3.23: DCS plots for 1,1-difluoroethylene (3.16, 3.17), cis-1,2-difluoroethylene (3.18, 3.19), trans-1,2-difluoroethylene (3.20, 3.21), and trifluoroethylene (3.22, 3.23). Impact energies are indicated on each figure. In each figure, the squares (□) are the elastic DCS × 0.1, the circles (○) are the N→V DCS, and the triangles (Δ) are the N→T DCS.

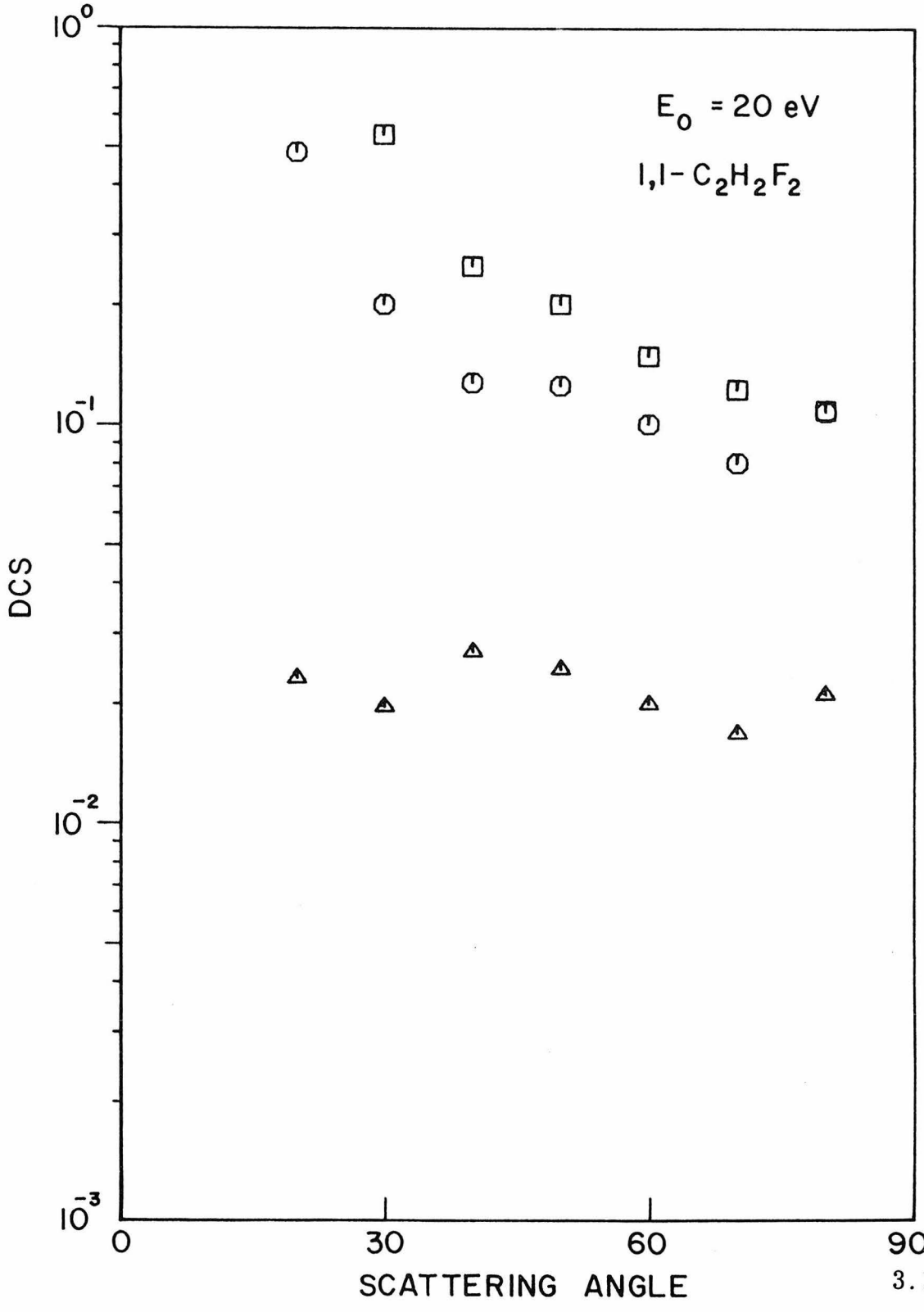
E_o = 20 eV
1,1-$C_2H_2F_2$
DCS
10^0
10^{-1}
10^{-2}
10^{-3}
0
30
60
90
SCATTERING ANGLE

3.16

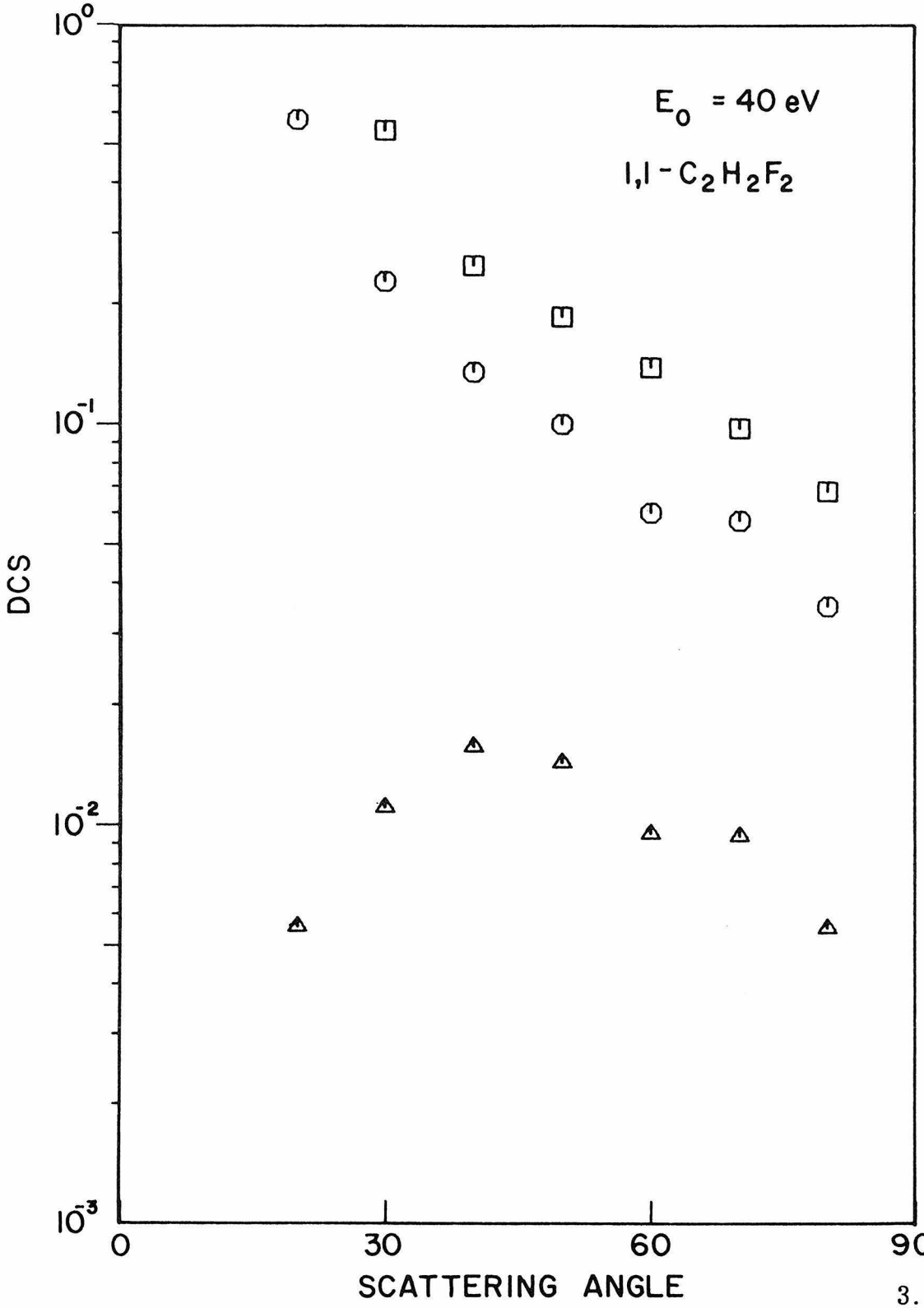
E_0 = 40 eV
1,1 - $C_2H_2F_2$
DCS
10^0
10^{-1}
10^{-2}
10^{-3}
0
30
60
90
SCATTERING ANGLE

3.17

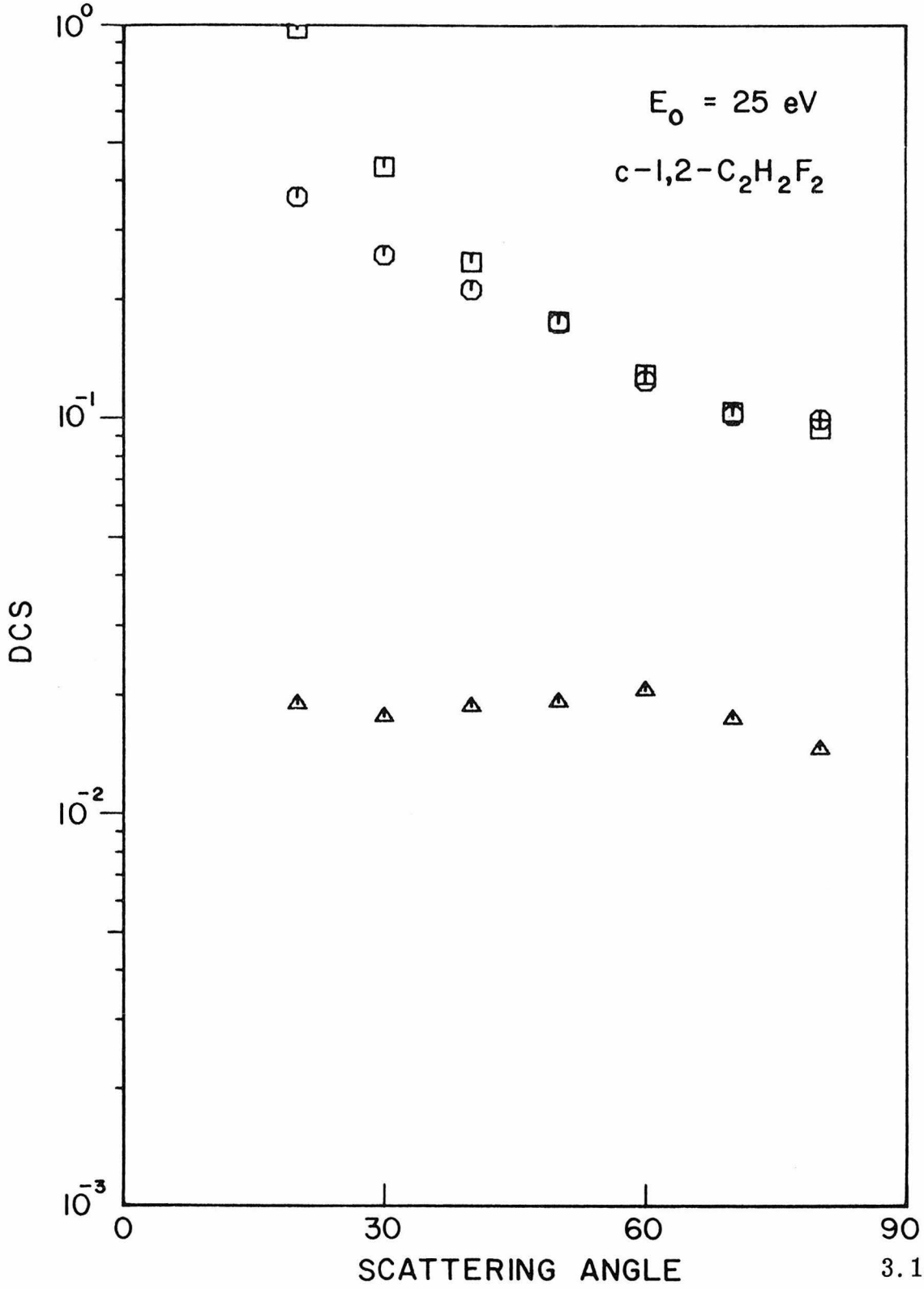
10^0
10^{-1}
10^{-2}
10^{-3}
DCS
E_o = 25 eV
c-1,2-$C_2H_2F_2$
0
30
60
90
SCATTERING ANGLE

3.18

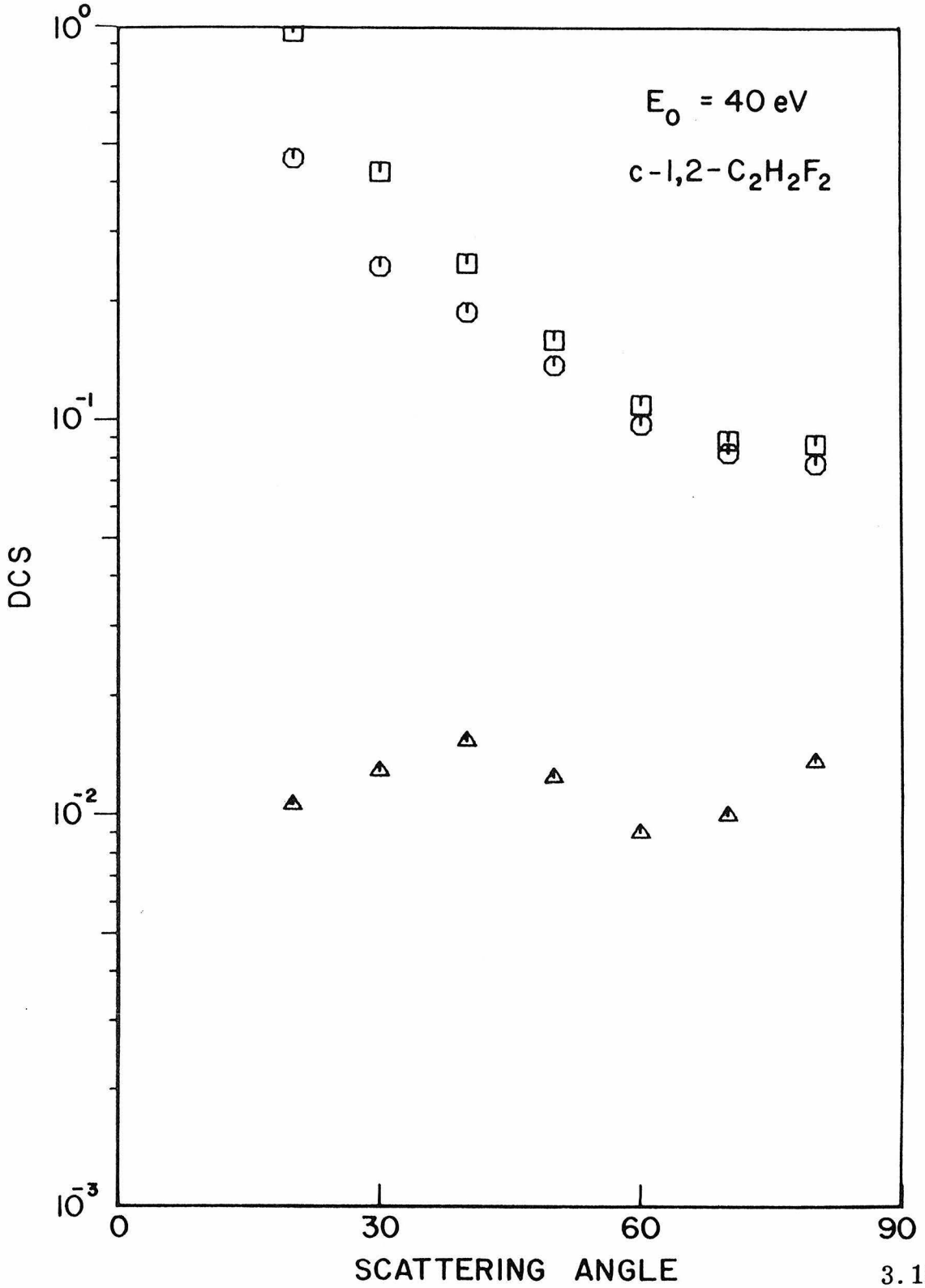
E_0 = 40 eV
c-1,2-$C_2H_2F_2$
DCS
10^0
10^{-1}
10^{-2}
10^{-3}
0
30
60
90
SCATTERING ANGLE

3.19

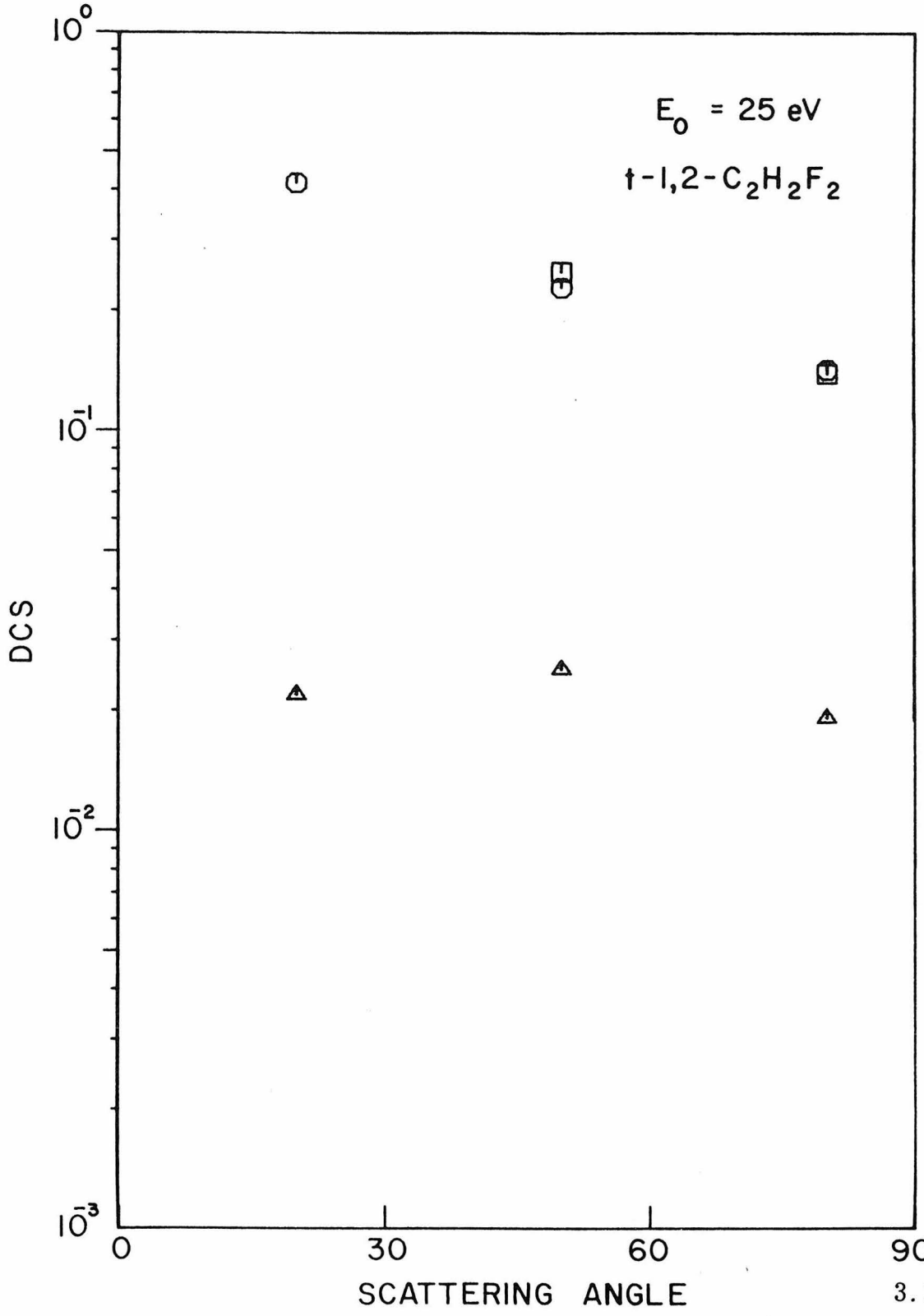
E_0 = 25 eV
t-1,2-$C_2H_2F_2$
DCS
10^0
10^{-1}
10^{-2}
10^{-3}
0
30
60
90
SCATTERING ANGLE

3.20

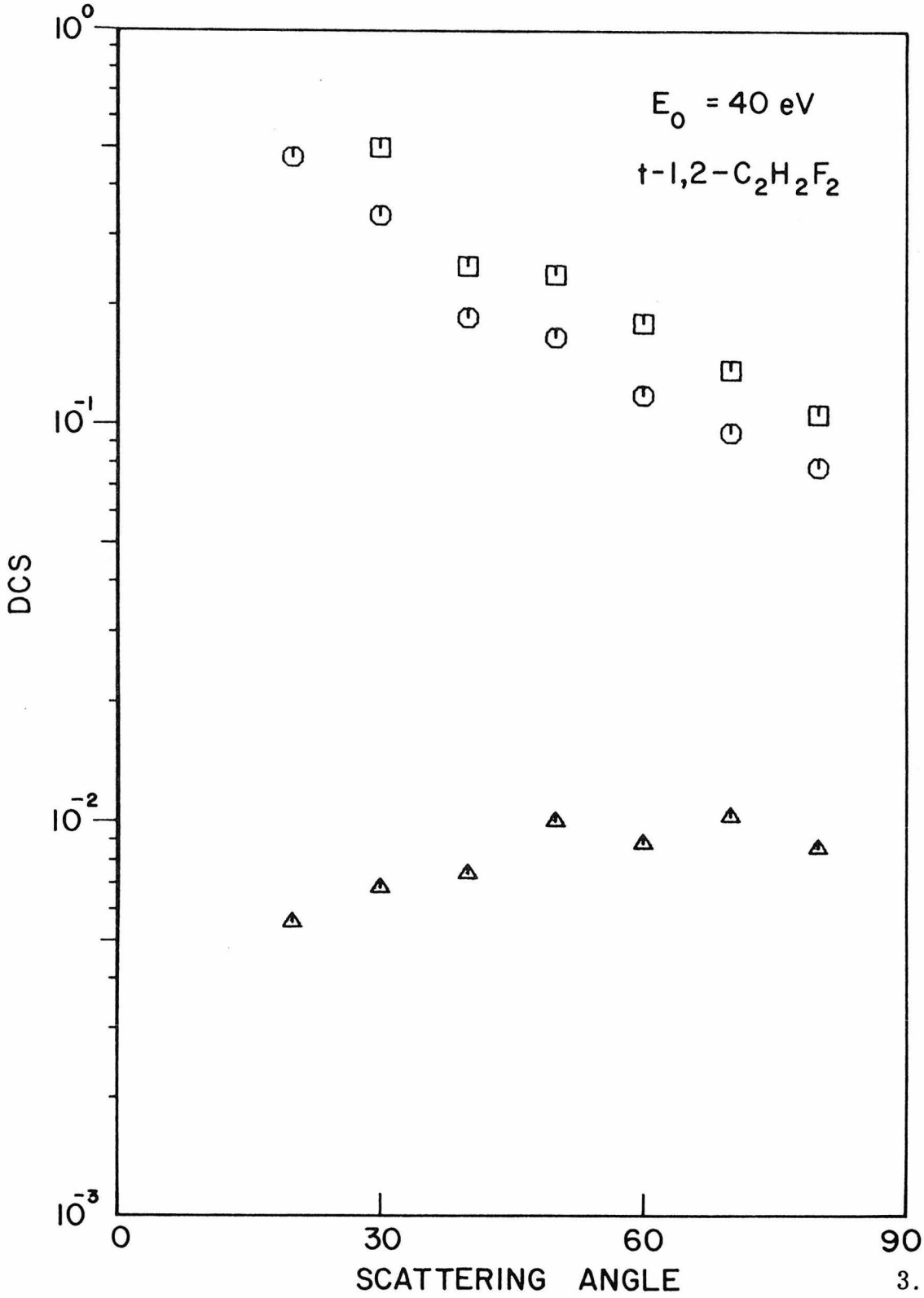
E_0 = 40 eV
t-1,2-$C_2H_2F_2$
DCS
10^0
10^{-1}
10^{-2}
10^{-3}
0
30
60
90
SCATTERING ANGLE

3.21

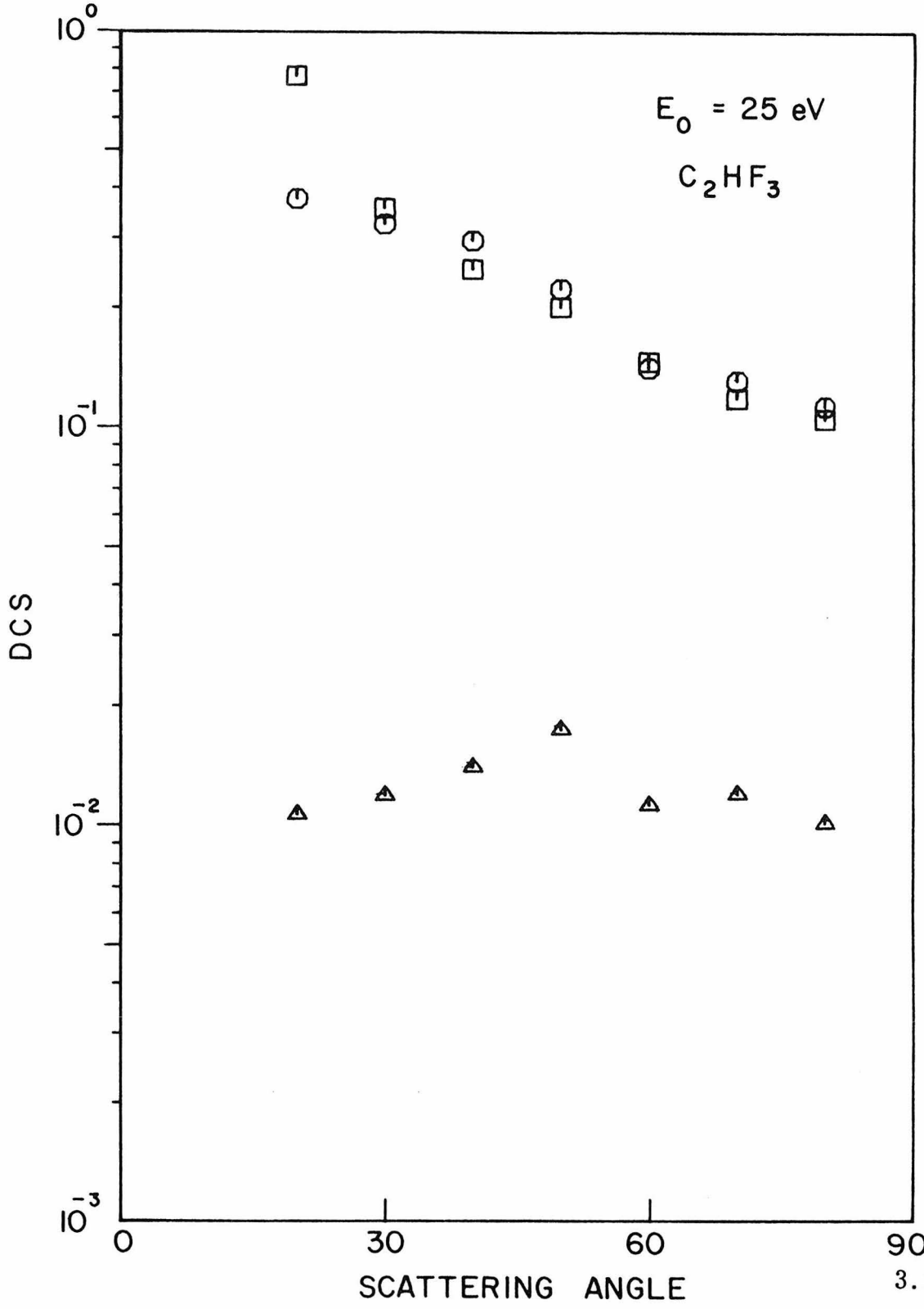

3.22

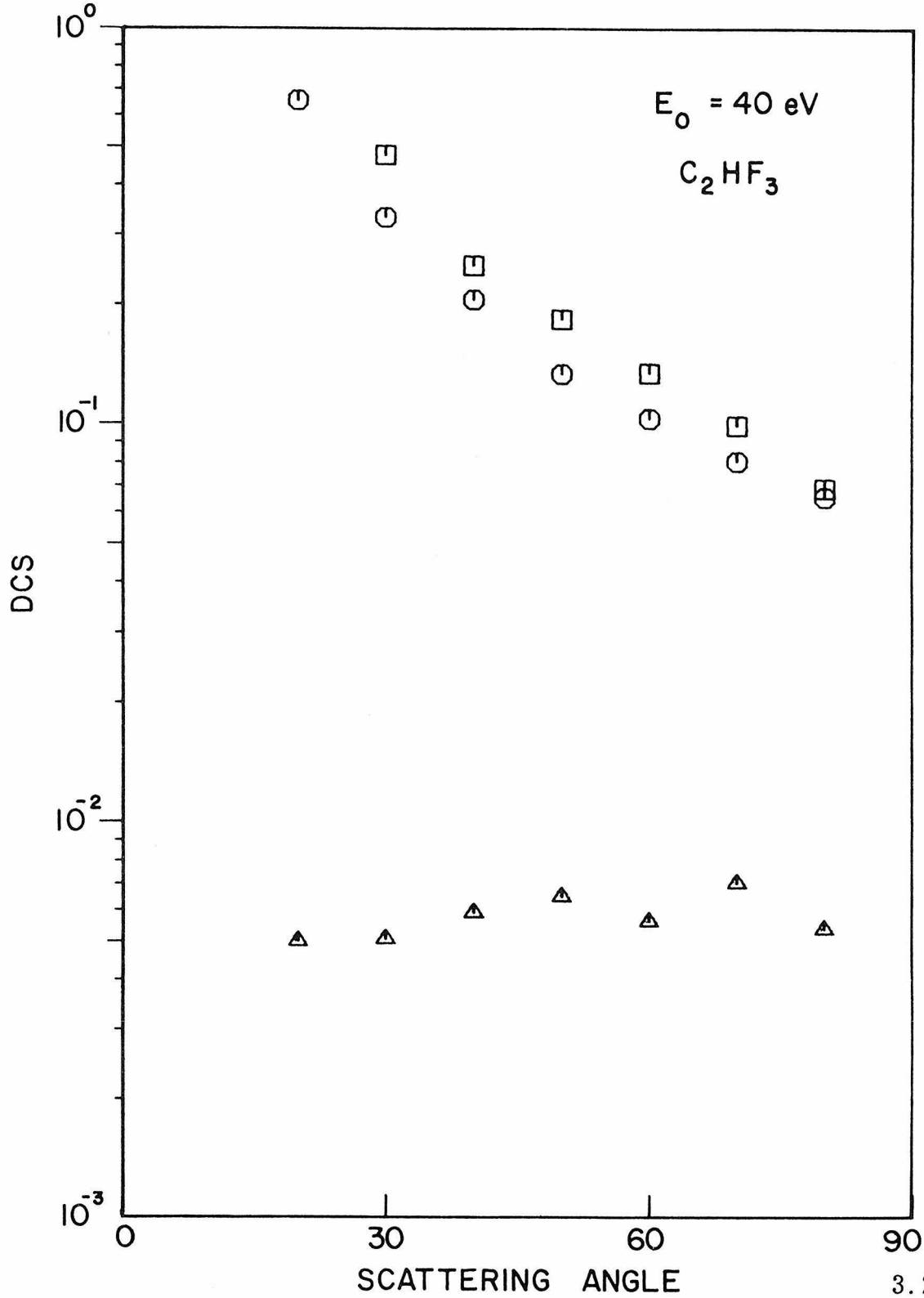

3.23

Figure 3.24: Energy-loss spectrum of tetrafluoroethylene taken at $\theta = 0^{\circ}$, $E_0 = 40$ eV, resolution = 90 meV, scattering chamber pressure = 4.0 mtorr.

Figure 3.25: Energy-loss spectrum of tetrafluoroethylene taken at $\theta = 60^{\circ}$, $E_0 = 40$ eV, resolution = 125 meV, scattering chamber pressure = 5.2 mtorr.

Figures 3.26 and 3.27: DCS curves for tetrafluoroethylene with an impact energy of 25 eV and 40 eV, respectively. Squares (□) are elastic DCS × 0.1, circles (○) are N→V DCS, and triangles (△) are N→T DCS.

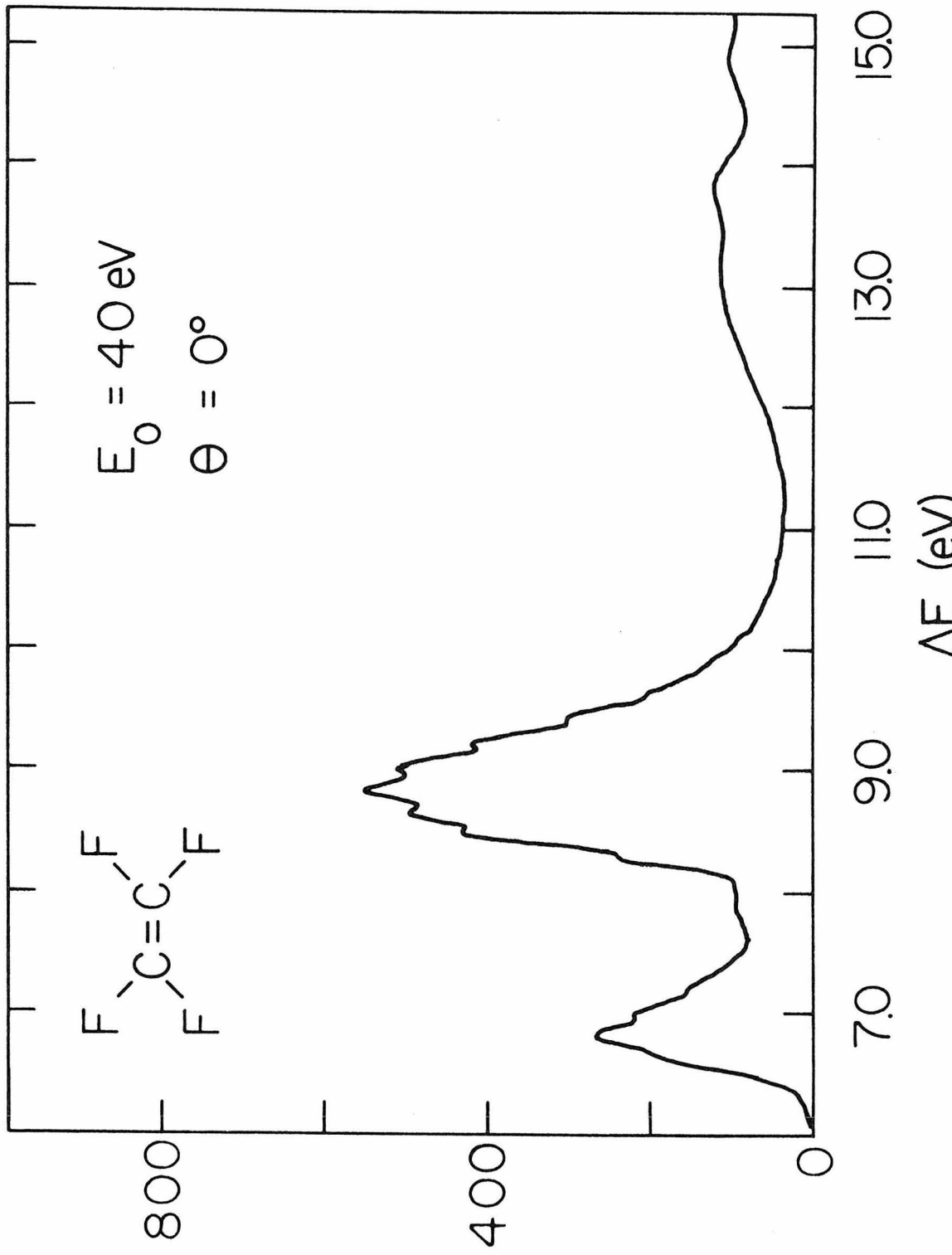
I (COUNTS / SEC)
800
400
0
7.0
9.0
11.0
13.0
15.0
ΔE (eV)
$E_0 = 40$ eV
$\theta = 0°$
F
C=C
F
F

3.24

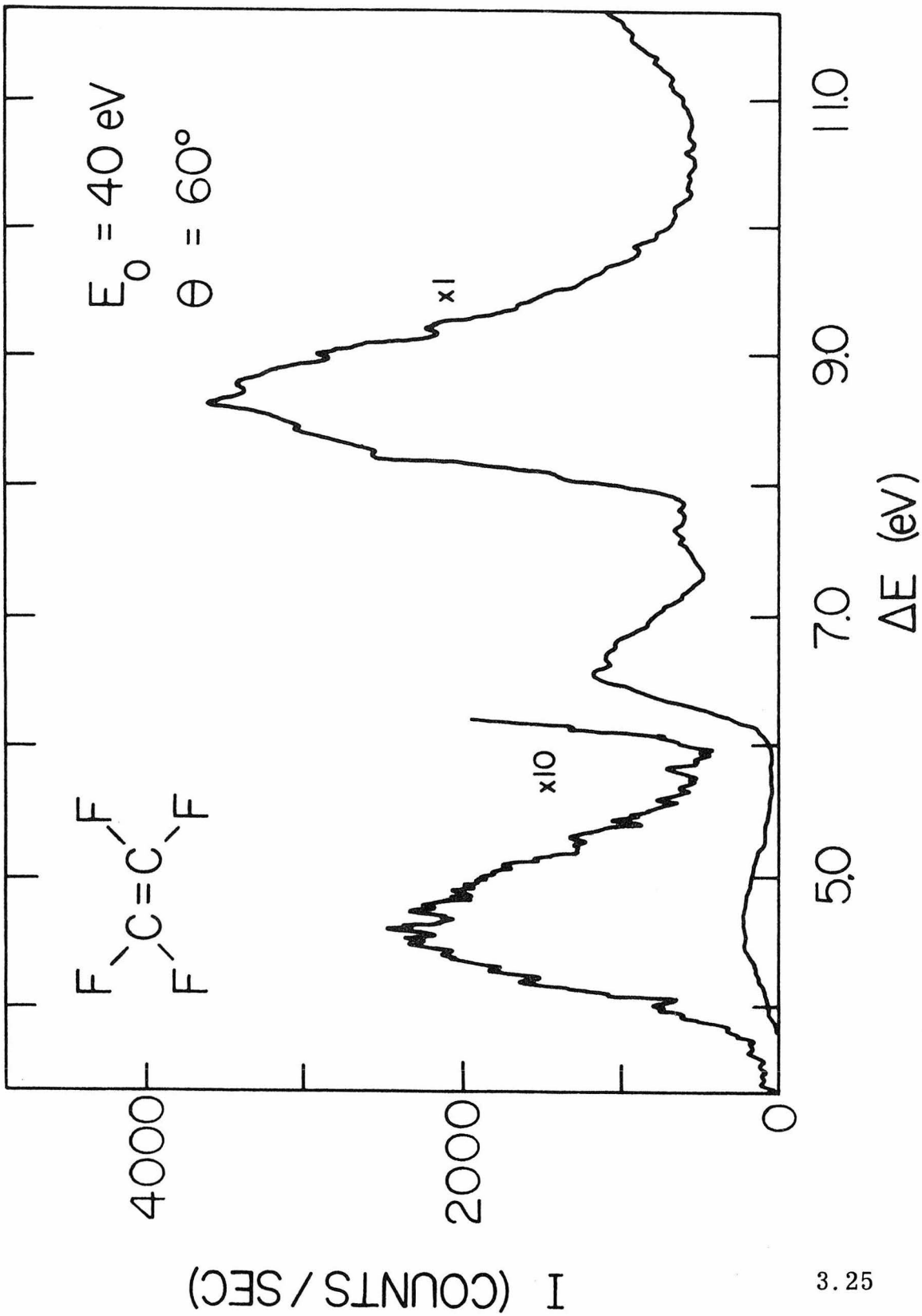
I (COUNTS / SEC)
4000
2000
0
5.0
7.0
9.0
11.0
ΔE (eV)
E_o = 40 eV
θ = 60°
×1
×10
F
F
C=C
F
F

3.25

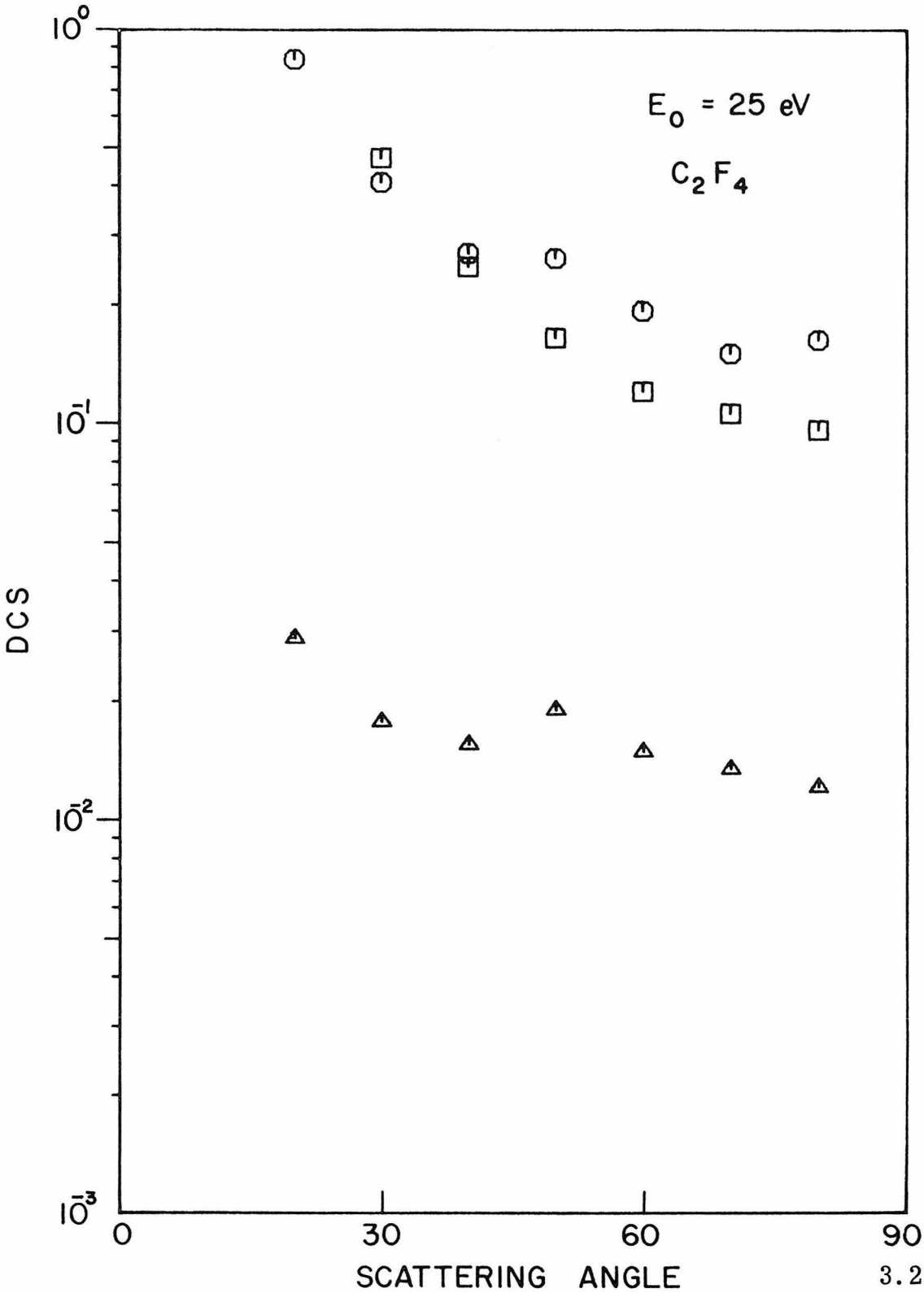

3.26

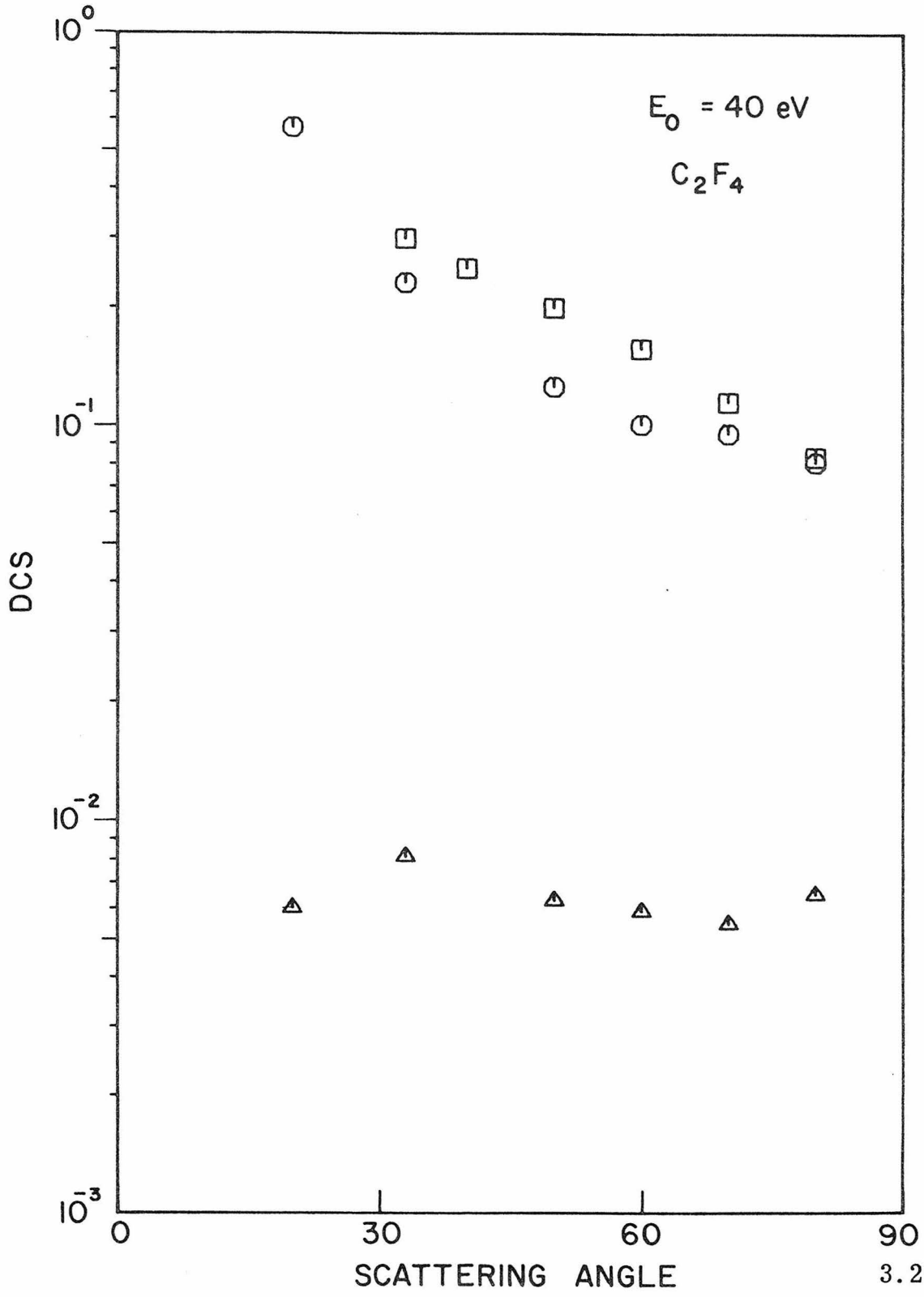

3.27

under this peak to that of the 8.84 eV transition is plotted in Figure 3.1f. The 8.84 eV transition apparently corresponds to the N→V transition in ethylene based on its Franck-Condon bandwidth and intensity, and was previously assigned on this basis [3]. It is possible that the weak singlet→singlet transition at 7.7 eV may correspond to the N→V transition, but if this is so, then it represents a radical change in transition intensity from the other fluoroethylenes.

While the N→T transition shows a slight shift to higher energies, the corresponding N→V transition exhibits a large positive shift of 1.2 eV as compared with the N→V transition in trifluoroethylene. The optical value of 8.88 eV agrees well with the results of the present study. A previous explanation [3] of the N→V transition energy shift was the possible increased resistance to torsional motion in the excited state caused by removal of the final hydrogen. It was argued that this would lead to an increase in the energy of the excited state and thus raise the N→V transition energy. To test this idea, measurements were made of the excitation spectra of chlorotrifluoroethylene (see Appendix E). Here, the fourth hydrogen is replaced by another halogen, chlorine, which should have even a greater effect on the torsional motion than fluorine. For this molecule, the N→V peak location by electron impact is 7.85 eV [28]. Thus, no appreciable shift was produced by replacement of the last hydrogen by chlorine. Therefore, the origin of the shift in the N→V transition of perfluoroethylene is presumably not a steric effect. The optical studies of the chlorine-substituted ethylenes [29] also support

this conclusion because no major shift is seen in the N→V transition energy in going from chloroethylene to tetrachloroethylene. In addition, the N→V transition energies are similar to that found in ethylene.

An alternate explanation of the transition energy shift has been made by Salahub [9]. Before configuration interaction, his calculations predict a hypsochromic shift in the N→V transition energy of tetrafluoroethylene of 0.31 eV to 1.14 eV relative to the N→V transition energies of the other fluoroethylenes. When CI is included in the calculation, the corresponding shifts are between 1.28 eV and 2.08 eV. Thus, CI including $\sigma \rightarrow \sigma^*$ excitations is more effective in lowering the N→V transition energy of the hydrogen containing fluoroethylenes than that of tetrafluoroethylene. Salahub suggests that this is due to the much higher energy of states involving $\sigma \rightarrow \sigma^*$ excitations from C-C-F σ orbitals when compared with the energy of states involving C-C-H σ orbitals. The C-C-H orbitals are present in all of the fluoroethylenes except tetrafluoroethylene. In agreement with this argument, Mulliken [30] has recently pointed out the importance of such σ-π mixing for the accurate description of the V state of ethylene. The effect of CI appears to account for 30% to 70% of the calculated shift, however, the remainder is still not explained by this argument.

A number of Rydberg and superexcited states were observed in the tetrafluoroethylene spectra and are discussed in the next section.

3.4.4. Rydberg and Superexcited States

From their optical data in the 6 eV to 10 eV region, Belanger and Sandorfy [3] have fitted a large number of peaks to three Rydberg series, all converging to the first ionization potential. Even though vibrational structure has been resolved in the photoelectron spectra of the fluoroethylenes [10, 12], the lack of resolved structure in these electron impact results precludes the use of vibrational spacings to assign peaks as was successfully done with cyclopropeone [24]. As an alternate means of identification, we have used the results of the present study, along with the photoionization values of the first and second ionization potentials, to determine term values associated with each transition, as outlined by Brundle et. al. [10]. It has been shown that the term value for a given $N \rightarrow R_n$ Rydberg transition, where n indexes the respective transitions, will remain relatively constant within a series of molecules regardless of the degree of substitution [31]. The term value is defined as the difference between the vertical ionization potential and the Rydberg transition energy. This characteristic also appears to be valid even when the Rydberg series converges to a higher ionization potential, so long as that higher IP is used to find the term value. Using this technique, it is possible to assign all Rydberg transitions in the 6 eV to 10 eV region of each of the spectra, as well as several of the superexcited states. Superexcited states are fit into a Rydberg series leading to higher ionization potentials based on their term values. The locations of the $N \rightarrow R_n$ peaks, their corresponding term values and assignments are listed in Table 2, along with those

superexcited states that could be assigned by this method. Despite some variation in the term values, the resulting assignments in the 6 eV to 10 eV region are all in agreement with those found in the optical study. The average 3s, 3p and 3d term values of 3.7 eV, 2.5 eV, and 1.7 eV are found to be similar to the corresponding term values (3.9 eV, 2.7 eV, and 1.6 eV, respectively) in the fluorine-substituted methanes [21].

It has been suggested that $\sigma \rightarrow \sigma^*$ transitions may occur above 10 eV in the fluoroethylenes [6]. Since a number of superexcited states listed in Table 1 do not seem to be members of higher Rydberg series, it is possible that some of them correspond to such valence transitions.

Recently, Reinke [32] has measured the total absorption cross sections of vinyl fluoride and 1,1-difluoroethylene from 10 eV to 22 eV using synchrotron radiation. In both cases, he observed a number of features beyond the first ionization potential corresponding to excitations to superexcited states. In vinyl fluoride, these peaks occurred at 11.0, 11.35, 12.55, 14.95, and 16.55 eV. When these values (shown in parentheses in Table 1) are compared to the results of the present study, the first four peak locations are seen to be in good agreement. The same holds true in the case of 1,1-difluoroethylene, where Reinke's data show peaks at 11.3, 12.3, 13.9, 14.3, 14.9, 18.4, and 20.25 eV. Again, each of the first four locations are in good agreement with the present results.

3.5. Photochemistry

The quenching of the 1^3B_{1u} excited state of benzene by vinyl fluoride and 1,1-difluoroethylene has been studied by Das Gupta and Phillips [33]. Vinyl fluoride was found to be almost 20 times more effective than 1,1-difluoroethylene for quenching of the 1^3B_{1u} state. The quenching is presumably by triplet→triplet energy transfer since the 0-0 band for excitation of the $^3B_{1u}$ state in benzene occurs at 3.66 eV [34]. The rate of such energy transfer in solids is governed by the overlap of the singlet→triplet absorption spectrum of the acceptor with the phosphorescence spectrum of the donor [35], and it has been suggested that a similar spectral overlap criterion applies in the gas phase as well [36, 37]. The phosphorescence curve for $^3B_{1u}$ benzene is known to extend from about 2.68 eV to 3.65 eV [34]. Comparison of this upper limit of the donor phosphorescence with the lower limits of the Franck-Condon regions of the acceptors vinyl fluoride (3.4 eV) and 1,1-difluoroethylene (3.8 eV) shows that the origin of this wide disparity in the quenching cross sections is due to the differing amounts of spectral overlap.

A number of experimental measurements have been made of the quenching cross section for mercury in the 6^3P_1 state at 4.89 eV by the fluoroethylenes [38-42]. The cross sections all fall within the range from $30A^2$ to $10A^2$ as compared with $31A^2$ for ethylene [43]. It is not surprising that the quenching cross sections for the fluoroethylenes and ethylene are comparable, since the postulated quenching mechanism is the formation of the lowest excited triplet state of the olefin [43]. While the peaks of

the singlet→triplet transitions of the fluoroethylenes are somewhat below the energy of the Hg excited state, the broad Franck-Condon region results in sufficient spectral overlap with the Hg $6^3P_1 \rightarrow 1^1S_0$ emission line at 4.89 eV to yield large quenching cross sections for all fluoroethylenes.

3.6. Conclusions

In each of the six fluoroethylenes, a spin-forbidden, singlet→triplet transition has been observed between 4.1 eV and 4.7 eV.

With the exception of the large blue shift in the N→V transition energy in tetrafluoroethylene, the singlet→singlet ($\pi \rightarrow \pi^*$) electronic transition energies of the fluoroethylenes are all relatively similar and not particularly sensitive to fluorine atom substitution. This behavior is also consistent with conclusions drawn from earlier ionization potential studies. The hypsochromic shift in tetrafluoroethylene appears not to be due to any torsional barrier effects, but may be at least partly caused by the interaction of the $\pi \rightarrow \pi^*$ excited state with higher energy $\sigma \rightarrow \sigma^*$ configurations.

The term value method has proven very useful in assigning and organizing several of the superexcited states into higher Rydberg series. In general, the term values found for the fluoroethylenes are comparable to those determined in other molecules. Additional superexcited states which apparently do not fit into Rydberg series are observed, and may be $\sigma \rightarrow \sigma^*$ valence type transitions.

The Franck-Condon bandshapes obtained in these electron impact studies have been used in conjunction with the spectral overlap criterion to explain differing observed rates of gas phase photochemical reactions. This result lends further support to the use of the spectral overlap criterion in the gas phase.

Table 1

Ground to Excited State Transition Energies of the Fluoroethylenes

Molecule	Transition Energies (eV) N → T Expt. Present work	N → T Expt. Other work	N → T Calc.[a]	N → V Expt. Present work	N → V Expt. Optical[b] work	N → V Calc.[a]	N → Superexcited states
C_2H_3F	4.40 (3.4 - 5.4)[c]	4.4[d]	5.30	7.50	7.44	8.17	11.0, 12.4, 15.2 (11.0, 11.35, 12.55, 14.95, 16.55)[f]
1,1-$C_2H_2F_2$	4.63 (3.8 - 5.5)	4.6[e]	5.43	7.50	7.50	8.19	11.0, 12.3, 13.8, 14.1 14.8 (11.3, 12.3, 13.9, 14.3, 14.9, 18.4, 20.25)[f]
c-1,2-$C_2H_2F_2$	4.28 (3.7 - 5.4)	-	4.58	7.82	7.81	7.41	10.9, 11.4, 12.0, 12.5 13.0, 14.6, 14.8
t-1,2-$C_2H_2F_2$	4.18 (3.5 - 5.2)	-	4.58	7.39	7.28	7.40	11.0, 12.0, 13.0, 13.7 15.2, 16.8
$C_2H\ F_3$	4.43 (3.5 - 5.4)	-	5.27	7.65	7.61	8.17	12, 0, 12.9, 13.8, 15.2
C_2F_4	4.68 (3.6 - 5.6)	-	6.00	8.84	8.88	9.16	11.4, 13.3, 13.9, 15.0 15.5

[a] Reference 9

[b] Reference 3

[c] Estimated Franck-Condon region

[d] Reference 4

[e] Reference 5

[f] Reference 32

Table 2

Transition Energies, Term Values, and Assignments of Rydberg Series in the Fluoroethylenes

	C_2H_3F		$1,1\text{-}C_2H_2F_2$		$cis\text{-}1,2\text{-}C_2H_2F_2$	
First I.P.	10.58		10.72		10.43	
3s	7.02	3.56	6.95	3.77	6.52	3.91
3p	8.08	2.50	8.23	2.49	8.38	2.05
4s	8.67	1.91	9.08	1.64	8.81	1.62
3d	8.87	1.71	9.26	1.46	9.01	1.42
4p	9.37	1.21	9.44	1.28	9.20	1.23
5s	9.72	.86	9.81	.91	9.55	.88
5p	9.84	.74	10.01	.71	-	-
6s	10.03	.55	10.11	.61	-	-
Second I.P.	13.79		14.79		13.97	
3s	10.22	3.57	10.98	3.81	10.25	3.72
3p	-	-	12.27	2.52	11.43	2.54
4s	12.38	1.41	-	-	12.47	1.50
Third I.P.			18.22			
3s	-	-	14.77	3.45	-	-

	$trans\text{-}1,2\text{-}C_2H_2F_2$		C_2HF_3		C_2F_4	
First I.P.	10.38		10.53		10.54	
3s	6.44	3.94	6.56	3.97	6.62	3.92
3p	7.88	2.50	7.98	2.55	8.28	2.26
4s	8.68	1.70	8.74	1.79	8.84	1.70
3d	8.80	1.58	8.91	1.62	9.04	1.50
4p	8.97	1.41	9.31	1.22	9.44	1.10
5s	9.53	.58	9.53	1.00	9.65	.89
5p	-	-	-	-	-	-
6s	-	-	-	-	-	-
Second I.P.	13.90		14.68		15.93	
3s	10.20	3.70	11.45	3.23	-	-
3p	11.96	1.94	12.05	2.63	13.89	2.04
4s	-	-	12.93	1.75	-	-

Table 3

Ratios of Intensities of the (N → T) Transition to the (N → V) Transition

θ (deg)	C_2H_3F (20 eV)	1,1-$C_2H_2F_2$ (25 eV)	c-1,2-$C_2H_2F_2$	t-1,2-$C_2H_2F_2$	C_2HF_3	C_2F_4
20	0.025	0.050	0.052	0.053	0.028	0.034
30	0.035	0.098	0.068	-	0.036	0.044
40	0.055	0.195	0.088	-	0.048	0.057
50	0.074	0.194	0.111	0.111	0.078	0.072
60	0.088	0.199	0.166	-	0.080	0.078
70	0.107	0.207	0.173	-	0.092	0.090
80	0.110	0.196	0.148	0.134	0.090	0.070
			E_o = 40 eV			
10	0.004	0.005	0.005	0.004	0.002	0.003
20	0.010	0.017	0.023	0.012	0.009	0.010
30	0.021	0.033	0.031	0.020	0.015	0.034*
40	0.034	0.054	0.050	0.040	0.029	0.041
50	0.060	0.100	0.090	0.060	0.049	0.050
60	0.074	0.125	0.114	0.075	0.059	0.058
70	0.089	0.145	0.121	0.109	0.070	0.071
80	0.099	0.160	0.150	0.111	0.081	0.081

* θ = 33°

Table 4a

Differential Cross Sections (DCS) for Monofluoroethylene

(Normalized to 1.0 at 40°)

E_o = 25 eV

θ (deg)	Elastic	N→V	N→T
20	4.67	0.253	0.00641
30	1.79	0.71	0.00602
40	1.00	0.128	0.00698
50	0.716	0.094	0.00659
60	0.499	0.067	0.00593
70	0.387	0.056	0.00601
80	0.347	0.053	0.00581

E_o = 40 eV

20	6.66	0.243	0.00234
30	2.08	0.126	0.00264
40	1.00	0.083	0.00278
50	0.636	0.059	0.00353
60	0.425	0.039	0.00290
70	0.306	0.029	0.00262
80	0.253	0.025	0.00245

Table 4b

Differential Cross Sections (DCS) for 1,1-difluoroethylene

(Normalized to 1.0 at 40°)

E_o = 20 eV

θ (deg)	Elastic	N→V	N→T
20	5.55	0.194	0.00925
30	2.14	0.800	0.00787
40	1.00	0.051	0.01080
50	0.799	0.050	0.00973
60	0.593	0.040	0.00796
70	0.488	0.032	0.00670
80	0.433	0.043	0.00842

E_o = 40 eV

20	8.80	0.231	0.00223
30	2.17	0.091	0.00444
40	1.00	0.054	0.00629
50	0.744	0.040	0.00575
60	0.555	0.024	0.00381
70	0.392	0.023	0.00375
80	0.272	0.014	0.00221

Table 4c

Differential Cross Sections (DCS) for cis-1, 2-difluoroethylene

(Normalized to 1.0 at 40°)

E_o = 20 eV

θ (deg)	Elastic	N→V	N→T
20	3.91	0.146	0.00759
30	1.74	0.104	0.00707
40	1.00	0.085	0.00750
50	0.707	0.070	0.00772
60	0.579	0.050	0.00827
70	0.418	0.041	0.00699
80	0.379	0.040	0.00588

E_o = 40 eV

20	3.86	0.184	0.00423
30	1.70	0.098	0.00516
40	1.00	0.075	0.00614
50	0.637	0.055	0.00497
60	0.438	0.039	0.00360
70	0.356	0.033	0.00399
80	0.348	0.031	0.00547

Table 4d

Differential Cross Sections (DCS) for trans-1,2-difluoroethylene

(Normalized to 1.0 at 40°)

E_o = 20 eV

θ (deg)	Elastic	N→V	N→T
20	4.40	0.166	0.00874
50*	1.00	0.091	0.01012
60	0.555	0.057	0.00766

E_o = 40 eV

20	4.58	0.188	0.00222
30	1.99	0.134	0.00272
40	1.00	0.074	0.00296
50	0.949	0.066	0.00401
60	0.716	0.047	0.00352
70	0.545	0.038	0.00413
80	0.421	0.031	0.00343

* Normalized to 1.0 at 50°.

Table 4e

Differential Cross Sections (DCS) for Trifluoroethylene

(Normalized to 1.0 at 40°)

E_o = 25 eV

θ (deg)	Elastic	N→V	N→T
20	3.07	0.150	0.00426
30	1.42	0.130	0.00475
40	1.00	0.118	0.00501
50	0.801	0.089	0.00698
60	0.583	0.056	0.00449
70	0.472	0.052	0.00479
80	0.417	0.045	0.00405

E_o = 40 eV

20	6.97	0.261	0.00200
30	1.90	0.132	0.00203
40	1.00	0.082	0.00236
50	0.730	0.053	0.00259
60	0.534	0.041	0.00224
70	0.394	0.032	0.00280
80	0.274	0.026	0.00214

Table 4f

Differential Cross Sections (DCS) for Tetrafluoroethylene

(Normalized to 1.0 at 40°)

E_o = 20 eV

θ (deg)	Elastic	N → V	N → T
20	4.70	0.335	0.01152
30	1.88	0.103	0.00709
40	1.00	0.108	0.00620
50	0.659	0.105	0.00761
60	0.481	0.077	0.00597
70	0.424	0.060	0.00539
80	0.384	0.065	0.00485

E_o = 40 eV

20	5.44	0.227	0.00240
33*	1.19	0.092	0.00325
40	1.00	-	-
50	0.793	0.050	0.00251
60	0.623	0.042	0.00235
70	0.457	0.038	0.00218
80	0.331	0.032	0.00259

* Reference 27.

References

1. A. J. Merer and R. S. Mulliken, Chem. Rev. 69, 639 (1969).
2. A. Kuppermann, J. K. Rice, and S. Trajmar, J. Phys. Chem. 72, 3894 (1968); S. Trajmar, J. K. Rice, and A. Kuppermann, Advan. Chem. Phys. 18, 15 (1970).
3. G. Belanger and C. Sandorfy, J. Chem. Phys. 55, 2055 (1971).
4. J. H. Moore, Jr., J. Phys. Chem. 76, 1130 (1972).
5. R. M. O'Malley and K. R. Jennings, Int. J. Mass. Spec. Ion Phys., App. 1-3, 2 (1969).
6. M. A. Landau, S. S. Dubov, and A. N. Medvedev, Russ. J. Phys. Chem. 43, 3 (1969).
7. S. Meza and U. Wahlgren, Theoret. Chim. Acta. (Berl.) 21, 323 (1971).
8. D. T. Clark, J. N. Murrell, and J. M. Tedder, J. Chem. Soc. 1250 (1963).
9. D. R. Salahub, Theoret. Chim. Acta. (Berl.) 22, 330 (1971); D. R. Salahub, Ph.D. Thesis, Université de Montréal (1970).
10. C. R. Brundle, M. B. Robin, N. A. Kuebler, and H. Bosch, J. Am. Chem. Soc. 94, 1451 (1972).
11. R. Bralsford, D. V. Harris, and W. C. Price, Proc. Roy. Soc. (London) A258, 459 (1960).
12. R. F. Lake and Sir H. Thompson, Proc. Roy. Soc. (London) A315, 323 (1970).
13. C. Lifshitz and F. A. Long, J. Phys. Chem. 67, 2463 (1963).
14. W. C. Price, Chem. Rev. 41, 257 (1947).

15. G. L. Caldow and C. A. Coulson, Tetrahedron Supp. 7, 127 (1965).

16. M. A. Landau, S. S. Dubov, and A. N. Medvedev, Russ. J. Phys. Chem. 42, 827 (1968).

17. O. A. Mosher, W. M. Flicker, and A. Kuppermann, J. Chem. Phys. 59, 6502 (1973).

18. O. A. Mosher, M. S. Foster, W. M. Flicker, J. L. Beauchamp, and A. Kuppermann, J. Chem. Phys., to be published.

19. O. A. Mosher, W. M. Flicker, and Aron Kuppermann, J. Chem. Phys., to be published.

20. M. J. Coggiola, O. A. Mosher, W. M. Flicker, and A. Kuppermann, Chem. Phys. Letters 26, xxxx (1974).

21. W. R. Harshbarger, M. B. Robin, and E. N. Lassettre, J. Electron Spectrosc. 1, 319 (1972/73).

22. V. I. Makarov and L. S. Polak, High Energy Chem. 4, 1 (1970).

23. R. H. Huebner, R. J. Celotte, S. R. Mielczarek, and C. E. Kuyatt, J. Chem. Phys. 59, 5434 (1973).

24. W. R. Harschbarger, N. A. Kuebler, and M. B. Robin, J. Chem. Phys. 60, 345 (1974).

25. R. L. Platzman, Radiation Res. 17, 419 (1962); R. L. Platzman, Vortex 23, 372 (1962).

26. Y. Hatano, S. Shida, and S. Sato, Bull. Chem. Soc. Japan 41, 1120 (1968).

27. The author wishes to thank W. M. Flicker for measuring this 33° spectrum.

28. The corresponding N→T transition in C_2ClF_3 is located at 4.43 eV with a Franck-Condon band from 3.6 eV to 5.2 eV. See also Appendix E.

29. A. D. Walsh, Trans. Faraday Soc. 41, 35 (1945).

30. R. S. Mulliken, Chem. Phys. Letters 25, 305 (1974).

31. M. B. Robin, Int. J. Quantum Chem., Sym. No. 6, 257 (1972).

32. D. Reinke, Report number F41-73/6, Deutsches Elektronen-Synchrotron DESY, Hamburg, 1973.

33. G. Das Gupta and D. Phillips, J. Phys. Chem. 76, 3688 (1972).

34. T. V. Ivanova and B. YaSveshnikov, Optics and Spectrosc. 11, 322 (1961).

35. D. L. Dexter, J. Chem. Phys. 21, 836 (1953).

36. M. W. Schmidt and E. K. C. Lee, J. Am. Chem. Soc. 90, 5919 (1968).

37. M. W. Schmidt and E. K. C. Lee, J. Am. Chem. Soc. 92, 3579 (1970).

38. B. Atkinson, J. Chem. Soc. 2684 (1952).

39. A. R. Trobridge and K. R. Jennings, Trans. Faraday Soc. 61, 2168 (1965).

40. A. R. Trobridge and K. R. Jennings, Proc. Chem. Soc. (London) 335 (1964).

41. M. G. Bellas, Y. Rousseau, O. P. Strausz, and H. E. Gunning, J. Chem. Phys. 41, 768 (1964).

42. O. P. Strausz, R. J. Norstrom, D. Salahub, R. K. Gosavi, H. E. Gunning, and I. G. Csizmadia, J. Am. Chem. Soc. 92, 6395 (1970).

43. R. J. Cvetanovic´, Progr. React. Kinet. 2, 39 (1964).

Appendix E. Electron Impact Spectroscopy of Chlorotrifluoroethylene

During the course of the studies on the electronic spectra of the fluoro-substituted ethylenes (described in Part II), electron impact excitation spectra of chlorotrifluoroethylene (CTFE) were also measured. The results of those additional measurements are presented here. A complete study of CTFE (θ = 0° to 80°) was performed with an impact energy of 40 eV, while a few spectra were remeasured at E_0 = 25 eV and 60 eV for confirmation purposes. Representative spectra are shown in Figures E-1 - E-3, with cross section ratio and DCS curves given in Figures E-4 and E-5, respectively. A summary of the peak locations is given in Table 1, while the cross section ratio and DCS values are listed in Tables 2 and 3, respectively.

The CTFE sample was obtained from Matheson Gas Products, and prepared for use following the same procedure as for all other fluoroethylene samples. The raw data obtained at E_0 = 40 eV (25 eV and 60 eV, also) were analyzed following the same techniques outlined in Section 3 of Part II. The results reported here have a ± 0.05 eV uncertainty associated with the peak locations, while the uncertainty of the Franck-Condon band limits for the N → T transition is ± 0.1 eV.

Very little information exists on the electronic states of CTFE. The only spectroscopic study of CTFE in the energy region of interest is that of Lacker et. al. [1]. Absorption measurements in the 4.2 eV to 6.0 eV region showed a single feature with an onset of ~5.0 eV and extending beyond the upper limit of 6.0 eV.

Their measurements did not indicate the maximum intensity of this absorption, although at 5.3 eV, the extinction coefficient was only ~2. Hence, there is no means of determining to what transition this feature corresponds. Lacker et. al. do speculate that it may be due to the N→V transition, however the results of the present study indicate that it is more likely due to the N→3R transition. While Lacker et. al. may have seen the weak tail of the N→3R transition, overlap from the N→T band obscures the 5 eV region, so that this possibility cannot be ruled out. In any case, no previous spectra covering the range from 3 eV to 10 eV have been published.

The photoelectron spectrum of CTFE has been obtained by Lake and Thompson [2] using HeI radiation. Their results yielded a first I.P. of 10.24 eV (vertical) with successive I.P.s at 13.01, 13.66, 15.11 eV and higher. Using a simple MO treatment, Landau et. al. [3] calculated the first I.P. of CTFE to be 9.81 eV, in reasonable agreement with experimental findings.

Figure E-1 and E-2 show the energy-loss spectra of CTFE for $E_0 = 40$ eV and $\theta = 0^\circ$ and 80°, respectively. The first inelastic feature has an onset at 3.6 eV, extending to 5.2 eV with a peak at 4.43 eV. This absorption is assigned to the singlet→triplet, $\pi \rightarrow \pi^*$ transition corresponding to the N→T transition in ethylene. The strongest feature in each spectrum is the fully-allowed singlet→singlet $\pi \rightarrow \pi^*$ transition corresponding to the N→V absorption in ethylene. The peak of this band is at 7.80 eV. This peak location is within the range of values found for the N→V transitions in all of the fluoroethylenes, except

tetrafluoroethylene. This is in spite of the fact that CTFE, like tetrafluoroethylene, is a fully halogenated ethylene, and the latter molecule showed a very large hypsochromic shift in the N→V transition energy. As pointed out in ection 3.4.3 of Part II, a possible explanation of this difference between CTFE and tetrafluoroethylene lies in the effect of the configuration mixing between the C-C-X σ and π orbitals.

In addition to the N→T and N→V absorptions, several members of the 3R Rydberg series are also seen, especially in Figure E-1. The most prominent feature is the N→3s transition peaking at 6.51 eV. This and several other Rydberg transition energies are listed in Table 1. Figure E-3 shows a 10° spectrum of CTFE for E_0 = 60 eV covering the 6 eV to 16 eV energy-loss region. A number of superexcited state transitions are apparent above the first I.P. of 10.24 eV. These transition energies are also listed in Table 1. Following the term value approach used in analyzing many of the peaks in the fluoroethylenes, several of the Rydberg and superexcited state transitions have been identified (see Table 1).

Plots of the ratio of the area under the N→T transition with respect to the area under the N→V transition are shown in Figure E-4 for each angle measured from 10° to 80° (see Table 2). This curve is quantitatively similar to those found for each of the fluoroethylenes, and hence confirms the assignment of the forbidden singlet→triplet (N→T) transition. Further confirmation of the peak assignments is found in Figure E-5, which shows the

differential cross sections for the elastic, N→V and N→T peaks (see also Table 3).

In their studies of the quenching cross sections of Hg 6^3P_1 resonance radiation by substituted ethylenes, Bellas et. al. [4] included CTFE. They found from their results, a quenching cross section of $27.0A^2$ for CTFE. This value is to be compared with $\sim 31A^2$ for ethylene, determined in the same study. This similarity in cross sections is most likely due to the comparable locations and Franck-Condon bands of the N→T transition in each molecule.

In summary, then, the electronic structure of CTFE as determined by electron impact spectroscopy is very similar to the fluoro-substituted ethylenes other than tetrafluoroethylene.

Table 1

Ground to Excited State Transition Energies of Chlorotrifluoroethylene (in eV)

N → T			4.43 (3.6 - 5.2)[a]	
N → V			7.80	
			Term Value	Assignment
N → R	(I.P. = 10.24	6.51	3.74	3s
		7.79	2.45	3p
		8.26	1.98	4s
		8.50	1.74	3d
		8.94	1.30	4p
		9.60	0.64	5s
	(I.P. = 13.01)	10.30	2.71	3p
		11.40	1.61	4s
N → Superexcited State		11.0		
		12.0		
		12.7		
		13.3		
		14.4		
		15.4		

[a]Estimated Franck-Condon Region

Table 2

Ratio of Intensity of the (N → T) Transition to the (N → V) Transition for Chlorotrifluoroethylene

E_o = 40 eV

θ (deg)	Ratio
10	0.005
20	0.020
30	0.037
40	0.052
50	0.095
60	0.118
70	0.129
80	0.153

Table 3

Differential Cross Sections (DCS) for Chlorotrifluoroethylene

(Normalized to 1.0 at 40°)

E_o = 40 eV

θ (deg)	Elastic	N→V	N→T
20	7.21	0.261	0.00207
30	2.90	0.141	0.00231
40	1.00	0.088	0.00251
50	0.771	0.050	0.00225
60	0.553	0.042	0.00231
70	0.398	0.030	0.00240
80	0.310	0.021	0.00216

Figure E-1: Energy-loss spectrum of chlorotrifluoroethylene (CTFE) taken at $\theta = 0^{\circ}$, $E_o = 40$ eV, resolution = 58 meV, scattering chamber pressure = 4.8 mtorr.

Figure E-2: Energy-loss spectrum of CTFE taken at $\theta = 80^{\circ}$, $E_o = 40$ eV, resolution = 125 meV, scattering chamber pressure = 3.3 mtorr.

Figure E-3: Energy-loss spectrum of CTFE taken at $\theta = 10^{\circ}$, $E_o = 60$ eV, resolution = 125 meV, scattering chamber pressure = 3.1 mtorr.

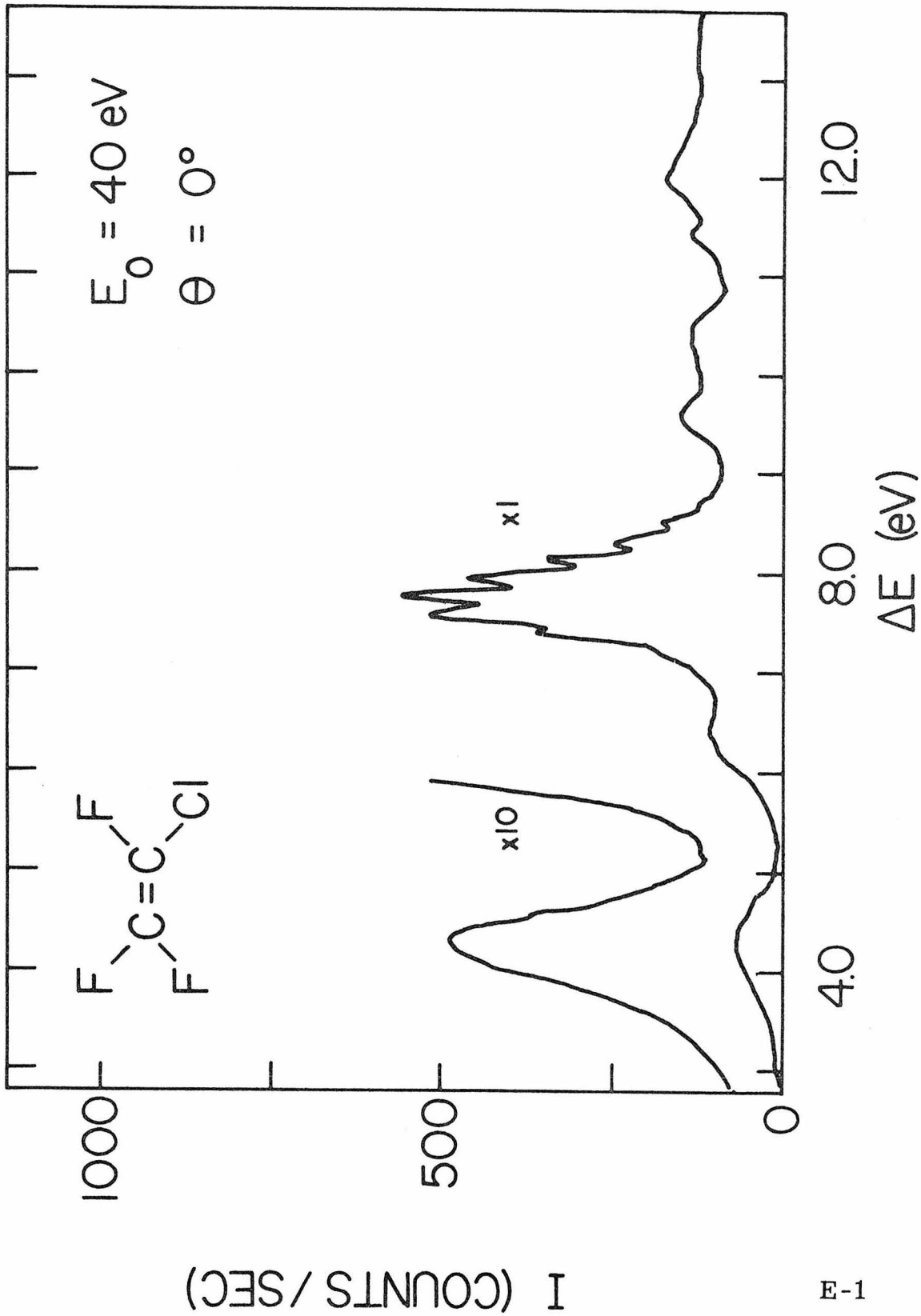

E-1

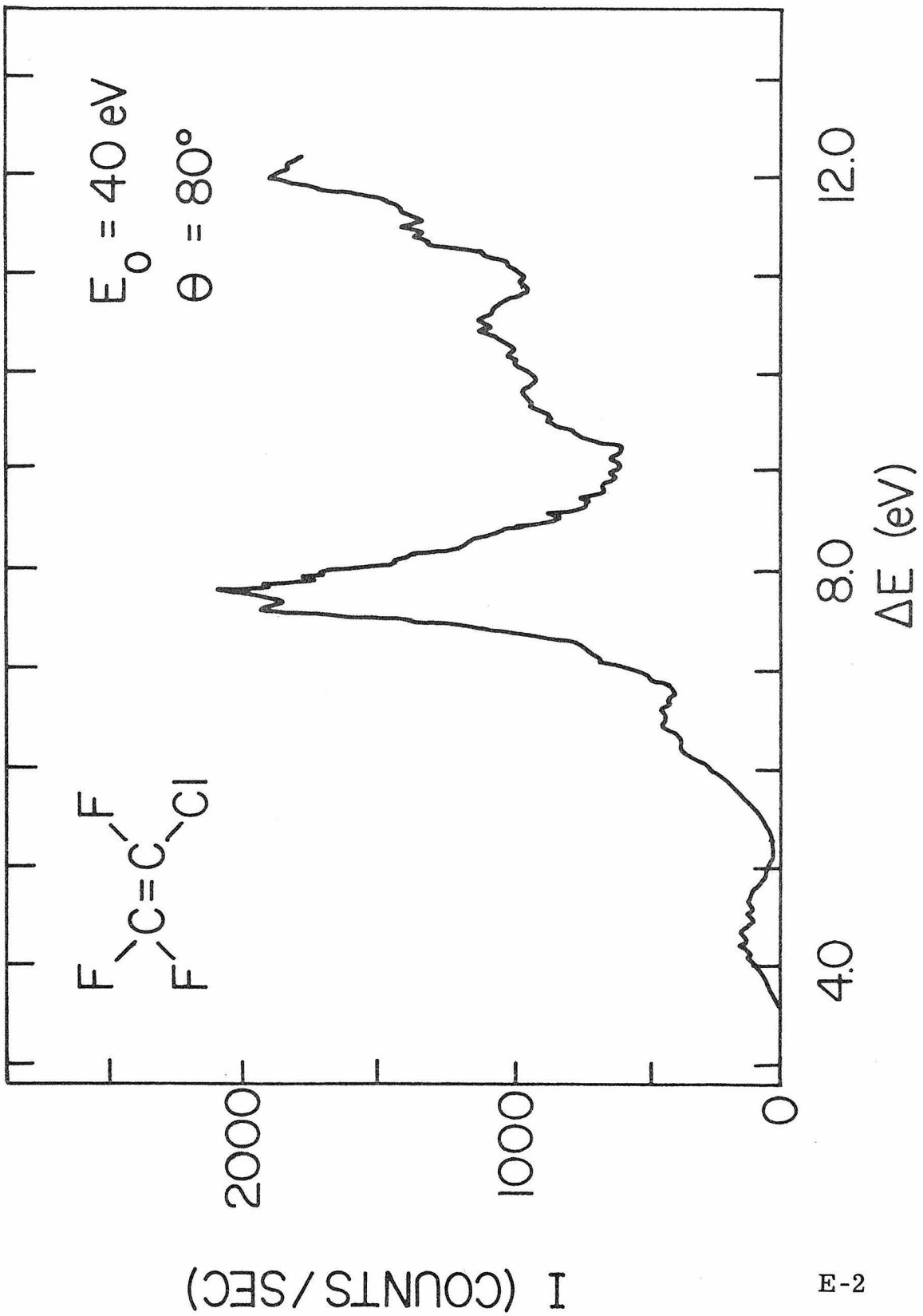
$E_0 = 40$ eV
$\Theta = 80°$
F
C=C
F
F
Cl
I (COUNTS/SEC)
2000
1000
0
4.0
8.0
12.0
ΔE (eV)

E-2

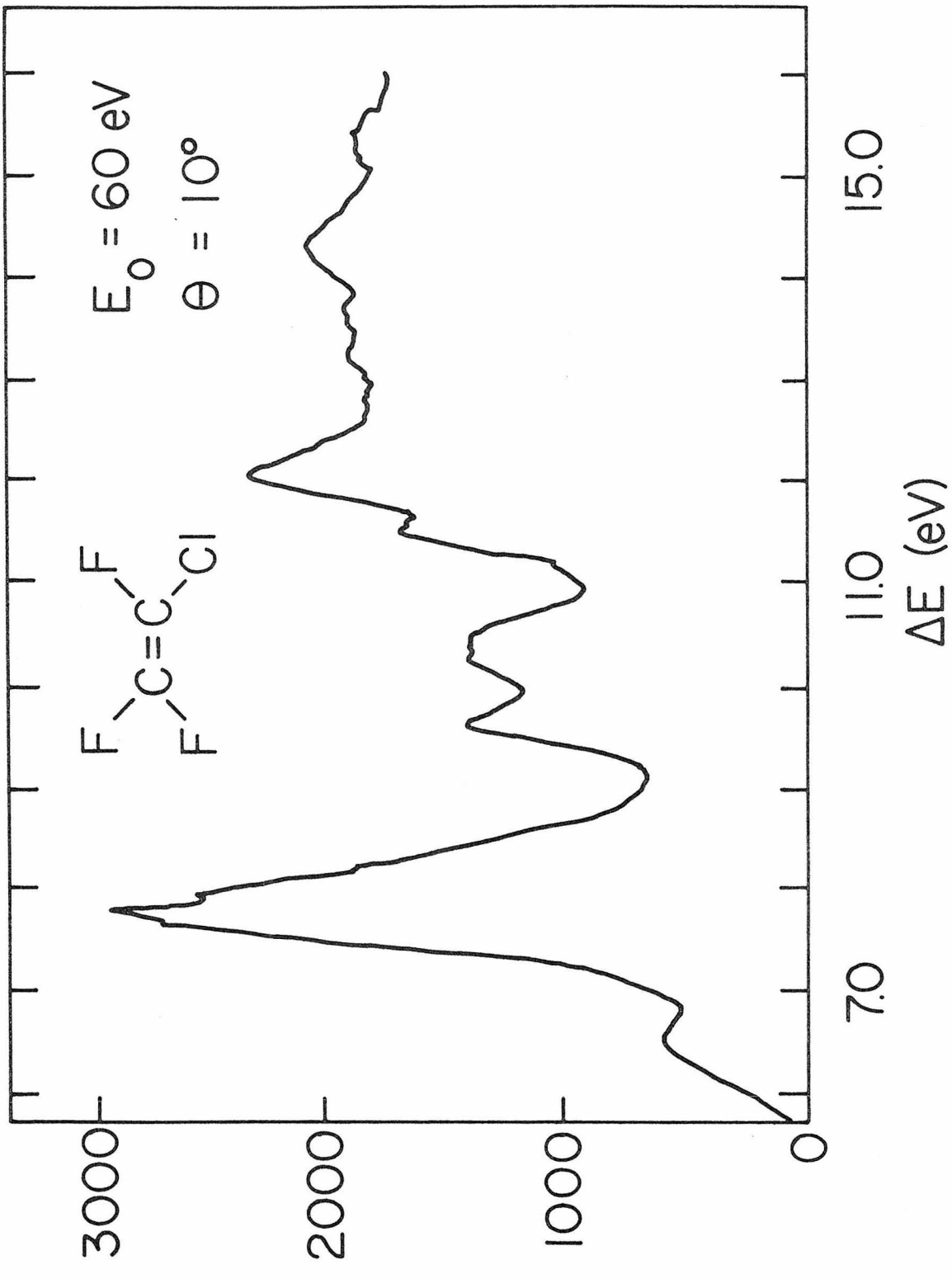
$E_0 = 60$ eV
$\theta = 10°$
F
C=C
F
F
Cl
I (COUNTS/SEC)
3000
2000
1000
0
7.0
11.0
15.0
ΔE (eV)

E-3

Figure E-4: Plot of the ratio of the area under the N→T transition to that under the N→V transition for CTFE at E_o = 40 eV.

Figure E-5: Differential cross section (DCS) plots for CTFE at 40 eV impact energy. The circles (○) correspond to the elastic DCS × 0.1, the squares (□) to the N→T DCS, and the triangles (Δ) to the N→V DCS. The 40° elastic DCS value has been arbitrarily set to 1.0

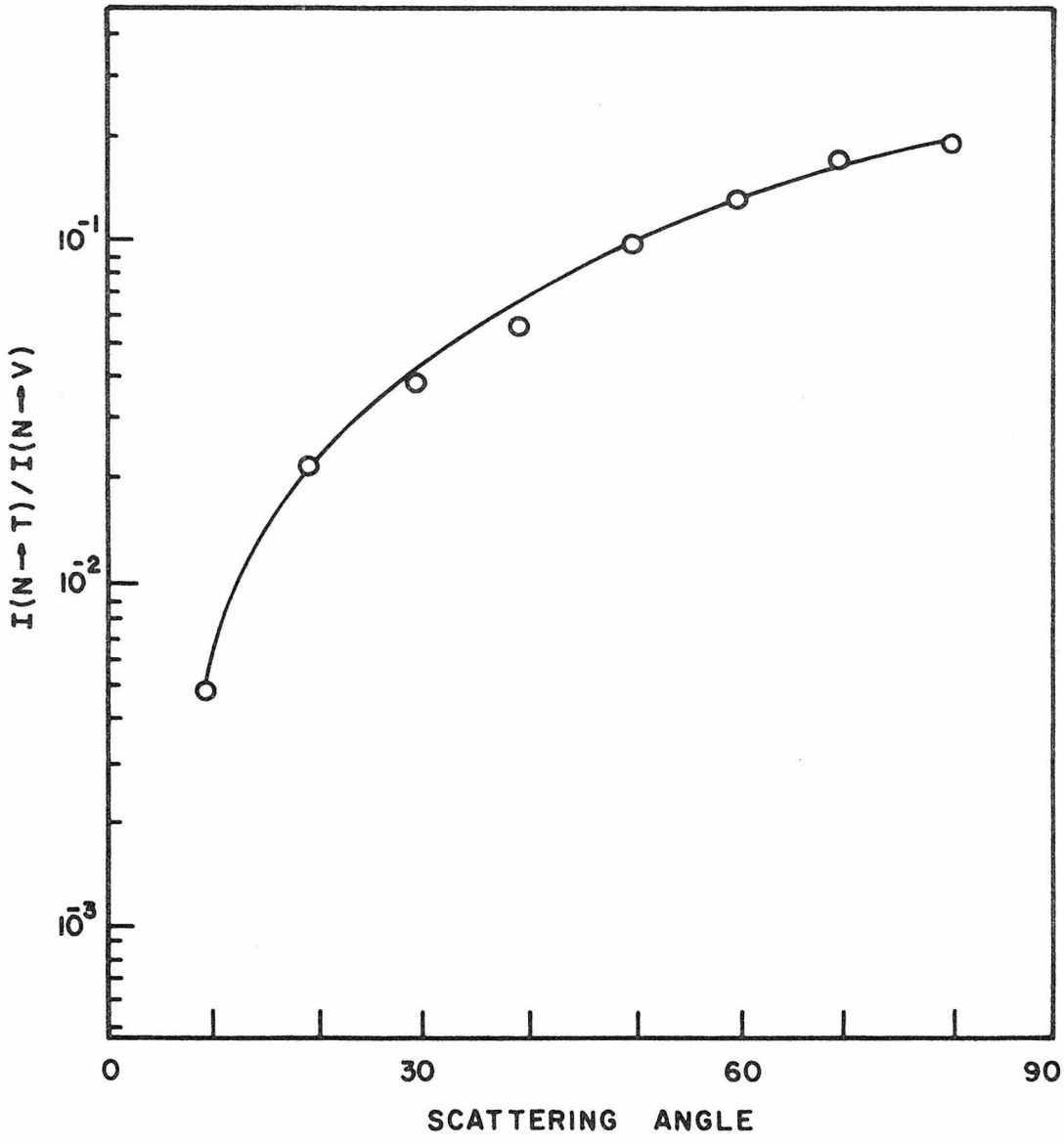

E-4

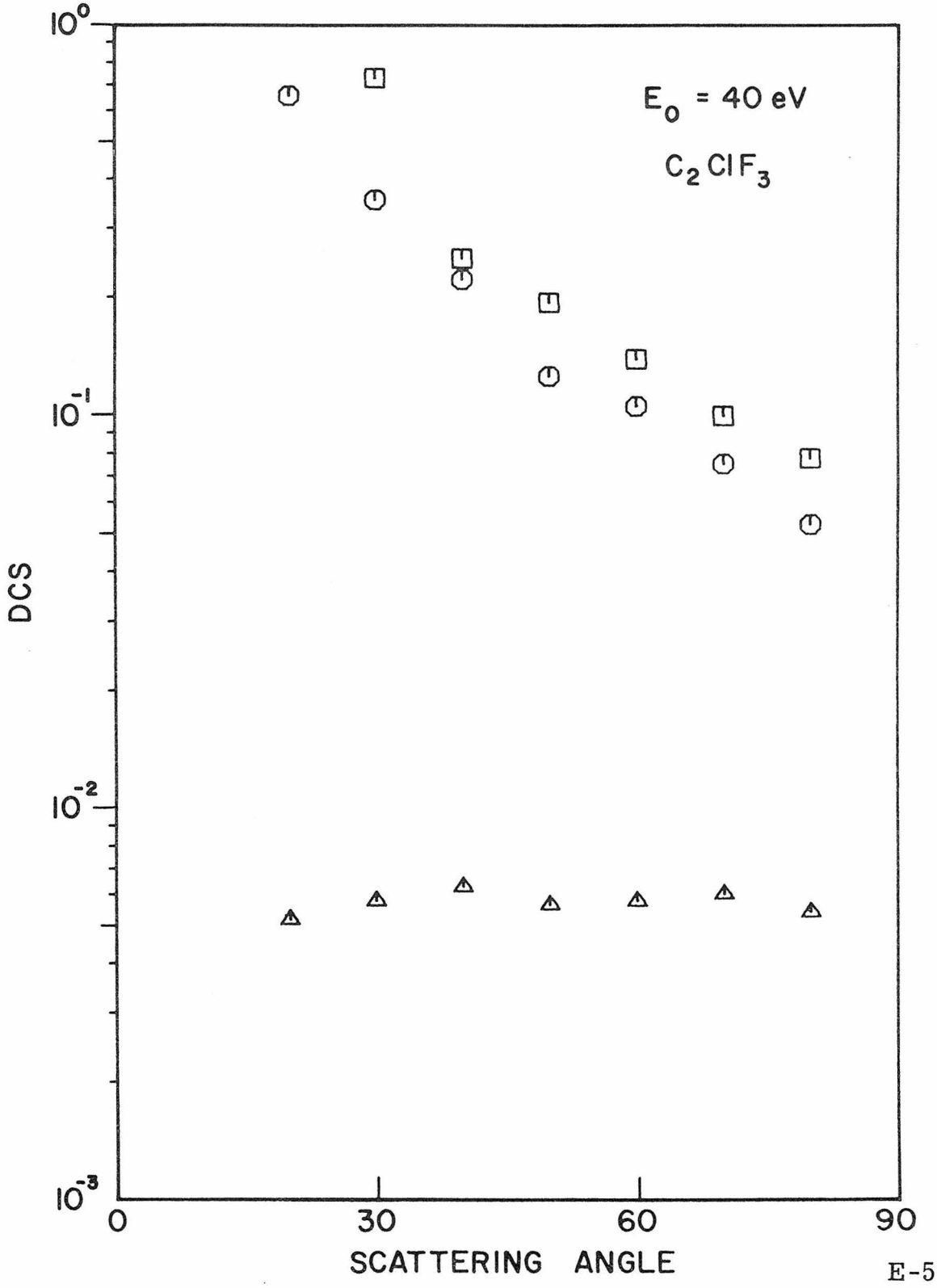

E-5

References

1. J. R. Lacker, L. E. Hummel, E. F. Bohmfolk, and J. D. Park, J. Am. Chem. Soc. 72, 5486 (1950).
2. R. F. Lake and Sir H. Thompson, Proc. Roy. Soc. (London) A315, 323 (1970).
3. M. A. Landau, V. V. Sheluchenko, S. S. Dubov, and V. A. Ivanov, Russ. J. Phys. Chem. 42, 835 (1968).
4. M. G. Bellas, Y. Rousseau, O. P. Strausz, and H. E. Gunning, J. Chem. Phys. 768 (1964).